FERMILAB-THESIS-2011-33

Charmed Baryon Spectroscopy and Search for CP Violation in $D^0 \to K^0_S \pi^+ \pi^-$ at CDF

Zur Erlangung des akademischen Grades eines

Doktors der Naturwissenschaften

von der Fakultät für Physik des
Karlsruher Institut für Technologie (KIT)

genehmigte

Dissertation

von

Dipl.-Phys. Felix Wick

aus Zweibrücken

Tag der mündlichen Prüfung:	28. Oktober 2011
Referent:	Prof. Dr. M. Feindt
Korreferent:	Prof. Dr. G. Quast

Operated by Fermi Research Alliance, LLC under Contract No. DE-AC02-07CH11359 with the United States Department of Energy

Contents

1. Introduction

Particle physics is the science of the fundamental matter in nature and its interactions. Since the dimensions of the elementary particles, the quarks and leptons, are very small, at least eight orders of magnitude smaller than atoms, the findings are theoretically described in the context of quantum field theories. The current knowledge is summarized in the Standard Model of elementary particle physics, the basic aspects of which are outlined in Chapter 2.

High energy densities are needed to experimentally probe the principles of particle physics. For that purpose large particle accelerators are used to collide electrons, protons, or the corresponding antiparticles with almost the speed of light. In these collisions, resembling the conditions in the universe shortly after the big bang, many new and sometimes heavy particles are created according to Einstein's mass-energy equivalence. After a usually short lifetime they decay to lighter ones and can be identified by their specific signatures in large particle detectors. For this work, data accumulated with the CDF II detector at the Tevatron proton-antiproton collider located at Fermilab are used. The Tevatron collider and the CDF II detector are described in Chapter 3.

Because of the mentioned quantum character and the vast number of examined particle collisions, statistical methods are applied to extract the quantities of interest from the collected data samples. For instance, the desired signal events can be selected by means of artificial neural networks combining several properties of the studied decay signatures. The statistical tools employed in this work are briefly discussed in Chapter 4.

The strong interaction, one of the four fundamental forces in nature, is responsible for the formation of nucleons out of the two lightest quarks referred to as up and down. Also heavier versions of the nucleons, generally called baryons, can be built by the strong interaction with the help of the heavier quark flavors. A specific example is the Λ_c^+, where one up quark is substituted by a charm quark. The first of two separate analyses presented in this work deals with precision measurements of the properties of $\Lambda_c(2595)^+$, $\Lambda_c(2625)^+$, $\Sigma_c(2455)^{++,0}$, and $\Sigma_c(2520)^{++,0}$ baryons and is described in Chapter 5. All these baryons contain a charm quark and a combination of two light quarks. They correspond to orbital angular momentum ($\Lambda_c(2595)^+$, $\Lambda_c(2625)^+$) and isospin ($\Sigma_c(2455)^{++,0}$, $\Sigma_c(2520)^{++,0}$) excitations of the groundstate Λ_c^+. In the analysis at hand the masses and widths of the mentioned charmed baryons are measured in their decays to the final states $\Lambda_c^+\pi^+\pi^-$ and $\Lambda_c^+\pi^\pm$ with $\Lambda_c^+ \to p\,K^-\,\pi^+$. The large number of charmed baryons collected by the

CDF II detector allows to determine these resonance parameters with high precision. This is especially important as previous measurements are based on rather small data samples and some of the reported results are inconsistent.

The second analysis, presented in Chapter 6, is a search for CP violation in the Dalitz plot of the decay $D^0 \to K^0_S \pi^+ \pi^-$. A CP violating process proceeds with a different rate when all involved particles are substituted by their antiparticles, referred to as charge conjugation C, and a spatial reflection through the point of origin, a so-called parity transformation, is performed. CP violating effects are only present in weak interactions transferring one quark flavor into another. In the studied process $D^0 \to K^0_S \pi^+ \pi^-$ a charm quark, enclosed in the D^0, decays to a strange quark, ending up in the K^0_S. In the past decades CP violation was observed in the strange and bottom quark sectors in decays of K and B mesons. These effects can be explained within the Standard Model by means of the Kobayashi-Maskawa mechanism. But CP violation is expected to be very small in the charm sector, that is in decays of D mesons. So any CP asymmetric processes found at the current experimental sensitivity would be a strong hint for physics beyond the Standard Model. However, up to now no such CP asymmetries could be detected. In this analysis the Dalitz plot technique is used to search for asymmetries in the resonant substructure of the D^0 and $\bar{D}^0$ three-body decays, where the production flavor, D^0 or $\bar{D}^0$, is determined by reconstructing the preceding decay $D^*(2010)^+ \to D^0 \pi^+$ and looking for the pion charge.

A conclusion of this work is finally given in Chapter 7.

2. Standard Model of Elementary Particle Physics

The Standard Model of elementary particle physics [1] classifies all known matter into two groups of fundamental particles, the quarks and the leptons. These are arranged in three generations each. Besides the electron, also its heavier counterparts, the muon and the tau, belong to the leptons, as well as an associated neutrino for each. Whereas electron, muon, and tau carry one elementary charge, neutrinos are uncharged. The first generation of quarks consists of the up and the down quark, which are the basic building blocks of the proton and the neutron. The up quark carries $+\frac{2}{3}$ and the down quark $-\frac{1}{3}$ of the elementary charge. In the second and third generation they are substituted by the charm and strange respective top and bottom quarks, in which the particle masses increase from generation to generation. Aside, there exist antiparticles for all quarks and leptons that carry the opposite charge than their corresponding particle.

All these elementary particles are subjected to four different interactions, the strong, the weak, and the electromagnetic interaction, as well as the gravitation. However, the gravitation is not included in the framework of the Standard Model. The other three fundamental forces are described by means of quantum field theories which explain the corresponding force mediation by the exchange of interaction specific gauge bosons with spin quantum number 1. On the contrary, the quarks and leptons are fermions with spin quantum number $\frac{1}{2}$. The strength of the different interactions are characterized by dimensionless coupling constants α that generally depend on the involved momentum transfer.

Within the Standard Model, electromagnetic forces are described by the theory of quantum electrodynamics (QED). In that they are caused by the exchange of massless and uncharged photons which couple to the electric charge of the quarks and leptons. Because of the vanishing rest mass of the photon the range of the electromagnetic force is infinite.

Quantum chromodynamics (QCD) [2, 3] is the theory of the strong interaction, in which the role of the electric charge is taken over by the so-called color charge. Each quark carries such a charge in one of the illustrating colors red, green, or blue. Antiquarks carry the corresponding anticolors. Leptons carry no color charge and thus do not interact strongly. With the three color charges of the QCD, instead of the single electric charge of the QED, follows an exact SU(3) color symmetry. This leads to the existence of eight massless propagator particles, referred to as gluons,

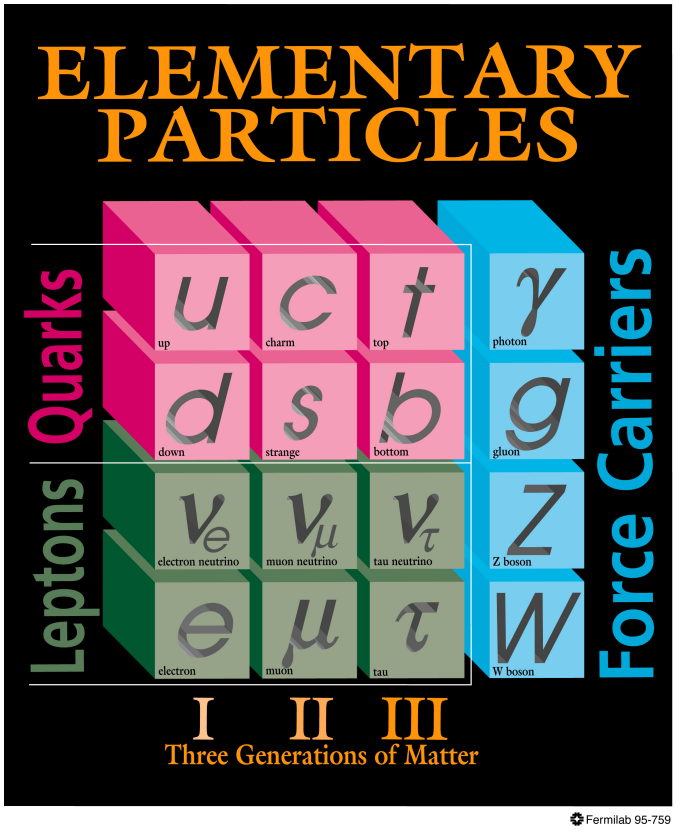

Figure 2.1.: The Standard Model of elementary particles. [4]

that carry color and anticolor at the same time. Corresponding to the SU(3) rule of group theory,

$$3 \otimes \bar{3} = 8 \oplus 1\,, \tag{2.1}$$

there is an additional singlet besides the mentioned gluon octet. However, because of its invariance towards rotations in the color space this singlet is not exchanged between color charges. Since gluons carry color charges themselves, they also interact between each other, what in turn leads to a short range of the strong force.

The weak force is mediated by three gauge bosons, the electrically neutral Z^0 with a rest mass of about $91\,\mathrm{GeV}/c^2$ and the charged $W^\pm$ which are emitted in the decays of heavier to lighter quarks. Their rest mass amounts about $80\,\mathrm{GeV}/c^2$. The high masses of the gauge bosons lead to the relative weakness at low energies and a very short range of the weak interaction. However, it affects all quarks and leptons and thus is the only force, except for the gravitation, that has an effect on neutrinos.

An overview of the elementary particles described above is shown in Figure 2.1. In the following, Standard Model aspects of importance for this work are described

in more detail.

2.1. Particle Zoo

The strong interaction facilitates the formation of compound quark states which fulfill the requirement of color neutrality. These particles are called hadrons and exist in some variety, what motivated the term of the particle zoo. Possible occurrences are combinations of a quark and an antiquark, so-called mesons, or of three quarks respective three antiquarks, referred to as baryons.

The reason for the requirement of color neutrality is the observation that quarks are never found out of hadrons, what means that they do not exist as free particles. This property of the strong interaction is referred to as confinement and is based on the self-interaction of gluons, which leads to an increase of the strong coupling constant α_s with the distance between two color charged objects. If a quark and an antiquark, produced as pair in a high energetic particle reaction, move away from each other, their relative potential increases and at a distance of about 10^{-15} m the energy is sufficient for the production of an additional quark-antiquark pair, what results in the formation of two color neutral mesons that include all involved quarks and antiquarks. This process, including the corresponding situation where two quark-antiquark pairs are produced to build two baryons, is called hadronization.

On the other hand, at small distances the potential of the strong interaction between two quarks is very low. This property, called asymptotic freedom, implies that the quarks can be treated as nearly free particles, allowing calculations in the framework of perturbation theory. Besides the mentioned constituents, the so-called valence quarks, there exist also gluons and sea quarks in the hadrons. These virtual particles are continually produced and annihilated by the strong interaction. Because their quantum numbers cancel in average, they can be neglected for the classification of the various hadrons.

For energetic reasons heavy hadrons decay to lighter particles, where the decay times are very different for the three interactions. Because of their particle-antiparticle structure all mesons finally end as leptons or photons. However, the lightest baryon, the proton, is stable due to the conservation of baryon number. In order to observe mesons or heavier baryons they have to be produced first. For this purpose, stable or long lived particles are accelerated to high energies and subsequently brought to collision. In this way a large variety of particles with different quark contents could be observed in the course of time.

2.1.1. Mesons

Since quarks are spin-$\frac{1}{2}$ particles, mesons can have two different spin quantum numbers s. For a parallel orientation of the two quark spins, one gets $s = 1$,

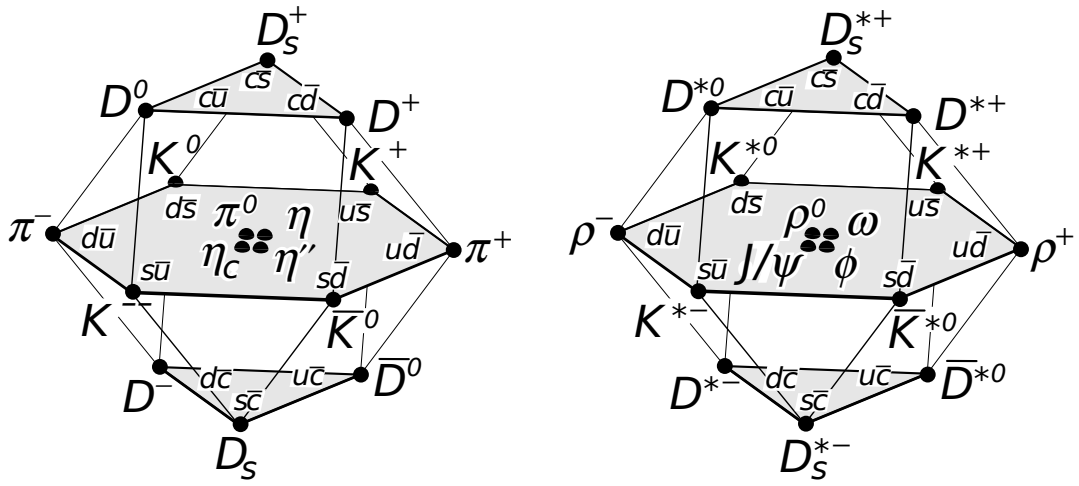

Figure 2.2.: Pseudoscalar (left) and vector meson multiplets (right) including the four lightest quarks. [1]

for an antiparallel orientation $s = 0$. That means s is an integer value and thus mesons are bosons. If there is no orbital excitation, meaning the value of the orbital angular momentum quantum number l is zero, the mesons with $s = 1$ are referred to as vector mesons, the ones with $s = 0$ are called pseudoscalars. The vector mesons have the quantum numbers $J^P = 1^-$ and the pseudoscalar mesons $J^P = 0^-$. Thereby, J is the total angular momentum resulting from the spin and orbital angular momentum as $|l - s| < J < |l + s|$, and P is the parity. It follows $P = (-1)^{l+1}$ because $P = 1$ is assigned to quarks and $P = -1$ to antiquarks.

Neglecting the mass differences between the three lightest quark flavors (u,d,s), the different light mesons can be classified by means of the SU(3) flavor symmetry. According to Equation 2.1, the resulting states are arranged in an octet and a singlet. By including the charm quark, the described symmetry can be expanded to a SU(4) symmetry. However, this symmetry is stronger broken because of the higher mass of the charm quark. Thus, the different states have clearly distinct masses according to their quark contents. Following

$$4 \otimes \bar{4} = 15 \oplus 1\,, \tag{2.2}$$

there are 16 particles which are arranged in Figure 2.2, vertically after their charm contents and horizontally after their strange contents and isospin. Those are the pseudoscalar and the vector mesons in their ground state without orbital angular momentum or radial excitation. Just like for atoms, the hadron masses increase with higher radial or orbital angular momentum excitations, as well as parallel spin orientation of their constituent quarks. Therefore, the vector mesons are heavier than the corresponding pseudoscalar mesons.

2.1.2. Baryons

Baryons consist of three valence quarks and are therefore fermions with spin quantum numbers $s = \frac{1}{2}$ or $s = \frac{3}{2}$. So they have to obey the Pauli principle and their state function,

$$\mid qqq\rangle_A = \mid \text{color}\rangle_A \cdot \mid \text{space, spin, flavor}\rangle_S \,, \tag{2.3}$$

is antisymmetric under the interchange of any two quarks. Since all bound states are color singlets, $\mid \text{color}\rangle$ is always antisymmetric, what requires the rest of the state function to be symmetric. In case of a vanishing orbital excitation $l = 0$, $\mid \text{space}\rangle$ is symmetric. The spin part is also symmetric for $s = \frac{3}{2}$, but has a mixed symmetry for $s = \frac{1}{2}$.

Taking into account only the three lightest quark flavors (u, d, s) and referring to SU(3) symmetry, there exists a baryon multiplet structure of

$$3 \otimes 3 \otimes 3 = 10_S \oplus 8_M \oplus 8_M \oplus 1_A \,, \tag{2.4}$$

one decuplet, two octets and one singlet. The subscripts mean symmetry (S), antisymmetry (A), or mixed symmetry (M) under the interchange of any two quarks. Therefore, $s = \frac{3}{2}$ can be assigned to the decuplet and $s = \frac{1}{2}$ to the two octets. The antisymmetric singlet state is forbidden for $l = 0$.

Like for mesons, the SU(3) symmetry can be expanded to a stronger broken SU(4) symmetry by including the charm quark. Following

$$4 \otimes 4 \otimes 4 = 20_S \oplus 20_M \oplus 20_M \oplus 4_A \,, \tag{2.5}$$

four SU(4) multiplets can be built for the baryons including the four lightest quarks, basing on the SU(3) multiplets from Equation 2.4. All constituents of a particular multiplet have the same quantum numbers J^P. In Figure 2.3 two different ground state SU(4) multiplets are shown, one with the SU(3) decuplet and one with the SU(3) nucleon octet in the ground plane. That means the first one has the quantum numbers $J^P = \frac{3}{2}^+$ and the second one $J^P = \frac{1}{2}^+$, where the parity of baryons is calculated as $P = (-1)^l$. For the excited states there exist also 20-plets or quadruplets with the corresponding quantum numbers. The quadruplet states must have at least $l = 1$ because the antisymmetric ground state is forbidden. This results in the quantum numbers $J^P = \frac{3}{2}^-$ or $J^P = \frac{1}{2}^-$, respectively.

2.2. CP Violation

The gravitational, electromagnetic, and strong interactions are invariant under the discrete transformations of parity P, meaning the spatial reflection through the point of origin, charge conjugation C, and time reversal T. However, the weak interaction violates P and C maximally. This is expressed in the observation that

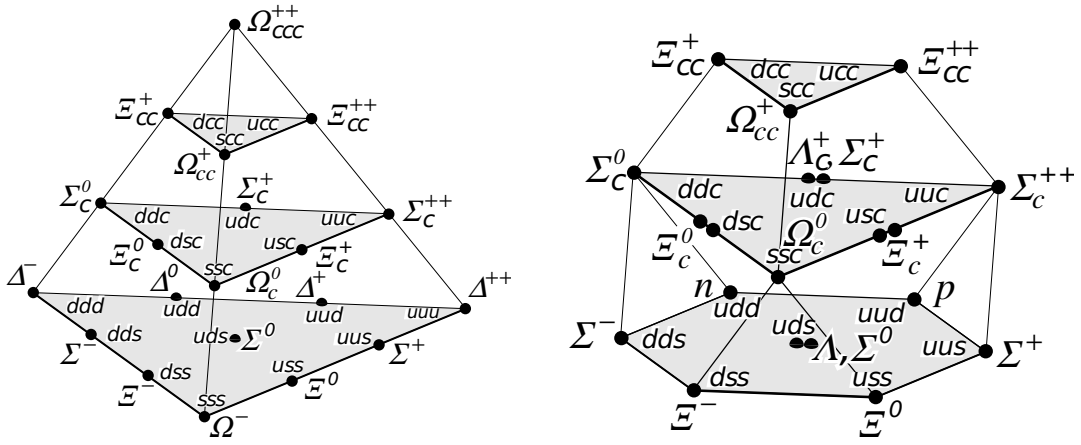

Figure 2.3.: Baryon multiplets including the four lightest quarks with the quantum numbers $J^P = \frac{3}{2}^+$ (left) and $J^P = \frac{1}{2}^+$ (right). [1]

only left-handed neutrinos and right-handed antineutrinos exist, where right(left)-handed means that the spin of the neutrino points in the (opposite) direction of its momentum.

Whereas the combined CPT symmetry is conserved for all quantum field theories, the CP and thus also the T symmetry are violated in the weak interaction. The origin of this CP violation in the Standard model and the different occurring CP violating effects are described in the following.

2.2.1. CKM Matrix

In the Standard Model, the CP violation in weak interactions is explained by the Cabibbo-Kobayashi-Maskawa (CKM) mechanism [5, 6] which describes the mixing of quarks by the coupling of an up-type and a down-type quark to a $W^{\pm}$ boson. The particular strength of these couplings is given by the unitary CKM quark mixing matrix

$$V = \begin{pmatrix} V_{ud} & V_{us} & V_{ub} \\ V_{cd} & V_{cs} & V_{cb} \\ V_{td} & V_{ts} & V_{tb} \end{pmatrix} , \tag{2.6}$$

where the subscripts indicate the two involved quark types. This interaction represents the only process in the Standard Model that allows to change the quark flavors.

The CKM matrix is composed of four physical parameters, for instance three real mixing angles and one imaginary, CP violating phase. The so-called Wolfenstein

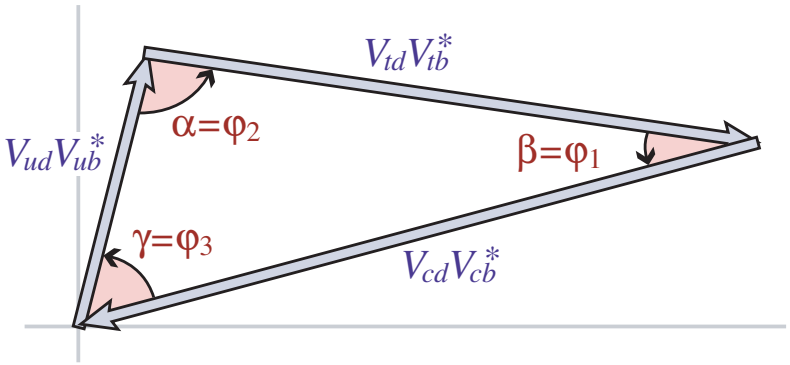

Figure 2.4.: One of the unitarity triangles of the CKM matrix. The enclosed area is proportional to the amount of CP violation. [1]

parametrization is an expansion approach of the CKM matrix given by

$$V = \begin{pmatrix} 1-\lambda^2/2 & \lambda & A\lambda^3(\rho - i\eta) \\ -\lambda & 1-\lambda^2/2 & A\lambda^2 \\ A\lambda^3(1-\rho-i\eta) & -A\lambda^2 & 1 \end{pmatrix} + \mathcal{O}(\lambda^4) \tag{2.7}$$

where the four parameters are named λ, A, ρ, and η, the latter being the CP violating phase and $\lambda \approx 0.22$ the expansion parameter. This parametrization shows the hierarchical structure of the CKM matrix, the diagonal elements being near to 1 and the off-diagonal elements small, especially V_{ub} and V_{td}.

The unitarity constraint of the CKM matrix causes several relations among the different matrix elements, the most famous one being

$$V_{ud}V_{ub}^* + V_{cd}V_{cb}^* + V_{td}V_{tb}^* = 0\,. \tag{2.8}$$

The graphical representation of this relation is a triangle in the complex plane shown in Figure 2.4. The amount of CP violation in the Standard Model is proportional to the enclosed area in this unitarity triangle, and can thus be expressed by the three marked CKM angles.

2.2.2. Types of CP Violating Effects

CP violation shows up in several occasions that can be divided into three categories, direct CP violation, indirect CP violation, and CP violation in the interference of mixing and decay. These different types are described in the following by means of a few examples.

Indirect CP Violation

The neutral mesons K^0, D^0, B^0, and B_s^0 can mix with their charge conjugate states through so-called box diagrams, second-order processes of the weak interaction.

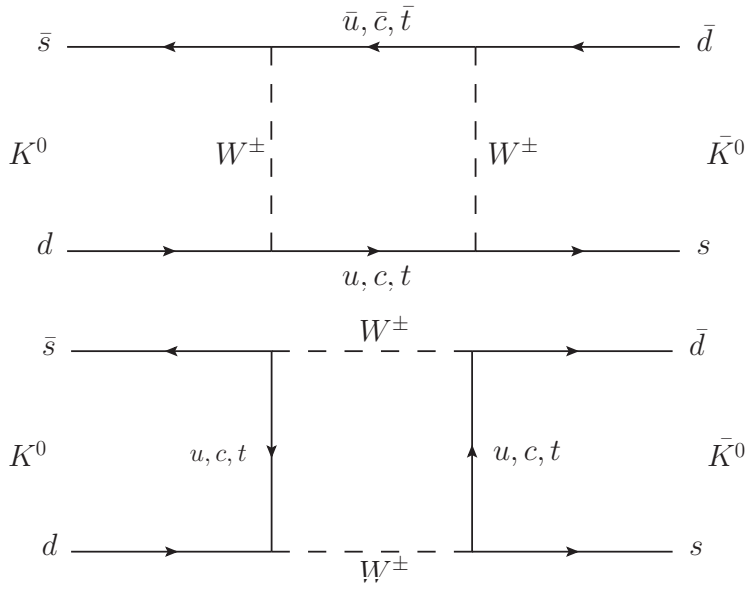

Figure 2.5.: Box diagrams for the K^0-$\bar{K^0}$ mixing.

The K^0-$\bar{K^0}$ mixing is illustrated by Figure 2.5.

It leads to the definition of

$$\begin{aligned} \mid K_1^0\rangle &= \frac{1}{\sqrt{2}}(\mid K^0\rangle + \mid \bar{K^0}\rangle)\,, \\ \mid K_2^0\rangle &= \frac{1}{\sqrt{2}}(\mid K^0\rangle - \mid \bar{K^0}\rangle) \end{aligned} \tag{2.9}$$

as CP eigenstates of the neutral kaons, where K_1^0 is CP-even ($CP \mid K_1^0\rangle = \mid K_1^0\rangle$) and K_2^0 is CP-odd ($CP \mid K_2^0\rangle = -\mid K_2^0\rangle$). Since C and P are multiplicative quantum numbers, the two- and three-pion final states are assigned as

$$\begin{aligned} K_1^0 &\to \pi\,\pi\,, \\ K_2^0 &\to \pi\,\pi\,\pi\,, \end{aligned}$$

where the decay to two pions has a much smaller lifetime because of more available phase space.

However, it turns out that the long-lived neutral kaon decays with a probability of about 10^{-3} to the two-pion final state [7]. So the CP eigenstates K_1^0, K_2^0 are not the exact mass eigenstates. These are given by

$$\begin{aligned} \mid K_S^0\rangle &= \frac{1}{\sqrt{1+|\epsilon|^2}}(\mid K_1^0\rangle + \epsilon \mid K_2^0\rangle)\,, \\ \mid K_L^0\rangle &= \frac{1}{\sqrt{1+|\epsilon|^2}}(\epsilon \mid K_1^0\rangle + \mid K_2^0\rangle)\,, \end{aligned} \tag{2.10}$$

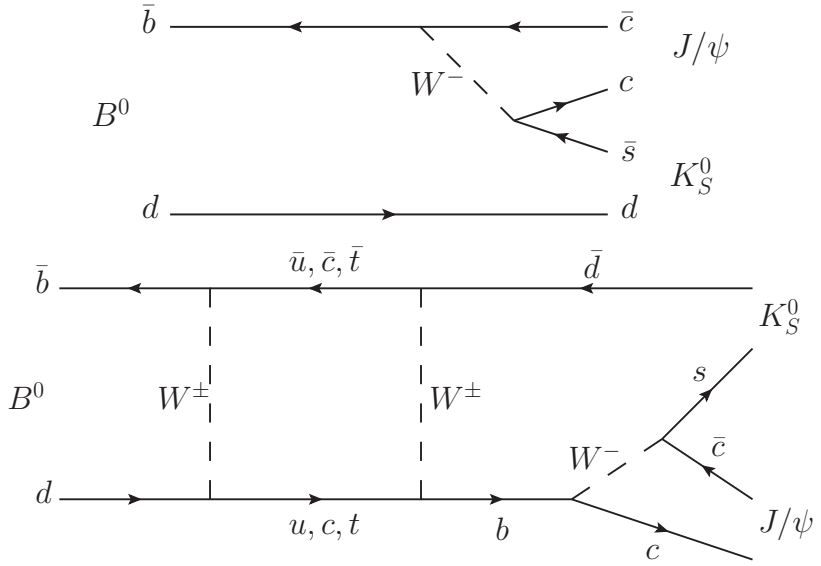

Figure 2.6.: $B^0 \to J/\psi\, K_S^0$ decay processes with and without B^0-$\bar{B}^0$ mixing, the interference of which leads to CP violation.

where the subscripts indicate the short respective long lifetime and ϵ represents the extent of indirect CP violation in the K^0-$\bar{K}^0$ mixing.

Direct CP Violation

Direct CP violation is defined as a difference between the decay rates of a specific process and its CP conjugate process. An example for this type of CP violation is the decay $B^0 \to K^+\,\pi^-$, meaning that the rate of $B^0 \to K^+\,\pi^-$ is unequal the one of $\bar{B}^0 \to K^-\,\pi^+$. For charged particles this is the only possibility for CP violation.

CP Violation in Interference of Mixing and Decay

A kind of combined type of CP violation can appear if mixing neutral mesons, for instance B^0, decay to a final state which is accessible from both B^0 and $\bar{B}^0$, that is a CP eigenstate. The most prominent example is the decay $B^0 \to J/\psi\, K_S^0$, for which the involved processes are illustrated in Figure 2.6.

The CP violation then arises from the interference of these two decay amplitudes with and without mixing before the decay.

3. Experimental Setup

The data used for this work were collected with the CDF II detector at the Tevatron proton-antiproton collider located at Fermilab near Chicago (USA). In the Tevatron, shown from aerial perspective in Figure 3.1, protons and antiprotons were accelerated in opposite directions to energies of 980 GeV and then brought to collision at the locations of the two particle detectors CDF II and DØ. With the center-of-mass energy of 1.96 TeV the Tevatron is the most powerful matter-antimatter collider ever built. The only terrestrial particle accelerator with a higher center-of-mass energy is the Large Hadron Collider at CERN which performs proton-proton collisions. The operation of the Tevatron from March 2001 till September 2011 is called Run II and the name CDF II is based upon this. In the years before, modifications of various accelerator and detector components were performed in order to achieve an increase of the center-of-mass energy and the luminosity compared to Run I from 1985 till 1995. The operation of the Tevatron was completed in September 2011. The Collider Detector at Fermilab (CDF) is a multipurpose detector consisting of several subcomponents to study the decay signatures of particles emanating from the high-energy proton-antiproton collisions.

3.1. Tevatron

The Tevatron represents the last element of the accelerator chain schematically shown in Figure 3.2. After the ionization of hydrogen gas to H^-, the first step is a Cockcroft-Walton generator which accelerates the hydrogen ions to an energy of 750 keV. Subsequently, a 150 m long linear accelerator (LINAC) increases their energy to 400 MeV. The LINAC consists of a series of superconducting high-frequency cavities, which leads to the formation of bunches of the afore continuous particle current. In order to create protons, the H^- ions are then conducted through a carbon foil which strips the electrons. Afterwards, the so-called Booster, a synchrotron with a diameter of 75 m, accelerates the protons to 8 GeV before they are fed into the Main Injector. This ring accelerator with a circumference of circa 3 km increases the energy of the protons to 150 GeV before they are transferred to the Tevatron. Moreover, protons with a kinetic energy of 120 GeV are used to generate antiprotons. For this purpose, they are shot at a nickel block in the Target Hall. Thereby created antiprotons with an energy of 8 GeV are extracted from the other secondary particles by means of magnets. Before they are fed into the Main Injec-

Figure 3.1.: Bird's-eye view of the Tevatron.

tor, the antiprotons are first stored in the smaller Accumulator and subsequently in the Recycler, which is located in the Main Injector ring, to collect a sufficient number of antiprotons. Just like the protons, they are finally brought to 150 GeV by the Main Injector and then transferred to the Tevatron. The Tevatron is an underground proton-antiproton collider with a circumference of about 6.3 km. High frequency cavities are used to accelerate the protons and antiprotons to energies of 980 GeV, which results in a center-of-mass energy of 1.96 TeV. The particles are kept on their track by means of superconducting dipole magnets which are cooled down to 10 K by liquid helium. Because of their different electric charge a single beam pipe can be used for both protons and antiprotons, moving in opposite directions. At the same time, 36 proton and 36 antiproton bunches separated by gaps of 396 ns, a so-called store, are accelerated and collided in the Tevatron for approximately 15 to 20 hours. In this period the antiprotons for the next store are generated.

An important quantity for the performance of a particle accelerator is the luminosity $\mathcal{L}$ with the unit $\mathrm{cm}^{-2}\mathrm{s}^{-1}$. It is defined as the ratio of event rate $\mathrm{d}N/\mathrm{d}t$ and cross section σ of a considered process. This makes $\mathcal{L}$ a pure function of the accelerator properties, independent of the center-of-mass energy. The greater $\mathcal{L}$ is, the higher is the probability of a collision of the revolving particles. For a symmetric

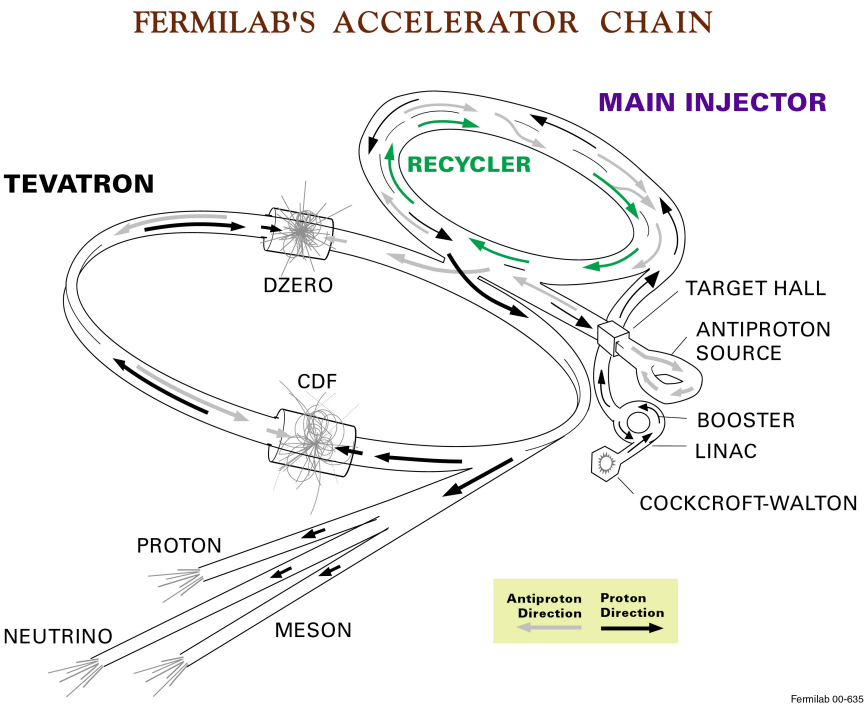

Figure 3.2.: The Fermilab accelerator chain. [4]

proton-antiproton collider the relation for $\mathcal{L}$ reads

$$\mathcal{L} = \frac{f N_B N_p N_{\bar{p}}}{4\pi\sigma_x\sigma_y}\,, \tag{3.1}$$

where N_B is the number of bunches, N_p and $N_{\bar{p}}$ are the numbers of protons respective antiprotons per bunch, f refers to the rotational frequency, and $4\pi\sigma_x\sigma_y$ is the cross section area of the particle beams in the xy-plane transverse to the beam line with the resolutions σ_x and σ_y. During a store the instantaneous luminosity decreases because of the loss of particles and the widening of the beams. The Run II development of the instantaneous luminosity of the Tevatron at the beginning of stores, referred to as peak luminosity, is shown in Figure 3.3.

By means of the time-integrated luminosity the expected yield N of a certain process with cross section σ can be calculated as

$$N = \sigma \cdot \int \mathcal{L}\,\mathrm{d}t\,. \tag{3.2}$$

The unit of the integrated luminosity is declared in inverse pico- or femtobarn (pb^{-1}, fb^{-1}), where $1\,\mathrm{b} = 10^{-28}\,\mathrm{m}$. The integrated luminosity of the Tevatron since the beginning of Run II is shown in Figure 3.4.

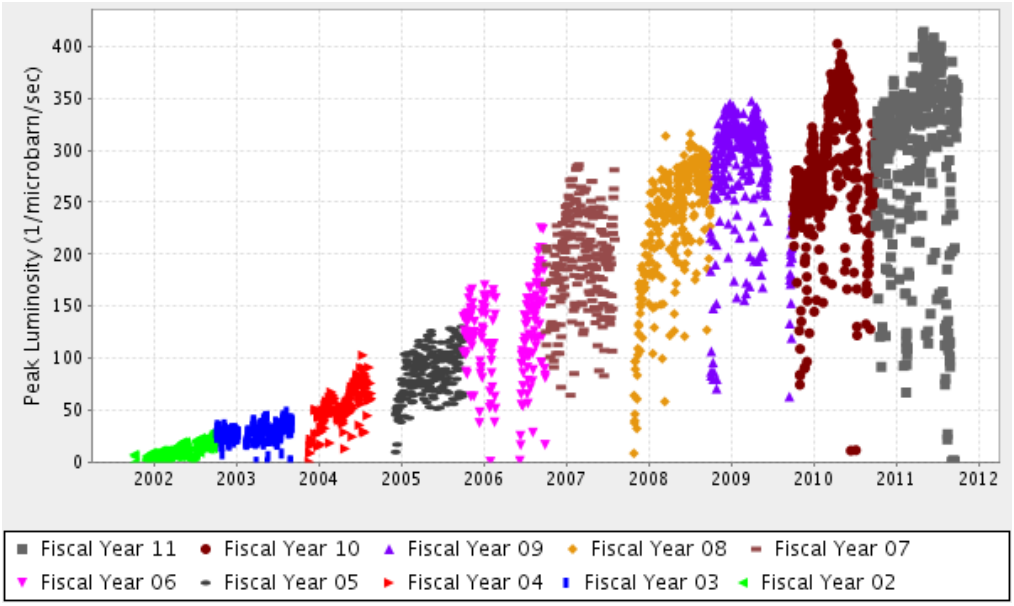

Figure 3.3.: Peak luminosity of the Tevatron. [8]

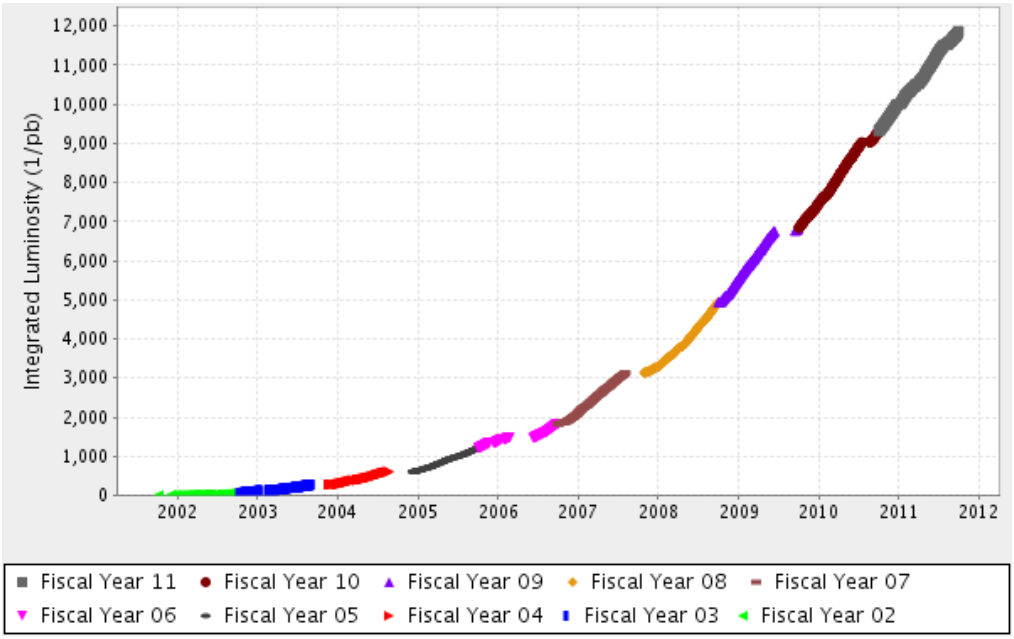

Figure 3.4.: Integrated luminosity of the Tevatron. [8]

3.2. CDF II Detector

Many different particles are produced in the high-energy collisions of protons and antiprotons at the Tevatron. The most interesting ones are very short-lived and decay via particular channels to stable or long-lived particles whose tracks, momenta and energies can be measured by means of the CDF II detector [9, 10]. This multipurpose particle detector has a size of about 12 m in each dimension and consists of several subcomponents that are arranged cylinder-symmetrically around the collision region of the beam pipe. An end view, an isometric view, and an elevation view of the CDF II detector are shown in Figures 3.5–3.7. In the following, its different subdetectors are described in detail.

A right-handed coordinate system is used in the description of the detector, where the z-axis points in the direction of the Tevatron proton beam and the y-axis is perpendicular to the collider plane. The polar angle θ and the azimuthal angle ϕ are defined correspondingly. Two important quantities for the description of particle signatures in the detector are the rapidity and the pseudorapidity. The rapidity of a track is invariant under Lorentz transformations in beam direction and can be calculated from the energy and the momentum component in beam direction as

$$y = \frac{1}{2} \cdot \ln\left(\frac{E + p_z}{E - p_z}\right) . \tag{3.3}$$

For massless objects it is equivalent to the pseudorapidity

$$\eta = -\ln\left(\tan\frac{\theta}{2}\right) , \tag{3.4}$$

which vanishes for $\theta = \frac{\pi}{2}$ and diverges for $\theta = 0$.

3.2.1. Tracking System

The tracks of charged particles in the CDF II detector are measured by means of a silicon detector and an open-cell drift chamber. These devices are arranged in a uniform, axial magnetic field of 1.4 T strength, which is generated by a superconducting solenoid made of an aluminum-stabilized NbTi conductor. The solenoid has a length of 4.8 m and is located at a radius of 1.5 m from the beam pipe. Its cooling is provided by a cryostat utilizing liquid helium. The Lorentz force generated by the magnetic field bends the track of a charged particle traversing the detector and the particle momentum can thus be calculated from the measured curvature. Furthermore, the sign of the electric charge can be determined from the direction of the curvature. A longitudinal cut of the different subdetectors of the tracking system, including their η-coverage, is shown in Figure 3.8.

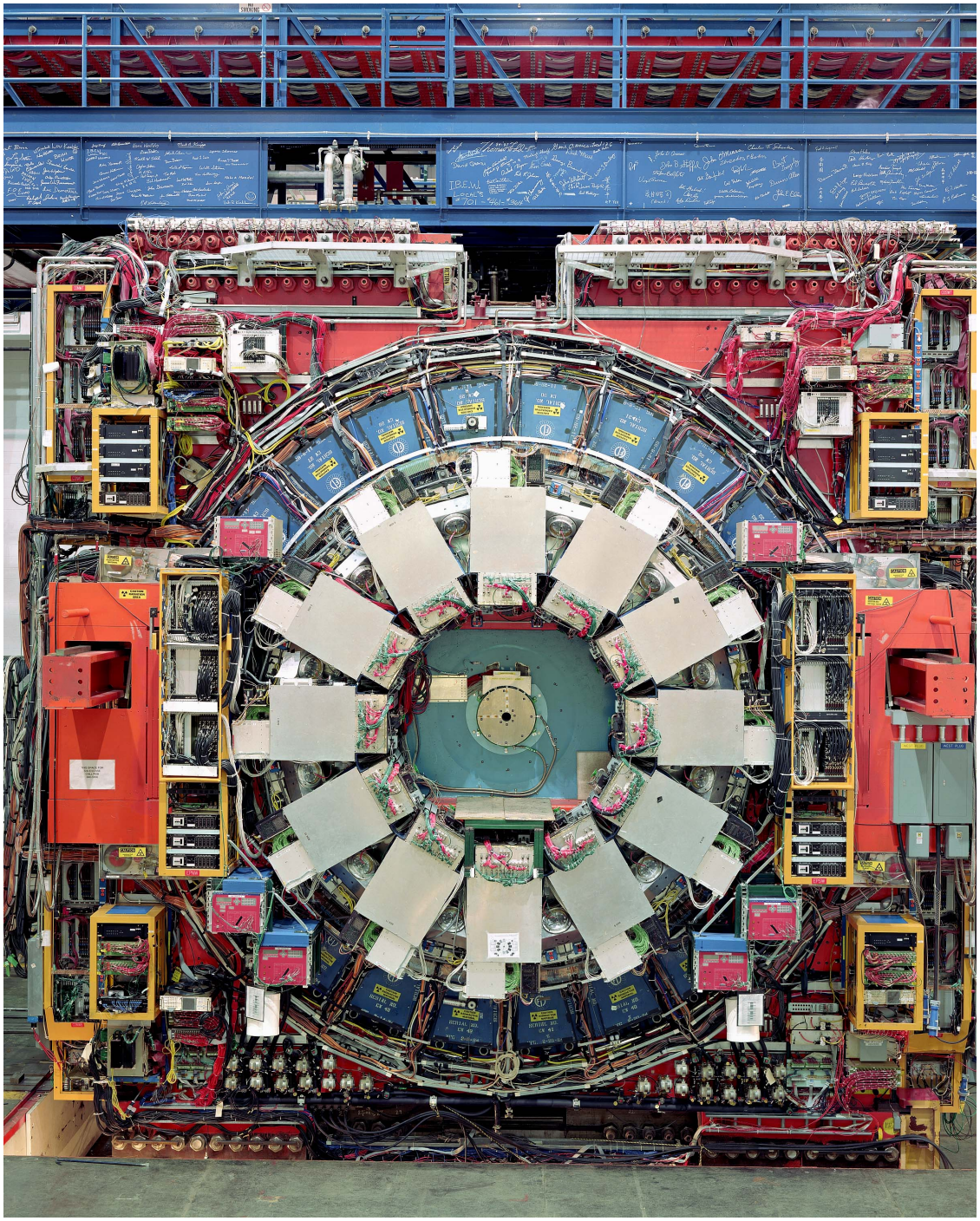

Figure 3.5.: End view of the CDF II detector. [11]

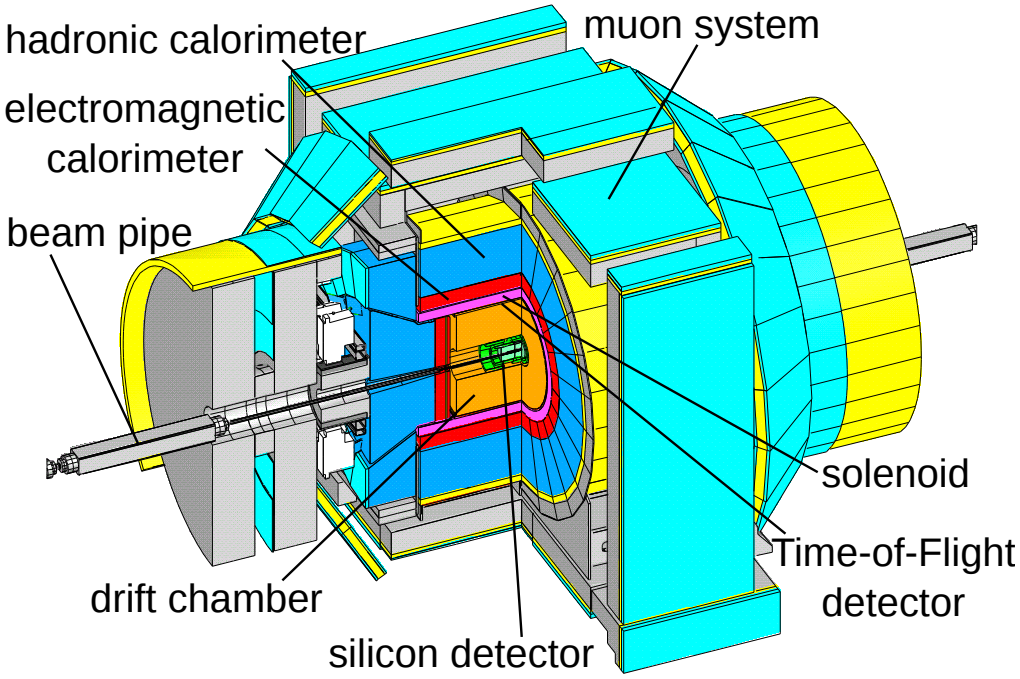

Figure 3.6.: Isometric view of the CDF II detector. [11]

Silicon Detector

The inner tracking volume up to a radius of 28 cm is filled with the silicon detector, covering the region $|\eta| < 2.0$. It is comprised of 6–7 layers of double-sided silicon microstrip detectors, allowing a three-dimensional track finding. These are referred to as Silicon VerteX Detector (SVX II) [12] and Intermediate Silicon Layers (ISL) [13], where the SVX II consists of the first 5 layers and the ISL adds 1–2 to higher radii. An additional layer of single-sided silicon, called Layer00 (L00) [14], is mounted directly on the beam-pipe at a radius of 1.5 cm.

The principle of operation of silicon microstrip detectors is that of a pn junction in inverse direction. The traversing of a charged ionizing particle produces electron-hole pairs that can be detected as electric signals at the corresponding microstrips. The silicon detector provides an excellent resolution of the impact parameter d_0, defined as the distance of closest approach of the track to the interaction point in the plane transverse to the beam line. The provided vertex resolution is approximately 15 µm in the transverse and 70 µm in the longitudinal direction.

Drift Chamber

The open-cell drift chamber of the CDF II detector, located at a radius of 40 to 137 cm from the beam pipe, is called Central Outer Tracker (COT) [15] and provides a transverse momentum resolution of $\sigma(p_T)/p_T^2 \approx 0.1\%/(\mathrm{GeV}/c)$. It measures the

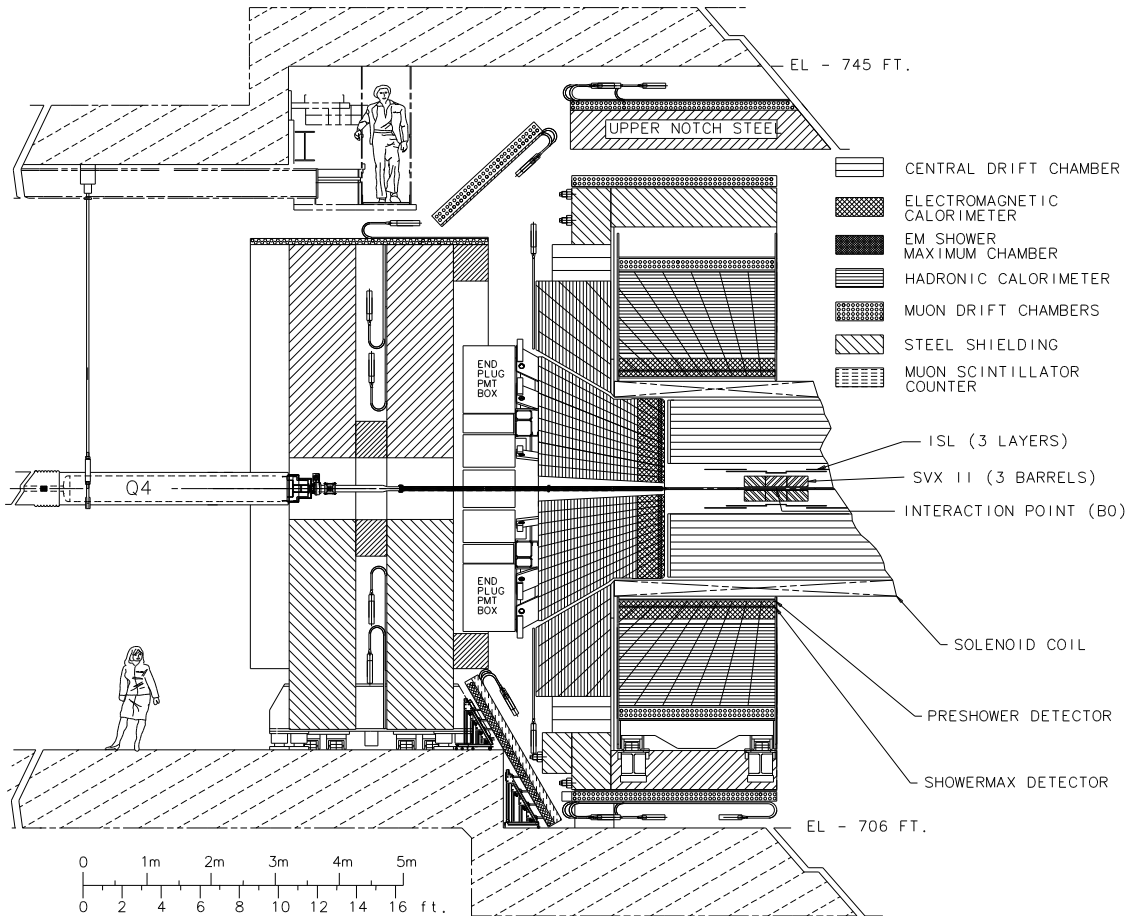

Figure 3.7.: Elevation view of the CDF II detector. [11]

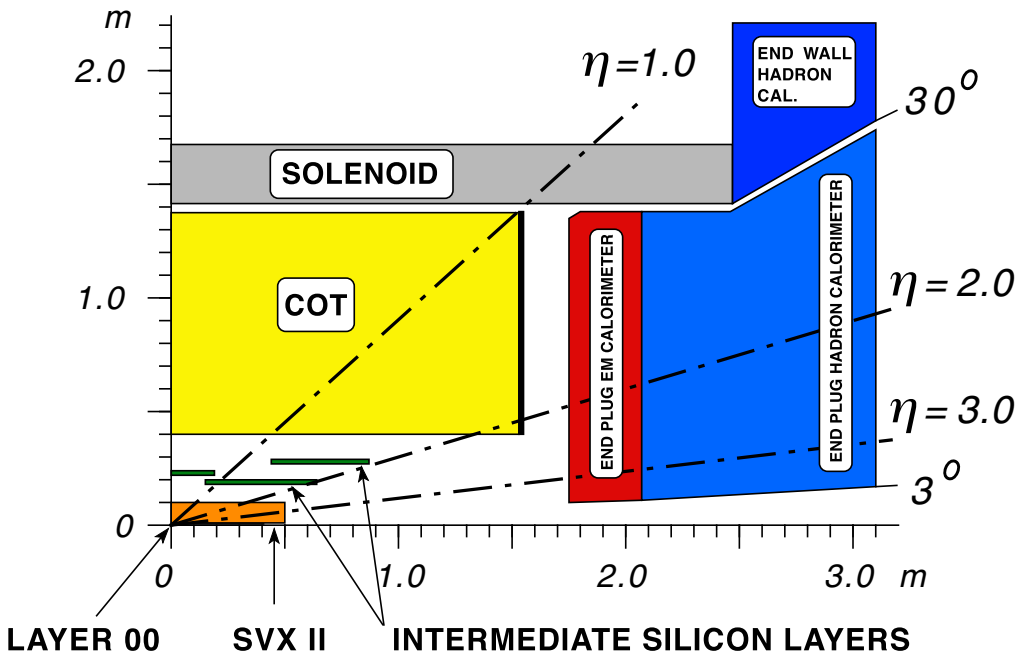

Figure 3.8.: Tracking system. [11]

ionization of a gas medium, an argon-ethane 1:1 mixture, caused by the traversing of a charged particle. The track of the ionizing particle can then be determined by the drift of the ionization electrons to the nearest sense wires. The COT consists of 2520 cells, each of which has 12 sense and 13 potential wires. The cells are arranged in eight superlayers. Four of these, referred to as axial layers, have their wires aligned parallel to the beam. The wires of the other four, called stereo layers, are shifted by an angle of 2 degrees to allow a three-dimensional measurement. The COT covers the region $|\eta| < 1.0$.

3.2.2. Particle Identification

At CDF two different measurements are used for the particle identification of charged pions, kaons, and protons, namely the specific ionization energy loss $\mathrm{d}E/\mathrm{d}x$ in the COT and the information from a Time-of-Flight detector (TOF) [16].

The value $\mathrm{d}E/\mathrm{d}x$ of a charged particle in matter is mass-dependent and can be calculated for a given momentum by means of the Bethe-Bloch formula. The measurement of $\mathrm{d}E/\mathrm{d}x$ and the momentum in the COT can thus provide information about the particle type at hand.

The TOF, located between the COT and the solenoid at a distance of 138 cm from the beam pipe, is used to measure the time a particle needs to travel the distance from the collision point to one of its 216 scintillator bars which are read

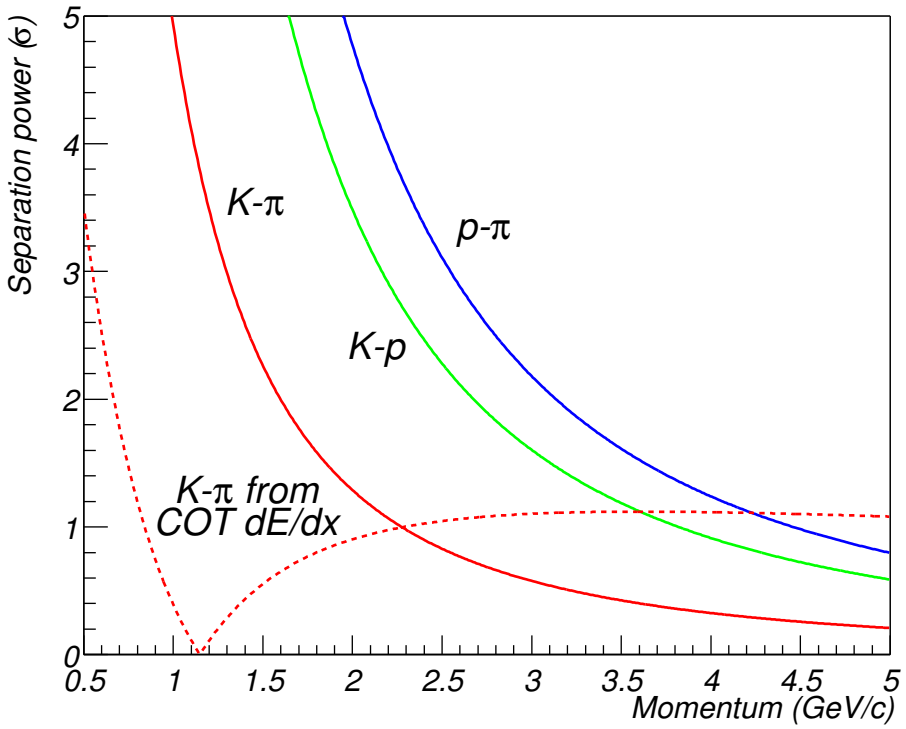

Figure 3.9.: Particle identification. The continuous lines refer to TOF information.

out by photomultipliers via lightguides. This time depends on the mass m of the particle as

$$t = s\sqrt{1 + \frac{m^2}{p^2}}\,, \tag{3.5}$$

where s is the length of the track and p its measured momentum.

The information from the TOF and $\mathrm{d}E/\mathrm{d}x$ measurements are complementary and their capabilities to separate the different charged particles are shown in Figure 3.9. An improved hadron identification can be achieved by a likelihood combination of the available information, what offers about 1.5σ separation between kaons, or protons, and pions over the whole momentum range.

3.2.3. Calorimeters

The CDF calorimeters [17], located outside of the solenoid, are sampling calorimeters, consisting of alternating layers of absorbing material, lead for the electromagnetic and iron for the hadronic calorimeter, and scintillators. They are employed to determine the energies of the particles produced in the proton-antiproton collisions

by completely absorbing them. The number of secondary particles produced by the interactions of the incident particle with the absorbing material is proportional to the energy of the incident particle and can be measured by the scintillators which are connected to photomultipliers.

The produced secondary particles are referred to as shower, where one distinguishes between electromagnetic and hadronic showers. The former arise from the interactions of high energetic photons or electrons, respective positrons, with matter. By multiple pair production and bremsstrahlung processes this leads to a cascade of photons and electron-positron pairs. Electromagnetic showers can also originate from the decays of neutral pions to two photons. Hadronic showers consist of secondary hadrons and arise from the inelastic scattering of an incident hadron by the nucleons of the absorbing material via the strong interaction. Since the mean free path is considerably greater for the strong than for the electromagnetic interaction, more material is necessary for the hadronic calorimeter and therefore, it is arranged further outside than the electromagnetic calorimeter.

In the electromagnetic calorimeter, so-called shower maximum and preshower detectors are placed to enable the linking of tracks and improve the identification of the particles causing the showers. Furthermore, the central calorimeters are geometrically complemented by corresponding end plug calorimeters, covering the region $|\eta| < 3.6$.

3.2.4. Muon Detectors

Because of their relatively long lifetime of 2.2 µs muons decay mostly far outside of the detector. Furthermore, their compared to electrons 207 times higher mass leads to negligible bremsstrahlung effects and in turn to a long range in matter. Since all other particles, except of the nearly non-interacting neutrinos, are almost completely absorbed by the detector material and the additional steel shielding, muons can be detected by their ionization tracks in the outermost layer of the CDF II detector, the muon system [18]. This consists of several drift chambers and scintillation counters, covering the region $|\eta| < 1.5$.

3.2.5. Trigger and Data Acquisition System

The effective bunch crossing rate of protons and antiprotons in the CDF II detector is 1.7 MHz, corresponding to one collision every 0.6 µs. The storing of all resulting events with its signatures in the various subdetectors is infeasible. But only a small fraction of these are physically interesting events from hard, inelastic scattering with the production of additional particles. The aim of the trigger system is the extraction of the few interesting events out of the huge amount of data. A three-level trigger system is used for the online event selection. It reduces the data

rate from level to level, allowing a longer processing time and thus an increasing complexity of the information contributing to the trigger decision.

An exact set of trigger decisions for the three levels is called a trigger path. Several of these are used depending on the different kinds of physics studies. The trigger path used for the analyses described in this work is referred to as two track trigger [19]. It is designed to collect hadronic decays of long-lived particles such as b and c hadrons.

The most important device for the two track trigger at level-1 is the extremely fast tracker (XFT) [20]. It identifies charged particles using information from the COT and measures their transverse momenta and azimuthal angles around the beam direction. The basic requirement at level-1 is two charged particles with transverse momentum greater than $2\,\mathrm{GeV}/c$.

At level-2, the silicon vertex trigger (SVT) [21, 22] adds silicon hit information to the XFT tracks, thus allowing the precise measurement of impact parameters of tracks. The two level-1 tracks are required to have impact parameters between 0.1 and 1 mm and to be consistent with coming from a common vertex displaced from the interaction point by at least 100 µm in the plane transverse to the beam line.

The level-3 trigger is implemented in software and provides the final online selection by confirming the first two trigger-level decisions using a more precise reconstruction similar to the offline software [23]. It finally reduces the data rate to less than 200 Hz and the accepted events are then written to permanent storage media.

4. Statistical Tools

In this chapter the statistical methods used in the presented analyses are described. These include the basics of the fitting procedure and the employed multivariate selection technique.

4.1. Parameter Estimation

A common problem in the statistical analysis of large datasets is the determination of the parameters describing the probability density function (PDF) that underlies the considered quantity. One way to accomplish such a parameter estimation is the so-called maximum likelihood method. In order to get a measure for the goodness of the performed parameter estimation one can refer to a χ^2 test. Both methods are described below.

4.1.1. Maximum Likelihood Method

Let $\mathrm{f}(\vec{x};\vec{a})$ be the PDF of the z random variables $x_1, x_2, ..., x_z$ depending on the p parameters $a_1, a_2, ..., a_p$. Given a data set of N independent measurements $\vec{x}_i$, the likelihood function

$$L(\vec{a}) = \prod_{i=1}^{N} \mathrm{f}(\vec{x}_i;\vec{a}) \tag{4.1}$$

is the product of the individual probability densities. The estimate of the maximum likelihood method then corresponds to the parameter values for which the likelihood function is maximal. Instead of the likelihood function itself, it is numerically favorable to maximize its logarithm

$$\mathcal{L}(\vec{a}) = \ln L(\vec{a}) = \sum_{i=1}^{N} \ln \mathrm{f}(\vec{x}_i;\vec{a})\,, \tag{4.2}$$

leading to the same result because of the monotonic behavior of the logarithm. So, the p-dimensional system of equations

$$\frac{\partial \mathcal{L}}{\partial a_k} = 0 \tag{4.3}$$

has to be solved for the searched parameters a_k, the components of $\vec{a}$, fulfilling the normalization condition of the probability density

$$\int \mathrm{f}(\vec{x};\vec{a})\mathrm{d}\vec{x} = 1\,. \tag{4.4}$$

Furthermore, because of the large number of available minimizing program packages it is in practice often favorable to search for the minimum instead of the maximum. For that purpose the sign of $\mathcal{L}$ is simply inverted.

Binned Maximum Likelihood Fit

A binned maximum likelihood fit is an application of the described maximum likelihood method with the aim of fitting a parametrized function to a data distribution represented by a histogram, meaning divided in bins. To perform a binned maximum likelihood fit the negative logarithm of the likelihood function has a general form of

$$-\ln\mathcal{L}(\vec{a}) = -\sum_{j=1}^{J}\ln\left(\frac{\mu_j^{n_j}e^{-\mu_j}}{n_j!}\right) = -\sum_{j=1}^{J}n_j\ln\mu_j + \sum_{j=1}^{J}\mu_j + \sum_{j=1}^{J}\ln(n_j!)\,, \tag{4.5}$$

where $\vec{a}$ are the free parameters, J is the number of bins in the histogram of the corresponding distribution, n_j is the number of entries in bin j, and μ_j is the expected number of entries in bin j. The values μ_j are obtained using the underlying function that depends on the parameters $\vec{a}$. This function is evaluated at the bin center to calculate the expectation for μ_j.

4.1.2. χ^2 Test

To use the χ^2 test as benchmark for a performed fit, one considers a histogram of the fitted quantity. The value F_j is the evaluation of the fit function, depending on the parameters $\vec{a}$, for the center x_j of bin j, and n_j is the corresponding number of entries. The uncertainty on F_j results from Poisson statistics as $\sqrt{F_j}$. The χ^2 value can then be calculated as

$$\chi^2 = \sum_{j=1}^{N}\left(\frac{n_j - F_j}{\sqrt{F_j}}\right)^2\,, \tag{4.6}$$

where N is the number of bins in the histogram. The smaller the resulting χ^2 value, the better the agreement between data and fit function. Therefore, the χ^2 method can give a quantitative estimate of the fit quality.

The χ^2 distribution of a particular fit depends on the corresponding number of degrees of freedom NDF, that is the number of bins in the considered histogram

minus the number of free parameters in the fit function. NDF being also the mean value of the χ^2 distribution, one expects the relation

$$\frac{\chi^2}{\mathrm{NDF}} \approx 1\,. \tag{4.7}$$

for an adequate description of the data by the fit function.

4.2. Multivariate Analysis

The usual situation in particle physics is that besides the signal events, the behavior of which one wants to examine, there are also background events in the studied data sets, and the aim is to reduce the background as far as possible by retaining as much of the signal as possible. The most basic way to achieve such a signal selection is the application of distinct requirements, referred to as cuts, on quantities whose distributions are different for signal and background. However, since only the projections on individual axes of the variable space are considered, possible correlations between the different variables are not regarded in this approach. That can lead to a higher loss of signal or retention of background events and therefore to a non-optimal classification.

A better way to perform such a classification, where the different separating variables are correlated to each other, is in the application of so-called multivariate analysis techniques bearing the ability to handle complex correlations. There are many different approaches for that purpose, and in the following the method of artificial neural networks is described, where the main focus is on the NeuroBayes program package which is used for the analyses presented in this work.

4.2.1. Artificial Neural Networks

Topology

A neural network consists of multiple nodes, each of which featuring several inputs for information from other nodes but only one output. The values of the inputs are weighted individually and summed up afterwards. The result of this summation is finally transformed to the interval [-1,+1] by means of the sigmoid function $S(t)$,

$$S(t) = \frac{2}{1+e^{-t}} - 1\,, \tag{4.8}$$

$$y = S\left(\sum_{i=1}^{n}(w_i \cdot x_i)\right)\,, \tag{4.9}$$

where w_i are the weights for the n input values x_i.

Depending on the type of the network, the individual nodes are connected in different ways. In the following, a three-layer feed-forward network is considered, meaning that the outputs of the first layer are only used as inputs for the nodes of the second layer, and the outputs of the second layer as inputs for the single output node in the third layer. Thereby, each input variable corresponds to one of the nodes in the first layer allowing the feeding of the data to the network. The output value of the single node of the third layer makes the desired classification quantity combining all the individual separation capabilities of the input variables.

The resulting function for the output y in dependence of the n input values x_i is

$$y = S\left[\sum_{j=1}^{m} v_j \cdot S\left(\sum_{i=1}^{n}(w_{ij} \cdot x_i)\right)\right], \tag{4.10}$$

where v_j are the weights for the connections from the m nodes of the second layer to the output node and w_{ij} are the weights for the connections from the first to the second layer.

Network Training

Before the application of a neural network, it has to learn the features of the specific problem first. This is done by iterative adjustment of the individual connection weights, referred to as network training, with the aim of minimizing the the deviations between the calculated network output values and the truth which has to be known for the training data set.

For N training events k, these deviations can be obtained, for example, by means of an entropy cost function

$$E(\vec{w}) = \sum_{k}^{N} \ln\left(\frac{1}{2}(1 + y_k(\vec{w}) \cdot T_k)\right), \tag{4.11}$$

where y_k are the calculated values for the network output variable depending on the collectivity of the connection weights $\vec{w}$, and T_k the known truths (either 1 for signal or -1 for background). The minimum of the cost function can then be determined with the gradient descent for instance.

4.2.2. NeuroBayes

To obtain a reasonable result, it is usually necessary to preprocess the data by means of statistical and numerical methods before feeding it to the neural network. For that purpose the NeuroBayes program package [24, 25], a multivariate analysis tool based on the neural network technique, comprises a powerful preprocessing algorithm before utilizing a neural network.

The preprocessing consists of several steps. The first one is a flattening of the combined signal and background distributions of the various input variables, meaning that for each distribution a histogram with 100 non-equidistant bins is filled in a way that each bin is populated by approximately the same number of entries. From that the signal fraction, defined as the number of signal events divided by the sum of the numbers of signal and background events, is calculated for each bin and the resulting histogram is parametrized by a spline function in order to smooth the distribution and thus avoid the learning of statistical fluctuations. The evaluation of the spline function in each bin is then transformed by a Gaussian distribution with mean 0 and standard deviation 1. Finally, the transformed variables are decorrelated by a rotation of their covariance matrix.

According to the Bayes' theorem, the NeuroBayes output can be interpreted as *a posteriori* signal probability, where the *a priori* signal and background probabilities are given by the numbers of signal and background events used for the network training.

Instead of feeding the preprocessed input variables to a neural network, they can also be projected on a single output quantity corresponding to the *a posteriori* signal probability. This approach is used for the analyses described in this work. For simplification of the notation, it is referred to as network training as well.

4.2.3. ${}_s\mathcal{P}lot$ Technique

In most of the cases a considered data set consists of at least two types of events, for example signal and background. Given the situation that one knows the distribution of a particular variable, referred to as discriminating variable y, and the distribution of another so-called control variable x, being independent from y, is unknown, the ${}_s\mathcal{P}lot$ technique [26,27] can be used to unfold the different contributions in the distribution of x.

To apply the ${}_s\mathcal{P}lot$ technique it is necessary to know the total signal and background yields, in the following named N_1 and N_2, as well as the corresponding PDFs $\mathrm{f}_1(\mathrm{y})$ and $\mathrm{f}_2(\mathrm{y})$. These can be obtained for example by fitting a function consisting of a signal and a background part to the distribution of y.

The ${}_s\mathcal{P}lot$ weights, with which the individual events are multiplied to obtain the unfolding in x, can then be calculated as

$$ {}_s\mathcal{P}_n(y_e) = \frac{\sum_{j=1}^{2} \mathbf{V}_{nj}\, \mathrm{f}_j(y_e)}{\sum_{k=1}^{2} N_k\, \mathrm{f}_k(y_e)}\,, \tag{4.12} $$

where n stands for signal or background, the N_k mean the corresponding yields, y_e is the discriminating variable for the considered event e and the $f_j(y_e)$ are the probability density functions for signal and background, respectively. $\mathbf{V}_{nj}$ is the

covariance matrix, the inverse of which can be calculated via

$$\mathbf{V}_{nj}^{-1} = \sum_{e=1}^{N} \frac{\mathrm{f}_n(y_e)\mathrm{f}_j(y_e)}{(\sum_{k=1}^{2} N_k \mathrm{f}_k(y_e))^2} \,. \tag{4.13}$$

The ${}_s\mathcal{P}lot$ weights offer the properties

$$\sum_{e=1}^{N} {}_s\mathcal{P}_n(y_e) = N_n \,, \tag{4.14}$$

$${}_s\mathcal{P}_1(y_e) +_s \mathcal{P}_2(y_e) = 1 \,. \tag{4.15}$$

To make a long story short, the ${}_s\mathcal{P}lot$ technique is an advanced sideband subtraction, where all events in a given range of the distribution of a discriminating variable receive both a signal and a background weight depending on the corresponding values of the signal and background PDFs as well as the overall yields. By means of these weights separate signal and background distributions of an independent control variable can be determined.

4.2.4. NeuroBayes with ${}_s\mathcal{P}lot$ Weights

In order to train a neural network for selection purposes in particle physics, usually simulated events are used as signal and real data from mass sideband regions as background sample. However, this choice of training data sets has the drawback that one has to rely on the correctness of the simulation, that is its consistency with experimental data. A solution for this is the usage of real data for the signal training sample, too. But the problem is that the signal is always polluted with background events. So a method is needed to statistically subtract the background from the signal events.

As described in Section 4.2.3, this can be accomplished by means of the ${}_s\mathcal{P}lot$ technique. In the training, each candidate enters with the ${}_s\mathcal{P}lot$ weight calculated from the signal probability that is derived from its mass. In the terminology used above, this means that the mass is the discriminating variable and the network input quantities are the control variables. Based on these ${}_s\mathcal{P}lot$ weights, the neural network can then learn the features of signal and background events without using simulated events.

5. Charmed Baryon Spectroscopy

In this chapter, measurements of the masses and widths of the charmed baryons $\Lambda_c(2595)^+$ and $\Lambda_c(2625)^+$ in their decays to $\Lambda_c^+\pi^+\pi^-$ as well as $\Sigma_c(2455)^{++,0}$ and $\Sigma_c(2520)^{++,0}$ in their decays to $\Lambda_c^+\pi^\pm$ final states are described. The Λ_c^+ is reconstructed in its decay to $p\,K^-\,\pi^+$. Throughout this work the use of a specific particle state implies the use of the charge-conjugate state as well.

The measurements of the resonance properties are performed through fits to the reconstructed mass distributions calculated from the measured momenta of the final state tracks. All expected cross-feeds and threshold effects are taken into account. Exploiting the largest available charmed baryon sample, masses and decay widths are measured with uncertainties comparable to the world averages for Σ_c states, and significantly smaller uncertainties than the world averages for excited Λ_c^+ states.

This chapter is organized as follows. After a survey of the theoretical predictions and the experimental status in Section 5.1, the candidate reconstruction and selection are described in Section 5.2 and 5.3. In Section 5.5 the sample of simulated events used for the determination of the detector mass resolutions is presented. Explanations of the fits involved in the measurements are given in Section 5.6, followed by a discussion of systematic uncertainties in Section 5.7. Finally, the results and conclusions are presented in Section 5.8.

The published results of these studies can be found in Reference [28].

5.1. Theoretical Predictions and Experimental Status

Hadrons containing a b or c quark are referred to as heavy-quark hadrons and provide an interesting laboratory for studying and testing QCD. Because the strong coupling constant α_s is large for interactions involving small momentum transfer, masses and decay widths of the heavy-quark states cannot be calculated within the framework of perturbative QCD. As a result, many different approaches have been developed, for example, based on heavy-quark effective theory (HQET) [29], nonrelativistic and relativistic potential models [30], or lattice QCD [31].

In the limit of HQET, heavy-quark mesons, comprised of one heavy and one light quark, are the closest analogy to the hydrogen atom, which provided important tests of quantum electrodynamics. Heavy-quark baryons, comprised of one heavy and two light quarks, extend the hydrogen atom analogy of HQET by treating the two light quarks as a diquark system. This leads to degenerate spin-1/2 states resulting from the combination of a spin-0, or a spin-1, light diquark with the heavy quark, and thus represents a complementary situation compared to heavy-quark mesons. Measurements of the mass spectrum and spin splittings of heavy-quark baryons are important for validating the theoretical techniques, and build confidence in their predictions for other heavy flavor studies.

In this analysis, the properties of heavy-quark baryons that contain a c quark, namely the resonances $\Lambda_c(2595)^+$, $\Lambda_c(2625)^+$, $\Sigma_c(2455)^{++,0}$, and $\Sigma_c(2520)^{++,0}$, are measured. Thereby, the numbers in parentheses indicate the approximate masses in MeV/c^2. For simplification, $\Sigma_c(2455)^{++,0}$ and $\Sigma_c(2520)^{++,0}$ are referred to as Σ_c, wherever the omitted information is not crucial. Furthermore, $\Lambda_c(2595)^+$ and $\Lambda_c(2625)^+$ are referred to as Λ_c^{*+}.

From all known charmed baryons, the Λ_c^+ with the quark contents *cud* and the quantum numbers $J^P = \frac{1}{2}^+$ is the one with the lowest mass ($m = 2286.46 \pm 0.14\,\mathrm{MeV}/c^2$ [1]). The quark model predicts the resonances $\Sigma_c(2455)$ ($J^P = \frac{1}{2}^+$) and $\Sigma_c(2520)$ ($J^P = \frac{3}{2}^+$) to be isospin excitations of the Λ_c^+. This means that their wave functions are symmetric under the interchange of the two light quarks (spin-1 light diquark), whereas the Λ_c^+ is antisymmetric (spin-0 light diquark). In the $\Sigma_c(2520)$ case, all quark spins are aligned parallel, resulting in $s = \frac{3}{2}$. Like the Λ_c^+ itself, the $\Sigma_c(2455)$ has $s = \frac{1}{2}$. As can be seen in Figure 2.3, the Σ_c states are isospin triplets Σ_c^0, Σ_c^+, and Σ_c^{++} which differ only by their light quark contents. They decay strongly to $\Lambda_c^+\,\pi^{-,+,0}$. These decays proceed via P-wave, meaning a relative angular momentum of $L = 1$ between the two decay products, because of parity conservation in strong interactions and the pion quantum numbers $J^P = 0^-$. The Σ_c^+ states are not studied in this analysis, because they are difficult to reconstruct with the CDF II detector due to the inefficiency in π^0 identification.

The orbitally excited ($l = 1$) Λ_c^+ states $\Lambda_c(2595)^+$ ($J^P = \frac{1}{2}^-$) and $\Lambda_c(2625)^+$ ($J^P = \frac{3}{2}^-$) belong to antisymmetric quadruplets and are therefore isospin singlets,

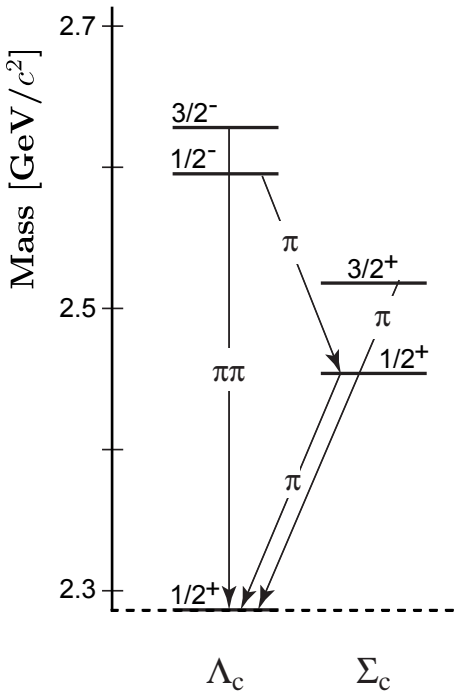

Figure 5.1.: $\Sigma_c(2455)$, $\Sigma_c(2520)$, $\Lambda_c(2595)^+$, and $\Lambda_c(2625)^+$ baryons with its decays to Λ_c^+.

just like the Λ_c^+ itself. Since the pion has isospin-1, the decay $\Lambda_c^{*+} \to \Lambda_c^+ \pi^0$ is forbidden by isospin conservation. So the Λ_c^{*+} resonances decay to the Λ_c^+ ground state and two oppositely charged pions. Because of parity conservation, and also angular momentum conservation in the $\Lambda_c(2625)^+$ case, these decays proceed via P-wave. Another possibility with the same three body final state is the resonant decay through $\Sigma_c(2455)\,\pi$. The $\Sigma_c(2520)\,\pi$ channel is kinematically disfavored for both $\Lambda_c(2595)^+$ and $\Lambda_c(2625)^+$. In the case of $\Lambda_c(2595)^+$, the decay to $\Sigma_c(2455)\,\pi$ proceeds via S-wave, meaning a vanishing relative angular momentum between the two decay products, and is very close to threshold. As turns out, this is the dominant decay channel and distorts considerably the $\Lambda_c(2595)^+$ signal shape. For

Table 5.1.: Theoretical predictions for the masses of the charmed baryons under study. All values are given in MeV/c^2.

Hadron	[32]	[33]	[34, 35]	[36]	[37]
$\Sigma_c(2455)$	2452	2455	2439	2400 ± 310	2393
$\Sigma_c(2520)$	2538	2519	2518	2560 ± 240	2489
$\Lambda_c(2595)^+$	$\cdots$	2625	2598	2530 ± 220	$\cdots$
$\Lambda_c(2625)^+$	$\cdots$	2636	2628	2580 ± 240	$\cdots$

Table 5.2.: World average values of the mass differences between the charmed baryon resonances and the Λ_c^+ mass, ΔM, and their natural widths, Γ [1].

Hadron	ΔM [MeV/c^2]	Γ [MeV/c^2]
$\Sigma_c(2455)^{++}$	167.56 ± 0.11	2.23 ± 0.30
$\Sigma_c(2455)^0$	167.30 ± 0.11	2.2 ± 0.4
$\Sigma_c(2520)^{++}$	231.9 ± 0.6	14.9 ± 1.9
$\Sigma_c(2520)^0$	231.6 ± 0.5	16.1 ± 2.1
$\Lambda_c(2595)^+$	308.9 ± 0.6	$3.6^{+2.0}_{-1.3}$
$\Lambda_c(2625)^+$	341.7 ± 0.6	< 1.9 at 90% C.L.

$\Lambda_c(2625)^+$, angular momentum conservation requires at least a P-wave decay to $\Sigma_c(2455)\,\pi$, what is in turn forbidden by parity conservation. So it would have to proceed via D-wave, meaning a relative angular momentum of $L = 2$ between the two decay products, and therefore rather decays nonresonantly. The spectrum of the described charmed baryons $\Sigma_c(2455)$, $\Sigma_c(2520)$, $\Lambda_c(2595)^+$, and $\Lambda_c(2625)^+$ with its decays to the Λ_c^+ groundstate is visualized in Figure 5.1.

Some theoretical predictions of the resonance masses are summarized in Table 5.1, where [32] uses lattice QCD, [33–35] are based on the quark model, [36] employs QCD sum rules and [37] uses a bag model. There are a few calculations that predict the $\Sigma_c(2455)$ natural width in the region of 1–3 MeV/c^2 [38–43] and the $\Sigma_c(2520)$ width to be about 18 MeV/c^2 [43]. No predictions are available for the $\Lambda_c(2595)^+$ and $\Lambda_c(2625)^+$ widths.

Experimental observation of all four states studied here and measurements of some of their properties have been reported earlier [44–51]. The world average masses and widths are listed in Table 5.2, omitting Σ_c^+ states. For $\Sigma_c(2455)$, many measurements exist with most of the information coming from CLEO [44] and FOCUS [45]. Experimental information on the $\Sigma_c(2520)$ states comes exclusively from CLEO [46,47] and it is worth noting that the two measurements of the $\Sigma_c(2520)^{++}$ mass are inconsistent. For $\Lambda_c(2595)^+$ and $\Lambda_c(2625)^+$ three experiments have contributed, namely ARGUS [48] (19 $\Lambda_c(2595)^+$ and 51 $\Lambda_c(2625)^+$ events), E687 at Fermilab [49, 50] (14 $\Lambda_c(2595)^+$ and 40 $\Lambda_c(2625)^+$ events) and CLEO [51] (112 $\Lambda_c(2595)^+$ and 245 $\Lambda_c(2625)^+$ events), all of which suffer from rather small data samples. In addition, Blechman and co-authors [52] showed that a more sophisticated treatment of the mass line shape, which takes into account the proximity of the $\Lambda_c(2595)^+$ mass to the sum of the masses of its decay products, yields a $\Lambda_c(2595)^+$ mass which is 2–3 MeV/c^2 lower than the one observed. The $\Sigma_c(2455)$ and $\Sigma_c(2520)$ decay directly to $\Lambda_c^+\pi$, whereas the $\Lambda_c(2595)^+$ and $\Lambda_c(2625)^+$ end mainly in a $\Lambda_c^+\pi\pi$ final state with dominating decays through intermediate Σ_c resonances. Therefore, these four resonances contribute to each other's background, which requires a dedicated cross-feed background modeling in each case.

Table 5.3.: Requirements of the two track trigger to be fulfilled by at least two tracks in each event. There are three different versions of the trigger decisions depending on the instantaneous luminosity.

low luminosity	medium luminosity	high luminosity
$p_T > 2.0\,\mathrm{GeV}/c$	$p_T > 2.0\,\mathrm{GeV}/c$	$p_T > 2.5\,\mathrm{GeV}/c$
$0.1 < \lvert d_0\rvert < 1.0\,\mathrm{mm}$	$0.1 < \lvert d_0\rvert < 1.0\,\mathrm{mm}$	$0.1\,\mathrm{mm} < \lvert d_0\rvert < 1.0\,\mathrm{mm}$
$L_{xy} > 0.1\,\mathrm{mm}$	$L_{xy} > 0.1\,\mathrm{mm}$	$L_{xy} > 0.1\,\mathrm{mm}$
$2^\circ < \Delta\phi < 90^\circ$	$2^\circ < \Delta\phi < 135^\circ$	$2^\circ < \Delta\phi < 135^\circ$
	opposite charge	opposite charge
	$\sum p_T > 5.5\,\mathrm{GeV}/c$	$\sum p_T > 6.5\,\mathrm{GeV}/c$

5.2. Data Set and Reconstruction

The analysis is performed on a data set collected between February 2002 and June 2009 corresponding to an integrated luminosity of $5.2\,\mathrm{fb}^{-1}$. The data were accumulated using the displaced two track vertex trigger described in Section 3.2.5. A listing of the exact requirements of this trigger path can be found in Table 5.3.

The offline reconstruction of candidates starts with refitting tracks using pion, kaon and proton mass hypotheses to properly take into account differences in the multiple scattering and ionization energy loss. In the second step, three tracks, one with pion, one with kaon, and one with proton mass hypotheses, are combined to form a Λ_c^+ candidate. The three tracks are subjected to a kinematic fit that constrains them to originate from a common vertex. The proton and pion candidates are required to have the same charge and the total charge of all three tracks has to be ± 1. To construct $\Sigma_c(2455)$ and $\Sigma_c(2520)$ candidates each Λ_c^+ candidate is combined with one of the remaining tracks in the event using a pion mass hypothesis. The $\Lambda_c(2595)^+$ and $\Lambda_c(2625)^+$ candidates are obtained by combining each Λ_c^+ candidate with all possible oppositely charged track pairs taken from the remaining tracks in the event using the pion mass hypothesis for each of them. The tracks forming each excited baryon candidate are subjected to a kinematic fit that constrains them to originate from a common point. In each step of the reconstruction, standard quality requirements on tracks and vertices are used to ensure well-measured masses and decay-positions.

5.3. Candidate Selection

The selection of the candidates is done in two steps. In each one some quality requirements are imposed first to suppress the most obvious background. For the surviving candidates a neural network is used to distinguish signal from background. Since all final states feature a Λ_c^+ daughter, the first step is the Λ_c^+ selection. In

the second step, a dedicated selection of the four states under study is performed.

All neural networks are constructed with the NeuroBayes package and trained, only using data, by means of the ${}_s\mathcal{P}lot$ technique. The approach is further described in Section 4.2.4.

Since we use only data for the neural network trainings, we randomly split each sample into two parts (even and odd event numbers) and train two networks. Each of them is then applied to the complementary subsample in order to maintain a selection which is trained on a sample independent from the one to which it is applied. This approach avoids a bias of the selection originating from statistical fluctuations possibly learnt by the network. All figures in this section concerning the network trainings are for the case of even-numbered events. The corresponding figures for odd-numbered events look qualitatively identical and are shown in Appendix A.

Additionally, using candidates from two different mass regions populated by background only for the training, we verify that the network selection does not depend on the mass or create an artificial excess in the spectrum. The outcome of this test is presented in Section 5.3.5.

5.3.1. Λ_c^+ Selection

Because the examined resonances all decay to final states containing a Λ_c^+ baryon, the first and most important step is to perform a good selection of $\Lambda_c^+ \to p\,K^-\,\pi^+$ candidates. In order to get a higher number of signal events, a separate data sample is used for the network training, which is not restricted to particular $\Lambda_c^+\,\pi^\pm$ or $\Lambda_c^+\,\pi^+\,\pi^-$ final states, but only requires a Λ_c^+ candidate. However, not all available data is employed for this because a random subset of the above mentioned data set is sufficient for the Λ_c^+ network training. This subset is chosen to be distributed evenly in time.

Precuts

The precuts shown in Table 5.4 are performed before the training of the Λ_c^+ neural network to throw away candidates which are most likely background. This increases the signal to background ratio and by this means also improves the performance of the subsequent network training.

The cuts on the COT hits and the transverse momenta of the kaon and pion candidates are track quality requirements, whereas the χ^2 value is a quality criterion for the Λ_c^+ vertex fit. The cut on the transverse momentum of the track with acquired proton mass is stricter than the ones for the kaon and pion tracks because it is most likely one of the two tracks which fulfill the trigger requirement of a transverse momentum of at least $2\,\mathrm{GeV}/c$. Since the Λ_c^+ decays weakly and therefore possesses a relatively long mean lifetime of $\tau = (200 \pm 6) \cdot 10^{-15}\,\mathrm{s}$, another

Table 5.4.: Λ_c^+ precuts.

COT Stereo Hits (all tracks)	$\geqq 10$
COT Axial Hits (all tracks)	$\geqq 10$
$p_T(p)$	$> 1.9\,\mathrm{GeV}/c$
$p_T(K)$	$> 0.4\,\mathrm{GeV}/c$
$p_T(\pi)$	$> 0.4\,\mathrm{GeV}/c$
$L_{xy}(\Lambda_c^+)$	$> 0.25\,\mathrm{mm}$
$LL_p(p)$	> 0.6
$LL_K(K)$	> 0.2
$\chi^2(\Lambda_c^+)$	< 22.0

cut is applied on the displacement of the associated secondary vertex, projected onto the Λ_c^+ transverse momentum direction, to the beam, L_{xy}.

In addition, particle identification information from the TOF and $\mathrm{d}E/\mathrm{d}x$ from the COT is employed. For each track t, the two sources of information are combined into a single variable

$$LL_i(t) = \frac{P^i_{\mathrm{d}E/\mathrm{d}x}(t) P^i_{TOF}(t)}{\sum_{j=\pi,K,p} f_j P^j_{\mathrm{d}E/\mathrm{d}x}(t) P^j_{TOF}(t)}, \tag{5.1}$$

where the index i denotes the hypothesis of the particle type. The $P^i_{TOF}(t)$ is the probability to observe the measured time-of-flight given a particle of type i, and $P^i_{\mathrm{d}E/\mathrm{d}x}(t)$ is the probability to observe the measured $\mathrm{d}E/\mathrm{d}x$. The fractions f_j are $f_\pi = 0.7$, $f_K = 0.2$, and $f_p = 0.1$, as estimated from TOF information of a generic background sample. The requirement $LL_p > 0.6$ is applied on the proton track and $LL_K > 0.2$ on the kaon track. In case TOF or $\mathrm{d}E/\mathrm{d}x$ information is not available for a given track, the corresponding requirement is not imposed. These quantities are very useful for the selection of Λ_c^+ candidates because most of the tracks in the detector are caused by pions.

Neural Network

The Λ_c^+ network training is based on the mass distribution after application of the precuts in the range $2256.46 < M(pK^-\pi^+) < 2316.46\,\mathrm{MeV}/c^2$ shown in Figure 5.2. A fit with a Gaussian signal and a linear background function defines the PDFs used to calculate the ${}_s\mathcal{P}lot$ weights.

The full list of input quantities of the neural network, sorted by their importance, can be found in Table 5.5. In the table, d_0 denotes the impact parameter with respect to the primary vertex of the $p\bar{p}$ interaction for a track in the plane transverse to the beam direction, σ_{d_0} its uncertainty, $\chi^2(\Lambda_c^+)$ the quality of the kinematic fit of the Λ_c^+ candidate, and $\cos(\sphericalangle(\Lambda_c^+, t))$ the cosine of the angle between the momentum

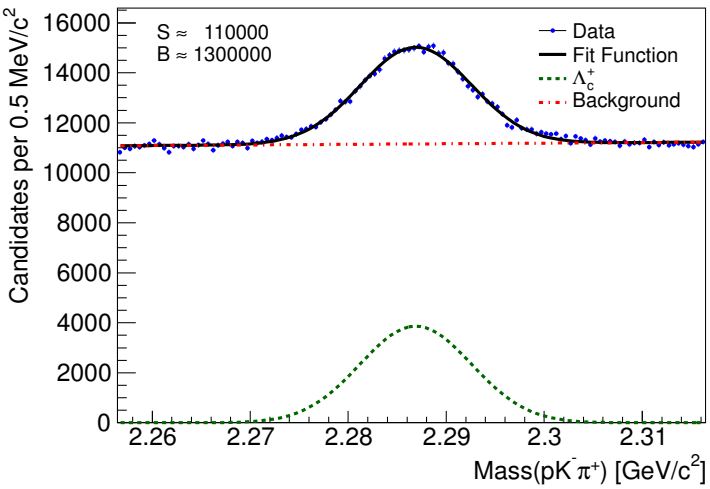

Figure 5.2.: Invariant mass distribution of the even-numbered Λ_c^+ candidates after application of the precuts in Table 5.4. All candidates used to fill this histogram are fed to the network as training pattern. The corresponding ${}_s\mathcal{P}lot$ weights are calculated by means of the fitted signal and background functions.

Table 5.5.: Inputs to the neural network for the Λ_c^+ selection sorted by their importance.

Index	Variable	Index	Variable
1	$LL_p(p)$	8	$p_T(p)$
2	$\sigma_{L_{xy}}(\Lambda_c^+)$	9	$\cos(\sphericalangle(\Lambda_c^+, K))$
3	$LL_K(K)$	10	$p_T(\pi)$
4	$\cos(\sphericalangle(\Lambda_c^+, p))$	11	$d_0/\sigma_{d_0}(K)$
5	$\chi^2(\Lambda_c^+)$	12	$p_T(K)$
6	$L_{xy}(\Lambda_c^+)$	13	$d_0/\sigma_{d_0}(p)$
7	$d_0/\sigma_{d_0}(\pi)$		

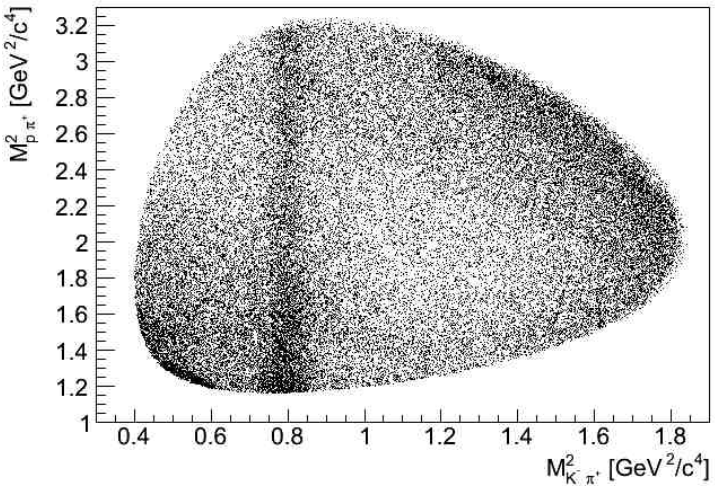

Figure 5.3.: Dalitz plot of the decay $\Lambda_c^+ \to p\,K^-\,\pi^+$.

of the Λ_c^+ candidate in the lab frame and the momentum of the proton or kaon track in the Λ_c^+ rest frame. These helicity angles carry information about the resonant substructure of the decay $\Lambda_c^+ \to p\,K^-\,\pi^+$. As visualization, Figure 5.3 shows one of the corresponding Dalitz plots (see Section 6.4). The resonance $K^*(892)^0$ is clearly visible as band structure at its squared mass on the $M^2_{K^-\pi^+}$ axis and also interference regions in the Dalitz plot can be seen. Only for the creation of this plot, the cuts on the particle identification quantities are tightened to $LL_p(p) > 4.0$, $LL_K(K) > 2.0$ and the Λ_c^+ mass window is chosen as $2276.46 < M(pK^-\pi^+) < 2296.46\,\mathrm{MeV}/c^2$ in order to reduce the background contamination.

Figure 5.4 shows the correlation matrix of the input variables of the network for Λ_c^+ selection before decorrelation. There are no large correlations among the different quantities.

In figure 5.5 separate distributions of the input variables, produced during the individual preprocessing, are shown. The black data points in the histograms represent the bin-by-bin signal fraction of the flattened spectra of the training events. Flat means that in every bin is approximately the same amount of signal plus background events. Spline fits (red) are used to avoid learning of statistical fluctuations.

For some variables, extra classes of events are created which are not regarded by the network training. For example, it was already mentioned that there is a lack of the particle identification information for some events and the corresponding variables are set to a value of -999. Furthermore, not the whole range of the cosine of the angles from -1 to 1 is used in the network training because there are value regions which offer no separation power between signal and background.

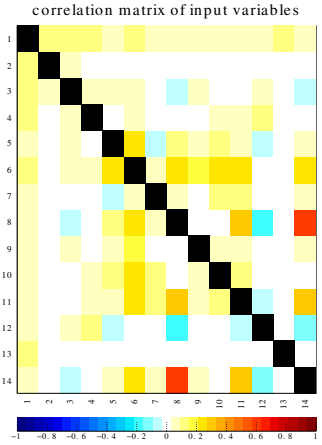

1	target
2	$LL_p(p)$
3	$LL_K(K)$
4	$\chi^2(\Lambda_c^+)$
5	$L_{xy}(\Lambda_c^+)$
6	$\sigma_{L_{xy}}(\Lambda_c^+)$
7	$p_T(p)$
8	$p_T(K)$
9	$p_T(\pi)$
10	$d_0/\sigma_{d_0}(p)$
11	$d_0/\sigma_{d_0}(K)$
12	$d_0/\sigma_{d_0}(\pi)$
13	$\cos(\sphericalangle(\Lambda_c^+, p))$
14	$\cos(\sphericalangle(\Lambda_c^+, K))$

Figure 5.4.: Correlation matrix of the variables for the Λ_c^+ network training with even-numbered events.

Figure 5.6 shows the usual (not flat) distributions of the different variables of the even-numbered Λ_c^+ network separately for signal and background candidates. The spectra of the signal candidates are determined by means of sideband subtractions according to the signal mass region $2276.46 < M(pK^-\pi^+) < 2296.46\,\mathrm{MeV}/c^2$ and the sidebands $2258.46 < M(pK^-\pi^+) < 2268.46\,\mathrm{MeV}/c^2$, $2304.46 < M(pK^-\pi^+) < 2314.46\,\mathrm{MeV}/c^2$. For the creation of the background distributions the mass regions $2264.16 < M(pK^-\pi^+) < 2266.46\,\mathrm{MeV}/c^2$, $2306.46 < M(pK^-\pi^+) < 2308.76\,\mathrm{MeV}/c^2$ are used. The thresholds in the p_T spectra at $2\,\mathrm{GeV}/c$ correspond to the two track trigger requirements and the complicated signal distributions of the helicity angles are due to the resonant substructure of the Λ_c^+ decay.

To demonstrate the ability of the neural network to classify signal and background, the mass distributions of Λ_c^+ candidates with even event numbers before and after requiring their neural network output to correspond to an *a posteriori* signal probability greater than 2.5% is shown in Figure 5.7. This requirement leads to a background reduction of 32% while keeping 97% of the signal. We use the output of the Λ_c^+ neural network as input to the neural networks for selecting the Σ_c and Λ_c^{*+} resonances.

A fit to the spectrum of the combined even- and odd-numbered Λ_c^+ candidates after requiring their neural network output to correspond to an *a posteriori* signal probability greater than 25% is shown in Figure 5.8. Two Gaussian functions with the same mean for the signal plus a linear function for the background shape are

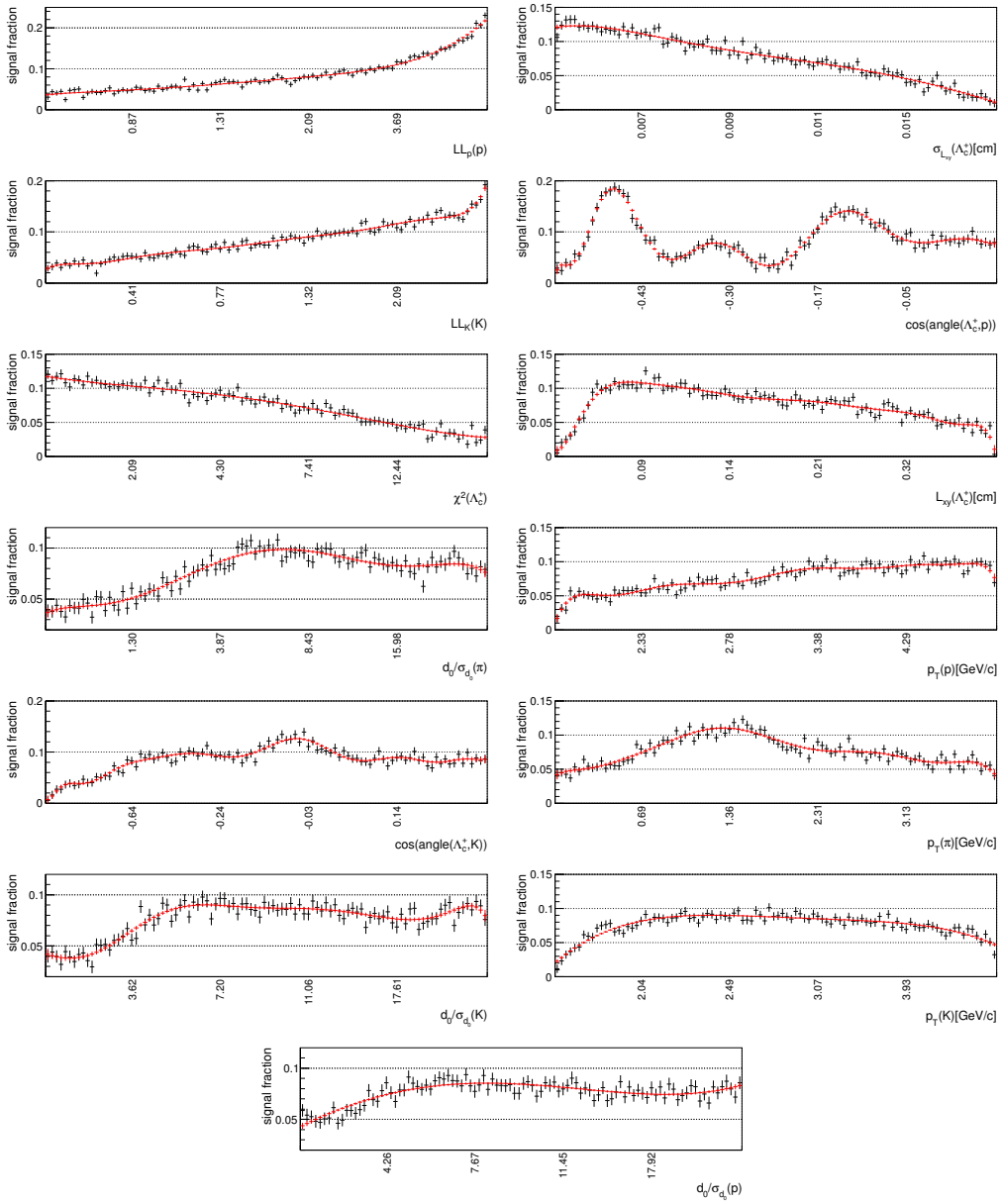

Figure 5.5.: Spline fits to the flat signal fraction distributions of the different input variables of the Λ_c^+ network training with even-numbered events.

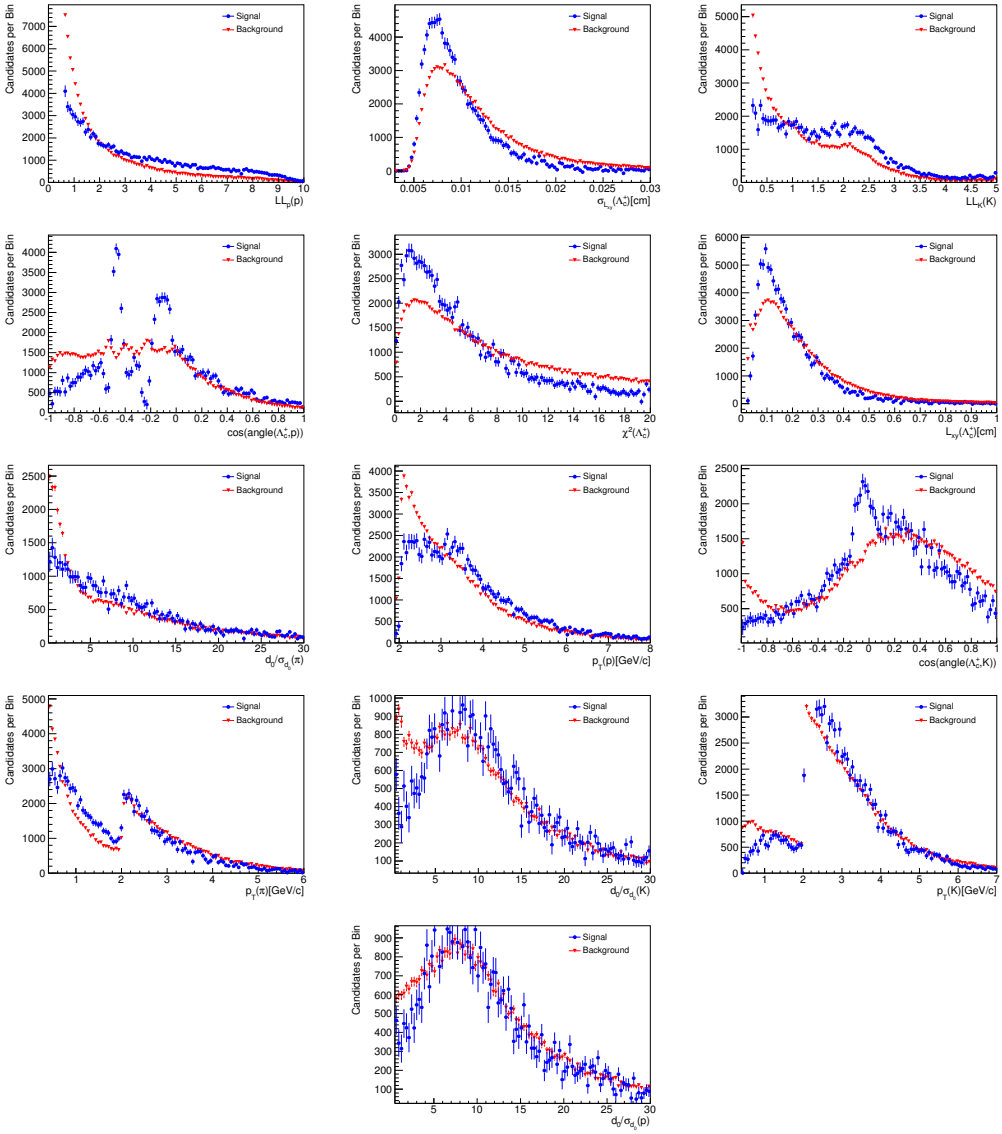

Figure 5.6.: Distributions of the different variables of the even-numbered Λ_c^+ network separately for signal and background candidates.

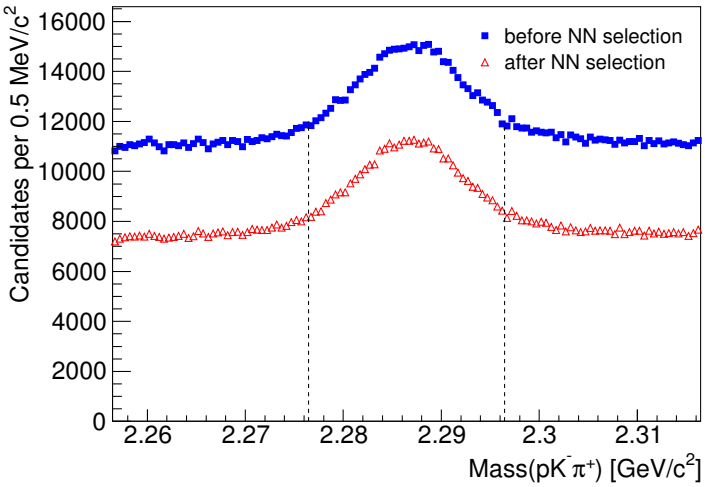

Figure 5.7.: The mass distributions of Λ_c^+ candidates before (blue full squares) and after (red open triangles) requiring their neural network output to correspond to an *a posteriori* signal probability greater than 2.5%. The vertical dashed lines indicate a $\pm 10\,\mathrm{MeV}/c^2$ region around the nominal Λ_c^+ mass [1] used for the selection of the Σ_c and Λ_c^{*+} states.

fitted to the mass distribution and the resulting values for the Λ_c^+ mass and width are

$$m(\Lambda_c^+) = (2286.79 \pm 0.04)\,\mathrm{MeV}/c^2,$$
$$\bar{\sigma}(\Lambda_c^+) = (6.40 \pm 0.60)\,\mathrm{MeV}/c^2.$$

Thereby, $\bar{\sigma}(\Lambda_c^+)$ is the weighted average of the two Gaussian standard deviations and corresponds in good approximation to the detector resolution, since the Λ_c^+ is a very narrow state because of its weak decay.

5.3.2. $\Sigma_c(2455)$ and $\Sigma_c(2520)$ Selection

The $\Sigma_c(2455)^{++,0}$ and $\Sigma_c(2520)^{++,0} \to \Lambda_c^+\,\pi^{+,-}$ selection starts with the application of a few loose requirements to remove the most obvious background, followed by the use of a neural network.

Precuts

The *a posteriori* signal probability of the Λ_c^+ neural network is required to be greater than 2.5% (see Figure 5.7), the $p_T(\pi)$ of the added pion to be greater than $400\,\mathrm{MeV}/c$, $d_0(\pi) < 1.5\,\mathrm{mm}$, and the mass of the Λ_c^+ candidate to be within $\pm 10\,\mathrm{MeV}/c^2$ of the nominal Λ_c^+ mass [1], $2276.46 < M(pK^-\pi^+) < 2296.46\,\mathrm{MeV}/c^2$

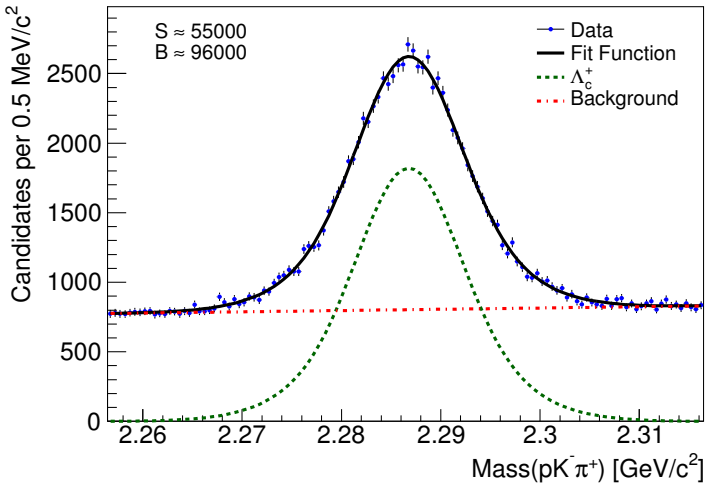

Figure 5.8.: Fit to the Λ_c^+ mass distribution after requiring their neural network output to correspond to an *a posteriori* signal probability greater than 25%.

(see Figure 5.7). These requirements are common for both neutral and doubly-charged states.

The resulting mass difference $\Delta M = M(\Sigma_c) - M(\Lambda_c^+)$ distributions of all the $\Lambda_c^+\pi^+$ and $\Lambda_c^+\pi^-$ candidates are shown in Figures 5.9 and 5.10. In the ΔM definition, $M(\Sigma_c)$ and $M(\Lambda_c^+)$ correspond to the reconstructed masses of the Σ_c and Λ_c^+ candidates. The mass differences are used rather than the pure invariant masses of the Σ_c candidates in order to improve the resolution which is limited by detector effects.

Neural Network

The neural network for the final selection of the $\Sigma_c(2455)$ and $\Sigma_c(2520)$ candidates uses five input quantities. Ordered by their importance, these are the output of the Λ_c^+ neural network $NN(\Lambda_c^+)$, the proper decay time of the Σ_c candidate $t(\Sigma_c) = (L_{xy}(\Sigma_c) \cdot M(\Sigma_c))/(c \cdot p_T(\Sigma_c))$, the quality of the kinematic fit of the Σ_c candidate $\chi^2(\Sigma_c)$, the uncertainty of the Σ_c impact parameter in the transverse plane $\sigma_{d_0}(\Sigma_c)$, and the impact parameter in the transverse plane of the pion from the Σ_c decay $d_0(\pi)$. Independent neural networks are employed for Σ_c^{++} and Σ_c^0.

The training itself is performed using candidates in the mass difference region from 155 to 180 MeV/c^2 shown in Figures 5.11 and 5.12. Although this includes only $\Sigma_c(2455)$ candidates, it is applied to select $\Sigma_c(2520)$ candidates as well. The ${}_s\mathcal{P}lot$ weights are determined by a fit to the ΔM distribution with a Gaussian function for the signal and a linear function for the background PDF.

The correlation matrices of the input variables can be found in Figures 5.13

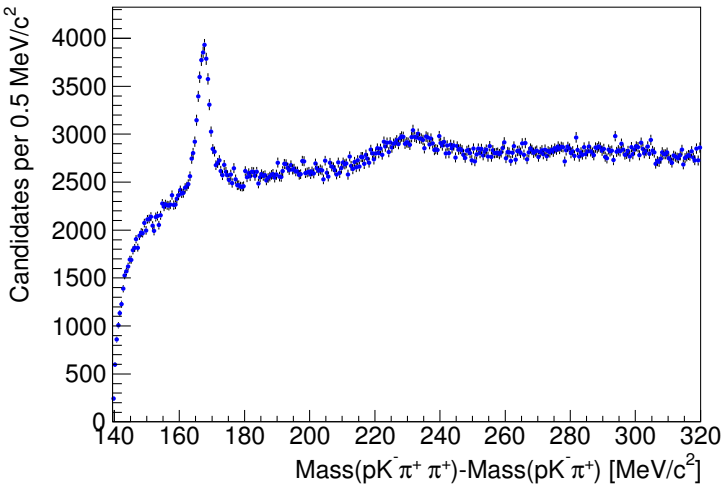

Figure 5.9.: Distribution of the mass difference $M(\Sigma_c^{++}) - M(\Lambda_c^+)$ after precuts.

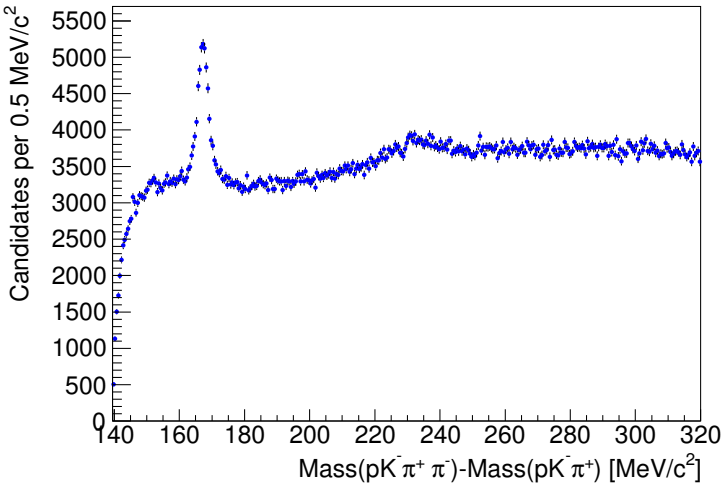

Figure 5.10.: Distribution of the mass difference $M(\Sigma_c^0) - M(\Lambda_c^+)$ after precuts.

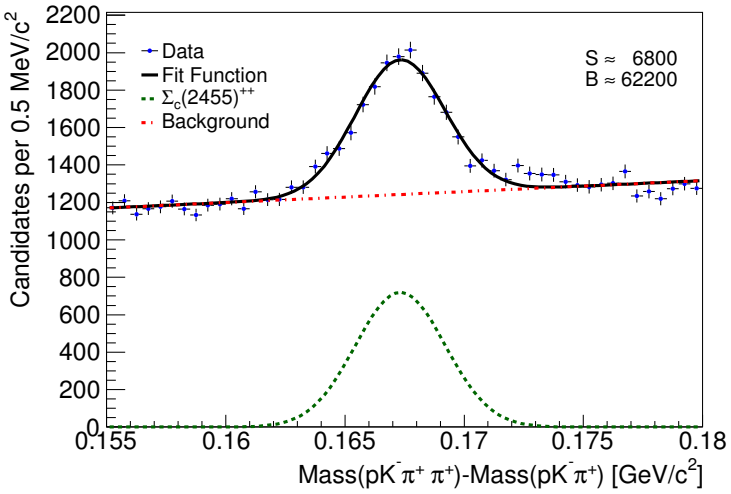

Figure 5.11.: Mass difference distribution of the even-numbered $\Sigma_c(2455)^{++}$ candidates after application of the precuts. All candidates used to fill this histogram are fed to the network as training pattern. The corresponding ${}_s\mathcal{P}lot$ weights are calculated by means of the fitted signal and background functions.

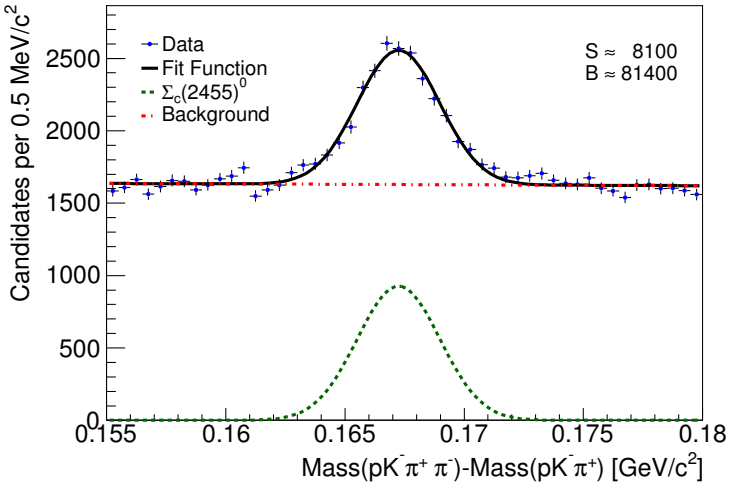

Figure 5.12.: Mass difference distribution of the even-numbered $\Sigma_c(2455)^0$ candidates after application of the precuts. All candidates used to fill this histogram are fed to the network as training pattern. The corresponding ${}_s\mathcal{P}lot$ weights are calculated by means of the fitted signal and background functions.

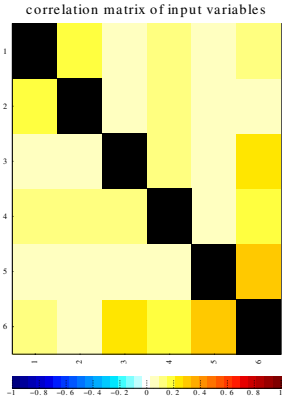

1 target
2 $NN(\Lambda_c^+)$
3 $d_0(\pi)$
4 $\chi^2_{\mathrm{3D}}(\Sigma_c^{++})$
5 $\sigma_{d_0}(\Sigma_c^{++})$
6 $ct(\Sigma_c^{++})$

Figure 5.13.: Correlation matrix of the Σ_c^{++} network training with even-numbered events.

and 5.14, and the flat signal fraction distributions of the individual preprocessing ordered by importance of the single input variables for the network in Figure 5.15 for the doubly-charged and Figure 5.16 for the uncharged case. Since the Σ_c states decay strongly and therefore have a very short lifetime, its decay length and the impact parameter of its decay products are small. However, it happens that part of the Σ_c candidates actually stem from b-decays, which leads to larger values for these quantities.

Figures 5.17 and 5.18 show the usual (not flat) distributions of the different variables of the even-numbered Σ_c^{++} and Σ_c^0 networks separately for signal and background candidates. Thereby, the spectra of the signal candidates are determined by means of sideband subtractions according to the signal mass difference region $163.816 < \Delta M < 170.876\,\mathrm{MeV}/c^2$ and the sidebands $156.756 < \Delta M < 160.286\,\mathrm{MeV}/c^2$, $174.406 < \Delta M < 177.936\,\mathrm{MeV}/c^2$. For the creation of the background distributions the mass difference regions $159.121 < \Delta M < 174.406\,\mathrm{MeV}/c^2$, $174.406 < \Delta M < 175.571\,\mathrm{MeV}/c^2$ are used. The peaks in the network output distributions are due to the training method described in Section 4.2.2.

In order to choose a value for a cut on the network output one needs to decide for an appropriate figure of merit. Here, the threshold on the output of the Σ_c neural network is chosen to maximize $S/\sqrt{S+B}$, where S is the number of signal $\Sigma_c(2455)$ events and B is the number of background events in ΔM between 162.3 and $172.3\,\mathrm{MeV}/c^2$. The S and B yields are derived from a fit to the ΔM distribution which uses a Gaussian function for the signal and a linear function for the background and covers the ΔM range used for the neural network training. Figures 5.19 and 5.20 show the values of $\mathrm{S}/\sqrt{\mathrm{S}+\mathrm{B}}$ in dependance on the cut on the network output variable for the combination of even- and odd-numbered events.

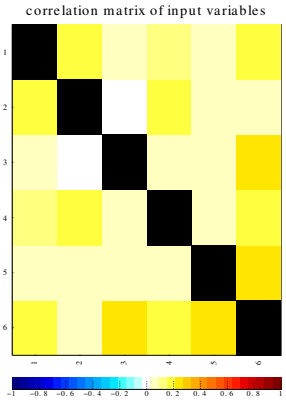

1 target
2 $NN(\Lambda_c^+)$
3 $d_0(\pi)$
4 $\chi^2_{\mathrm{3D}}(\Sigma_c^0)$
5 $\sigma_{d_0}(\Sigma_c^0)$
6 $ct(\Sigma_c^0)$

Figure 5.14.: Correlation matrix of the Σ_c^0 network training with even-numbered events.

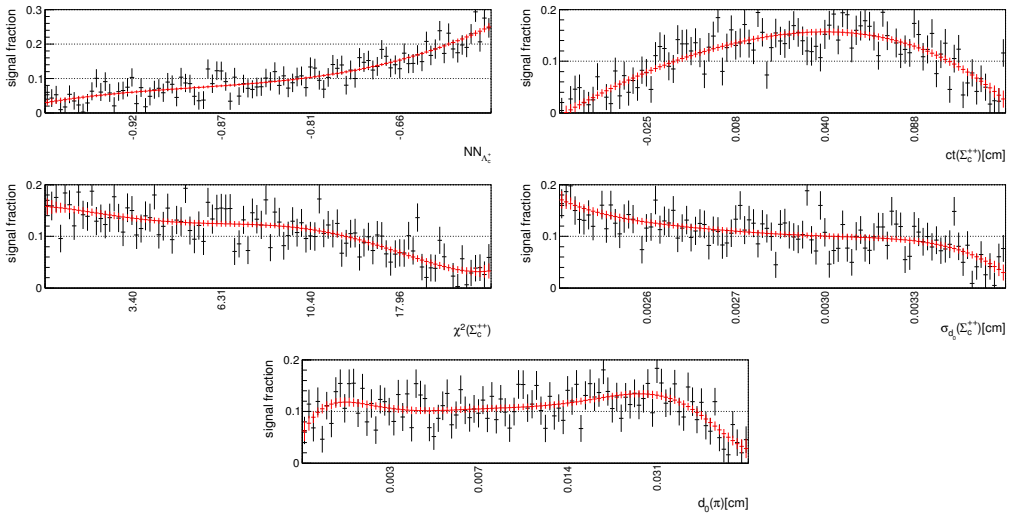

Figure 5.15.: Spline fits to the flat signal fraction distributions of the different input variables of the Σ_c^{++} network training with even-numbered events.

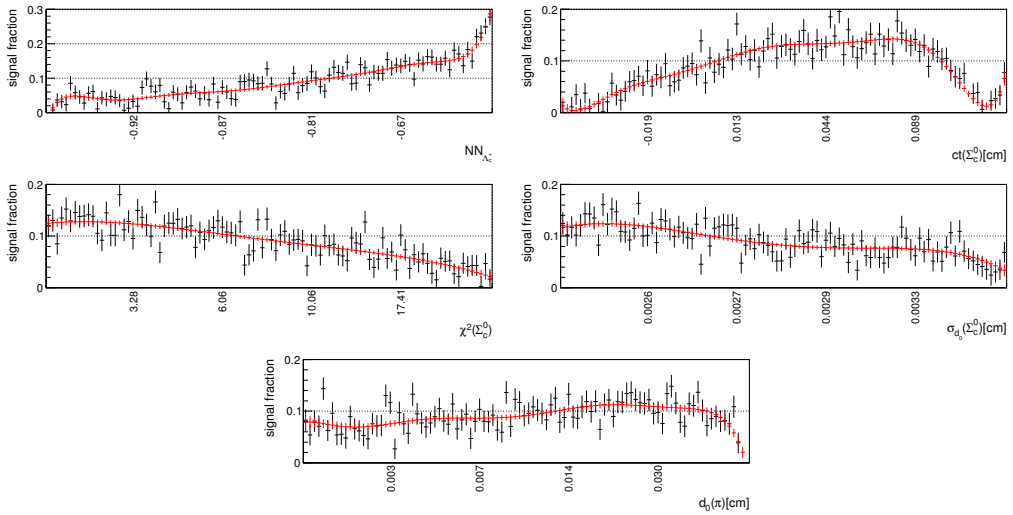

Figure 5.16.: Spline fits to the flat signal fraction distributions of the different input variables of the Σ_c^0 network training with even-numbered events.

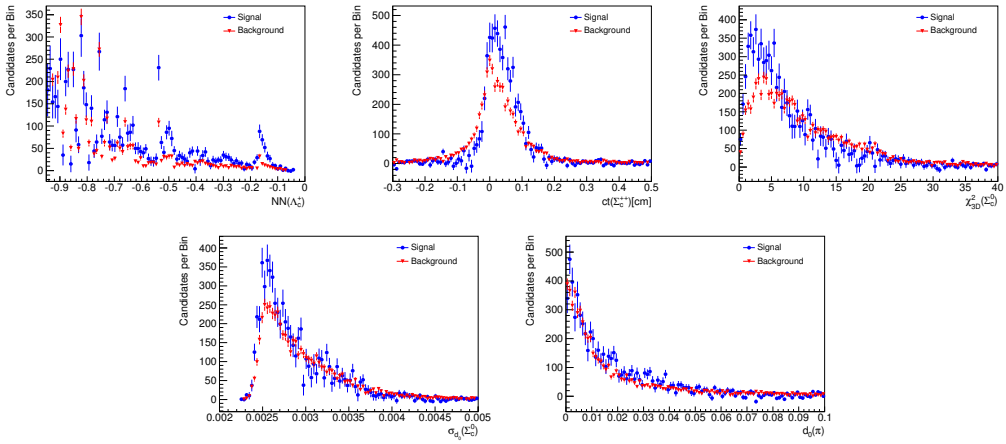

Figure 5.17.: Distributions of the different variables of the even-numbered Σ_c^{++} network separately for signal and background candidates.

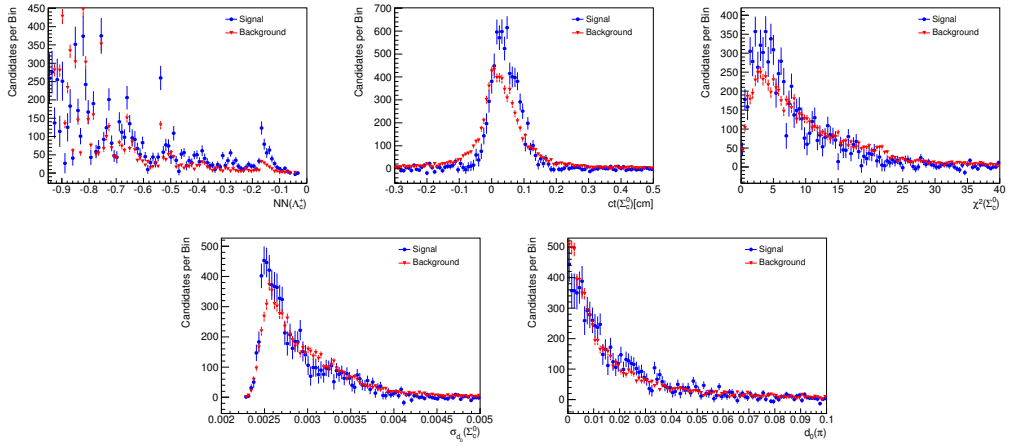

Figure 5.18.: Distributions of the different variables of the even-numbered Σ_c^0 network separately for signal and background candidates.

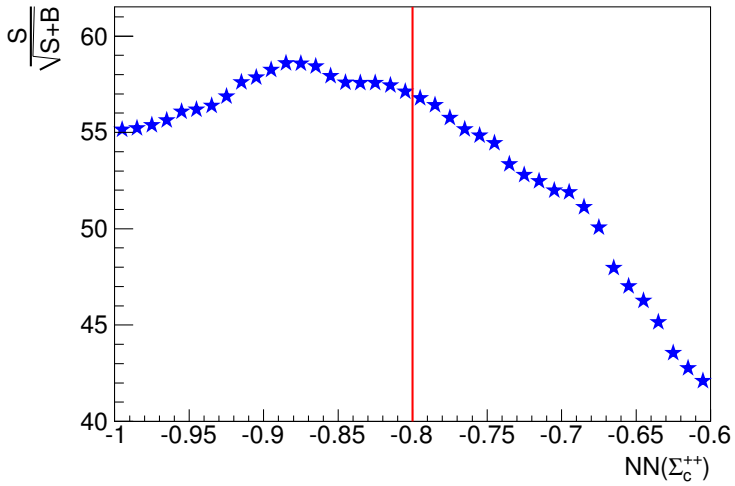

Figure 5.19.: $S/\sqrt{S+B}$ in dependance on the cut on the output variable of the Σ_c^{++} network.

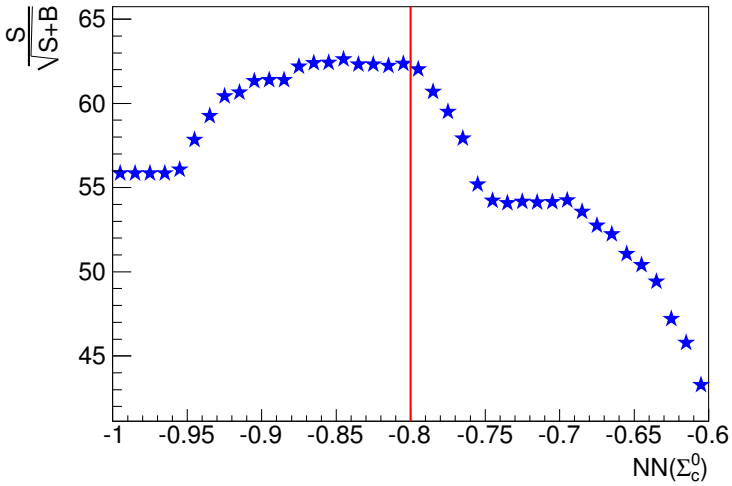

Figure 5.20.: $S/\sqrt{S+B}$ in dependance on the cut on the output variable of the Σ_c^0 network.

The resulting neural network output requirement of $NN(\Sigma_c) > -0.8$ is the same for both charge combinations and corresponds to an *a posteriori* signal probability of the neural networks greater than 10%. The mass difference distributions before and after applying the neural network selection are shown in Figures 5.21 and 5.22.

5.3.3. $\Lambda_c(2595)^+$ and $\Lambda_c(2625)^+$ selection

The $\Lambda_c(2595)^+$ and $\Lambda_c(2625)^+ \to \Lambda_c^+ \pi^+ \pi^-$ selection starts with the application of a few loose requirements to remove the most obvious background, followed by the use of a neural network.

Precuts

The *a posteriori* signal probability of the Λ_c^+ neural network is required to be greater than 2.5%, $2276.46 < M(pK^-\pi^+) < 2296.46\,\mathrm{MeV}/c^2$ (see Figure 5.7), $p_T(\pi)$ of both added pions to be greater than $400\,\mathrm{MeV}/c$, and the impact parameter of the object constructed from the two additional pions to be $d_0(\pi^+\pi^-) < 1.0\,\mathrm{mm}$. The resulting mass difference $\Delta M = M(\Lambda_c^{*+}) - M(\Lambda_c^+)$ distribution is shown in Fig. 5.23.

Neural Network

The ΔM region between 327 and $357\,\mathrm{MeV}/c^2$, shown in Figures 5.11, is used for the neural network training. Although this includes only $\Lambda_c(2625)^+$ candidates, it

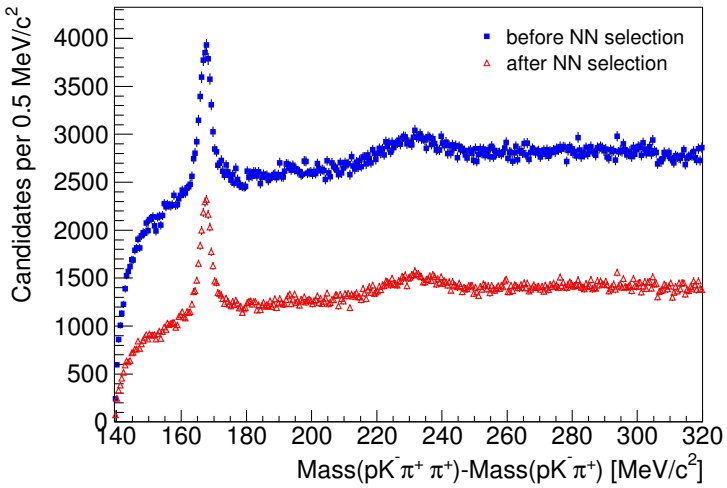

Figure 5.21.: Mass difference distributions of the $\Sigma_c(2455)^{++}$ candidates before (blue full squares) and after (red open triangles) applying the neural network selection.

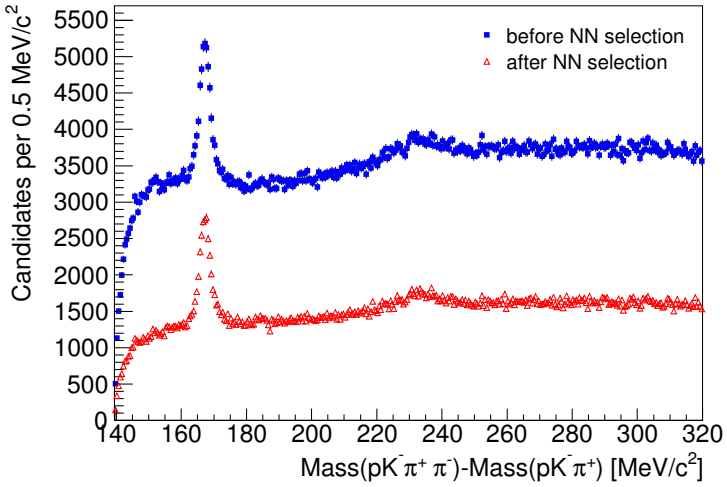

Figure 5.22.: Mass difference distributions of the $\Sigma_c(2455)^0$ candidates before (blue full squares) and after (red open triangles) applying the neural network selection.

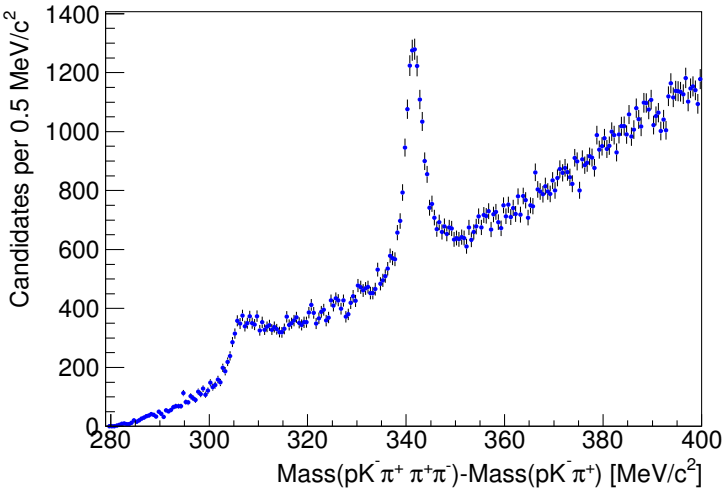

Figure 5.23.: Distribution of the mass difference $M(\Lambda_c^{*+}) - M(\Lambda_c^+)$ after precuts.

is applied to select $\Lambda_c(2595)^+$ candidates as well. The ${}_s\mathcal{P}lot$ weights are based on a fit to the ΔM distribution with a Gaussian function for the signal and a linear function for the background PDF.

The neural network uses four inputs. Ordered by their importance, these are the quality of the Λ_c^{*+} kinematic fit $\chi^2(\Lambda_c^{*+})$, the uncertainty of the impact parameter of the combined two-pion object $\sigma_{d_0}(\pi^+\pi^-)$, the output of the Λ_c^+ neural network $NN(\Lambda_c^+)$, and the proper decay time of the Λ_c^{*+} candidate $t(\Lambda_c^{*+})$. The correlation matrix of the input variables can be found in Figure 5.25 and the flat signal fraction distributions of the individual preprocessing in Figure 5.26.

Figure 5.27 shows the usual (not flat) distributions of the different variables of the even-numbered Λ_c^{*+} network separately for signal and background candidates. Thereby, the spectra of the signal candidates are determined by means of sideband subtractions according to the signal mass region $338.036 < \Delta M < 345.264\,\mathrm{MeV}/c^2$ and the sidebands $330.808 < \Delta M < 334.422\,\mathrm{MeV}/c^2$, $348.878 < \Delta M < 352.492\,\mathrm{MeV}/c^2$. For the creation of the background distributions the mass regions $331.459 < \Delta M < 334.422\,\mathrm{MeV}/c^2$, $348.878 < \Delta M < 351.841\,\mathrm{MeV}/c^2$ are used.

Again, the requirement that maximizes $S/\sqrt{S+B}$ is chosen. The S and B yields are derived from a fit to the ΔM distribution using a Gaussian function for the $\Lambda_c(2625^+)$ signal and a linear function for the background, where events in the region $336.7 < \Delta M < 346.7\,\mathrm{MeV}/c^2$ are considered. Figure 5.28 shows the values of $\mathrm{S}/\sqrt{\mathrm{S}+\mathrm{B}}$ in dependance on the cut on the network output variable for the combination of even- and odd-numbered events. The resulting neural network output requirement of $NN(\Lambda_c^{*+}) > -0.75$ corresponds to an *a posteriori* signal probability

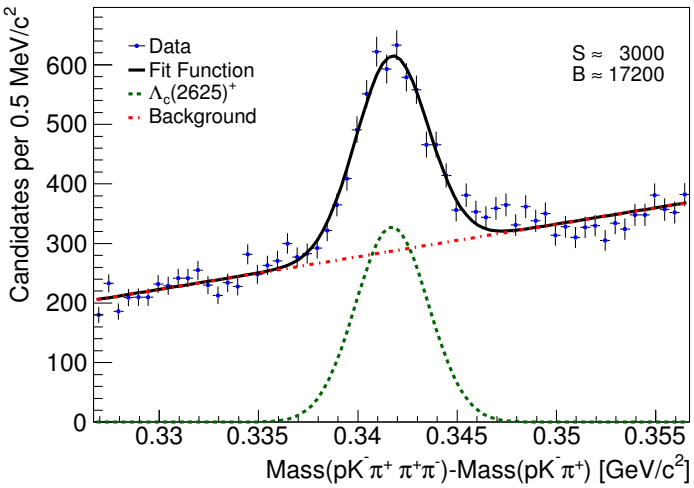

Figure 5.24.: Mass difference distribution of the even-numbered $\Lambda_c(2625)^+$ candidates after application of the precuts. All candidates used to fill this histogram are fed to the network as training pattern. The corresponding ${}_s\mathcal{P}lot$ weights are calculated by means of the fitted signal and background functions.

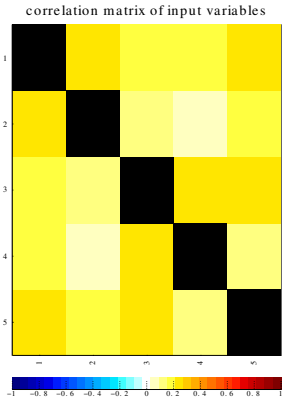

1 target
2 $NN(\Lambda_c^+)$
3 $ct(\Lambda_c^{*+})$
4 $\sigma_{d_0}(\pi_1\pi_2)$
5 $\chi^2(\Lambda_c^{*+})$

Figure 5.25.: Correlation matrix of the Λ_c^{*+} network training with even-numbered events.

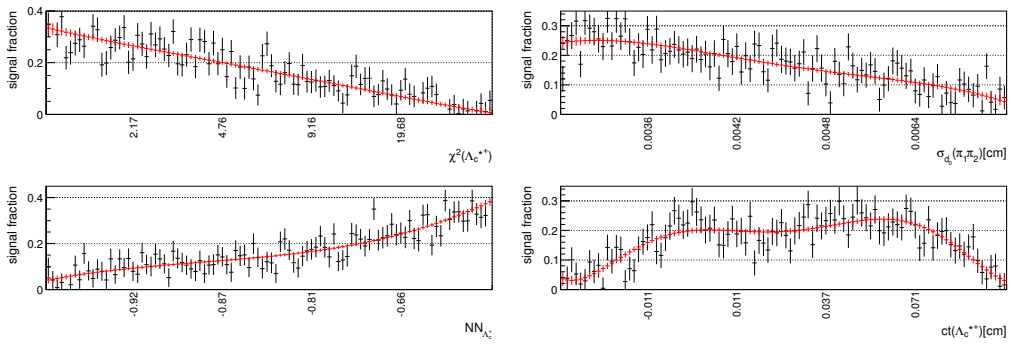

Figure 5.26.: Spline fits to the flat signal fraction distributions of the different input variables of the Λ_c^{*+} network training with even-numbered events.

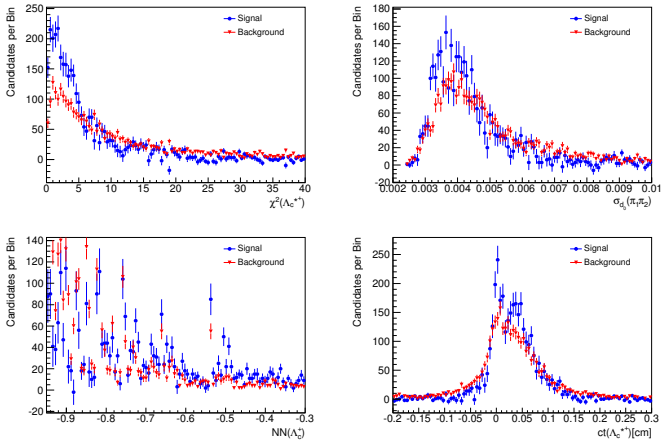

Figure 5.27.: Distributions of the different variables of the even-numbered Λ_c^{*+} network separately for signal and background candidates.

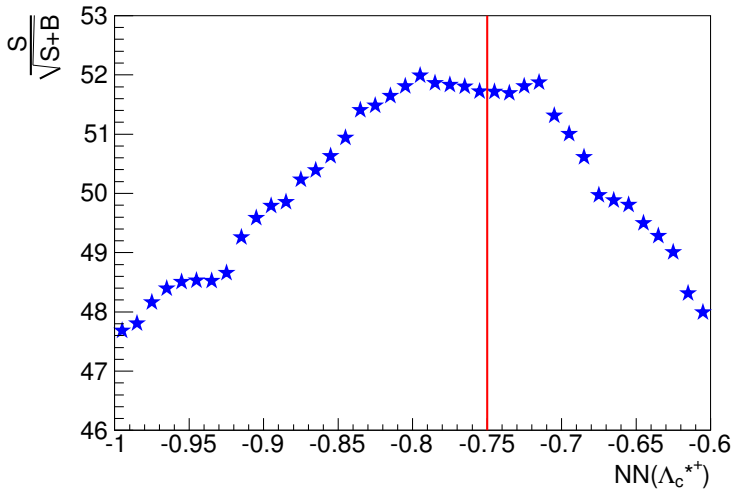

Figure 5.28.: $S/\sqrt{S+B}$ in dependance on the cut on the network output variable.

of the neural network greater than 12.5%. The mass difference distribution before and after applying the neural network selection is shown in Figure 5.29.

The wrong sign charge combinations $\Lambda_c^+\pi^-\pi^-$ can be used for validating the selection method. For that purpose, the exactly same cuts are applied as for the right sign charge combinations $\Lambda_c^+\pi^+\pi^-$. The resulting $M(\Lambda_c^+\pi^-\pi^-) - M(\Lambda_c^-)$ distribution can be found in Figure 5.30. No enhancements show up in the spectrum, the shape of which is qualitatively similar to the background in the right sign combinations, as can be seen in Figure 5.31.

5.3.4. Candidates from Λ_c^+ Sidebands

Candidates from the lower and upper Λ_c^+ mass sidebands $2261.46 < M(pK^-\pi^+) < 2266.46\,\mathrm{MeV}/c^2$ and $2306.46 < M(pK^-\pi^+) < 2311.46\,\mathrm{MeV}/c^2$, shown in Figure 5.32, are used to determine the combinatorial background without real Λ_c^+ candidates in the $\Sigma_c^{++,0}$ and Λ_c^{*+} spectra. The exactly same selection requirements as for the candidates from the corresponding signal mass window are imposed.

The usage of these Λ_c^+ sideband samples and thus the need for the same selection in both signal and sideband mass regions is the reason for not including the reconstructed Λ_c^+ mass in the networks for the excited states, although it would be a well separating variable.

Σ_c Candidates

For the $\Sigma_c^{++,0}$ background, the Λ_c^+ sideband candidates are combined with an additional pion track. The resulting distributions for the doubly-charged and uncharged

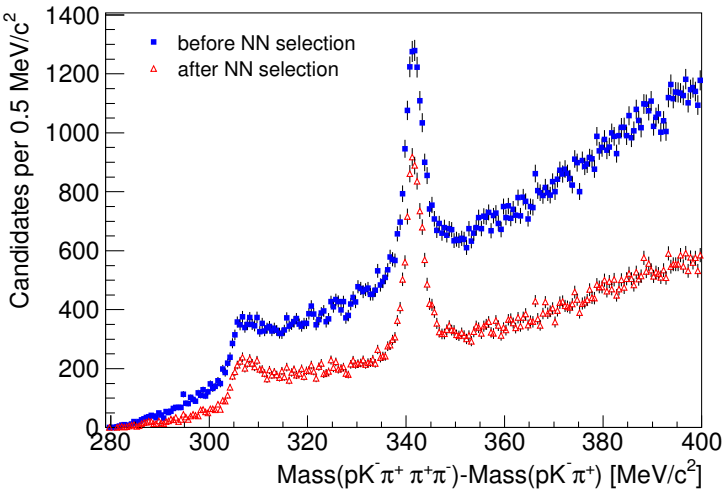

Figure 5.29.: Mass difference distributions of the Λ_c^{*+} candidates before (blue full squares) and after (red open triangles) applying the neural network selection.

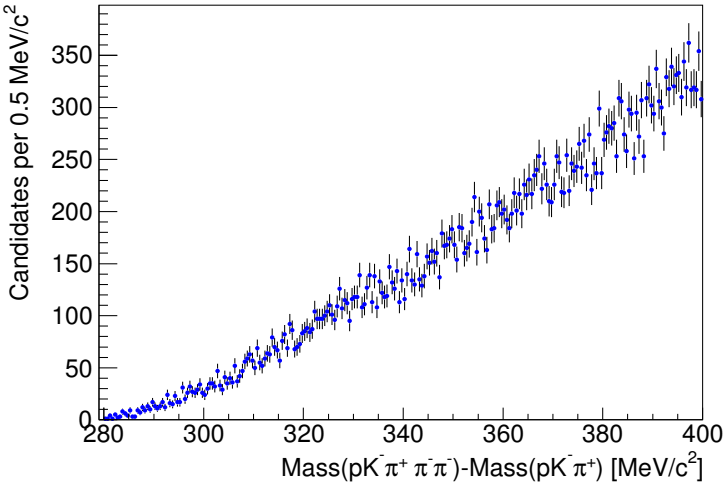

Figure 5.30.: Spectrum of the wrong sign charge combinations $M(\Lambda_c^+\pi^-\pi^-) - M(\Lambda_c^-)$ after selection cuts.

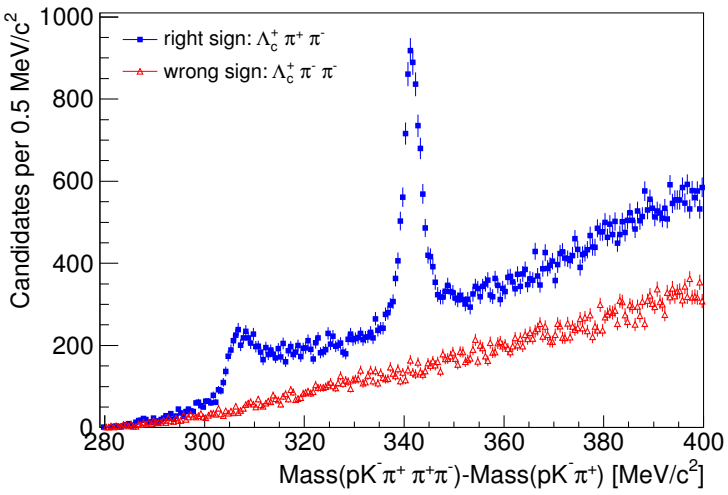

Figure 5.31.: Comparison of the Λ_c^* right and wrong sign charge combinations spectra after selection cuts.

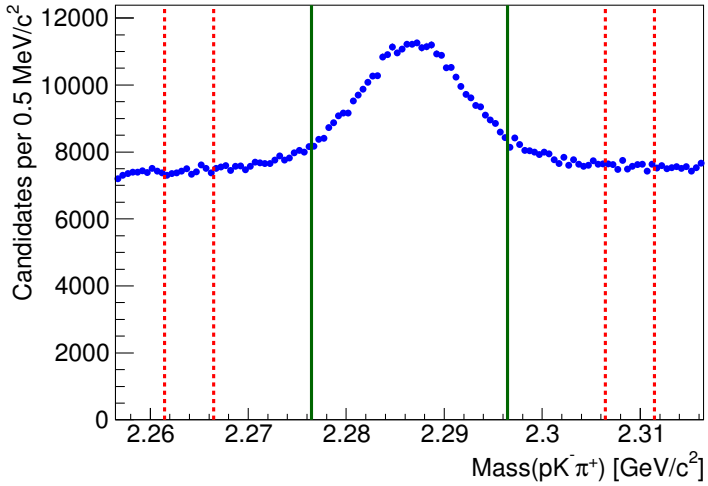

Figure 5.32.: Selected signal region (orange) as well as lower and upper Λ_c+ mass sidebands (red).

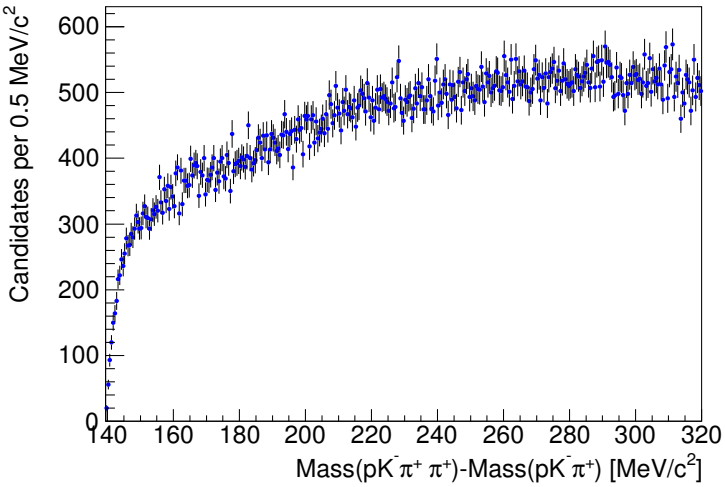

Figure 5.33.: Candidates from the Λ_c+ mass sidebands in Figure 5.32 combined with an additional π^+ track to form combinatorial Σ_c^{++} background without real Λ_c^+.

combinations can be found in Figures 5.33 and 5.34.

The peaking structure, which can be seen in both signal and Λ_c^+ sideband spectra of the uncharged combinations at a mass difference of around $150\,\mathrm{MeV}/c^2$ (Figures 5.22 and 5.34), is due to a $D^*(2010)^+$ decaying to $D^0\,\pi^+$ with $D^0 \to K^-\,\pi^+\,\pi^+\,\pi^-$. Thereby, one of the pions (π^+ in the uncharged and π^- in the doubly-charged case) from the D^0 decay is omitted in the reconstruction. Furthermore, the K^- is assigned proton mass and one of the π^+ is assigned kaon mass. The reason for this is that the proton has the highest momentum in the Λ_c^+ decay and the kaon has the highest momentum in the D^0 decay. Because of the Λ_c^- charge requirement $p^-\,K^+\,\pi^-$, one further π^- is needed to fake a Λ_c^- candidate. Since there is no π^- left in the doubly-charged case, this explains the fact that there is no apparent peak in the $M(\Lambda_c^+\pi^+) - M(\Lambda_c^+)$ distribution.

Λ_c^{*+} Candidates

For the Λ_c^{*+} background, the Λ_c^+ sideband candidates are combined with two additional pion tracks. The resulting distribution can be found in Figure 5.35.

5.3.5. Validation of Neural Networks

In order to check that the employed networks for the excited states are not able to learn the mass difference or to create some artificial structures, background versus background trainings are performed and the resulting spectra after application

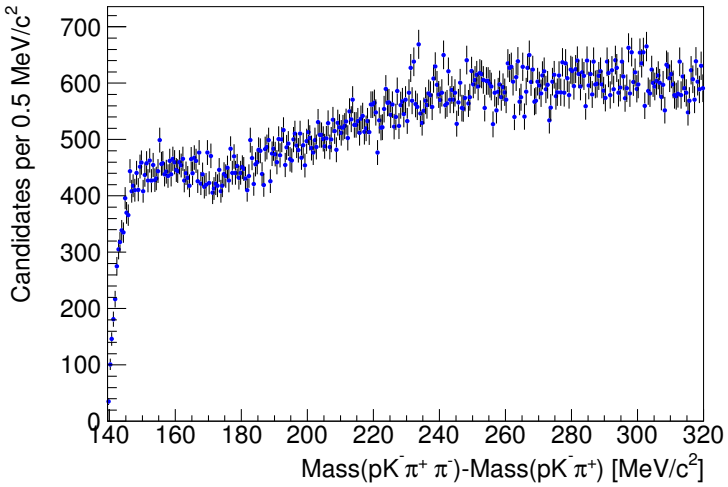

Figure 5.34.: Candidates from the Λ_c+ mass sidebands in Figure 5.32 combined with an additional π^- track to form combinatorial Σ_c^0 background without real Λ_c^+.

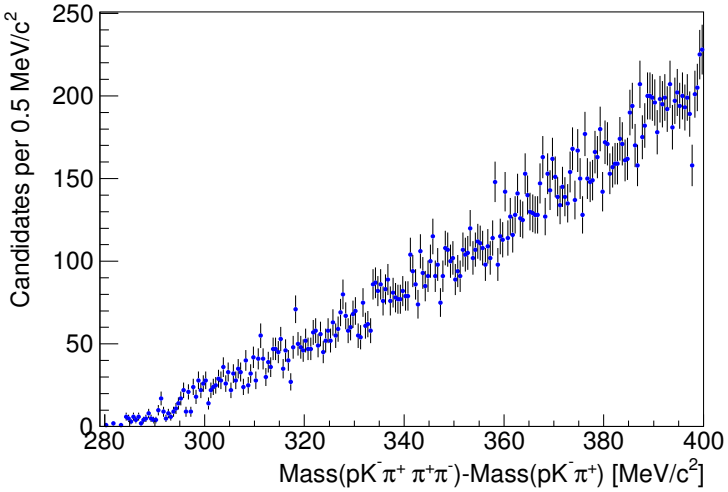

Figure 5.35.: Candidates from the Λ_c+ mass sidebands in Figure 5.32 combined with two additional pion tracks ($\pi^+\pi^-$) to form combinatorial Λ_c^{*+} background without real Λ_c^+.

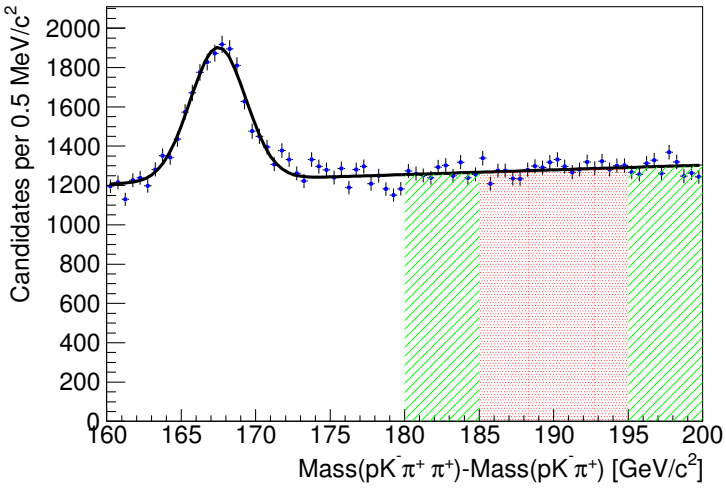

Figure 5.36.: Upper $\Sigma_c(2455)^{++}$ sideband used for the even-numbered background versus background training. The candidates populating the middle red respective outer green mass difference regions are used for the two classification patterns.

of the corresponding network cuts are considered. For that purpose, the upper $\Sigma_c(2455)^{++,0}$ respective $\Lambda_c(2625)^+$ mass difference sidebands are split into three regions, as can be seen in Figures 5.36–5.38. The candidates populating the region in the middle are used as signal pattern, whereas the candidates in the outer left and right regions serve as background sample. Again, the networks are split into one for the even-numbered and one for the odd-numbered events and afterwards applied crosswise.

The flat signal fraction distributions of the individual preprocessing are shown in Figures 5.39–5.41. As expected, none of the variables is able to distinguish between signal and background.

Figures 5.42–5.44 show the mass difference distributions after requiring the corresponding network output to be greater than 0 and combining the even- and odd-numbered candidates. Since the range of the network outputs is -1 to 1, this means that approximately half of the candidates are selected. The distributions in the upper sideband regions are still flat and no additional structures are created.

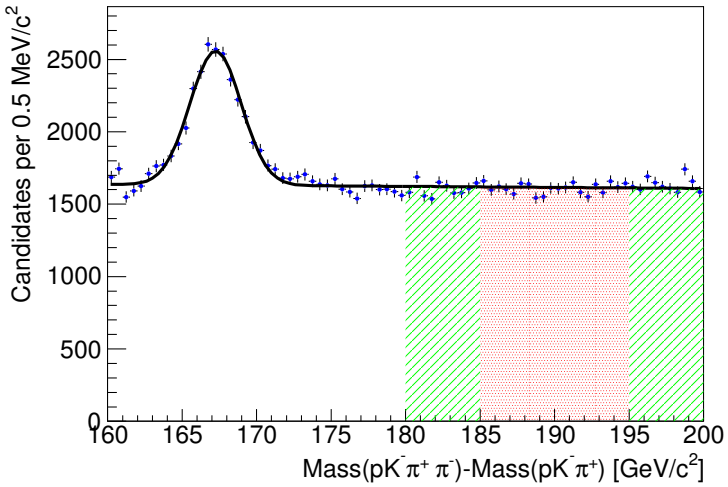

Figure 5.37.: Upper $\Sigma_c(2455)^0$ sideband used for the even-numbered background versus background training. The candidates populating the middle red respective outer green mass difference regions are used for the two classification patterns.

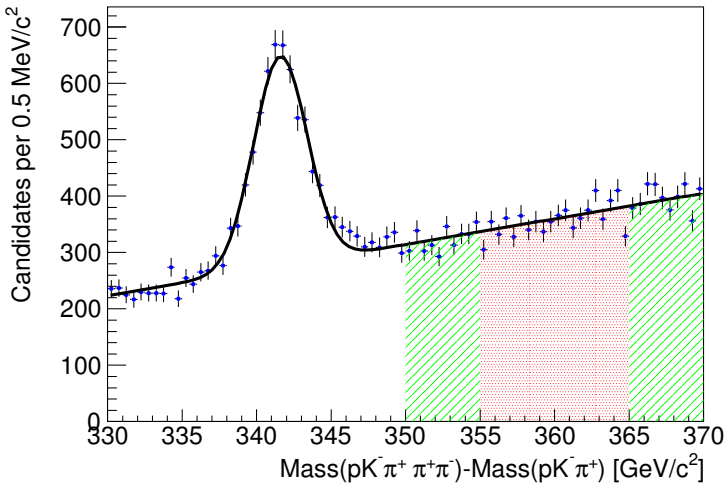

Figure 5.38.: Upper $\Lambda_c(2625)^+$ sideband used for the even-numbered background versus background training. The candidates populating the middle red respective outer green mass difference regions are used for the two classification patterns.

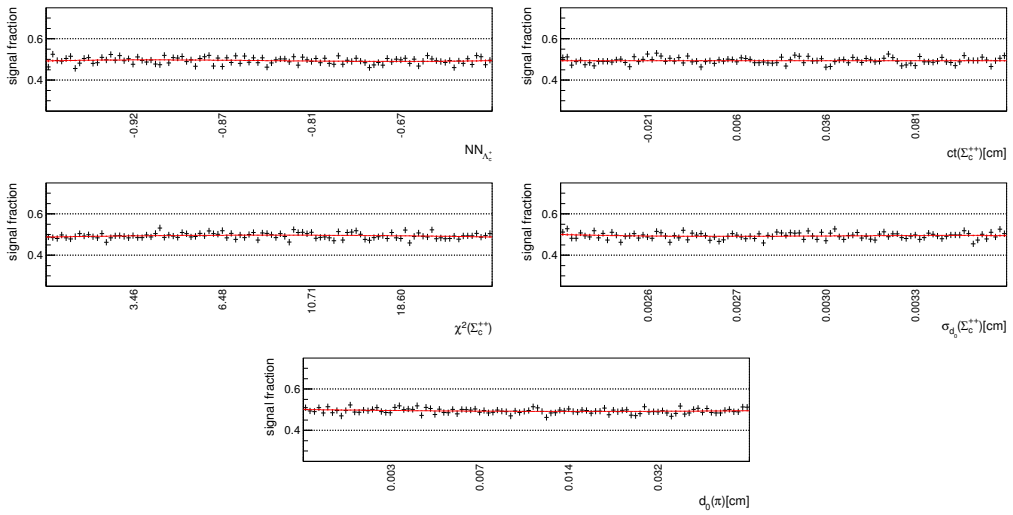

Figure 5.39.: Spline fits to the flat signal fraction distributions of the different input variables of the Σ_c^{++} background versus background network training with even-numbered events.

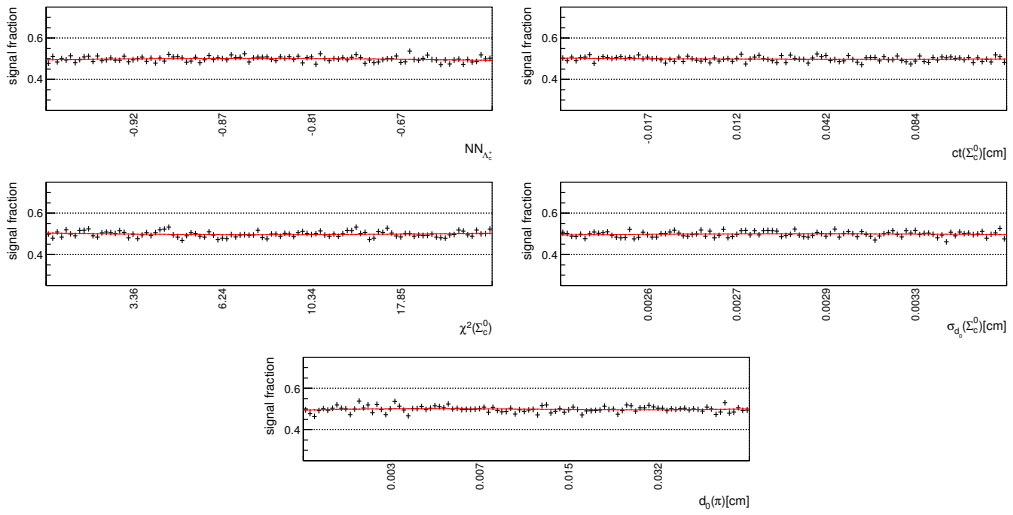

Figure 5.40.: Spline fits to the flat signal fraction distributions of the different input variables of the Σ_c^0 background versus background network training with even-numbered events.

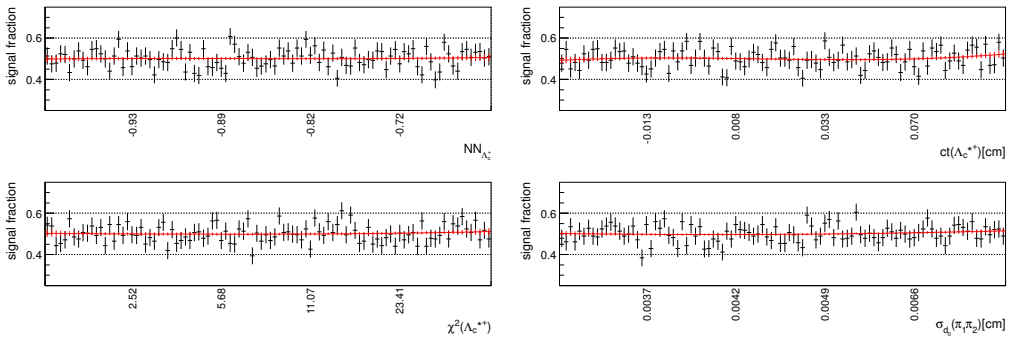

Figure 5.41.: Spline fits to the flat signal fraction distributions of the different input variables of the Λ_c^* background versus background network training with even-numbered events.

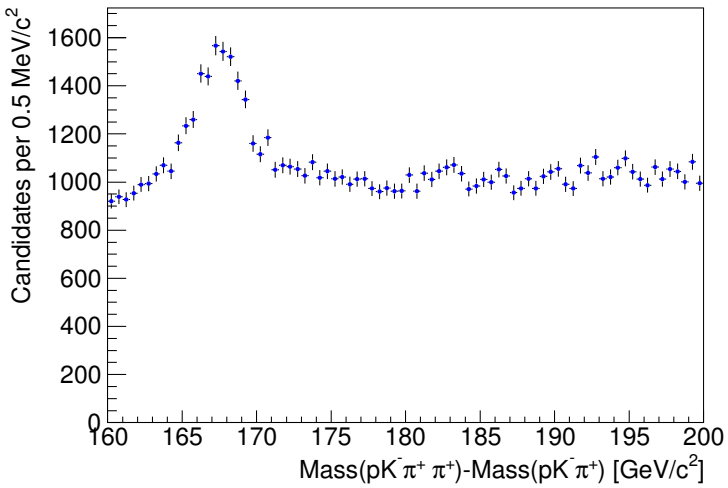

Figure 5.42.: Σ_c^{++} mass difference distributions with a background versus background network output cut at 0.

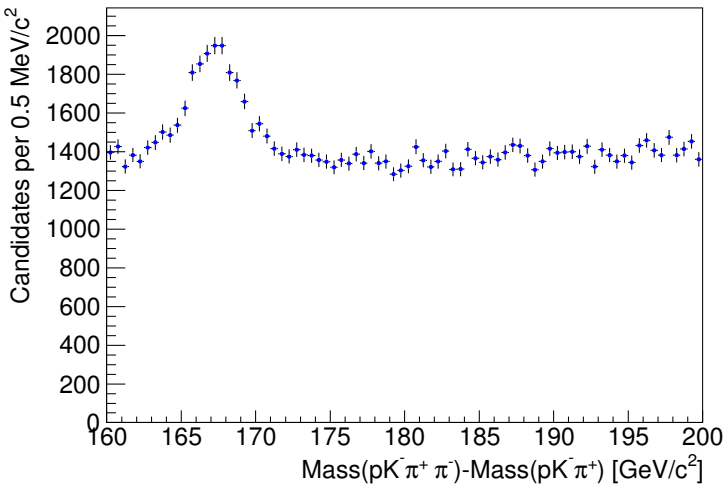

Figure 5.43.: Σ_c^0 mass difference distributions with a background versus background network output cut at 0.

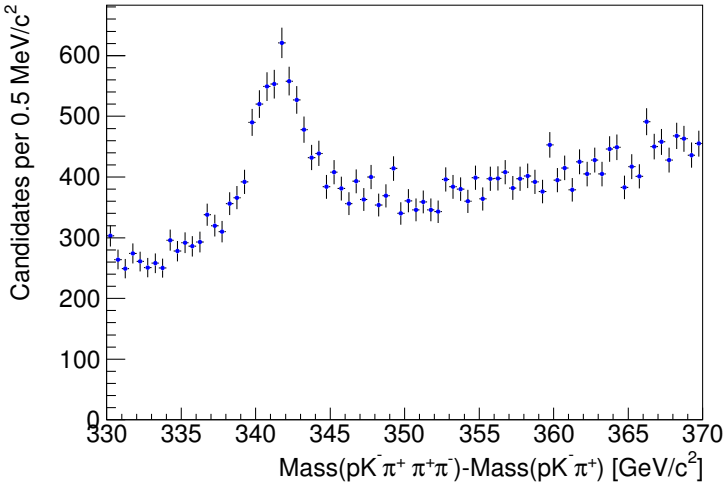

Figure 5.44.: Λ_c^* mass difference distributions with a background versus background network output cut at 0.

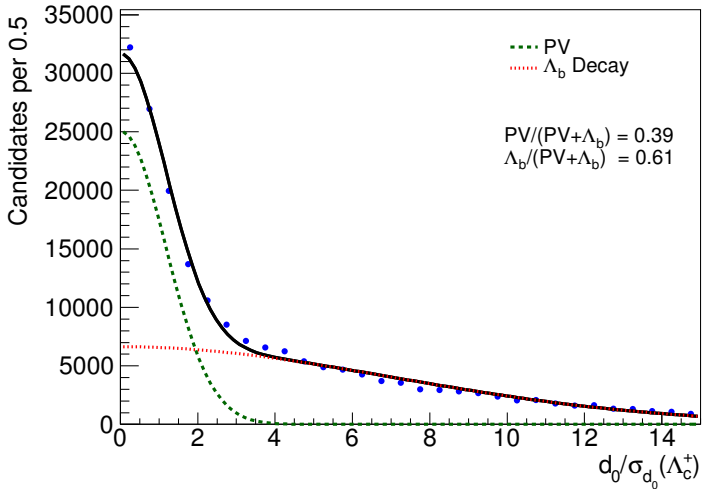

Figure 5.45.: Distribution of $d_0/\sigma_{d_0}(\Lambda_c^+)$. The two Gaussian functions that are fitted to the distribution serve to determine the fractions of the Λ_c^+ events produced at the primary vertex and those stemming from decays of longer lived particles.

5.4. Production of Charmed Baryons

The two track trigger, designed to accumulate hadrons containing a b quark, requires basically two tracks with transverse momenta greater than $2\,\mathrm{GeV}/c$ and impact parameters greater than 0.1 mm per event (see Table 5.3). Because of its about six times smaller lifetime compared to hadrons containing a b quark and the three-body final state, these requirements are hard to fulfill for a Λ_c^+ produced at the primary vertex and decaying to $pK^-\pi^+$. Therefore, it can be assumed that a considerable part of the triggered Λ_c^+ events, and thus also of its studied excited states, actually originates from decays of particles containing a b quark. Because of baryon number conservation the best candidate for this is the Λ_b^0.

The Λ_c^+ data sample used for the network training described in Section 5.3.1 is employed to validate this assumption. Figure 5.45 shows the sideband subtracted distribution of $d_0/\sigma_{d_0}(\Lambda_c^+)$ after application of the precuts listed in Table 5.4 and the requirement $\mathrm{NN}(\Lambda_c) > -0.95$ on the Λ_c^+ network output. For particles produced at the primary vertex one expects the distribution to correspond to a Gaussian function with $\mu = 0$ and $\sigma = 1$, independent of the lifetime. In contrast, the Gaussian would be significantly broader for Λ_c^+ events originating from decays of longer lived particles like Λ_b^0. Therefore, two Gaussian functions are fitted to the distribution in order to determine the fractions of the Λ_c^+ events produced at the primary vertex and those stemming from decays of b hadrons. The fit indicates that about 60% of the Λ_c^+ events are not produced at the primary vertex.

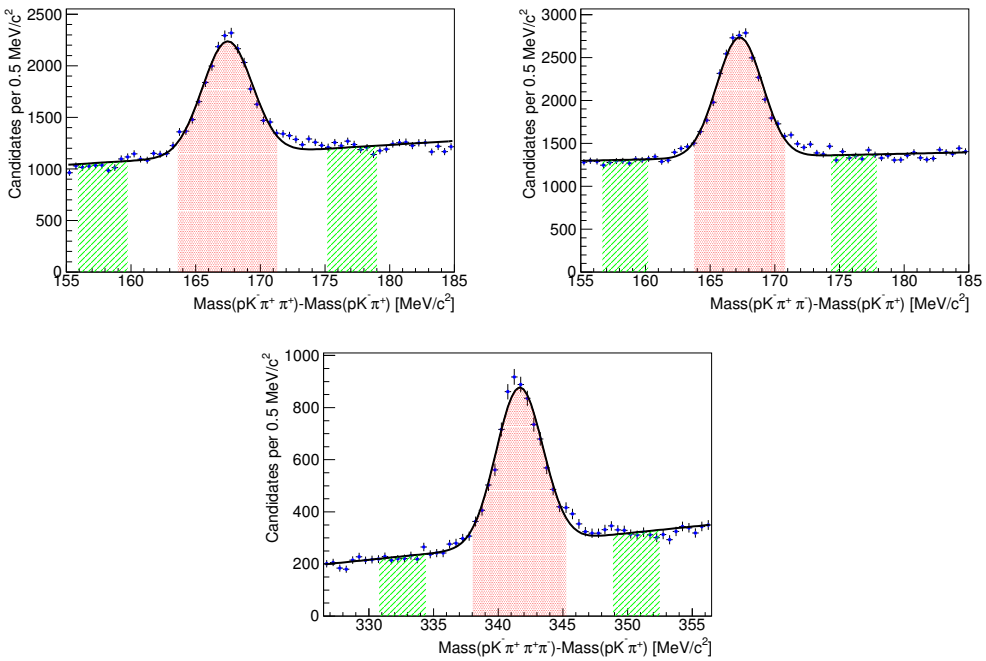

Figure 5.46.: Mass difference distributions used for the sideband subtractions of the p_T spectra. The signal regions are indicated by red and the lower and upper sidebands by green.

5.5. Simulated Events

Simulated events are used to estimate the detector mass resolutions of the charmed baryons studied here.

As determined by the study of the impact parameter distributions described in Section 5.4, the sample of charmed baryons recorded by the trigger consists of approximately equal contributions from Λ_b^0 decays and direct $c\bar{c}$ production. Since the resolution is mainly determined by kinematics and just a tiny fraction of $c\bar{c}$ events passes the trigger requirements, only one sample starting with Λ_b^0 is generated.

The generated particles are then inclusively decayed into all possible charmed baryons by means of the EVTGEN package [53], and the charmed baryons are further decayed to the channels studied here, where the Λ_c^+ is forced to decay into $pK^-\pi^+$ with its resonance structure taken into account.

Afterwards, the generated events are passed through the detector simulation. Since the trigger selection is rather inefficient for Λ_c^+, instead of running the trigger simulation, the kinematic selection is imitated using quantities from the offline reconstruction. After detector simulation, the events are reconstructed by the same software used for data.

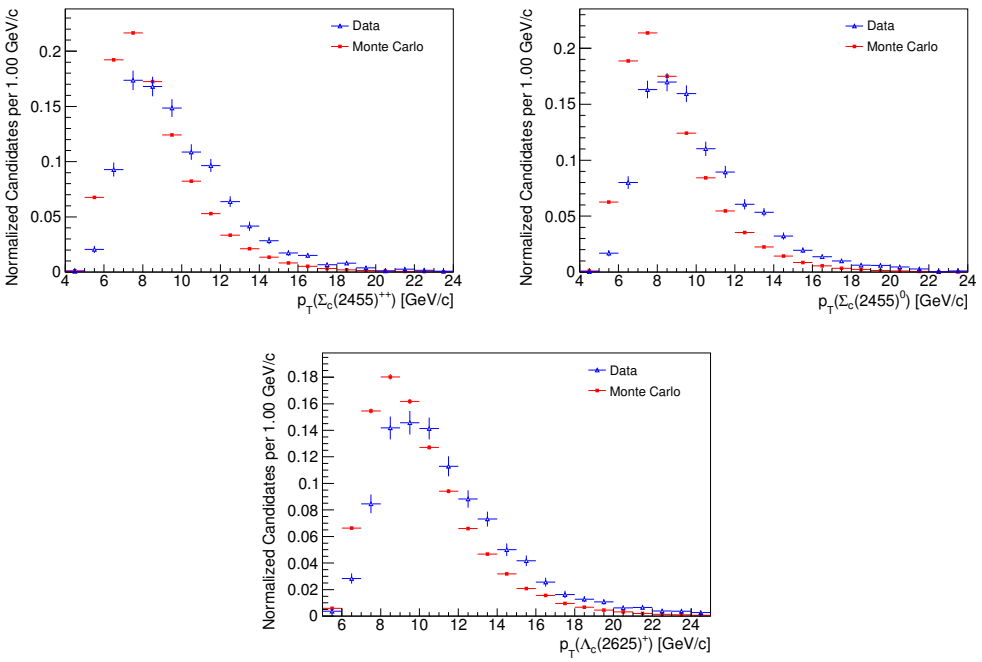

Figure 5.47.: Normalized transverse momentum distributions in sideband subtracted data (blue) and Monte Carlo simulations (red) before reweighting.

Finally, the selection described in Section 5.3 is also applied to the simulated events. The detector resolutions are then obtained by subtracting the corresponding generated mass difference ΔM_{gen} from the reconstructed one ΔM_{rec}.

These distributions are reweighted according to the discrepancies between simulated events and real data in the transverse momenta of the resonances $\Sigma_c(2455)$ and $\Lambda_c(2625)^+$ in order to describe the detector resolutions as realistic as possible. Thereby, sideband subtractions in bins of p_T are used to get rid of the background contaminations in real data. The mass difference distributions with the signal regions and sidebands can be found in Figure 5.46. Figure 5.47 shows the normalized p_T distributions in sideband subtracted data and Monte Carlo simulations before reweighting. It turns out that all Monte Carlo spectra are slightly shifted towards lower transverse momenta. After bin-by-bin reweighting of these histograms, the resulting factors are used to reweight the transverse momentum distributions of the respective decay products. The according distributions before and after reweighting can be found in Figures 5.48–5.50, showing that the procedure improves the agreement between data and simulations.

The $\Sigma_c(2520)$ and $\Lambda_c(2595)^+$ Monte Carlo samples are reweighted with the discrepancies between simulated events and real data in $p_T(\Sigma_c(2455))$ respective $p_T(\Lambda_c(2625)^+)$.

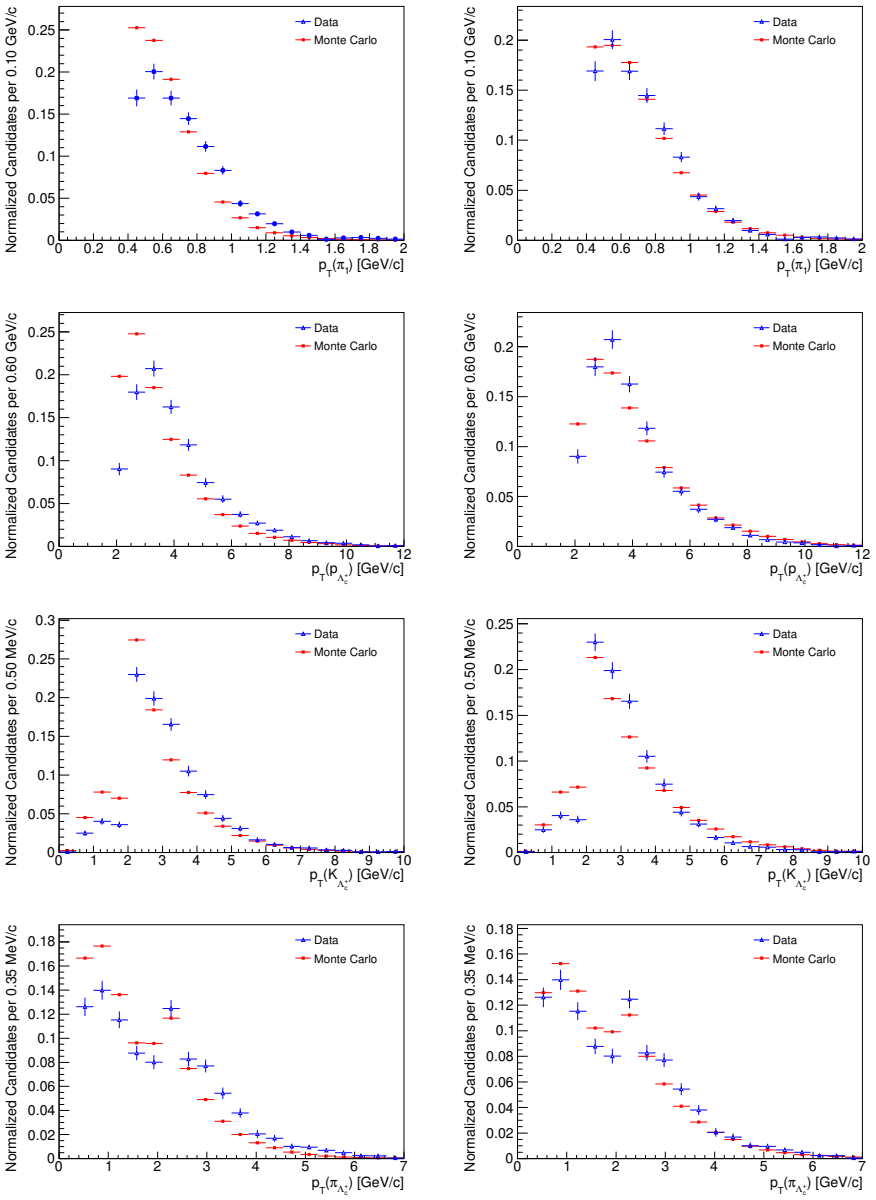

Figure 5.48.: Normalized transverse momentum distributions of the $\Sigma_c(2455)^{++}$ decay products in sideband subtracted data (blue) and Monte Carlo simulations (red) before (left column) and after (right column) Monte Carlo reweighting.

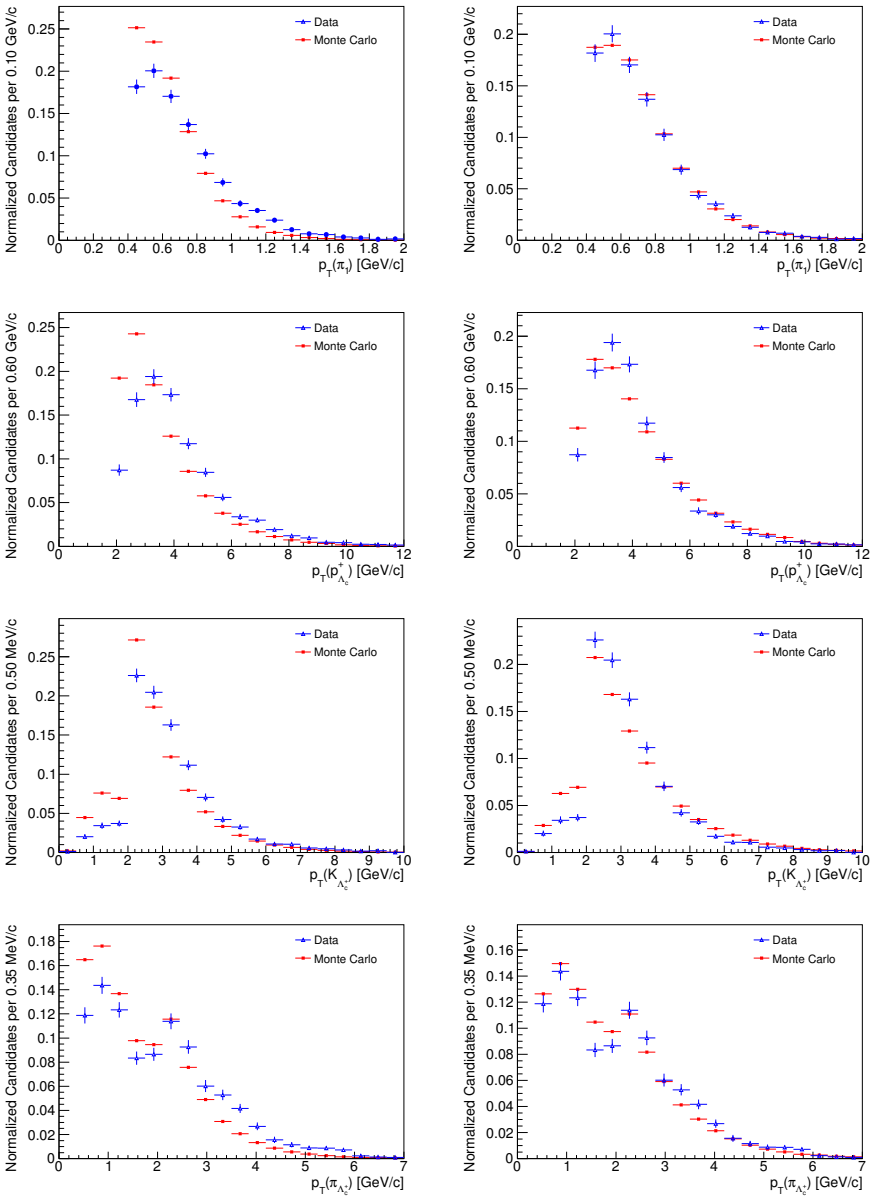

Figure 5.49.: Normalized transverse momentum distributions of the $\Sigma_c(2455)^0$ decay products in sideband subtracted data (blue) and Monte Carlo simulations (red) before (left column) and after (right column) Monte Carlo reweighting.

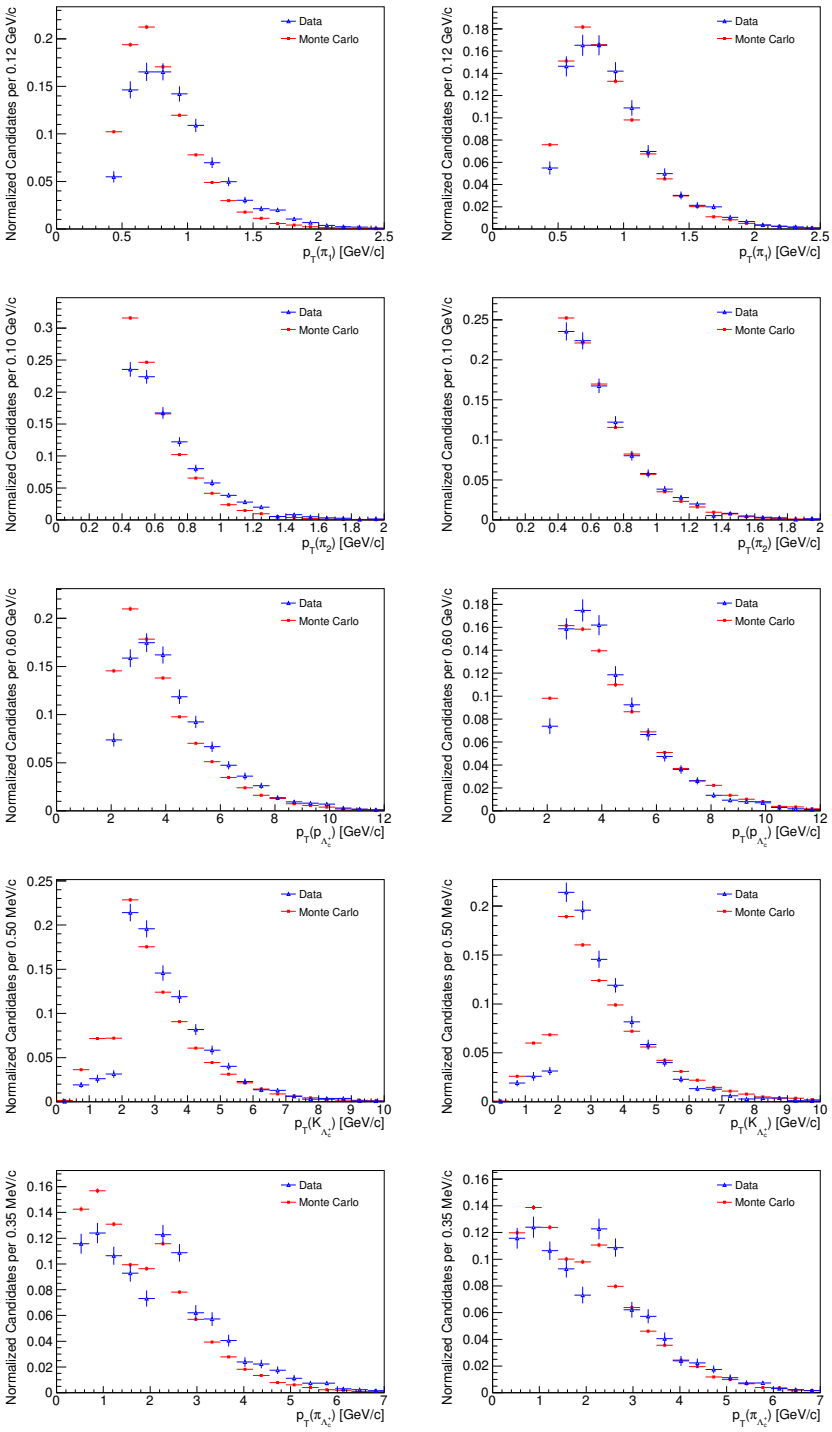

Figure 5.50.: Normalized transverse momentum distributions of the $\Lambda_c(2625)^+$ decay products in sideband subtracted data (blue) and Monte Carlo simulations (red) before (left column) and after (right column) Monte Carlo reweighting.

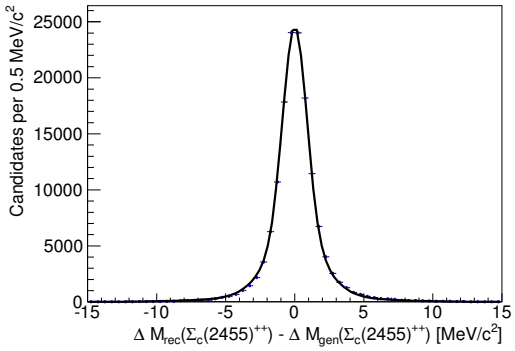

Figure 5.51.: Simulated detector resolution for $\Sigma_c(2455)^{++}$.

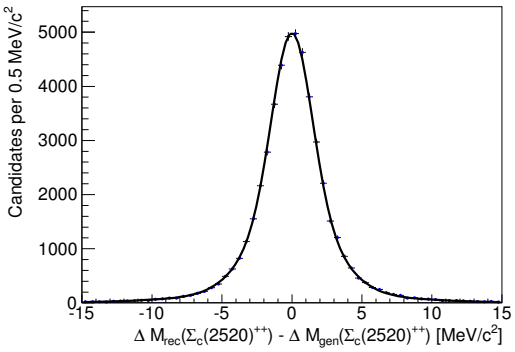

Figure 5.52.: Simulated detector resolution for $\Sigma_c(2520)^{++}$.

The resulting mass residual distributions of the studied resonances can be found in Figures 5.51–5.56. A combination of three Gaussian functions is used to fit the distributions in each case:

$$\mathrm{f}(x) = \mathrm{frac}_2 \cdot (\mathrm{frac}_1 \cdot G_1(x) + (1 - \mathrm{frac}_1) \cdot G_2(x)) + (1 - \mathrm{frac}_2) \cdot G_3(x)\,. \qquad (5.2)$$

With the range of the fractions frac_1, frac_2 being limited to [0,1] and the Gaussian functions $G_1(x)$, $G_2(x)$, $G_3(x)$ being normalized, $\mathrm{f}(x)$ is also normalized and an overall factor has to be multiplied in order to fit the considered distribution. In Tables 5.6 and 5.7 the fit results for the different parameters can be found for the Σ_c and Λ_c^{*+} resonances, respectively. Thereby, σ means the standard deviation of the corresponding Gaussian function and all the means are set to zero. As expected, for both $\Sigma_c(2455)$ and $\Sigma_c(2520)$ the resolutions of the uncharged and doubly-charged states are consistent within the assigned uncertainties.

Table 5.8 shows a comparison between the average resolutions

$$\bar{\sigma} = \mathrm{frac}_2 \cdot (\mathrm{frac}_1 \cdot \sigma_1 + (1 - \mathrm{frac}_1) \cdot \sigma_2(x)) + (1 - \mathrm{frac}_2) \cdot \sigma_3(x) \qquad (5.3)$$

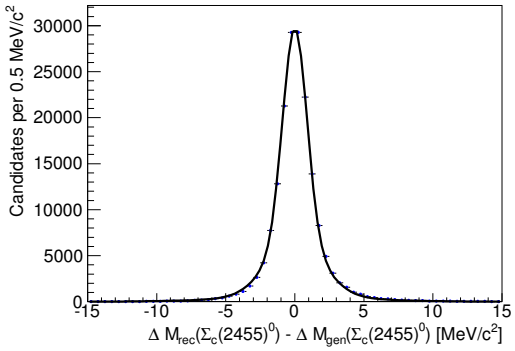

Figure 5.53.: Simulated detector resolution for $\Sigma_c(2455)^0$.

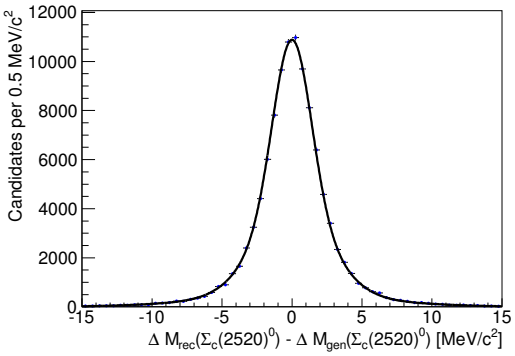

Figure 5.54.: Simulated detector resolution for $\Sigma_c(2520)^0$.

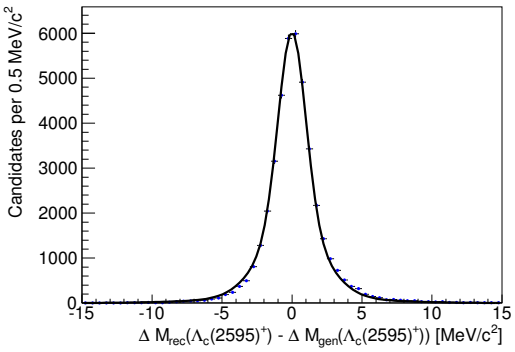

Figure 5.55.: Simulated detector resolution for $\Lambda_c(2595)^+$.

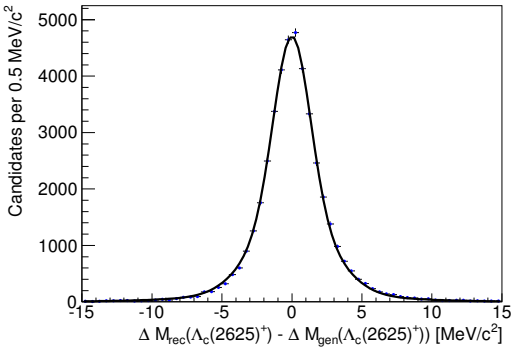

Figure 5.56.: Simulated detector resolution for $\Lambda_c(2625)^+$.

Table 5.6.: Fit results for the parameters of the three Gaussian functions that are fitted to the simulated mass resolutions of the different Σ_c resonances reweighted by means of the $\Sigma_c(2455)^{++,0}$ p_T spectra.

	$\Sigma_c(2455)^{++}$	$\Sigma_c(2520)^{++}$	$\Sigma_c(2455)^0$	$\Sigma_c(2520)^0$
frac_1	0.621 ± 0.009	0.517 ± 0.026	0.629 ± 0.007	0.522 ± 0.017
frac_2	0.918 ± 0.002	0.879 ± 0.005	0.931 ± 0.001	0.873 ± 0.004
$\sigma_1[\text{MeV}/c^2]$	0.863 ± 0.007	1.392 ± 0.030	0.874 ± 0.006	1.357 ± 0.020
$\sigma_2[\text{MeV}/c^2]$	1.938 ± 0.020	2.709 ± 0.052	1.996 ± 0.016	2.659 ± 0.035
$\sigma_3[\text{MeV}/c^2]$	4.938 ± 0.039	6.663 ± 0.086	5.161 ± 0.025	6.291 ± 0.058
$\bar{\sigma}[\text{MeV}/c^2]$	1.573 ± 0.015	2.589 ± 0.046	1.556 ± 0.011	2.529 ± 0.031

Table 5.7.: Fit results for the parameters of the three Gaussian functions that are fitted to the simulated mass resolutions of the $\Lambda_c(2595)^+$ and $\Lambda_c(2625)^+$ resonances reweighted by means of the $\Lambda_c(2625)^+$ p_T spectrum.

	$\Lambda_c(2595)^+$	$\Lambda_c(2625)^+$
frac_1	0.551 ± 0.019	0.511 ± 0.024
frac_2	0.919 ± 0.007	0.913 ± 0.005
$\sigma_1[\text{MeV}/c^2]$	0.966 ± 0.019	1.287 ± 0.028
$\sigma_2[\text{MeV}/c^2]$	2.165 ± 0.058	2.651 ± 0.051
$\sigma_3[\text{MeV}/c^2]$	5.303 ± 0.169	6.624 ± 0.082
$\bar{\sigma}[\text{MeV}/c^2]$	1.814 ± 0.045	2.363 ± 0.046

Table 5.8.: Comparison between the determined average detector resolutions $\bar{\sigma}$ with and without Monte Carlo reweighting.

	$\bar{\sigma}_{\text{not rew.}}[\text{MeV}/c^2]$	$\bar{\sigma}_{\text{rew.}}[\text{MeV}/c^2]$
$\Sigma_c(2455)^{++}$	1.52 ± 0.01	1.57 ± 0.01
$\Sigma_c(2520)^{++}$	2.52 ± 0.05	2.59 ± 0.05
$\Sigma_c(2455)^{0}$	1.50 ± 0.02	1.56 ± 0.01
$\Sigma_c(2520)^{0}$	2.47 ± 0.03	2.53 ± 0.03
$\Lambda_c(2595)^{+}$	1.77 ± 0.04	1.81 ± 0.05
$\Lambda_c(2625)^{+}$	2.29 ± 0.05	2.36 ± 0.05

determined with and without Monte Carlo reweighting. The differences of $3-4\%$ are small compared to the assigned systematic uncertainties on the mass resolutions of 20% (see Section 5.7.1).

5.6. Fitting Procedures

To determine the mass differences relative to the Λ_c^+ and the widths of the six studied states, binned maximum likelihood fits to three separate mass difference distributions are performed. The first two are $\Lambda_c^+\pi^+$ and $\Lambda_c^+\pi^-$, where the states $\Sigma_c(2455)^{++,0}$ and $\Sigma_c(2520)^{++,0}$ are studied. The last one is $\Lambda_c^+\pi^+\pi^-$ for $\Lambda_c(2595)^+$ and $\Lambda_c(2625)^+$. In the case of the Σ_c states, part of the background comes from Λ_c^{*+} decays and thus has different properties compared to the combinatorial background. On the other hand, when fitting Λ_c^{*+} states, there is a background contribution from random $\Sigma_c^{++,0}\pi^{-,+}$ combinations which have a threshold close to the $\Lambda_c(2595)^+$ state.

The negative logarithm of the likelihood function has the general form of Equation 4.5 and the expected number μ_j of entries in bin j are obtained using the function

$$\mu(\Delta M) = N_1 \cdot s_1(\Delta M) + N_2 \cdot s_2(\Delta M) + b(\Delta M)\,, \tag{5.4}$$

where $s_1(\Delta M)$ and $s_2(\Delta M)$ are the PDFs for the two signals, $b(\Delta M)$ is the background function and N_i are the corresponding numbers of events. All three PDFs depend on a subset of the free parameters $\vec{a}$. The function is evaluated at the bin center to calculate the expectation for μ_j. While the general structure is the same in all three fits, the PDFs are specific to Σ_c and Λ_c^{*+} states.

5.6.1. Two-Body Line Shapes from $\Lambda_c^{*+} \to \Lambda_c^+\,\pi^+\,\pi^-$ Decays

Figure 5.57 shows the scatter plot of the two-body invariant mass distributions $M(\Lambda_c^+\pi^\mp) - M(\Lambda_c^+)$ of candidates with $M(\Lambda_c^+\pi^+\pi^-) - M(\Lambda_c^+) < 405\,\mathrm{MeV}/c^2$ subjected to the selection cuts described in Section 5.3.3. The horizontal respective vertical bands at $\Lambda_c^+\pi^\pm$ mass differences of about $167\,\mathrm{MeV}/c^2$ correspond to the $\Sigma_c(2455)^{++,0}$ signals, whereas the two diagonal bands represent clusters of candidates originating from the $\Lambda_c(2625)^+$ (upper diagonal band) and $\Lambda_c(2595)^+$ (lower diagonal band) signal regions in the $\Lambda_c^+\pi^+\pi^-$ spectrum. Within the lower diagonal band, corresponding to $\Lambda_c(2595)^+$ combinations, most of the candidates are located at the intersections with the $\Sigma_c(2455)$ bands near the kinematical limits, indicating a resonant decay. In contrast, the upper diagonal band, corresponding to $\Lambda_c(2625)^+$ combinations, is uniformly populated, indicating a nonresonant decay. Therefore, the resonant $\Sigma_c(2455)\pi$ mode dominates the $\Lambda_c(2595)^+$ decay and the nonresonant $\Lambda_c^+\pi\pi$ mode dominates the $\Lambda_c(2625)^+$ decay, just like expected from the quantum number considerations in Section 5.1.

The two-body invariant mass spectra of the decay products of a three-body decay can be calculated separately for the nonresonant and the resonant parts. Considering a generic three-body decay with the particle masses

$$M \to m_1\, m_2\, m_3 \tag{5.5}$$

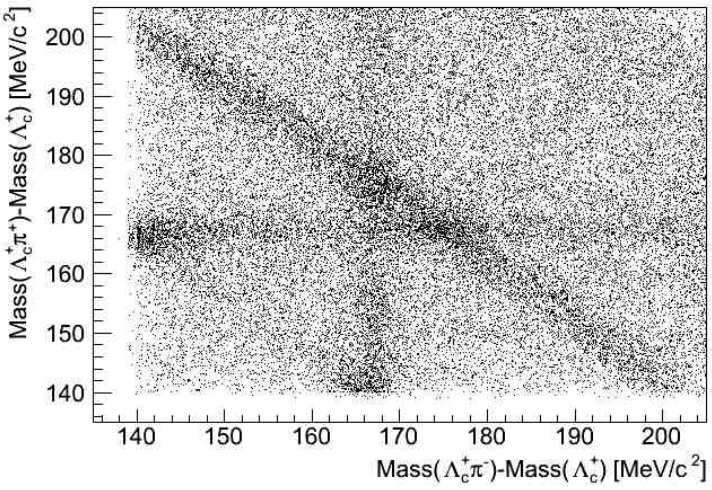

Figure 5.57.: Scatter plot of the two-body invariant mass distributions $M(\Lambda_c^+\pi^-) - M(\Lambda_c^+)$ and $M(\Lambda_c^+\pi^+) - M(\Lambda_c^+)$ of the Λ_c^{*+} candidates with $M(\Lambda_c^+\pi^+\pi^-) - M(\Lambda_c^+) < 405\,\mathrm{MeV}/c^2$.

and the invariant two-body masses m_{12} and m_{13}, the phase space is bounded by

$$m_1 + m_2 < m_{12} < M - m_3 \tag{5.6}$$

and

$$(m_{13}^{min}(m_{12}))^2 = (E_1^* + E_3^*)^2 - \left(\sqrt{E_1^{*2} - m_1^2} + \sqrt{E_3^{*2} - m_3^2}\right)^2 , \tag{5.7}$$

$$(m_{13}^{max}(m_{12}))^2 = (E_1^* + E_3^*)^2 - \left(\sqrt{E_1^{*2} - m_1^2} - \sqrt{E_3^{*2} - m_3^2}\right)^2 , \tag{5.8}$$

where

$$E_1^* = \frac{m_{12}^2 - m_2^2 + m_1^2}{2m_{12}} , \tag{5.9}$$

$$E_3^* = \frac{M^2 - m_{12}^2 - m_3^2}{2m_{12}} . \tag{5.10}$$

The nonresonant line shape for m_{12} then reads

$$\frac{\mathrm{d}N}{\mathrm{d}m_{12}} \propto \frac{(m_{13}^{max}(m_{12}))^2 - (m_{13}^{min}(m_{12}))^2}{2m_{12}} . \tag{5.11}$$

A single resonance described by a Breit-Wigner function with a mean mass μ_{12},

$$BW(m_{12}) \propto \frac{1}{2\pi} \cdot \frac{\Gamma_{12}}{(m_{12} - \mu_{12})^2 + \Gamma_{12}^2/4} , \tag{5.12}$$

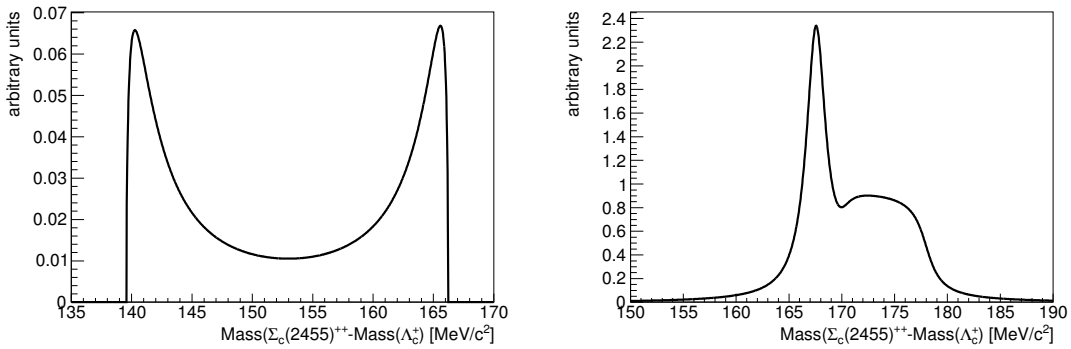

Figure 5.58.: Calculated line shape of intermediate $\Sigma_c(2455)^{++}$ resonances in $\Lambda_c(2595)^+$ (left) and $\Lambda_c(2625)^+$ (right) decays.

leads to a resonant line shape

$$\frac{\mathrm{d}N}{\mathrm{d}m_{12}} \propto \frac{(m_{13}^{max}(m_{12}))^2 - (m_{13}^{min}(m_{12}))^2}{2m_{12}} \cdot BW(m_{12})\,. \tag{5.13}$$

If there exists a single resonance $BW(m_{13})$ in the orthogonal dimension m_{13}, the orthogonal-resonant line shape can be calculated as

$$\frac{\mathrm{d}N}{\mathrm{d}m_{12}} \propto \frac{1}{2m_{12}} \cdot \int_{m_{13}^{min}}^{m_{13}^{max}} BW(m_{13}) m_{13} \mathrm{d}m_{13}\,. \tag{5.14}$$

These equations can be applied directly to the three-body decays of Λ_c^{*+} states in order to describe the $\Lambda_c^+\pi^\pm$ invariant mass spectra. Graphical illustrations of the corresponding functions can be found in Figure 5.58.

Figure 5.59 shows the $M(\Lambda_c^+\pi^\pm) - M(\Lambda_c^+)$ distributions for $\Lambda_c(2595)^+$, $302 < M(\Lambda_c^+\pi^+\pi^-) - M(\Lambda_c^+) < 312\,\mathrm{MeV}/c^2$, and $\Lambda_c(2625)^+$, $337.645 < M(\Lambda_c^+\pi^+\pi^-) - M(\Lambda_c^+) < 345.645\,\mathrm{MeV}/c^2$, candidates selected according to Section 5.3.3. In comparison with Figure 5.58, the resonant $\Sigma_c(2455)$ structures are clearly visible.

5.6.2. Σ_c Fits

The fits to the doubly-charged and uncharged Σ_c candidates are shown in Figures 5.60 and 5.61, respectively. In each of the two distributions two signals and several background components have to be parametrized. A 150–320 MeV/c^2 range is used to avoid complications arising from the description of the steep rise of the background at threshold.

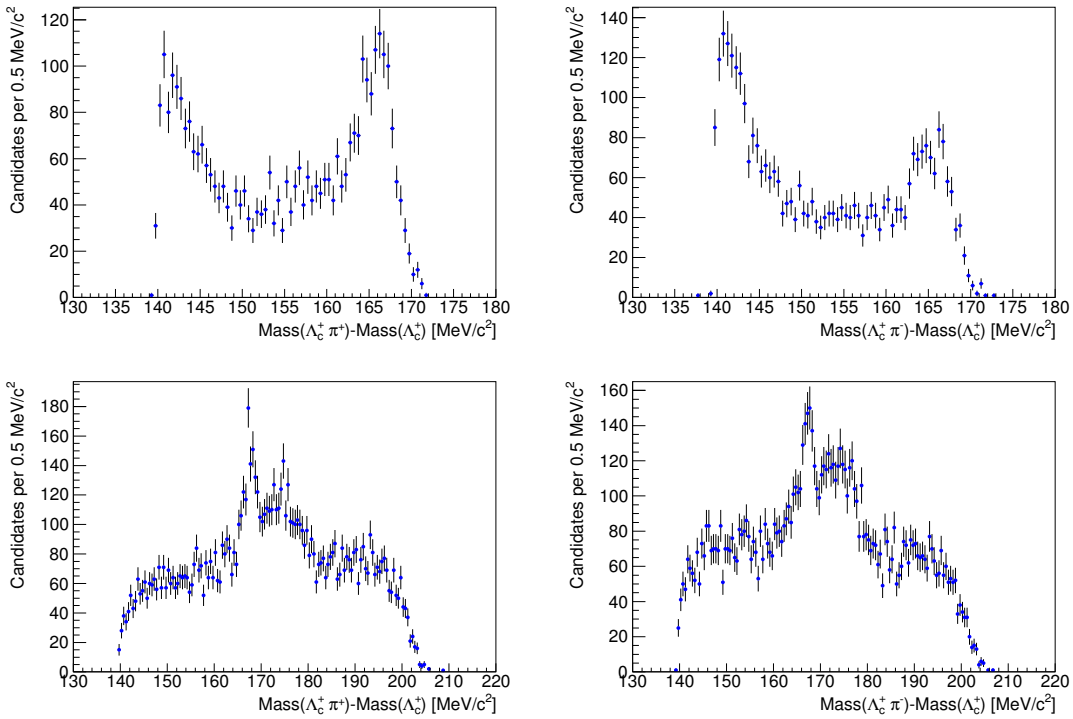

Figure 5.59.: $M(\Lambda_c^+\pi^\pm) - M(\Lambda_c^+)$ distributions for $\Lambda_c(2595)^+$ (top row) and $\Lambda_c(2625)^+$ (bottom row) candidates.

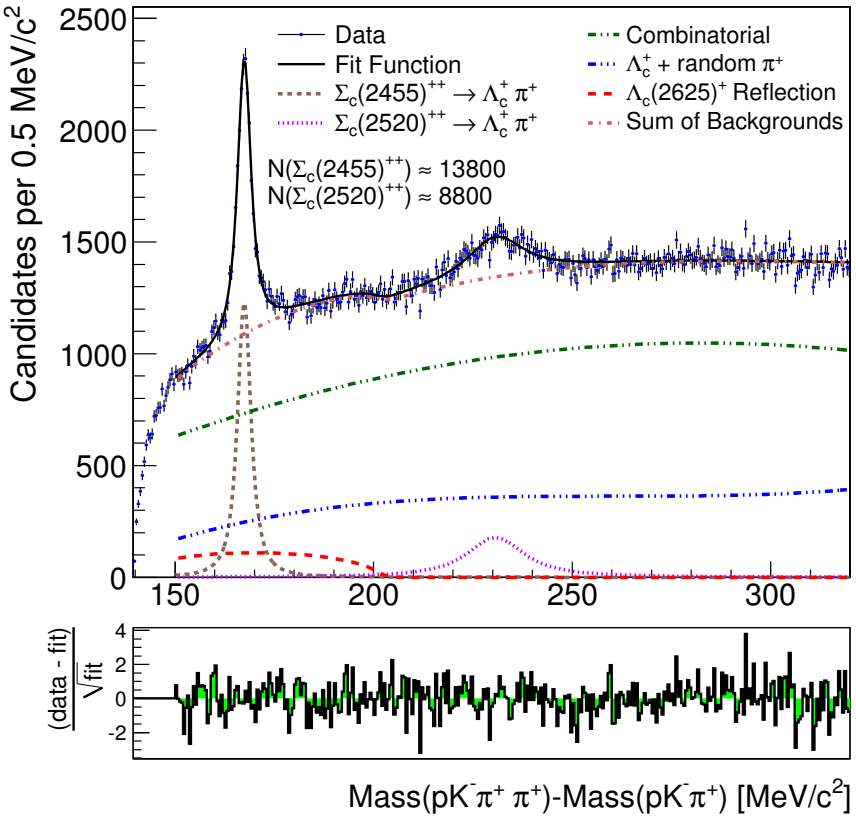

Figure 5.60.: The $M(pK^-\pi^+\pi^+) - M(pK^-\pi^+)$ distribution obtained from data together with the fit. The various lines correspond to the two signal contributions, the combinatorial background without real Λ_c^+, the background from real Λ_c^+ combined with a random pion, a reflection from $\Lambda_c(2625)^+$ decays, and the sum of all three background contributions.

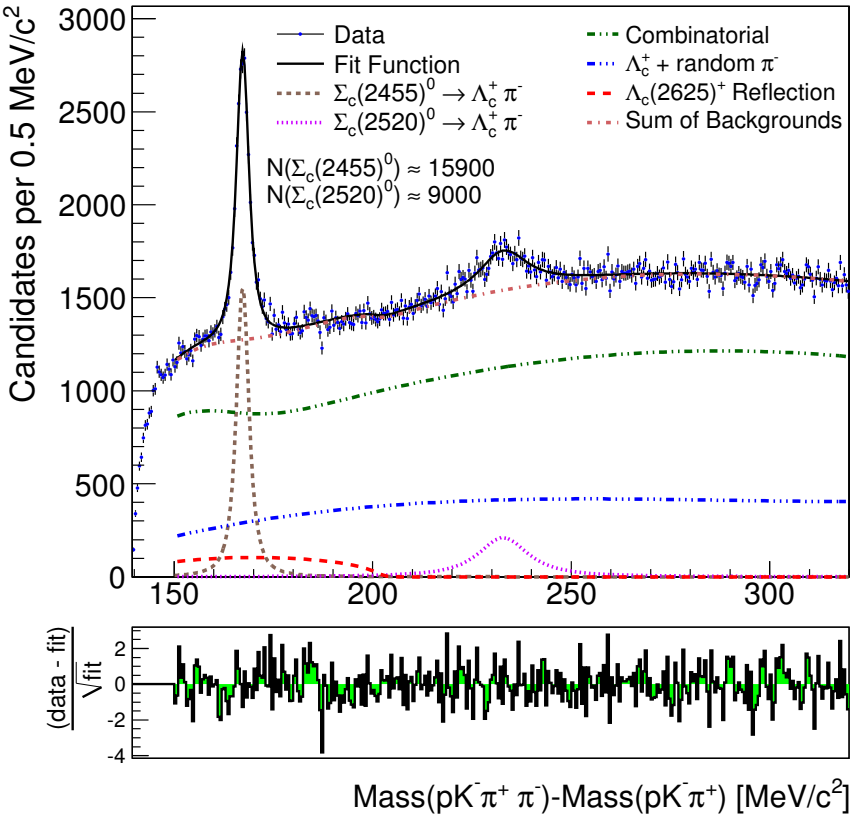

Figure 5.61.: The $M(pK^-\pi^+\pi^-) - M(pK^-\pi^+)$ distribution obtained from data together with the fit. Further explanations can be found in the caption of Figure 5.60.

Signal Structures

Both $\Sigma_c(2455)$ and $\Sigma_c(2520)$ are described by a nonrelativistic Breit-Wigner function,

$$\frac{\mathrm{d}N}{\mathrm{d}\Delta M} \propto \frac{\Gamma}{(\Delta M - \Delta M_0)^2 + \Gamma^2/4}, \tag{5.15}$$

convolved with the corresponding resolution function. As described in Section 5.5, the resolution functions consist of the weighted sum of three Gaussians. Technically, the convolution is realized as the normalized sum of three Voigt functions with the same Breit-Wigner part.

A single common scaling factor s is introduced for the widths of all three Gaussians to correct for a possible mismatch in our mass resolution estimate. This scaling factor is allowed to float within a Gaussian constraint in the fit, what corresponds to adding

$$0.5 \cdot \left(\frac{s-\mu}{\sigma}\right)^2 \tag{5.16}$$

with $\mu = 1$ and $\sigma = 0.2$, reflecting a 20% uncertainty on the mass resolution (see Section 5.7), to the negative logarithm of the likelihood.

Background Composition

Three different types of background are considered:

- random combinations without real Λ_c^+
- combinations of real Λ_c^+ with a random pion
- events due to the decay of Λ_c^{*+} to $\Lambda_c^+\pi^+\pi^-$

The random combinations without a real Λ_c^+ dominate and are described by a second-order polynomial with shape and normalization derived in a fit to the ΔM distribution from the Λ_c^+ mass sidebands $2261.46 < M(pK^-\pi^+) < 2266.46\,\mathrm{MeV}/c^2$ and $2306.46 < M(pK^-\pi^+) < 2311.46\,\mathrm{MeV}/c^2$ discussed in Section 5.3.4. For this purpose the histograms shown in Figures 5.34 and 5.33 are scaled by a factor 2 because the signal region in the Λ_c^+ mass distribution (see Figure 5.32) is twice as broad as the combination of lower and upper sideband. The fits to the distributions from the Λ_c^+ mass sidebands can be found in Figures 5.62 and 5.63. The difference between doubly-charged and neutral spectra is due to $D^*(2010)^+ \to D^0\,\pi^+$ mesons with multibody D^0 decays, where not all D^0 decay products are reconstructed. In order to describe this reflection, an additional Gaussian function is used.

In the Σ_c fits shown in Figures 5.60 and 5.61, this contribution is allowed to float within a Gaussian constraint implemented by the addition of

$$0.5 \cdot \vec{\Delta}^T \cdot \mathbf{V}^{-1} \cdot \vec{\Delta} \tag{5.17}$$

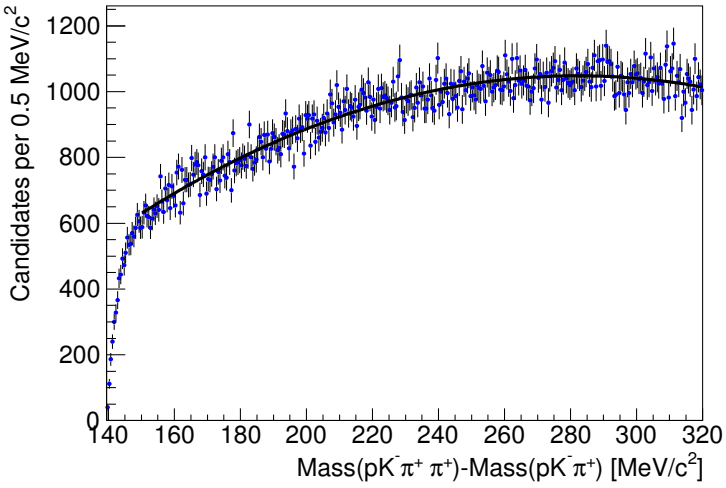

Figure 5.62.: Fit to the $M(pK^-\pi^+\pi^+) - M(pK^-\pi^+)$ distribution of the candidates from Λ_c^+ mass sidebands.

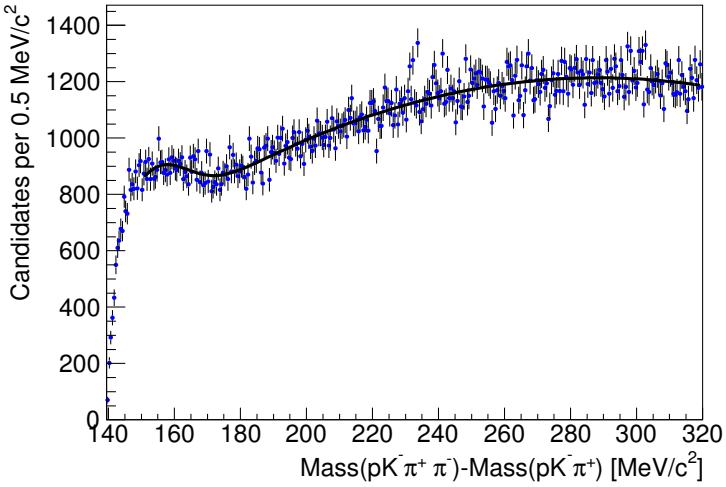

Figure 5.63.: Fit to the $M(pK^-\pi^+\pi^-) - M(pK^-\pi^+)$ distribution of the candidates from Λ_c^+ mass sidebands.

Table 5.9.: Results of the fit to the mass difference distribution of the Σ_c^{++} candidates.

	$\Sigma_c(2455)^{++}$	$\Sigma_c(2520)^{++}$
$\Delta M_0[\mathrm{MeV}/c^2]$	167.444 ± 0.038	230.731 ± 0.564
$\Gamma_0[\mathrm{MeV}/c^2]$	2.337 ± 0.418	15.031 ± 2.228
s	0.934 ± 0.167	1.017 ± 0.199

to the negative logarithm of the likelihood, where $\mathbf{V}$ is the covariance matrix of the fit to the ΔM distribution from the Λ_c^+ mass sidebands and $\vec{\Delta}$ is the vector of deviations between the fitted parameters and their values estimated by the corresponding Λ_c^+ sideband fit.

The second background source consisting of real Λ_c^+ combined with a random pion is modeled by a third-order polynomial, where all parameters are left free in the fit.

The background originating from Λ_c^{*+} decays is described using theoretical considerations that are further explained in Section 5.6.1. With good approximation, there are two states that contribute, namely $\Lambda_c(2595)^+$ and $\Lambda_c(2625)^+$, decaying into a $\Lambda_c^+\pi^+\pi^-$ final state. The $\Lambda_c(2595)^+$ decays dominantly to a $\Sigma_c\pi$ final state [1] and thus contributes mainly to the signal. Therefore, its contributions to the backgrounds in the $\Lambda_c\pi$ distributions is neglected. On the other hand, the $\Lambda_c(2625)^+$ decay is dominantly nonresonant [1]. To model it, a flat $\Lambda_c^+\pi^+\pi^-$ Dalitz plot is projected on the appropriate axis. Since the shape of the projection depends on the reconstructed $\Lambda_c(2625)^+ \to \Lambda_c^+\,\pi^+\,\pi^-$ mass, ten different values of this mass are used and their relative contributions are weighted according to the $\Lambda_c(2625)^+$ shape obtained from the fit to the $\Lambda_c^+\pi^+\pi^-$ data shown in Figure 5.64. This contribution amounts to about 2% of the total background.

Results

The fit results for the full $\Delta M(\Sigma_c)$ distributions, containing all signal and background components, can be found in Tables 5.9 and 5.10. Hereby, the central values ΔM_0 and the full widths at half maximum Γ of the Breit-Wigner functions correspond to the searched mass differences and decay widths of the examined resonances and s are the parameters for the resolution scaling factors implemented by Gaussian constraints. The χ^2 value of the Σ_c^{++} fit is 340 (324 degrees of freedom) and that of the Σ_c^0 fit is 384 (321 degrees of freedom).

5.6.3. Λ_c^* Fit

The fit for $\Lambda_c(2595)^+$ and $\Lambda_c(2625)^+$ is shown in Figure 5.64. It includes two signals and several background components and is performed in a ΔM region from 290 to

Table 5.10.: Results of the fit to the mass difference distribution of the Σ_c^0 candidates.

	$\Sigma_c(2455)^0$	$\Sigma_c(2520)^0$
$\Delta M_0[\mathrm{MeV}/c^2]$	167.279 ± 0.032	232.876 ± 0.427
$\Gamma[\mathrm{MeV}/c^2]$	1.653 ± 0.463	12.512 ± 1.952
s	1.070 ± 0.131	0.996 ± 0.197

$400\,\mathrm{MeV}/c^2$.

$\Lambda_c(2595)$ Line Shape

Previous measurements of the $\Lambda_c(2595)^+$ properties indicate that it decays dominantly to the final state $\Sigma_c\pi$, with the threshold very close to the $\Lambda_c(2595)^+$ mass [1]. This introduces an additional complication to the fit compared to the Σ_c case. Blechman *et al.* [52] showed that taking into account the mass dependence of the natural width yields a lower $\Lambda_c(2595)^+$ mass measurement than observed by previous experiments. With the present event sample a higher sensitivity is achieved to the details of the $\Lambda_c(2595)^+$ line shape than in previous analyses. Consequently, this dependence is included in the model.

The $\Lambda_c(2595)^+$ parametrization follows Reference [52]. The state is described by a nonrelativistic Breit-Wigner function of the form

$$\frac{\mathrm{d}N}{\mathrm{d}\Delta M} \propto \frac{\Gamma(\Lambda_c^+\pi^+\pi^-)}{(\Delta M - \Delta M_{\Lambda_c(2595)^+})^2 + (\Gamma(\Lambda_c^+\pi^+\pi^-) + \Gamma(\Lambda_c^+\pi^0\pi^0))^2/4}\,, \tag{5.18}$$

where $\Gamma(\Lambda_c^+\pi^+\pi^-)$ and $\Gamma(\Lambda_c^+\pi^0\pi^0)$ are the mass-dependent partial widths to the $\Lambda_c^+\pi^+\pi^-$ and $\Lambda_c^+\pi^0\pi^0$ final states. Assuming that those two final states saturate nearly 100% of the $\Lambda_c(2595)^+$ decay width, the sum in the denominator corresponds to the total width. The two partial widths are derived in Reference [54] as

$$\begin{aligned}\Gamma(\Lambda_c^+\pi^+\pi^-) = \frac{g_2^2}{16\pi^3 f_\pi^4} m_{\Lambda_c^+} \int \mathrm{d}E_1\mathrm{d}E_2 (|\vec{p}_2|^2|A(E_1)|^2 + |\vec{p}_1|^2|B(E_2)|^2 \\ + 2\vec{p}_1\cdot\vec{p}_2 \mathrm{Re}[A(E_1)B^*(E_2)]),\end{aligned} \tag{5.19}$$

$$\begin{aligned}\Gamma(\Lambda_c^+\pi^0\pi^0) = \frac{g_2^2}{16\pi^3 f_\pi^4} m_{\Lambda_c^+} \int \mathrm{d}E_1\mathrm{d}E_2 (|\vec{p}_2|^2|C(E_1)|^2 + |\vec{p}_1|^2|C(E_2)|^2 \\ + 2\vec{p}_1\cdot\vec{p}_2 \mathrm{Re}[C(E_1)C^*(E_2)]).\end{aligned} \tag{5.20}$$

Here, $f_\pi = 132\,\mathrm{MeV}/c^2$ is the pion decay constant [55], $m_{\Lambda_c^+}$ is the world average Λ_c^+ mass, E_1,E_2 are the energies of the two pions in the rest frame of the $\Lambda_c(2595)^+$,

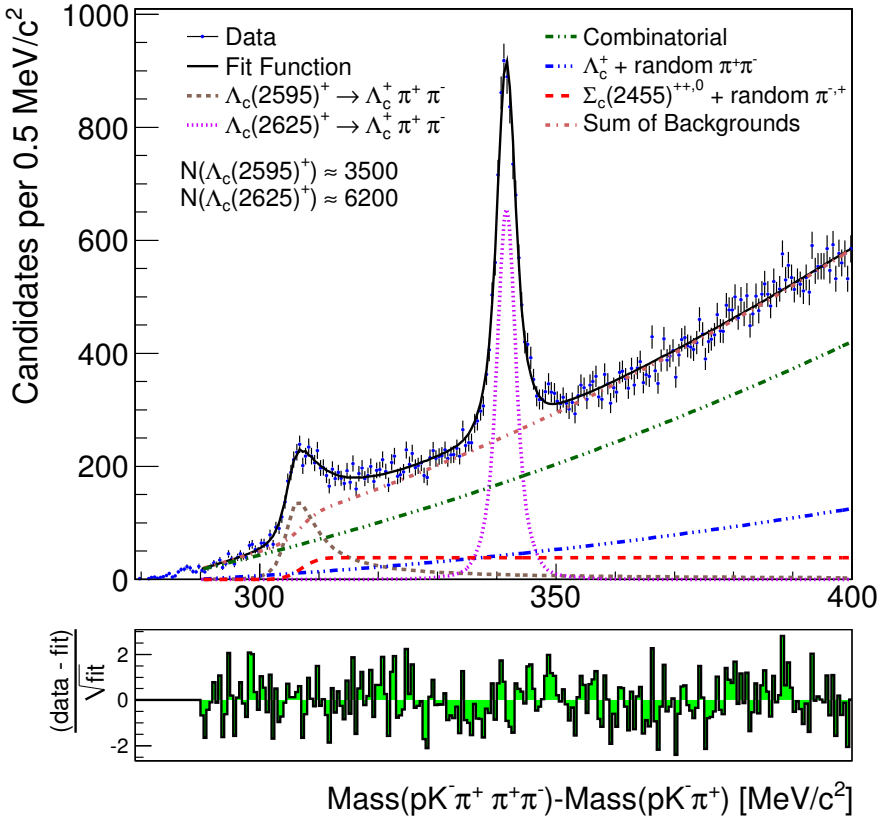

Figure 5.64.: The $M(pK^-\pi^+\,\pi^+\pi^-) - M(pK^-\pi^+)$ distribution obtained from data together with the fit. The various lines correspond to the two signal contributions, the combinatorial background without real Λ_c^+, the background from real Λ_c^+ combined with two random pions, the background from real $\Sigma_c(2455)^{++,0}$ combined with a random pion, and the sum of all three background contributions.

and $\vec{p}_1$,$\vec{p}_2$ are the corresponding momenta. Following Reference [52], the coupling constant g_2 is determined by the Σ_c decay width using the relation

$$\Gamma_{\Sigma_c} = \frac{g_2^2}{2\pi f_\pi^2} \frac{m_{\Lambda_c^+}}{m_{\Sigma_c}} |\vec{p}_\pi|^3, \tag{5.21}$$

with m_{Σ_c} being the world average mass of the $\Sigma_c(2455)$ and $\vec{p}_\pi$ the momentum of the pion from the $\Sigma_c(2455)$ decay to $\Lambda_c\pi$ in the $\Sigma_c(2455)$ rest frame. From the world average $\Gamma_{\Sigma_c} = 2.2\,\mathrm{MeV}/c^2$ [1] the value $g_2^2 = 0.365$ is obtained which is fixed in the fit. The amplitudes A, B, and C for the decays $\Lambda_c(2595)^+ \to \Sigma_c(2455)^0\,\pi^+$, $\Lambda_c(2595)^+ \to \Sigma_c(2455)^{++}\,\pi^-$, and $\Lambda_c(2595)^+ \to \Sigma_c(2455)^+\,\pi^0$ are parametrized as

$$A(E) = \frac{h_2 E}{\Delta m - \Delta m_{\Sigma_c^0} - E + i\Gamma_{\Sigma_c^0}/2}, \tag{5.22}$$

$$B(E) = \frac{h_2 E}{\Delta m - \Delta m_{\Sigma_c^{++}} - E + i\Gamma_{\Sigma_c^{++}}/2}, \tag{5.23}$$

$$C(E) = \frac{1}{2} \cdot \frac{h_2 E}{\Delta m - \Delta m_{\Sigma_c^{+}} - E + i\Gamma_{\Sigma_c^{+}}/2}. \tag{5.24}$$

In these definitions, $m_{\Sigma_c^{++,+,0}}$ and $\Gamma_{\Sigma_c^{++,+,0}}$ are the mass and the width of the $\Sigma_c(2455)^{++,+,0}$ taken from Reference [1]. The coupling constant h_2, defined in Reference [42], is related to the decay width of the $\Lambda_c(2595)^+$ and represents the actual quantity measured instead of the natural width. This approach describes a purely S-wave decay, a possible D-wave contribution is assumed to be negligible and ignored.

The double integral over the pion energies represents the available phase space of the corresponding three-body $\Lambda_c(2595)^+$ decay. This integration is performed for different values of $M(\Lambda_c(2595)^+) - M(\Lambda_c^+)$ by means of Monte Carlo simulated events, where the EVTGEN package [53] is used to set up the decay process. For illustration, the phase space distribution for $M(\Lambda_c(2595)^+) - M(\Lambda_c^+) = 306\,\mathrm{MeV}/c^2$ can be found in Figure 5.65.

The calculated dependence of the two partial widths on $M(\Lambda_c(2595)^+) - M(\Lambda_c^+)$ is shown in Fig. 5.66.

Signal Structures

For the description of the $\Lambda_c(2595)^+$ signal structure, the shape defined by Equation 5.18 is numerically convolved with a resolution function determined from simulation and consisting of three Gaussians with mean zero, as described in Section 5.5. As for the Σ_c case, a common, Gaussian constrained, scaling factor is introduced for the widths of all three Gaussians, in order to account for the uncertainty in

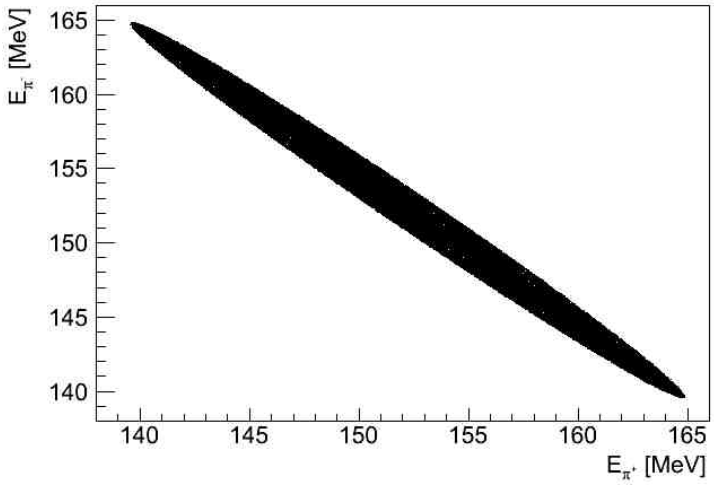

Figure 5.65.: Available phase space in $\Lambda_c(2595)^+ \to \Lambda_c^+ \pi^+ \pi^-$ for $M(\Lambda_c(2595)^+) - M(\Lambda_c^+) = 306\,\mathrm{MeV}/c^2$.

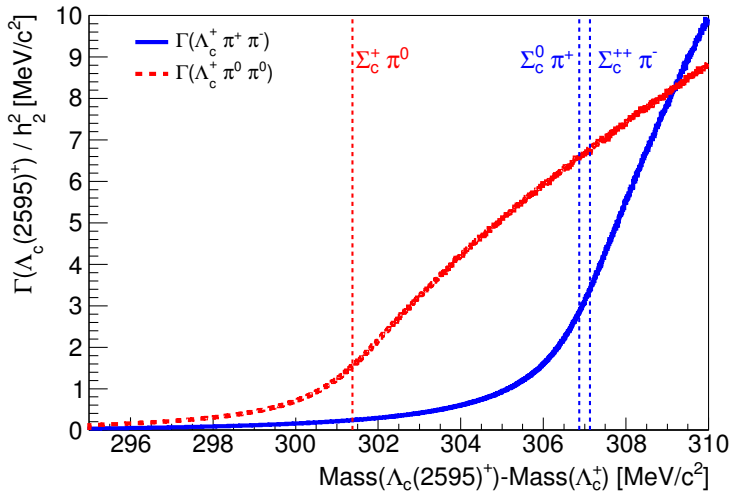

Figure 5.66.: Calculated dependence of $\Gamma(\Lambda_c^+\pi^+\pi^-)$ and $\Gamma(\Lambda_c^+\pi^0\pi^0)$ on $M(\Lambda_c(2595)^+) - M(\Lambda_c^+)$. The constant factor h_2^2 is determined by a fit to the experimental data.

the width of the resolution function. The numerical integration needed for this convolution is performed by means of Simpson's rule

$$\int_a^b g(x)\mathrm{d}x = \frac{b-a}{n} \cdot \frac{1}{3}(g(x_0) + 4g(x_1) + 2g(x_2) + 4g(x_3) + ... + 4g(x_{n-1}) + g(x_n)) \,, \tag{5.25}$$

where n is the number of supporting points and $x_i = a + i\frac{a-b}{n}$ with $i = 0, 1, ...n$.

The signal PDF for the $\Lambda_c(2625)^+$ is the nonrelativistic Breit-Wigner function of Equation 5.15 convolved with a three Gaussian resolution function determined from simulation, as described in Section 5.5. Again, all three Gaussians have mean zero and a common, Gaussian constrained, scaling factor for their widths is introduced. Technically, the convolution is realized as the normalized sum of three Voigt functions with the same Breit-Wigner part.

Background Composition

The background consists of three different sources:

- random combinations without real Λ_c^+
- combinations of real Λ_c^+ with two random pions
- real $\Sigma_c^{++,0}$ combined with a random pion

The combinatorial background without real Λ_c^+ dominates and is parametrized by a second-order polynomial whose parameters are determined in a fit to the ΔM distribution of candidates from the Λ_c^+ mass sidebands, $2261.46 < M(pK^-\pi^+) < 2266.46\,\mathrm{MeV}/c^2$ and $2306.46 < M(pK^-\pi^+) < 2311.46\,\mathrm{MeV}/c^2$ discussed in Section 5.3.4. For this purpose the histogram shown in Figure 5.35 is scaled by a factor 2 because the signal region in the Λ_c^+ mass distribution (see Figure 5.32) is twice as broad as the combination of lower and upper sideband. The resulting distribution is shown in Figure 5.67 together with the fit.

In the final fit, we keep the parameters for this background floating within a Gaussian constraint of the form of Equation 5.17 to the values found in the fit to the candidates from the Λ_c^+ mass sidebands.

The second source, consisting of real Λ_c^+ combined with two random pions, is parametrized by a second-order polynomial with all parameters allowed to float in the fit.

The final source of background are real Σ_c combined with a random pion. For this source, the main issue is to have the proper shape close to the threshold. Small imperfections at higher ΔM can be ignored, as the second background source has enough flexibility to absorb it. The PDF of this Σ_c background is based on a constant function defined from the threshold to the end of the fit range. In order to take into account the natural widths as well as resolution effects, we use the

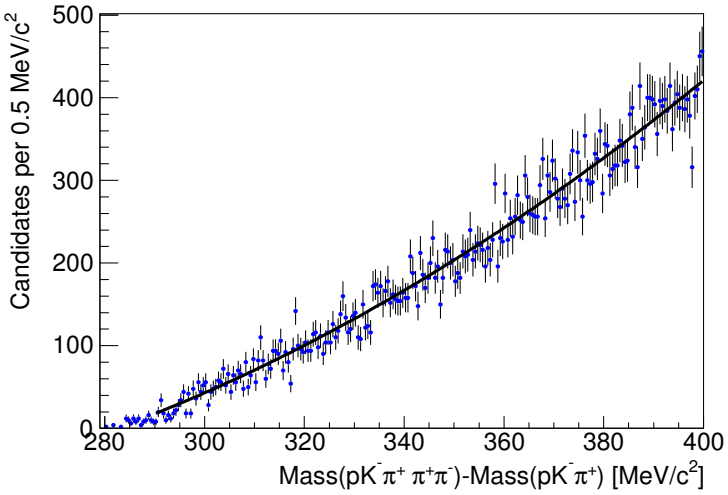

Figure 5.67.: Fit to the $M(pK^-\pi^+\,\pi^+\pi^-) - M(pK^-\pi^+)$ distribution of the candidates from Λ_c^+ mass sidebands.

weighted sum of ten such functions for both $\Sigma_c(2455)^{++}$ and $\Sigma_c(2455)^0$. Their thresholds and weights are chosen according to the shapes derived in the Σ_c fits shown in Figures 5.60 and 5.61. The size of this contribution is constrained to the $\Sigma_c(2455)$ yield obtained from the fits to the Λ_c^+ sideband subtracted $M(\Sigma_c) - M(pK^-\pi^+)$ distributions for candidates with $M(\Lambda_c^{*+}) - M(pK^-\pi^+) > 355\,\mathrm{MeV}/c^2$. These two distributions together with the fits including the functions defined in Section 5.6.1 are shown in Figure 5.68.

The sum of the $\Sigma_c(2455)$ candidates in the two distributions results the yield of the $\Sigma_c^{++,0}\pi^{-,+}$ background in this region, namely 3461 ± 135 candidates. It can be used to set the normalization of the corresponding background contribution. Again, this is done by means of a Gaussian constrained parameter in the likelihood function.

To verify the choice of a sum of constant functions for the PDF of this Σ_c background, the fitting procedure to the Λ_c^+ sideband subtracted $M(\Sigma_c) - M(pK^-\pi^+)$ distributions is repeated in bins of $15\,\mathrm{MeV}/c^2$ for the complete Λ_c^{*+} mass difference distribution. Figure 5.69 shows the sum of the resulting $\Sigma_c(2455)^{++}$ and $\Sigma_c(2455)^0$ signal yields in these bins, where the $\Lambda_c(2595)^+$ signal yield in each bin is subtracted according to the fit in Figure 5.64).

Results

The fit results for the full $\Delta M(\Lambda_c^{*+})$ distribution, containing all signal and background components, can be found in Table 5.11, where the central values ΔM_0 of the Breit-Wigner functions correspond to the searched mass differences, the full

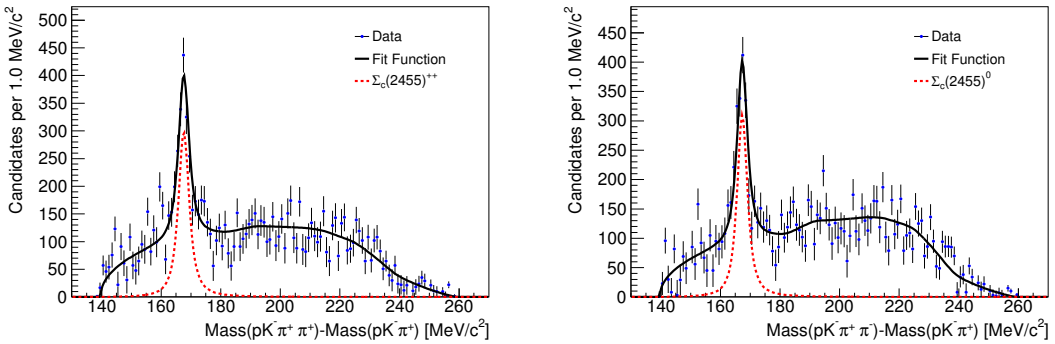

Figure 5.68.: Distributions of $M(\Sigma_c^{++}) - M(pK^-\pi^+)$ (left) and $M(\Sigma_c^0) - M(pK^-\pi^+)$ (right) for candidates with $M(\Lambda_c^{*+}) - M(pK^-\pi^+) > 355\,\mathrm{MeV}/c^2$ together with the fits.

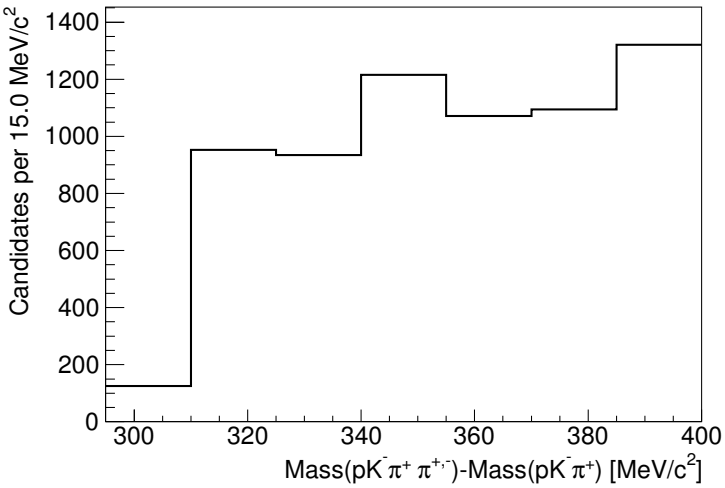

Figure 5.69.: Sum of the resulting numbers of $\Sigma_c(2455)^{++}$ and $\Sigma_c(2455)^0$ candidates in $\Lambda_c^+\,\pi^+\,\pi^-$ determined by fitting the two-body line shapes, where the number of $\Lambda_c(2595)^+$ signal candidates is subtracted in each bin.

Table 5.11.: Results of the fit to the mass difference distribution of the Λ_c^{*+} candidates.

	$\Lambda_c(2595)^+$	$\Lambda_c(2625)^+$
$\Delta M_0[\mathrm{MeV}/c^2]$	305.793 ± 0.153	341.645 ± 0.039
$\Gamma[\mathrm{MeV}/c^2]$	2.587 ± 0.376	0.096 ± 0.110
h_2^2	0.361 ± 0.052	
s	0.947 ± 0.145	

width at half maximum $\Gamma(\Lambda_c(2625))$ to the $\Lambda_c(2625)$ decay width, and h_2^2 to the squared pion coupling constant in $\Lambda_c(2595)^+ \to \Sigma_c(2455)\,\pi$. According to Figure 5.66, h_2^2 can be transferred to $\Gamma(\Lambda_c(2595)^+)$ by multiplying with the sum of $\Gamma(\Lambda_c^+\pi^+\pi^-)/h_2^2$ and $\Gamma(\Lambda_c^+\pi^0\pi^0)/h_2^2$ calculated at $\Delta M_0(\Lambda_c(2595)^+)$. The values s are the parameters for the resolution scaling factors implemented by Gaussian constraints. The χ^2 value of the fit is 227 (206 degrees of freedom).

Mass-Independent $\Lambda_c(2595)^+$ Width

As comparison, the χ^2 value of a fit with a mass-independent $\Lambda_c(2595)^+$ decay width, shown in Figure 5.70, increases to 286 (206 degrees of freedom). Whereas this fit does not describe the data properly, it leads to a higher measured value of the mass difference $\Delta M_0(\Lambda_c(2595)^+) = (307.486 \pm 0.158)\,\mathrm{MeV}/c^2$.

Upper Limit on $\Gamma(\Lambda_c(2625)^+)$

Since the measured value of $\Gamma(\Lambda_c(2625)^+)$ is not significantly different from zero, an upper limit on this quantity is calculated using a Bayesian approach with a uniform prior restricted to positive values.

This is done by performing the fitting procedure several times with fixed values of $\Gamma(\Lambda_c(2625)^+)$ from $\Gamma(\Lambda_c(2625)^+) = 0.0\,\mathrm{MeV}/c^2$ to $\Gamma(\Lambda_c(2625)^+) = 2.5\,\mathrm{MeV}/c^2$ and a step size of $0.01\,\mathrm{MeV}/c^2$. In order to account for the systematic uncertainty originating from the Monte Carlo simulations, a Gaussian constraint on the detector resolution of the $\Lambda_c(2625)^+$ signal is included in the likelihood function. The systematic uncertainty originating from the overall momentum scale (see Section 5.7.2) is included in the limit determination by employing another Gaussian constraint on a parameter additive to $\Gamma(\Lambda_c(2625)^+)$ with $\mu = 0$ and $\sigma = 0.2\,\mathrm{MeV}/c^2$.

In Figure 5.71 the likelihood values resulting from the fits are shown in dependence of the corresponding $\Gamma(\Lambda_c(2625)^+)$, where the dashed vertical line at $\Gamma(\Lambda_c(2625)^+) = 0.97\,\mathrm{MeV}/c^2$ is the 90% indication of the accordant integral. This value corresponds to the upper limit on $\Gamma(\Lambda_c(2625)^+)$ at the 90% credibility level. The small steps in the likelihood distribution are due to abrupt numerical changes in the minimization procedure.

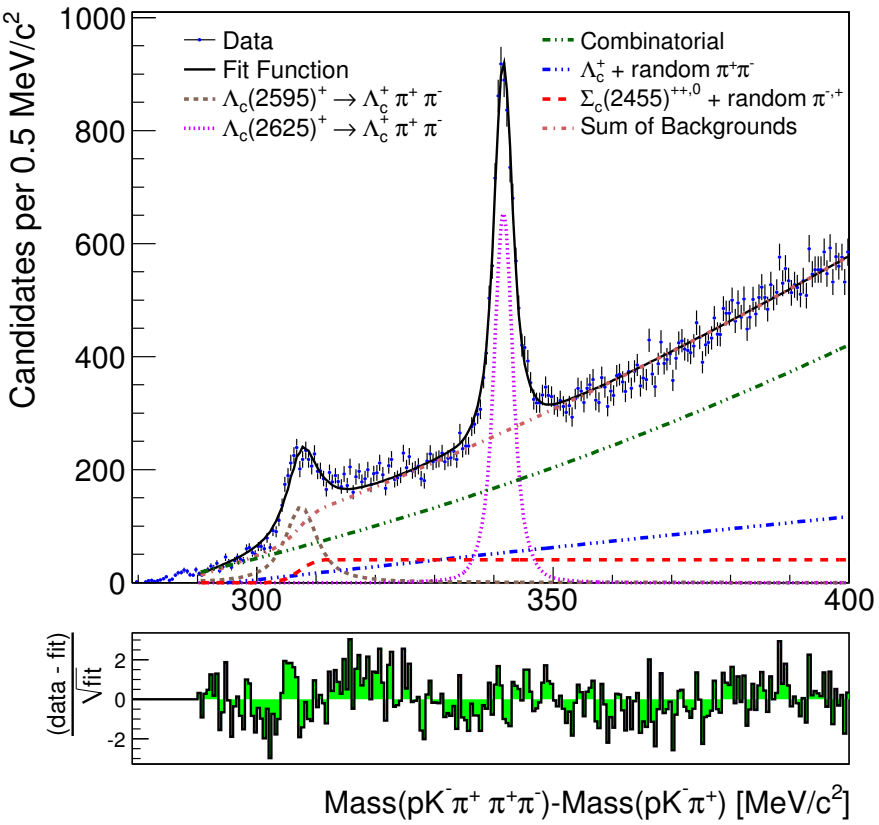

Figure 5.70.: The $M(pK^-\pi^+\,\pi^+\pi^-) - M(pK^-\pi^+)$ distribution obtained from data together with the fit, where a Breit-Wigner function with a mass-independent decay width is used to model the $\Lambda_c(2595)^+$ line shape. Further explanations can be found in the caption of Figure 5.64.

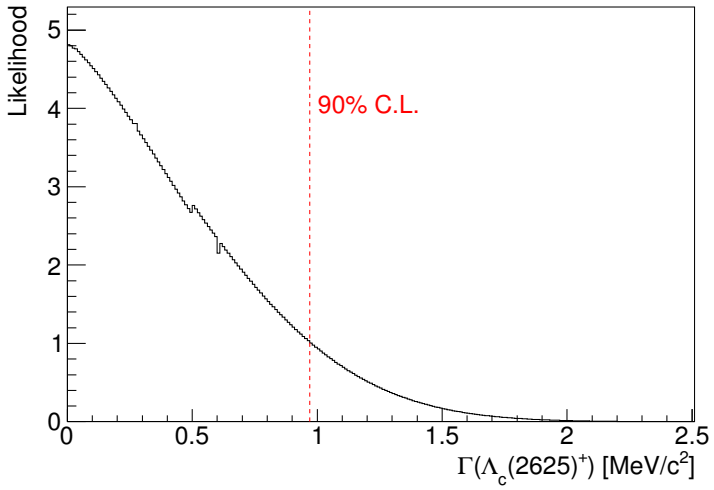

Figure 5.71.: Dependance of the likelihood value of the fit to the Λ_c^* mass difference distribution on $\Gamma(\Lambda_c(2625)^+)$ including systematic uncertainties. The dashed vertical line indicates the upper limit on $\Gamma(\Lambda_c(2625)^+)$ at the 90% credibility level obtained by integrating over the whole shown range.

Table 5.12.: Systematic uncertainties on the measurements of the mass differences and decay widths of the Σ_c^{++} resonances. The corresponding statistical uncertainties are listed for comparison.

Source	$\Delta M(\Sigma_c(2455)^{++})$ [MeV/c^2]	$\Gamma(\Sigma_c(2455)^{++})$ [MeV/c^2]	$\Delta M(\Sigma_c(2520)^{++})$ [MeV/c^2]	$\Gamma(\Sigma_c(2520)^{++})$ [MeV/c^2]
Resolution Model	···	0.40	···	0.69
Momentum Scale	0.12	0.20	0.12	0.20
Fit Model	0.02	···	0.11	1.16
External Inputs	···	···	···	···
Sum	0.12	0.45	0.16	1.36
Statistical	0.04	0.13	0.56	2.12

Table 5.13.: Systematic uncertainties on the measurements of the mass differences and decay widths of the Σ_c^0 resonances. The corresponding statistical uncertainties are listed for comparison.

Source	$\Delta M(\Sigma_c(2455)^0)$ [MeV/c^2]	$\Gamma(\Sigma_c(2455)^0)$ [MeV/c^2]	$\Delta M(\Sigma_c(2520)^0)$ [MeV/c^2]	$\Gamma(\Sigma_c(2520)^0)$ [MeV/c^2]
Resolution Model	···	0.45	···	0.70
Momentum Scale	0.12	0.20	0.12	0.20
Fit Model	0.02	···	0.11	1.16
External Inputs	···	···	···	···
Sum	0.12	0.49	0.16	1.37
Statistical	0.03	0.11	0.43	1.82

5.7. Systematic Uncertainties

Several systematic effects that can affect the measurements are investigated. Generally, they can be categorized as imperfect modeling by the simulation, limited knowledge on the momentum scale of the detector, ambiguities in the fit model, and uncertainties on the external inputs to the fit.

In this Section it is discussed how they can affect the results and in which way they are assessed. A summary of the assigned uncertainties can be found in Tables 5.12–5.14. To obtain the total systematic uncertainties, the contributions from all sources are added up in quadrature.

5.7.1. Mass Resolution Model

To properly describe the signal shapes, it is necessary to understand the intrinsic mass resolution of the detector. Since this is estimated by simulated events, it has to be verified that the resolution obtained from simulation agrees with that in real data on a 20%-level, which is assigned as systematic uncertainty in the

Table 5.14.: Systematic uncertainties on the measurements of the mass differences of the Λ_c^{*+} resonances and the pion coupling constant h_2^2 ($\Gamma(\Lambda_c(2595)^+)$). The corresponding statistical uncertainties are listed for comparison.

Source	$\Delta M(\Lambda_c(2595)^+)$ [MeV/c^2]	h_2^2	$\Gamma(\Lambda_c(2595)^+)$ [MeV/c^2]	$\Delta M(\Lambda_c(2625)^+)$ [MeV/c^2]
Resolution Model	0.06	0.03	0.22	···
Momentum Scale	0.12	0.03	0.20	0.12
Fit Model	···	···	···	···
External Inputs	0.15	0.06	0.36	···
Sum	0.20	0.07	0.47	0.12
Statistical	0.14	0.04	0.30	0.04

measurements.

Reference Decays

To estimate the reliance of the determined detector resolutions, $D^*(2010)^+ \to D^0\,\pi^+$ with $D^0 \to K^-\,\pi^+$ decays and $\psi(2S) \to J\!/\!\psi\,\pi^+\,\pi^-$ with $J\!/\!\psi \to \mu^+\,\mu^-$ decays are considered, as their decay topologies are similar to $\Sigma_c^{++,0} \to \Lambda_c^+\,\pi^{+,-}$ and $\Lambda_c^{*+} \to \Lambda_c^+\,\pi^+\,\pi^-$.

The $D^*(2010)^+$ and $\psi(2S)$ mass difference distributions for data and Monte Carlo simulations can be found in Figures 5.72–5.75.

For the $D^*(2010)^+$ case, three Voigt functions are used to describe the signal, where the widths of the Breit-Wigner parts are all set to the world average value of the $D^*(2010)^+$ decay width [1], $\Gamma(D^*(2010)^+) = 0.096\,\mathrm{MeV}/c^2$. The background in data is modeled by a third-order polynomial.

For the $\psi(2S)$ case, two Voigt functions are used to describe the signal with the widths of the Breit-Wigner parts set to the world average value of the $\psi(2S)$ decay width [1], $\Gamma(\psi(2S)) = 0.337\,\mathrm{MeV}/c^2$. The background in data is modeled by a linear function.

For comparison of the overall resolution scale between data and simulated events, the mass resolutions can be determined as weighted averages of the standard deviations of the Gaussian parts of the Voigt functions. The results are listed in Table 5.15.

Figure 5.76 shows the dependence of the $D^*(2010)^+$ resolution on the transverse momentum of the slow pion in $D^*(2010)^+ \to D^0\,\pi^+$ and Figure 5.77 the dependence of the $\psi(2S)$ resolution on the combined transverse momentum of the two slow pions in $\psi(2S) \to J/\psi\,\pi^+\,\pi^-$, separately for data and simulated events.

All discrepancies are found to be less than 20%, which is assigned as systematic uncertainty on the knowledge of the resolution function used in the studies of

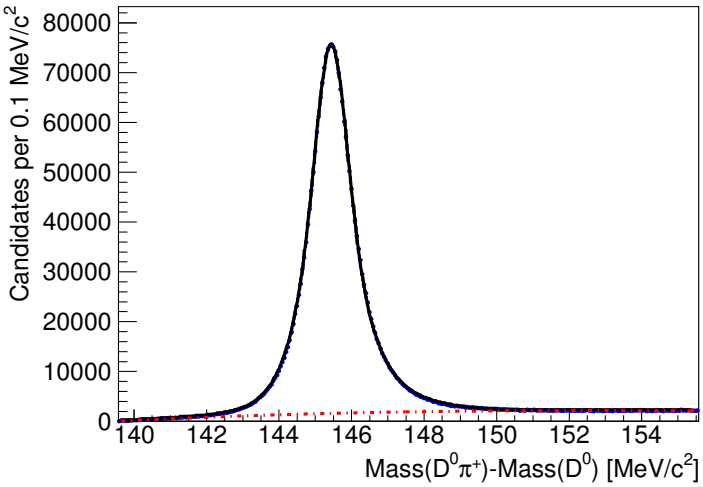

Figure 5.72.: $M(D^0\pi^+) - M(D^0)$ distribution in real data.

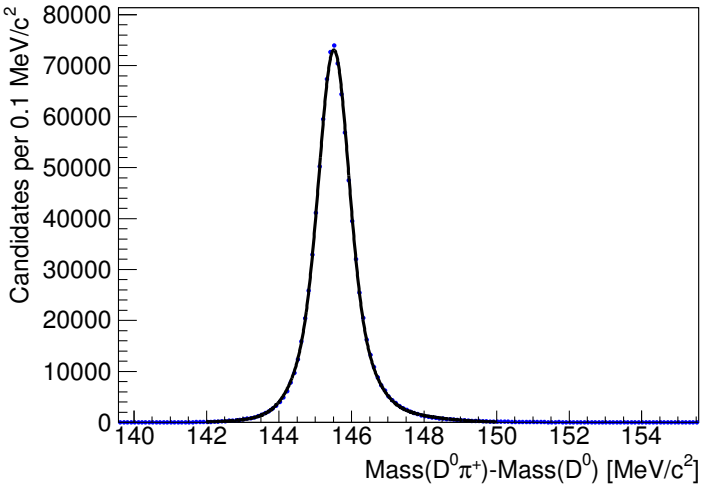

Figure 5.73.: $m(D^0\pi^+) - M(D^0)$ distribution for Monte Carlo simulated candidates.

Table 5.15.: Average $D^*(2010)^+$ and $\psi(2S)$) mass resolutions obtained from real data and Monte Carlo simulations.

	Data	Monte Carlo
$\bar{\sigma}(D^*(2010)^+)[\mathrm{MeV}/c^2]$	0.780 ± 0.005	0.671 ± 0.005
$\bar{\sigma}(\psi(2S))[\mathrm{MeV}/c^2]$	14.87 ± 0.45	14.65 ± 0.07

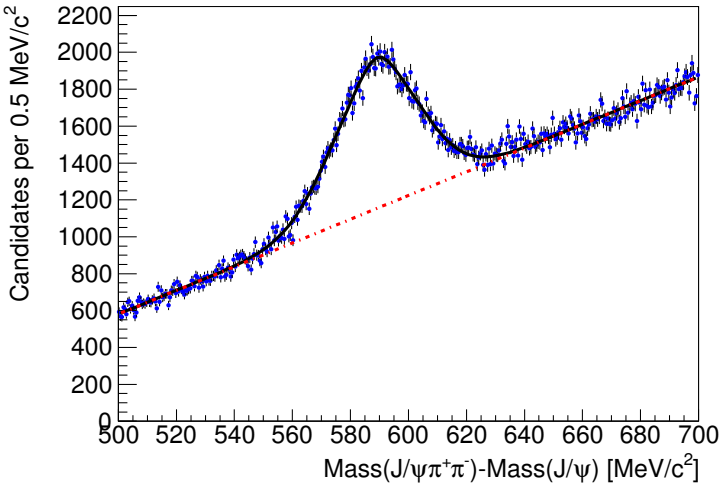

Figure 5.74.: $M(J/\psi\,\pi^+\,\pi^-) - M(J/\psi)$ distribution in real data.

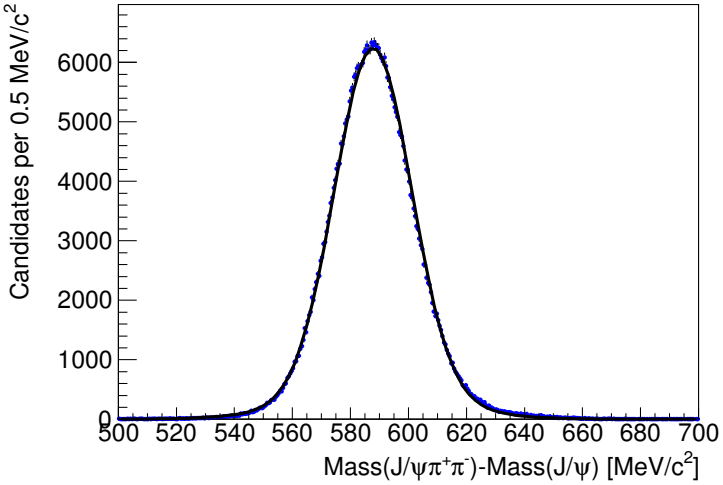

Figure 5.75.: $M(J/\psi\,\pi^+\,\pi^-) - M(J/\psi)$ distribution for Monte Carlo simulated candidates.

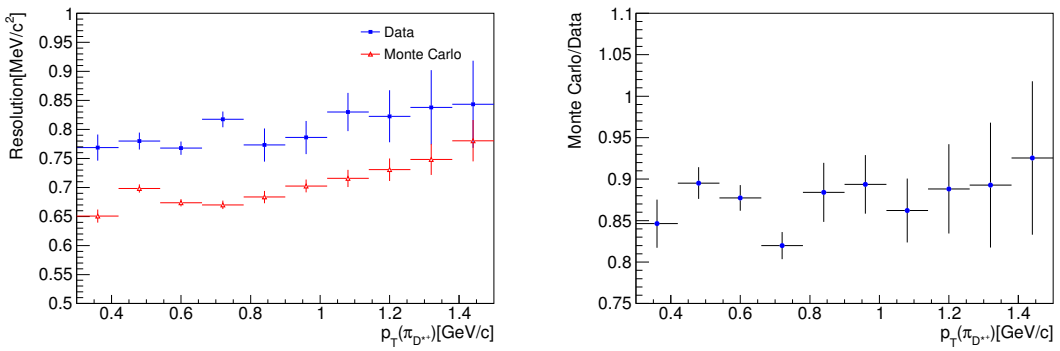

Figure 5.76.: Dependence of the $D^*(2010)^+$ mass resolution on the transverse momentum of the slow pion in $D^*(2010)^+ \to D^0\pi^+$ separately for data and Monte Carlo samples (left), together with a corresponding bin-by-bin comparison (right).

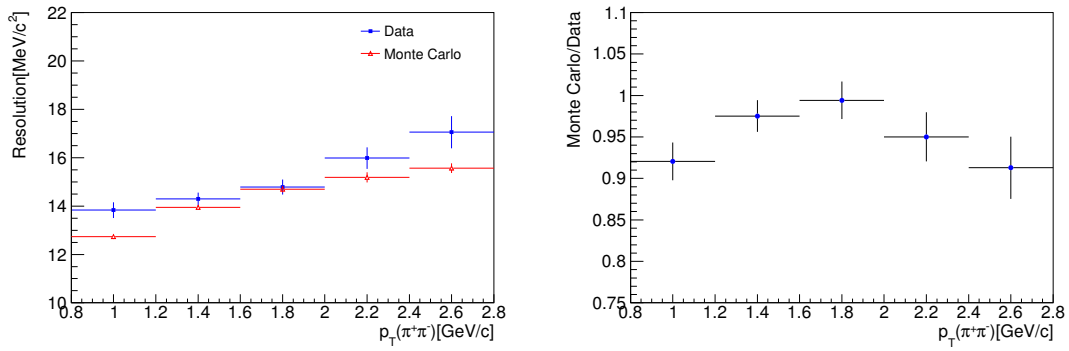

Figure 5.77.: Dependence of the $\psi(2S)$ mass resolution on the combined transverse momentum of the two slow pions in $\psi(2S) \to J/\psi\,\pi^+\,\pi^-$ separately for data and Monte Carlo samples (left), together with a corresponding bin-by-bin comparison (right).

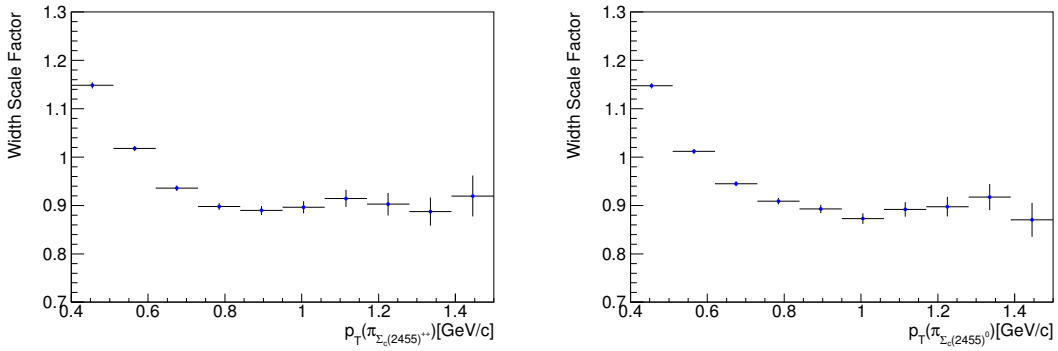

Figure 5.78.: $\Sigma_c(2455)^{++}$ and $\Sigma_c(2455)^0$ mass resolutions determined from Monte Carlo simulations in dependence on the transverse momentum of the slow pion in $\Sigma_c(2455)^{++,0} \to \Lambda_c^+ \pi^\pm$.

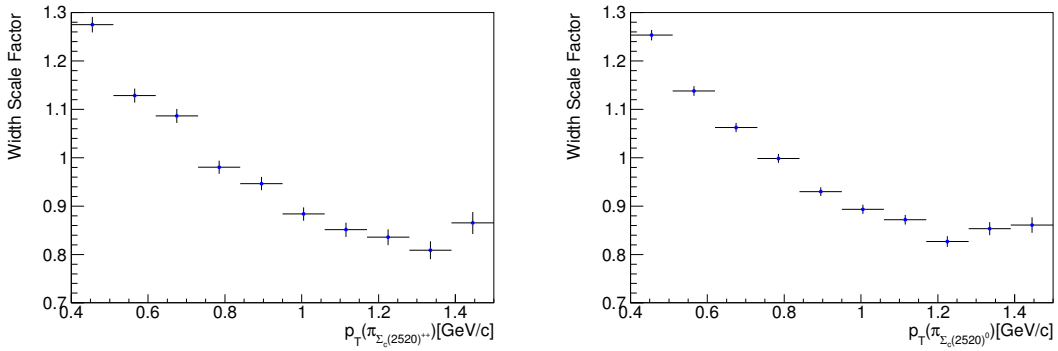

Figure 5.79.: $\Sigma_c(2520)^{++}$ and $\Sigma_c(2520)^0$ mass resolutions determined from Monte Carlo simulations in dependence on the transverse momentum of the slow pion in $\Sigma_c(2520)^{++,0} \to \Lambda_c^+ \pi^\pm$.

charmed baryons.

p_T Dependence

Since mass differences rather than masses are considered, the mass resolutions of the studied baryons basically depend on the transverse momenta of the slow pion(s) in the decays to $\Lambda_c^+\pi^\pm$ and $\Lambda_c^+\pi^+\pi^-$. These dependences are shown in Figures 5.78, 5.79, and 5.80. The detector resolutions are determined from Monte Carlo simulations as described in Section 5.5, and the parameters of the three Gaussian functions modeling the resolutions are fixed to the values resulting from the overall fit. The denoted width scaling factors are free fit parameters which are multiplied with the standard deviations of the three Gaussian functions.

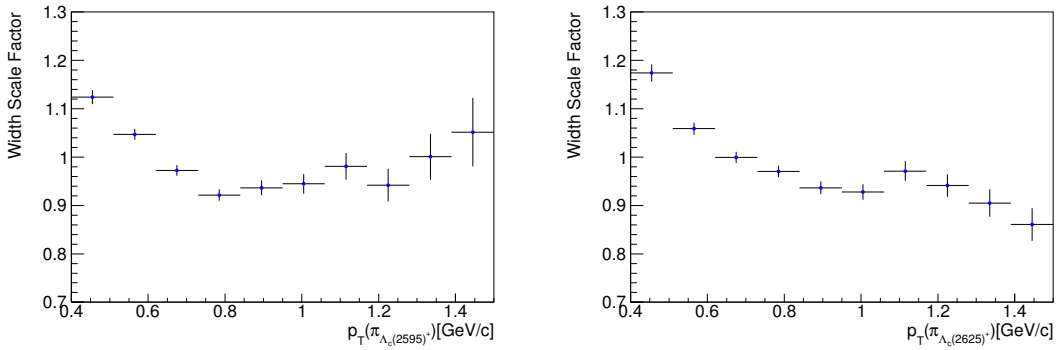

Figure 5.80.: $\Lambda_c(2595)^+$ and $\Lambda_c(2625)^+$ mass resolutions determined from Monte Carlo simulations in dependence on the transverse momentum of one of the slow pions in $\Lambda_c^{*+} \to \Lambda_c^+ \pi^+ \pi^-$.

Table 5.16.: Average width scaling factors $\langle w \rangle$ of the mass resolutions obtained from the convolution with the p_T distributions of sideband-subtracted data and reweighted Monte Carlo.

	Data	Monte Carlo
$\langle w \rangle(\Sigma_c(2455)^{++})$	1.006	0.971
$\langle w \rangle(\Sigma_c(2455)^0)$	1.009	0.967
$\langle w \rangle(\Lambda_c(2625)^+)$	1.004	0.937

By weighting these results with the corresponding p_T distributions for sideband-subtracted data and reweighted Monte Carlo, shown in Figures 5.48–5.50, average scaling factors $\langle w \rangle$ can be obtained. The resulting values are listed in Table 5.16 and show that the assigned systematic uncertainties of 20% are clearly sufficient to account for the deviations of the mass resolutions in data and Monte Carlo.

Luminosity Effects

The average hit density in the COT and the silicon detector has gone up with increasing instantaneous luminosity and the additional hits tend to degrade the track p_T resolutions what in turn also debases the mass resolutions.

Figure 5.81 shows the dependence of the $D^*(2010)^+$ detector resolution determined from real data on the instantaneous luminosity. Thereby, the parameters describing the resolution are fixed in the fitting procedure to their values resulting from the overall fit, except for a floating width scaling factor common for the three Gaussian standard deviations.

As expected, the mass resolution worsens with increasing instantaneous luminosity. But this effect is negligible in comparison to the assigned 20% systematic

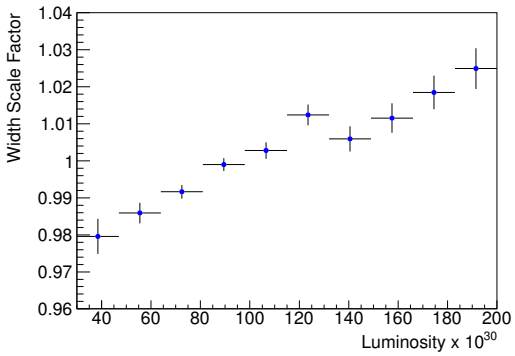

Figure 5.81.: Dependence of the $D^*(2010)^+$ detector resolution determined from real data on the instantaneous luminosity.

Table 5.17.: Mass resolution scaling factors s floating within Gaussian constraints in the fits.

Hadron	s
$\Sigma_c(2455)^{++}$	0.93 ± 0.17
$\Sigma_c(2455)^0$	1.07 ± 0.13
$\Sigma_c(2520)^{++}$	1.02 ± 0.20
$\Sigma_c(2520)^0$	1.00 ± 0.20
$\Lambda_c(2595)^+$	0.95 ± 0.15

uncertainty on the detector resolutions.

Estimation of the systematic Uncertainties

The contribution from the mass resolution uncertainty is already included in the uncertainties on the resonance parameters determined by the default fit with Gaussian constraint on the resolution scaling factor s, the resulting values for which are listed in Table 5.17. These values are consistent with 1, indicating that the resolution is well understood within the assigned uncertainty.

To disentangle it from the statistical component, the fits on data are repeated without multiplying the widths of the resolution function by the scaling factor s from Equation 5.16. The corresponding fit results can be found in Table 5.18.

The systematic uncertainty due to the imperfect modeling of the resolution function is then obtained by the difference in quadrature of the uncertainty of the fit with and without the Gaussian constraint. This uncertainty in the resolution has a large impact on the natural widths, but a negligible effect on the mass differences.

The systematic uncertainties calculated in this manner can be found in Tables 5.12–5.14. The one on $\Gamma(\Lambda_c(2625)^+)$ is considered separately in the upper

Table 5.18.: Results of the fits to the mass difference distributions without Gaussian constraints on the detector resolutions obtained from simulated events.

Hadron	ΔM_0 [MeV/c^2]	Γ [MeV/c^2]
$\Sigma_c(2455)^{++}$	167.444 ± 0.038	2.184 ± 0.128
$\Sigma_c(2455)^{0}$	167.279 ± 0.032	1.825 ± 0.110
$\Sigma_c(2520)^{++}$	230.731 ± 0.564	15.097 ± 2.117
$\Sigma_c(2520)^{0}$	232.877 ± 0.428	12.481 ± 1.823
$\Lambda_c(2595)^{+}$	305.816 ± 0.139	$h_2^2 = 0.352 \pm 0.043$
$\Lambda_c(2625)^{+}$	341.645 ± 0.039	0.099 ± 0.110

limit determination described in Section 5.6.

5.7.2. Momentum Scale

The accuracy of the momentum scale depends on the precision with which the magnetic field and the amount of material in the detector are known. The magnetic field is needed to relate the measured curvature of the tracks to their momentum. Knowledge on the amount of material is important to properly estimate the energy loss of particles traversing the detector. A systematic over- or underestimation of the measured momenta can in turn affect the observed masses and decay widths.

Both effects are originally calibrated using $J/\psi \to \mu^+ \mu^-$ decays [56]. A limitation of this calibration is that it uses muons that are required by the detector acceptance to have $p_T > 1.5\,\mathrm{GeV}/c$, while pions from Σ_c or Λ_c^{*+} decays typically have much lower p_T.

Reference Decays

To examine the effects on the mass differences of the studied resonances, the topologically similar decays $\psi(2S) \to J/\psi\,\pi^+\,\pi^-$ and $D^*(2010)^+ \to D^0\pi^+$ are considered. In Table 5.19, the results of the fits to the $M(D^*(2010)^+) - M(D^0)$ (Figure 5.72) and $M(\psi(2S)) - M(J/\psi)$ (Figure 5.74) distributions in data are compared to the world average values [1]. The deviations of the mass scale are smaller than $0.1\,\mathrm{MeV}/c^2$. In addition, the measured mass difference values are stable within the statistical uncertainties over the whole transverse momentum spectra of the involved pions.

Estimation of the systematic Uncertainties

The estimate of the uncertainty on the mass differences comes from the CDF analysis on the mass measurement of $X(3872)$ hadron [57]. There, $\psi(2S) \to J/\psi\,\pi^+\,\pi^-$

Table 5.19.: Measured $D^*(2010)^+$ and $\psi(2S)$ mass difference values compared to the world average values from PDG [1].

	measured value [MeV/c^2]	PDG [MeV/c^2]
$M(D^*(2010)^+) - M(D^0)$	145.447 ± 0.001	145.421 ± 0.010
$M(\psi(2S)) - M(J/\psi)$	589.168 ± 0.148	589.188 ± 0.028

decays are used to study the momentum scale uncertainties by comparing the measured $\psi(2S)$ mass with the world average value [1]. The difference of $0.06\,\mathrm{MeV}/c^2$ is added in quadrature to the value $0.1\,\mathrm{MeV}/c^2$ originating from a possible momentum dependence of the measured mass. Based upon this, a $0.12\,\mathrm{MeV}/c^2$ uncertainty is assigned on the mass differences of all states under study due to the imperfect knowledge of the momentum scale.

The corresponding effect on the natural widths was studied in the CDF measurements of the masses and widths of the excited charmed meson states D_1^0 and D_2^{*0} [58], and the $0.2\,\mathrm{MeV}/c^2$ found there are assigned as the uncertainty on the natural widths due to this source. To translate this uncertainty to the coupling constant h_2, it is assigned to the sum $\Gamma(\Lambda_c^+\pi^+\pi^-) + \Gamma(\Lambda_c^+\pi^0\pi^0)$ (see Equations 5.19 and 5.20), which is a function of h_2, and Gaussian error propagation is performed.

5.7.3. Fit Model

In terms of the fit model and procedure two effects are checked, the internal consistency of the fit and the shape of the signal PDFs. There is no explicit check of the background parametrizations performed as those are described by polynomials and any analytic function can be approximated by a polynomial of sufficient complexity. Since the fit quality does not indicate significant discrepancies between data and the model, one can conclude that the degree of the polynomial functions used is sufficient. Some backgrounds are determined from independent sources, but as the appropriate parameters are Gaussian constrained in the fit, the uncertainty originating from the sample size of the external sources, like Λ_c^+ mass sidebands, is already included in the statistical uncertainties of the results.

Internal Consistency

To check the internal consistency of the fit procedure, a large ensemble of statistical trials is generated using PDFs of the fit model with parameters obtained from the fit to data. Thereby, the numbers of randomly generated signal and background events are taken from Poisson statistics with the mean values chosen corresponding to the measured numbers in the data samples.

In detail the generation of a signal event works as follows:

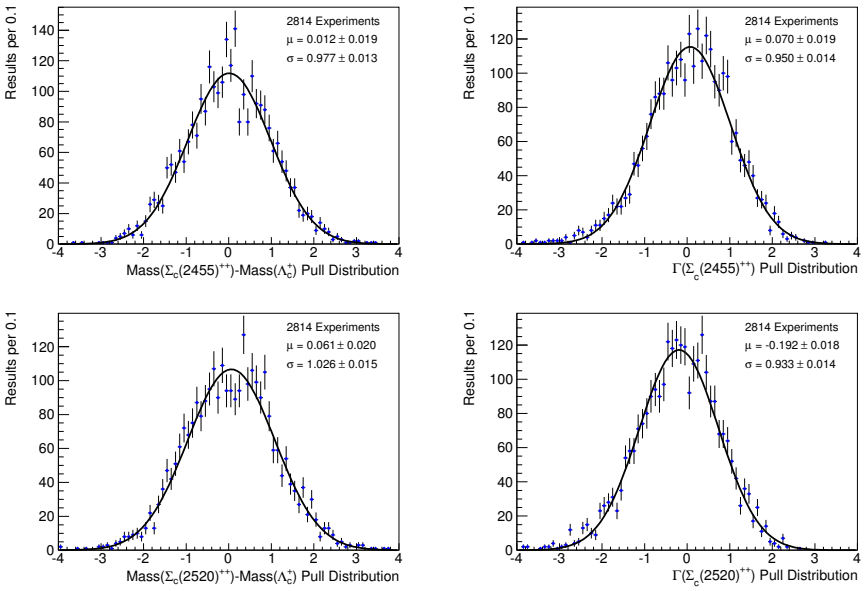

Figure 5.82.: Σ_c^{++} pull distributions between fitted and generated parameters of the pseudoexperiments.

- A random number is determined from a Breit-Wigner distributed PDF with the parameters for the mean value and the width taken from the corresponding fit to data.
- Since the resolutions consist of three weighted Gaussian functions obtained from Monte Carlo simulations, two random decisions according to these weights are made in order to choose a set of Gaussian parameters.
- From this Gaussian PDF another random number is determined which is added to the one obtained from the Breit-Wigner distribution.

The mass difference distributions of the pseudoexperiments are then fitted in the completely same manner as the real data and the deviations of the different parameters are quantified by pull distributions which are shown in Figures 5.82–5.84. These pull distributions are calculated by dividing the differences between the fitted and the generated parameters by the corresponding errors of the fits.

For a consistent fit the pull distributions are expected to follow a Gaussian function with mean zero and sigma one. Estimates of all physics parameters except the mass differences and natural widths of the $\Sigma_c(2520)$ resonances are found to be unbiased. The $\Sigma_c(2520)$ mass differences have small biases towards higher values and the $\Sigma_c(2520)$ natural widths are biased towards lower values. These biases on the $\Sigma_c(2520)$ resonance parameters result from the fairly low signal to background ratio and the flexibility in the background PDF, which tends to absorb the tails

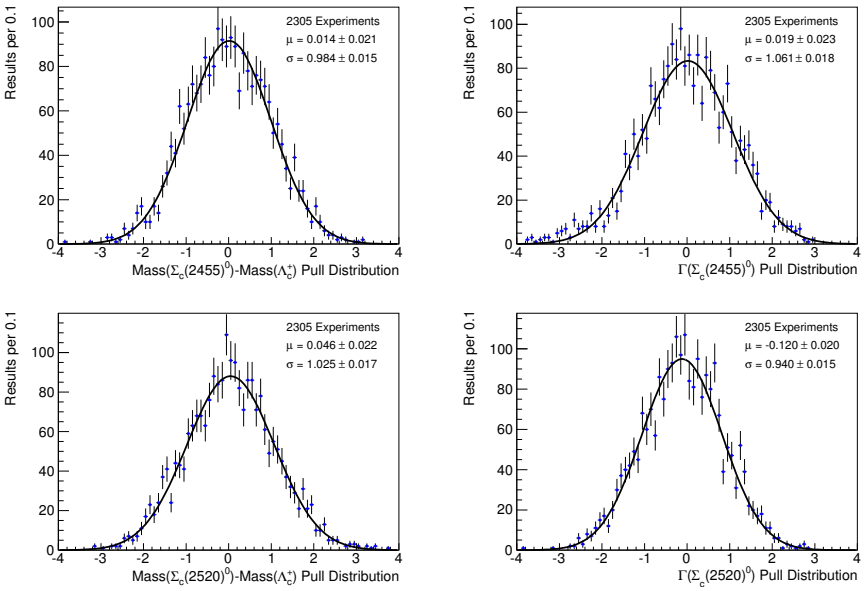

Figure 5.83.: Σ_c^0 pull distributions between fitted and generated parameters of the pseudoexperiments.

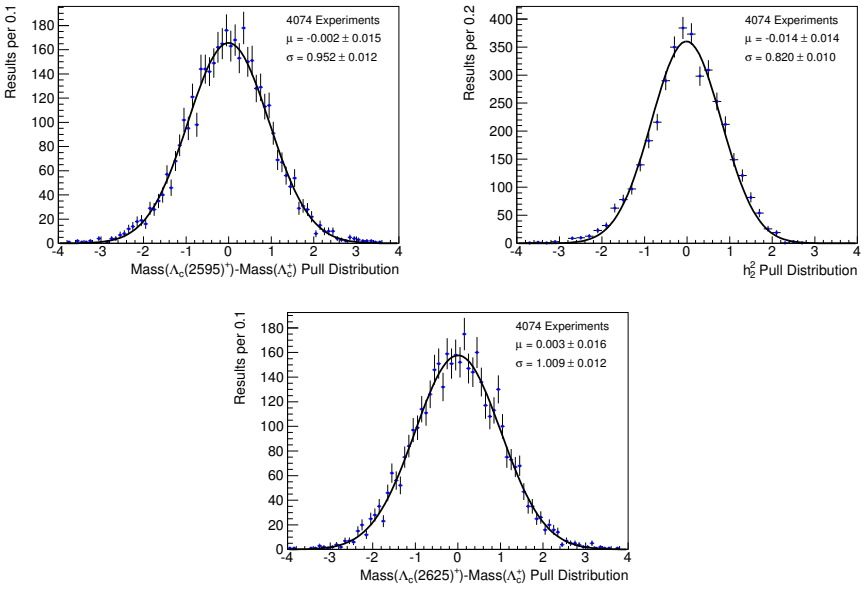

Figure 5.84.: Λ_c^{*+} pull distributions between fitted and generated parameters of the pseudoexperiments.

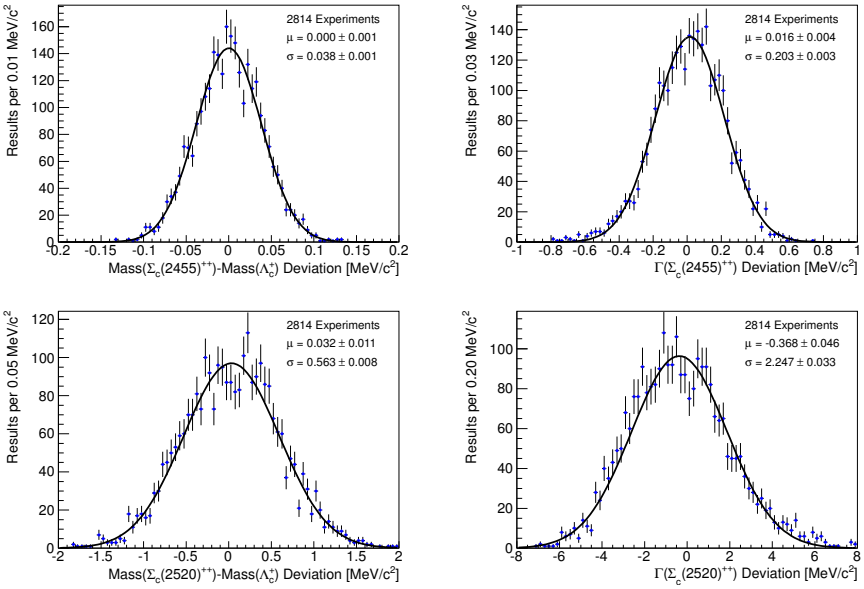

Figure 5.85.: Σ_c^{++} deviations between fitted and generated parameters of the pseudoexperiments.

of the relatively broad signal structure. In order to quantify these shifts, the differences between the fitted and the generated parameters are fitted by Gaussian functions (see Figures 5.85–5.87).

The study is repeated with a true value for the $\Sigma_c(2520)$ natural width below ($\Gamma = 7.5\,\mathrm{MeV}/c^2$) and above ($\Gamma = 20\,\mathrm{MeV}/c^2$) the measured value and the biases are found to have a small dependence on the true value. The pull and deviation distributions for the parameters $\Delta M(\Sigma_c(2520)^{++})$ and $\Gamma(\Sigma_c(2520)^{++})$ can be found in Figures 5.88 and 5.89, respectively. The biases are largest for a true value of the natural width of $20\,\mathrm{MeV}/c^2$ and consequently, these biases are assigned as systematic uncertainties on the mass differences and natural widths of the $\Sigma_c(2520)$ states.

Relativistic Breit-Wigner Functions

Concerning the uncertainty on the signal shape, a check is performed whether the signal parametrization using nonrelativistic Breit-Wigner functions provides a proper description. To estimate the effect of relativistic Breit-Wigner functions, pseudoexperiments are generated according to relativistic and afterwards fitted using nonrelativistic Breit-Wigner functions. The Σ_c and $\Lambda_c(2625)^+$ distributions are generated using a P-wave relativistic Breit-Wigner function of the form

$$\frac{\mathrm{d}N}{\mathrm{d}m} \propto \frac{m \cdot \Gamma(m)}{(m_0^2 - m^2)^2 + m_0^2 \cdot \Gamma^2(m)} \tag{5.26}$$

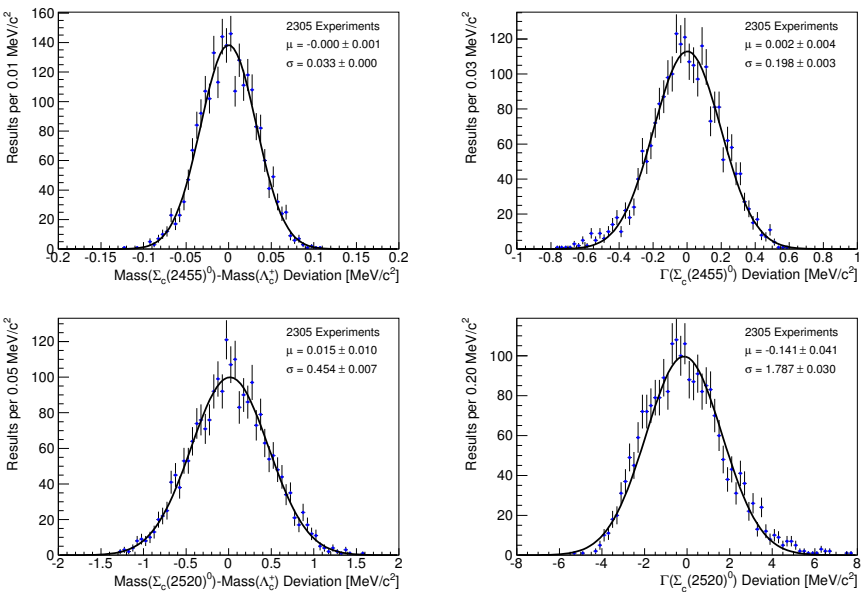

Figure 5.86.: Σ_c^0 deviations between fitted and generated parameters of the pseudoexperiments.

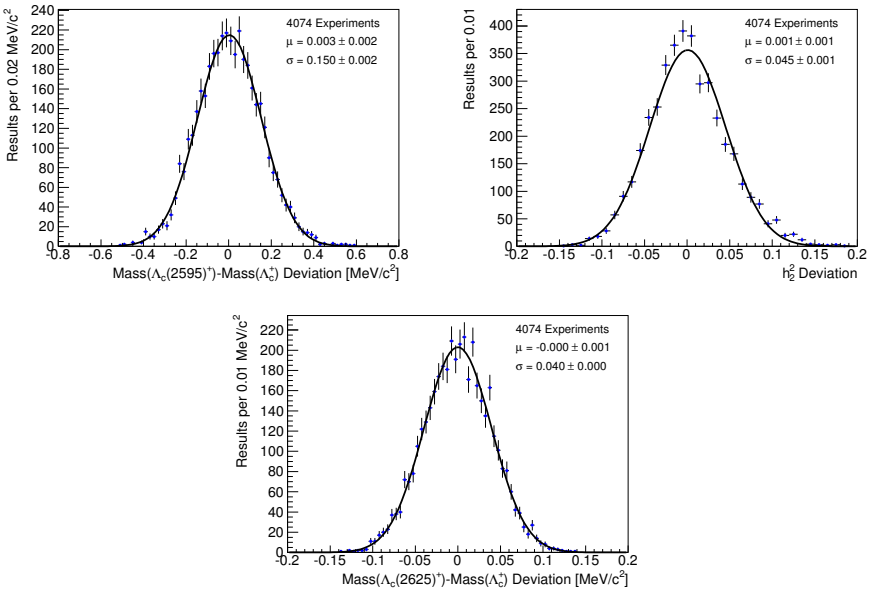

Figure 5.87.: Λ_c^* deviations between fitted and generated parameters of the pseudoexperiments.

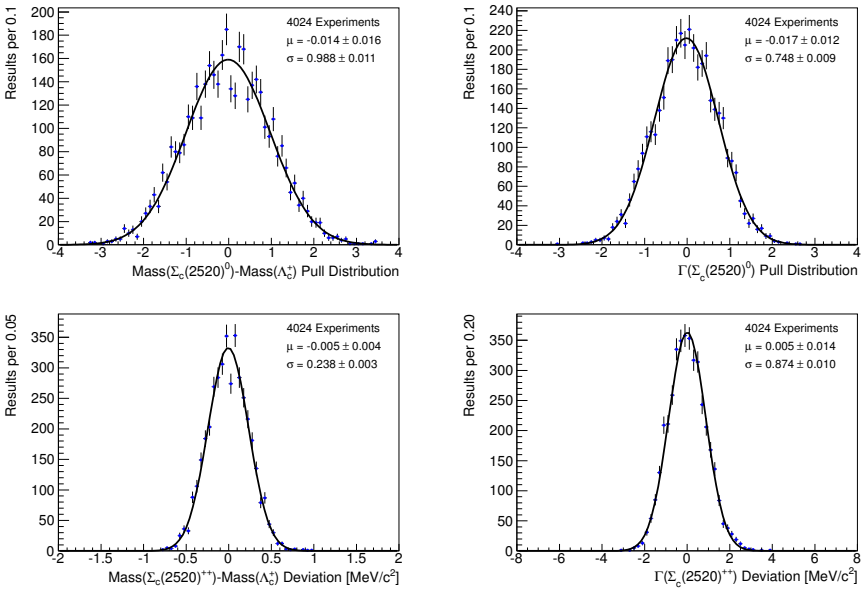

Figure 5.88.: $\Delta M(\Sigma_c(2520)^{++})$ and $\Gamma(\Sigma_c^{++})$ pull distributions and deviations between fitted and generated parameters of pseudoexperiments generated with $\Gamma(\Sigma_c(2520)^{++}) = 7.5\,\mathrm{MeV}/c^2$.

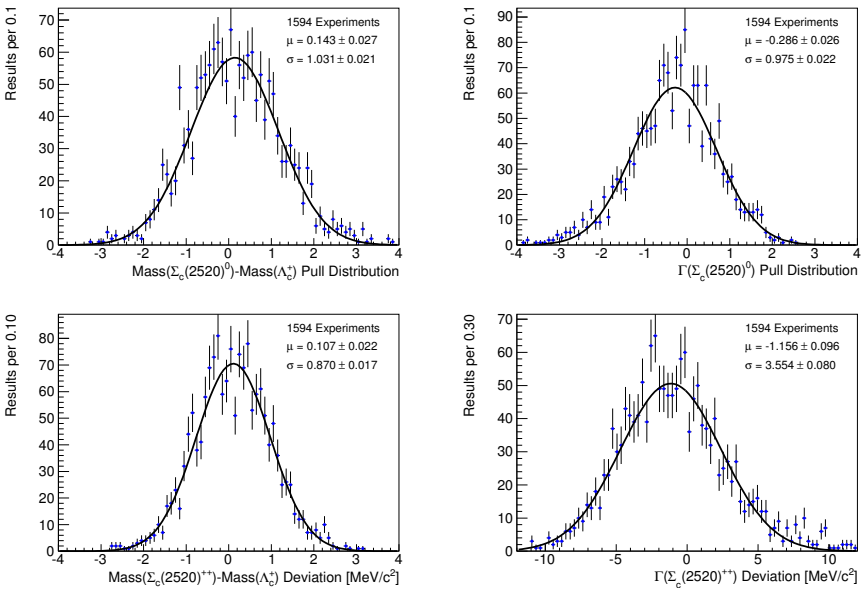

Figure 5.89.: $\Delta M(\Sigma_c(2520)^{++})$ and $\Gamma(\Sigma_c^{++})$ pull distributions and deviations between fitted and generated parameters of pseudoexperiments generated with $\Gamma(\Sigma_c(2520)^{++}) = 20.0\,\mathrm{MeV}/c^2$.

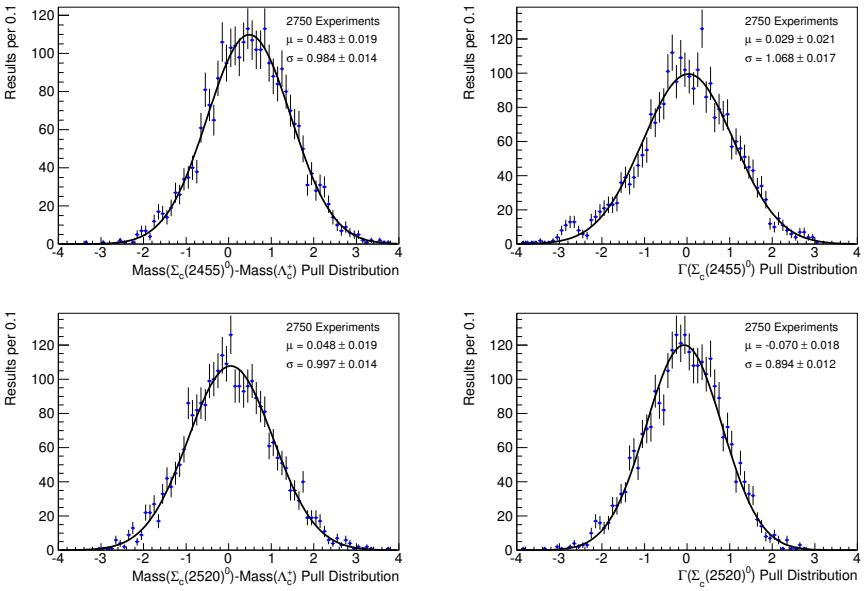

Figure 5.90.: Σ_c^0 pull distributions between fitted and generated parameters of the pseudoexperiments generated according to relativistic P-wave Breit-Wigner functions.

with

$$\Gamma(m) = \Gamma_0 \left(\frac{q}{q_0}\right)^3 \left(\frac{m_0}{m}\right) \left(\frac{1+q_0^2R^2}{1+q^2R^2}\right), \tag{5.27}$$

where $m = \Delta M + m_{\Lambda_c^+}$, R is the Blatt-Weisskopf radius set to $3\,(\mathrm{GeV}/c)^{-1}$ [59,60], m_0 and Γ_0 are the nominal mass and width, and $q(q_0)$ is the momentum of the daughters in the Σ_c or $\Lambda_c(2625)^+$ rest frame calculated from the reconstructed (nominal) mass. For the $\Lambda_c(2595)^+$ the nonrelativistic Breit-Wigner function of Equation 5.18 is replaced by a relativistic one and the variable width defined in Equations 5.19 and 5.20 is used.

Figures 5.90 and 5.91 show the corresponding pull distributions for the Σ_c^0 and Λ_c^* states. No shifts are observed in the cases of $\Sigma_c(2520)$ and Λ_c^{*+} resonances and thus the effect is assumed to be negligible. As shown in Figure 5.92, a deviation of $0.02\,\mathrm{MeV}/c^2$ between fitted and generated parameters in the $\Sigma_c(2455)$ mass difference is observed, which is assigned as a systematic uncertainty.

5.7.4. External Inputs

Finally, the line shape of the $\Lambda_c(2595)^+$ depends on the input values of the $\Sigma_c(2455)$ masses and widths and the pion decay constant f_π. We repeat the fit using values of those parameters smaller or larger by one standard deviation and take the stronger

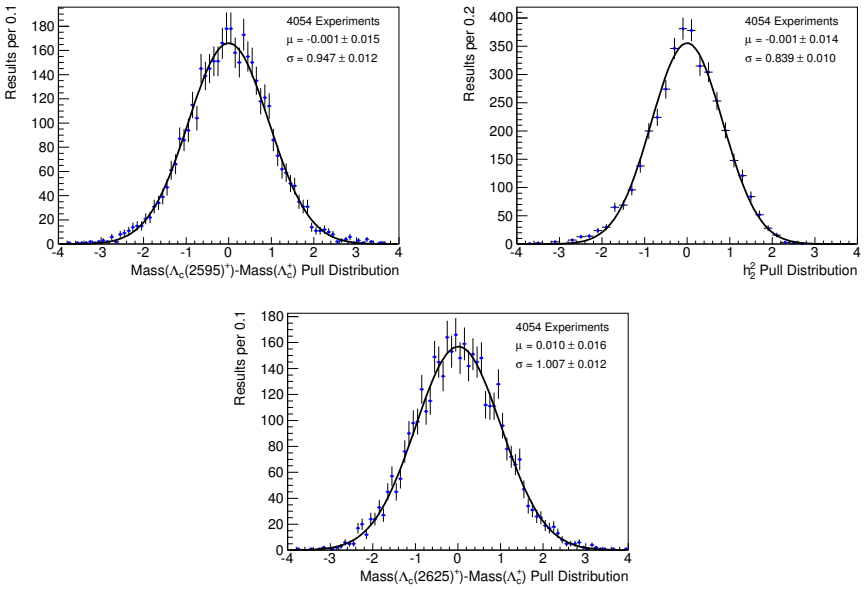

Figure 5.91.: Λ_c^* pull distributions between fitted and generated parameters of the pseudoexperiments generated according to relativistic Breit-Wigner functions.

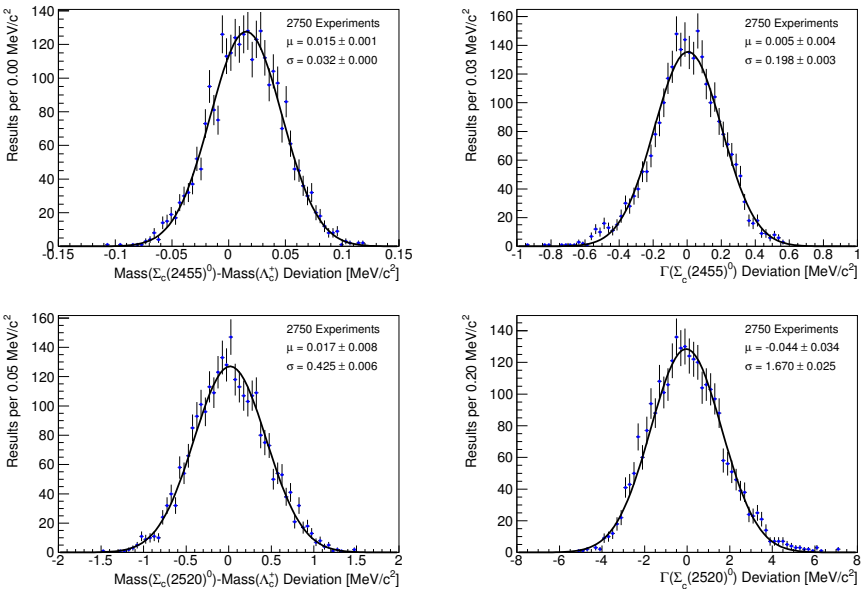

Figure 5.92.: Σ_c^0 deviations between fitted and generated parameters of the pseudoexperiments generated according to relativistic P-wave Breit-Wigner functions.

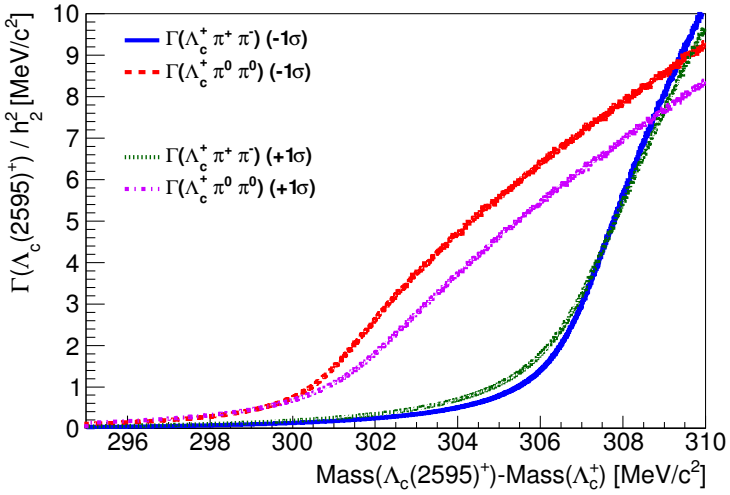

Figure 5.93.: Calculated dependences of $\Gamma(\Lambda_c^+\pi^+\pi^-)$ and $\Gamma(\Lambda_c^+\pi^0\pi^0)$ on $M(\Lambda_c(2595)^+) - M(\Lambda_c^+)$ for values of the $\Sigma_c(2455)$ masses and decay widths commonly shifted by one standard deviation down (-1σ) respective up ($+1\sigma$).

Table 5.20.: Results of the fits to the $\Lambda_c(2595)^+$ mass difference distribution, where the dependences of $\Gamma(\Lambda_c^+\pi^+\pi^-)$ and $\Gamma(\Lambda_c^+\pi^0\pi^0)$ on $M(\Lambda_c(2595)^+) - M(\Lambda_c^+)$ are calculated with values of the $\Sigma_c(2455)$ masses and decay widths commonly shifted by one standard deviation up respective down.

Shift	$\Delta M_0(\Lambda_c(2595)^+)$ [MeV/c^2]	h_2^2	$\Gamma(\Lambda_c(2595)^+)$ [MeV/c^2]
Up	305.945 ± 0.145	0.415 ± 0.065	2.945 ± 0.460
Down	305.651 ± 0.159	0.306 ± 0.041	2.224 ± 0.300

variation as systematic uncertainty.

The dependences of $\Gamma(\Lambda_c^+\pi^+\pi^-)$ and $\Gamma(\Lambda_c^+\pi^0\pi^0)$ on $M(\Lambda_c(2595)^+) - M(\Lambda_c^+)$, calculated with values of the $\Sigma_c(2455)$ masses and decay widths commonly shifted by one standard deviation up respective down [1] (see Table 5.2), are shown in Figure 5.93. The corresponding fit results can be found in Table 5.20.

According to Reference [55], f_π is known with an accuracy of $2\,\mathrm{MeV}/c^2$, $f_\pi = (132 \pm 2)\,\mathrm{MeV}/c^2$. Choosing $f_\pi = 130$ respective $f_\pi = 134$ instead of $f_\pi = 132$ results in an uncertainty of 3% on $\Gamma(\Lambda_c^+\pi^+\pi^-)$ and $\Gamma(\Lambda_c^+\pi^0\pi^0)$. The effect of the uncertainty on the world average $\Sigma_c(2455)$ masses and widths used as input is dominant compared to the effect of the uncertainty on f_π.

Table 5.21.: Measured resonance parameters of the charmed baryons under study, where the first uncertainty is statistical and the second is systematic.

Hadron	ΔM [MeV/c^2]	Γ [MeV/c^2]
$\Sigma_c(2455)^{++}$	$167.44 \pm 0.04 \pm 0.12$	$2.34 \pm 0.13 \pm 0.45$
$\Sigma_c(2455)^{0}$	$167.28 \pm 0.03 \pm 0.12$	$1.65 \pm 0.11 \pm 0.49$
$\Sigma_c(2520)^{++}$	$230.73 \pm 0.56 \pm 0.16$	$15.03 \pm 2.12 \pm 1.36$
$\Sigma_c(2520)^{0}$	$232.88 \pm 0.43 \pm 0.16$	$12.51 \pm 1.82 \pm 1.37$
$\Lambda_c(2595)^{+}$	$305.79 \pm 0.14 \pm 0.20$	$h_2^2 = 0.36 \pm 0.04 \pm 0.07$
$\Lambda_c(2625)^{+}$	$341.65 \pm 0.04 \pm 0.12$	

5.8. Results

Fits to the distributions $M(pK^-\pi^+\,\pi^+) - M(pK^-\pi^+)$, $M(pK^-\pi^+\,\pi^-) - M(pK^-\pi^+)$, and $M(pK^-\pi^+\,\pi^+\pi^-) - M(pK^-\pi^+)$ are performed and about 13800 $\Sigma_c(2455)^{++}$, 15900 $\Sigma_c(2455)^0$, 8800 $\Sigma_c(2520)^{++}$, 9000 $\Sigma_c(2520)^0$, 3500 $\Lambda_c(2595)^+$, and 6200 $\Lambda_c(2625)^+$ signal events are selected. The resonance parameters obtained can be found in Table 5.21.

For the width of the $\Lambda_c(2625)^+$ a value consistent with zero is observed and therefore an upper limit is calculated using a Bayesian approach with a uniform prior restricted to positive values. At the 90% credibility level $\Gamma(\Lambda_c(2625)^+) < 0.97\,\mathrm{MeV}/c^2$ is obtained. For easier comparison to previous results [48, 51], h_2^2 corresponds to a $\Lambda_c(2595)^+$ decay width of $\Gamma(\Lambda_c(2595)^+) = 2.59 \pm 0.30 \pm 0.47\,\mathrm{MeV}/c^2$, calculated at $\Delta M(\Lambda_c(2595)^+)$.

The precise measurement of the coupling constant h_2 can, for instance, be used to predict the width of the $\Xi_c(2645)$, as discussed in Reference [61]. Previously, it was calculated from the measured $\Lambda_c(2595)^+$ decay widths:

- $h_2^2 = 0.30^{+0.21}_{-0.14}$ [61]
- $|h_2| = 0.572^{+0.322}_{-0.197}$ [42]

In Reference [52], the method described in Section 5.6.3 was used for a fit to CLEO data:

- $h_2^2 = 0.24^{+0.23}_{-0.11}$

In Figures 5.94–5.96, the presented results are compared to previous measurements by other experiments. Except for $\Delta M(\Lambda_c(2595)^+)$, all measurements at hand agree with the previous world average values. For $\Delta M(\Lambda_c(2595)^+)$, it is shown that a mass-independent natural width does not describe the data and a value $3.1\,\mathrm{MeV}/c^2$ smaller than the existing world average is observed. This difference is the same size as estimated in Reference [52], where also an unpublished

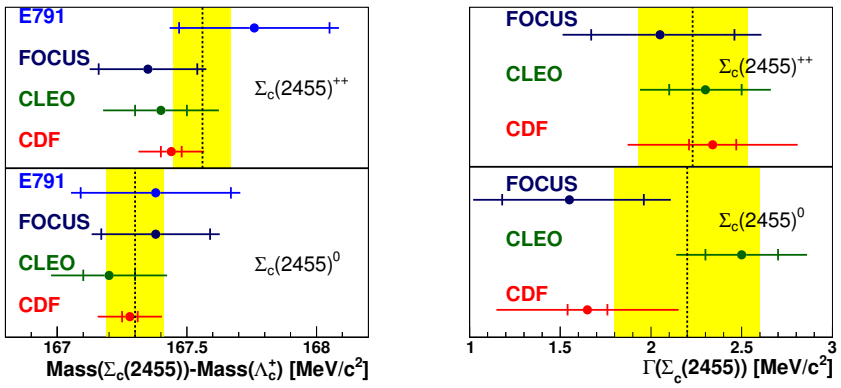

Figure 5.94.: Comparison of our results for the $\Sigma_c(2455)$ mass differences and decay widths with previous measurements by Fermilab E791 [62], FOCUS [45], and CLEO [44]. The error bars represent the statistical (vertical marks) as well as the combined statistical and systematic uncertainties. The vertical dashed line together with the surrounding box symbolizes the world average value and its uncertainty taken from Reference [1]. This average does not take into account the measurement at hand.

CLEO measurement of the $\Lambda_c(2595)^+$ decaying to $\Lambda_c^+\pi^0\pi^0$ is cited. This decay mode is not affected by the threshold effect occurring in the $\Lambda_c^+\pi^+\pi^-$ channel, and a mass difference $\Delta M = (306.3 \pm 0.7)\,\mathrm{MeV}/c^2$ is measured.

Since this data sample is 25 times larger than the ones studied so far, the results on the properties of Λ_c^{*+} states provide a significant improvement in precision compared to previous measurements. The precision for the Σ_c states is comparable to the precision of the world averages. Concerning the inconsistency of the two CLEO measurements [46, 47] of the $\Sigma_c(2520)^{++}$ mass, the data favor a smaller value.

Table 5.22 summarizes the results for the masses and widths of the studied charmed baryons with combined statistical and systematic experimental uncertainties. For the masses, another systematic uncertainty originates from the world average Λ_c^+ mass [1].

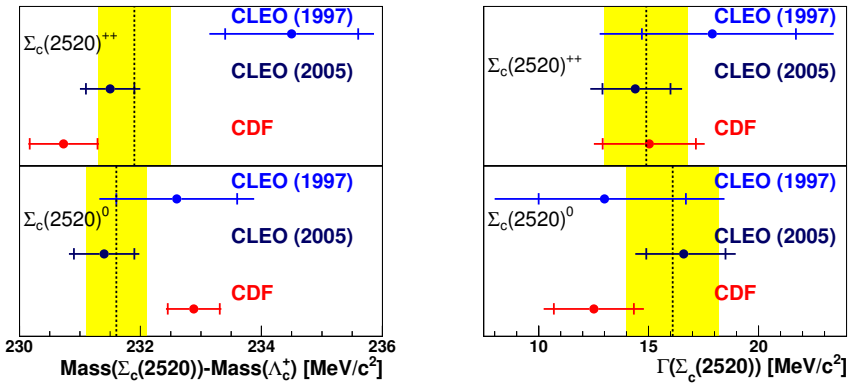

Figure 5.95.: Comparison of our results for the $\Sigma_c(2520)$ mass differences and decay widths with previous measurements by CLEO [46, 47]. Further explanations can be found in the caption of Fig. 5.94.

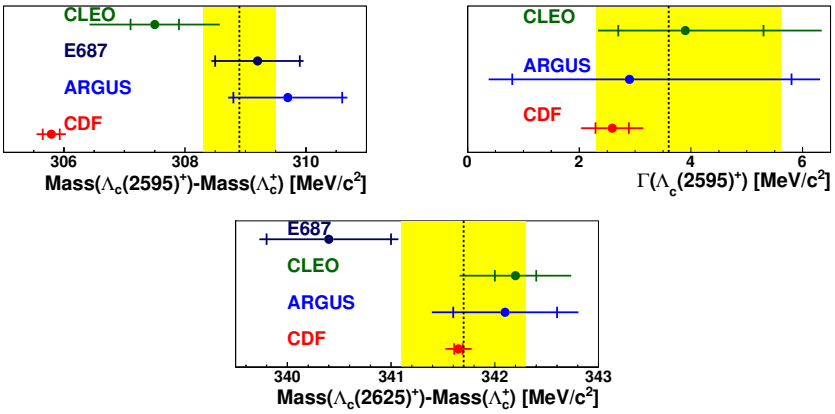

Figure 5.96.: Comparison of our results for the $\Lambda_c(2595)^+$ mass difference and decay width as well as the $\Lambda_c(2625)^+$ mass difference with previous measurements by CLEO [51], Fermilab E687 [49, 50], and ARGUS [48]. Further explanations can be found in the caption of Fig. 5.94.

Table 5.22.: Results for the masses and widths of the charmed baryons under study. The first uncertainty is the combined statistical and systematic experimental uncertainty. For the masses, the second uncertainty originates from the world average Λ_c^+ mass [1].

Hadron	M [MeV/c^2]	Γ [MeV/c^2]
$\Sigma_c(2455)^{++}$	$2453.90 \pm 0.13 \pm 0.14$	2.34 ± 0.47
$\Sigma_c(2455)^{0}$	$2453.74 \pm 0.12 \pm 0.14$	1.65 ± 0.50
$\Sigma_c(2520)^{++}$	$2517.19 \pm 0.46 \pm 0.14$	15.03 ± 2.52
$\Sigma_c(2520)^{0}$	$2519.34 \pm 0.58 \pm 0.14$	12.51 ± 2.28
$\Lambda_c(2595)^{+}$	$2592.25 \pm 0.24 \pm 0.14$	$h_2^2 = 0.36 \pm 0.08$
$\Lambda_c(2625)^{+}$	$2628.11 \pm 0.13 \pm 0.14$	< 0.97 at 90% C.L.

6. Search for CP Violation in $D^0 \to K^0_S \pi^+ \pi^-$

In this chapter, a search for time-integrated CP asymmetries in the resonant substructure of the three-body decay $D^0 \to K^0_S \pi^+ \pi^-$ is performed. For that purpose, the production flavor of the D^0 is tagged by the charge of the pion from the decay $D^*(2010)^+ \to D^0 \pi^+$, and the Dalitz plot technique is applied. Two different approaches are used, namely a full Dalitz fit employing the Isobar model [63] for the involved resonances and a model-independent bin-by-bin comparison of the D^0 and $\bar{D}^0$ Dalitz plots.

This chapter is organized as follows. After an overview of the physics potential of the decay $D^0 \to K^0_S \pi^+ \pi^-$ and the experimental status in Section 6.1, the candidate reconstruction and selection are described in Section 6.2 and 6.3. In Section 6.4 the resulting Dalitz plot used for the following measurements is presented. The sample of simulated events needed for the determination of the relative efficiency over the Dalitz plot is expounded in Section 6.5. The Dalitz fits to measure the different contributions to the resonant substructure of the decay as well as possible CP violating effects are described in Section 6.6, followed by a discussion of systematic uncertainties in Section 6.7 and the presentation of the results in Section 6.8. Finally, a complementary model-independent search for CP asymmetries involved in the Dalitz plot is depicted in Section 6.9.

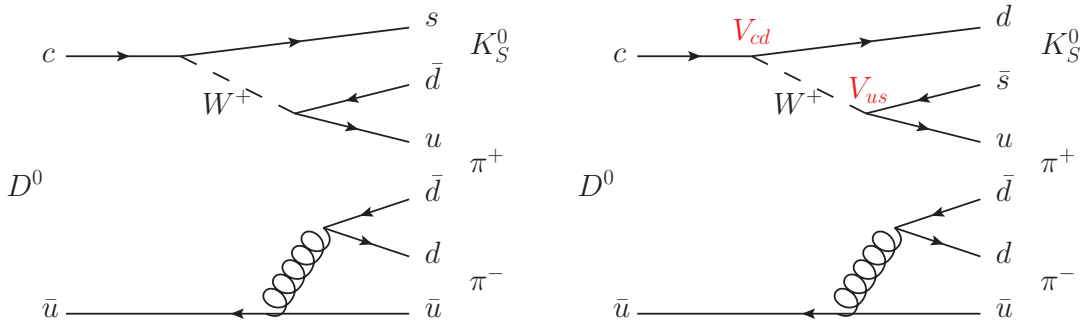

Figure 6.1.: Cabibbo allowed (left) and doubly Cabibbo suppressed (right) D^0 decay to the final state $K^0_S\pi^+\pi^-$.

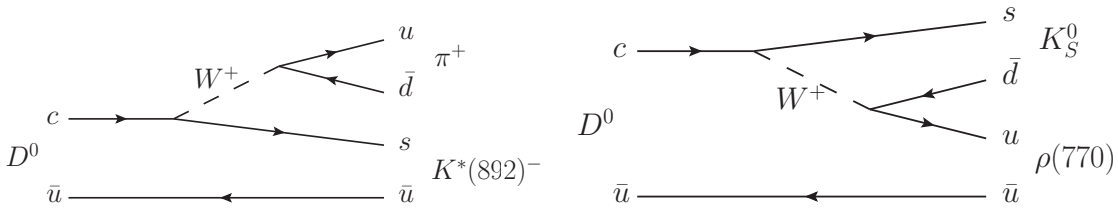

Figure 6.2.: Resonant D^0 decays to $K^*(892)^-\pi^+$ (left) and $K^0_S\rho(770)$ (right), the latter being a color suppressed mode.

6.1. Potential of the Decay $D^0 \to K^0_S \pi^+ \pi^-$

The decay $D^0 \to K^0_S \pi^+ \pi^-$ offers several opportunities for studies of flavor physics phenomena like neutral meson mixing and CP violation. In the following, the different measurements together with the corresponding experimental status are described briefly.

6.1.1. Study of the resonant Substructure

The first step in all analyses of the decay $D^0 \to K^0_S \pi^+ \pi^-$ is the study of its rich resonant substructure. This is accomplished by means of a fit to the corresponding Dalitz plot, the structure of which is described in Section 6.4.

As illustrated in Figure 6.1, the decay can either proceed via Cabibbo allowed or via doubly Cabibbo suppressed modes, where the latter means that the decay amplitude is decreased due to the two involved off-diagonal CKM matrix elements V_{cd} and V_{us}.

Consequently, there are three types of intermediate resonances in the decay, Cabibbo allowed, doubly Cabibbo suppressed, and CP eigenstates. The dominant

decay mode is the Cabibbo allowed $D^0 \to K^*(892)^- \pi^+$ which amounts to about 60% of the total branching fraction. The second largest contribution is from the intermediate CP eigenstate $K^0_S \rho(770)$. As shown in Figure 6.2, this mode is color suppressed compared to $K^*(892)^- \pi^+$ because the quark-antiquark pair originating from the W^+ has a definite color combination compared to three possibilities for the unsuppressed mode. There is also a measurable component originating from the doubly Cabibbo suppressed decay mode $D^0 \to K^*(892)^+ \pi^-$.

Results from the CLEO [64], Belle [65], and BABAR [66] experiments for the fit fractions of the different intermediate resonances are summarized in Table 6.1, where the employed models for the resonance description differ among the experiments. The fit fractions are a measure for the various relative branching fractions and offer an opportunity to compare the results of the different experiments. An exact definition is given in Equation 6.16. A CDF measurement of the resonant substructure of the decay $D^0 \to K^0_S \pi^+ \pi^-$ is presented in Section 6.6.2.

Earlier investigations of this decay channel are described in References [69–72].

6.1.2. D^0-$\bar{D}^0$ Mixing

A measurement of D^0-$\bar{D}^0$ mixing can be accomplished by a time-dependent Dalitz plot analysis of the decay $D^0 \to K^0_S \pi^+ \pi^-$. This means that variations of the D^0 and $\bar{D}^0$ Dalitz plots are studied as a function of the decay time. For that purpose, the production flavor, either D^0 or $\bar{D}^0$, has to be known. It can be determined by considering D^0 mesons originating from the decay $D^*(2010)^+ \to D^0 \pi^+$, where the charge of the pion defines the flavor of the D^0.

The CLEO [73], Belle [74], and BABAR [66] experiments measured the D^0-$\bar{D}^0$ mixing parameters

$$x = \frac{m_1 - m_2}{(\Gamma_1 + \Gamma_2)/2}\,, \qquad y = \frac{\Gamma_1 - \Gamma_2}{\Gamma_1 + \Gamma_2} \tag{6.1}$$

in this decay channel, where the subscripts refer to the mass eigenstates. The latter two experiments found hints for nonvanishing values indicating the existence of a small flavor oscillation in the D^0 system, like expected within the Standard Model and observed in other decay channels as well [75].

A difficulty for a possible CDF measurement is the two track trigger that is used for the accumulation of the data sample. Since this trigger requires tracks that are displaced from the primary vertex, the D^0 decay time distribution is affected in a complex way. The D^0-$\bar{D}^0$ mixing is not studied in the analysis described in this work.

Table 6.1.: Fit fractions FF of the intermediate resonances in $D^0 \to K^0_S \pi^+ \pi^-$ as reported by CLEO [64], Belle [65], and BABAR [67]. The given uncertainties are statistical, experimental systematic, and modeling systematic for CLEO, statistical only for Belle, and combined statistical and systematic for BABAR. Whereas CLEO and Belle use the Isobar model for all resonances [63], BABAR employs the K matrix parametrization for the description of the $\pi\pi$ S-wave contribution [68], and therefore the resonances $f_0(980)$, $f_0(1370)$, σ_1, and σ_2 are included in the listed fit fraction $\pi\pi$ S-wave. Further explanations of the different contributions can be found in the Sections 6.4 and 6.6.

Resonance	FF (CLEO) [%]	FF (Belle) [%]	FF (BABAR) [%]
$K^*(892)^-$	$65.7 \pm 1.3\,^{+1.1\ +1.4}_{-2.6\ -3.0}$	62.9 ± 0.8	55.7 ± 2.8
$K^*_0(1430)^-$	$7.3 \pm 0.7\,^{+0.4\ +3.1}_{-0.9\ -0.7}$	7.93 ± 0.09	10.2 ± 1.5
$K^*_2(1430)^-$	$1.1 \pm 0.2\,^{+0.3\ +0.6}_{-0.1\ -0.3}$	1.40 ± 0.06	2.2 ± 1.6
$K^*(1410)^-$	–	0.49 ± 0.07	–
$K^*(1680)^-$	$2.2 \pm 0.4\,^{+0.5\ +1.7}_{-0.3\ -1.5}$	0.06 ± 0.04	0.7 ± 1.9
$K^*(892)^+$	$0.34 \pm 0.13\,^{+0.31\ +0.26}_{-0.03\ -0.02}$	0.526 ± 0.016	0.46 ± 0.23
$K^*_0(1430)^+$	–	0.22 ± 0.04	< 0.05
$K^*_2(1430)^+$	–	0.093 ± 0.014	< 0.12
$K^*(1410)^+$	–	0.21 ± 0.03	–
$K^*(1680)^+$	–	0.30 ± 0.07	–
$\rho(770)$	$26.4 \pm 0.9\,^{+0.9\ +0.4}_{-0.7\ -2.5}$	21.2 ± 0.5	21.0 ± 1.6
$\omega(782)$	$0.72 \pm 0.18\,^{+0.04\ +0.10}_{-0.06\ -0.07}$	0.526 ± 0.014	0.9 ± 1.0
$f_0(980)$	$4.3 \pm 0.5\,^{+1.1}_{-0.4} \pm 0.5$	4.72 ± 0.05	–
$f_2(1270)$	$0.27 \pm 0.15\,^{+0.24\ +0.28}_{-0.09\ -0.14}$	1.82 ± 0.05	0.6 ± 0.7
$f_0(1370)$	$9.9 \pm 1.1\,^{+2.4\ +1.4}_{-1.1\ -4.3}$	1.9 ± 0.3	–
$\rho(1450)$	–	0.11 ± 0.04	–
σ_1	–	11.0 ± 0.7	–
σ_2	–	0.54 ± 0.10	–
nonresonant	$0.9 \pm 0.4\,^{+1.0\ +1.7}_{-0.3\ -0.2}$	5.0 ± 1.0	–
$\pi\pi$ S-wave	–	–	11.9 ± 2.6

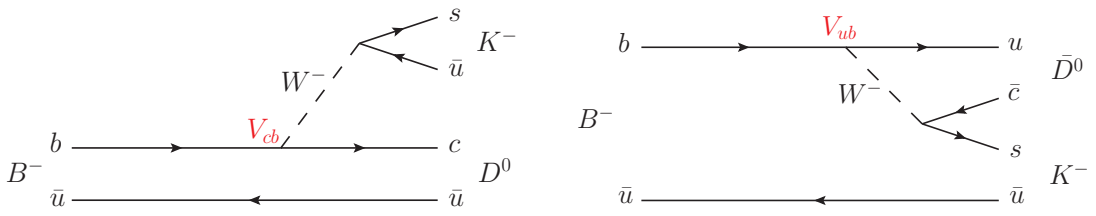

Figure 6.3.: The two tree-level diagrams of the decay $B^\mp \to D\,K^\mp$, the right one being CKM and color suppressed.

6.1.3. Search for CP Violation

In principal, CP violation in $D^0 \to K^0_S \pi^+ \pi^-$ could occur in all three types described in Section 2.2.2. However, the Standard Model expectations are, like for any CP violating effects in the charm sector, very small [76], in the order of $\mathcal{O}(10^{-6})$ for time-integrated ones with the dominant contribution due to K^0-$\bar{K}^0$ mixing [77]. Contrary, the current experimental sensitivity is much worse, in the order of $\mathcal{O}(10^{-2})$ [78]. So an observation of a CP asymmetry would be a strong hint for physics beyond the Standard Model.

Like for the measurement of D^0-$\bar{D}^0$ mixing, the production flavor can be tagged by the charge of the pion in $D^*(2010)^+ \to D^0 \pi^+$ to search for CP violation. Time-integrated CP asymmetries would show up as deviations in the structure of the D^0 and $\bar{D}^0$ Dalitz plots.

The CLEO collaboration performed a dedicated search for time-integrated CP violation in the Dalitz fit [78] which is specified in Section 6.6.3. Belle [74], and BABAR [66] allowed for CP violation in their measurements of the D^0-$\bar{D}^0$ mixing parameters. Up to now no hints for any CP violating effects in $D^0 \to K^0_S \pi^+ \pi^-$, like in the charm sector at all, could be found [75]. A CDF search for CP violation in $D^0 \to K^0_S \pi^+ \pi^-$ is presented in Sections 6.6.3 and 6.9.

6.1.4. Determination of CKM angle γ

Another application of the decay $D^0 \to K^0_S \pi^+ \pi^-$ is the determination of the CKM angle γ defined in Section 2.2.1. For that purpose, the D^0 is reconstructed in $B^\mp \to D\,K^\mp$, where D corresponds to either D^0 or $\bar{D}^0$, as illustrated in Figure 6.3. Since D^0 and $\bar{D}^0$ decay to the same final state, the two sketched decay amplitudes interfere. The participation of the CKM matrix elements V_{ub} and V_{cb} then leads to the opportunity to measure γ by comparing the $D^0 \to K^0_S \pi^+ \pi^-$ Dalitz plots originating from $B^+ \to D\,K^+$ and $B^- \to D\,K^-$

This method was proposed in Reference [79] and applied by the Belle [65], and BABAR [80] experiments. A complication for a possible CDF measurement is the necessity of the kaon identification in $B^\mp \to D\,K^\mp$ because the decay $B^\mp \to D\,\pi^\mp$ is

more frequent and hard to distinguish in the mass distribution. The determination of the CKM angle γ is not done in the analysis described in this work.

6.2. Data Set and Reconstruction

The analysis is performed on a data set collected between February 2002 and February 2010 corresponding to an integrated luminosity of $6.0\,\mathrm{fb}^{-1}$. The data were accumulated using the displaced two track vertex trigger (see Section 3.2.5 and Table 5.3).

The offline reconstruction of candidates starts with refitting tracks using pion mass hypothesis to properly take into account differences in the multiple scattering and ionization energy loss. In the second step, two oppositely charged tracks are combined to form a K^0_S candidate. To construct D^0 candidates each K^0_S candidate is then combined with all possible oppositely charged track pairs taken from the remaining tracks in the event. Finally, the $D^*(2010)^+$ candidates are obtained by combining each D^0 candidate with one of the still remaining tracks in the event. The tracks forming the K^0_S, D^0, and $D^*(2010)^+$ candidates are respectively subjected to kinematic fits that constrain them to originate from common vertices. In each step of the reconstruction, standard quality requirements on tracks and vertices are used to ensure well-measured masses and decay-positions.

6.3. Candidate Selection

The decay chain $D^*(2010)^+ \to D^0\,\pi^+$ with $D^0 \to K^0_S\,\pi^+\,\pi^-$ and $K^0_S \to \pi^+\,\pi^-$ is considered. For simplification, $D^*(2010)^+$ is abbreviated as D^{*+} in the following. For the selection of the D^{*+} candidates some quality requirements are imposed first to suppress the most obvious background. For the remaining candidates a neural network is used to distinguish signal from background.

Since we use only data for the neural network training, we randomly split the sample into two parts (even and odd event numbers) and train two networks. Each of them is then applied to the complementary subsample in order to maintain a selection which is trained on a sample independent from the one to which it is applied. This approach avoids a bias of the selection originating from statistical fluctuations possibly learnt by the network. All figures in this section concerning the network trainings are for the case of even-numbered events. The corresponding figures for odd-numbered events look qualitatively identical and are shown in Appendix B.

The neural networks are constructed with the NeuroBayes package and trained, only using data, by means of the ${}_s\mathcal{P}lot$ technique. The approach is further described in Section 4.2.4.

Precuts

The precuts shown in Table 6.2 are performed before the training of the neural networks to throw away candidates which are most likely background.

Table 6.2.: D^{*+} precuts.

COT Stereo Hits (all tracks)	$\geqq 10$
COT Axial Hits (all tracks)	$\geqq 10$
p_T (all tracks)	$> 0.4\,\mathrm{GeV}/c$
$p_T(D^{*+})$	$> 5.0\,\mathrm{GeV}/c$
$d_0/\sigma_{d_0}(\pi_{D^{*+}})$	< 15
$L_{xy}/\sigma_{L_{xy}}(D^0)$	> 1
$\chi^2(D^{*+})$	< 100
$\chi^2(D^0)$	< 100
$\chi^2(K^0_S)$	< 50

The requirements on the COT hits and the transverse momenta of the pion candidates are track quality requirements, whereas the χ^2 values are quality criteria for the different vertex fits.

Since the D^0 decays weakly and therefore possesses a relatively long mean lifetime of $\tau = (410.1 \pm 1.5) \cdot 10^{-15}\,\mathrm{s}$, a requirement is applied on the displacement of the associated secondary vertex, projected onto the D^0 transverse momentum direction, to the beam, divided by its uncertainty, $L_{xy}/\sigma_{L_{xy}}$.

The resulting D^0 invariant mass and D^{*+} mass difference $\Delta M = M(D^{*+}) - M(D^0)$ distributions are shown in Figures 6.4 and 6.5, respectively. In the ΔM definition, $M(D^{*+})$ and $M(D^0)$ correspond to the reconstructed masses of the D^{*+} and D^0 candidates. The mass difference is used rather than the pure invariant masses of the D^{*+} candidates in order to improve the resolution which is limited by detector effects. The D^0 mass window requirement shown in Figure 6.4 is applied for the creation of the $\Delta M(D^{*+})$ distribution in Figure 6.5, and vice versa.

Neural Network

The D^{*+} network training is based on the mass difference distribution after application of the precuts in the range $140 < \Delta M < 156\,\mathrm{MeV}/c^2$ shown in Figure 6.6. A fit with a Breit-Wigner convoluted with a Gaussian for the signal and a third-order polynomial for the background function defines the PDFs used to calculate the ${}_s\mathcal{P}lot$ weights.

The network uses five input quantities. Ordered by their importance, these are the transverse decay length of the D^0 candidate divided by its uncertainty $L_{xy}/\sigma_{L_{xy}}(D^0)$, the quality of the kinematic fit of the D^{*+} candidate $\chi^2(D^{*+})$, the impact parameter of the pion from the D^{*+} decay divided by its uncertainty $d_0/\sigma_{d_0}(\pi_{D^{*+}})$, the transverse momentum of the pion from the D^{*+} decay, and the reconstructed mass of the K^0_S candidate.

Figure 6.7 shows the correlation matrix of the input variables of the network

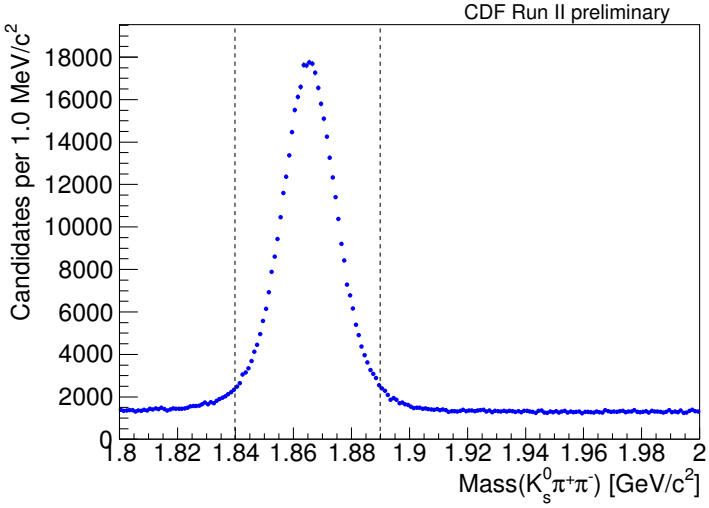

Figure 6.4.: Distribution of the D^0 mass after precuts. The window $1839.83 < M(D^0) < 1889.83\,\mathrm{MeV}/c^2$, indicated by the dashed vertical lines, is applied for the creation of the $\Delta M(D^{*+})$ distribution in Figure 6.5.

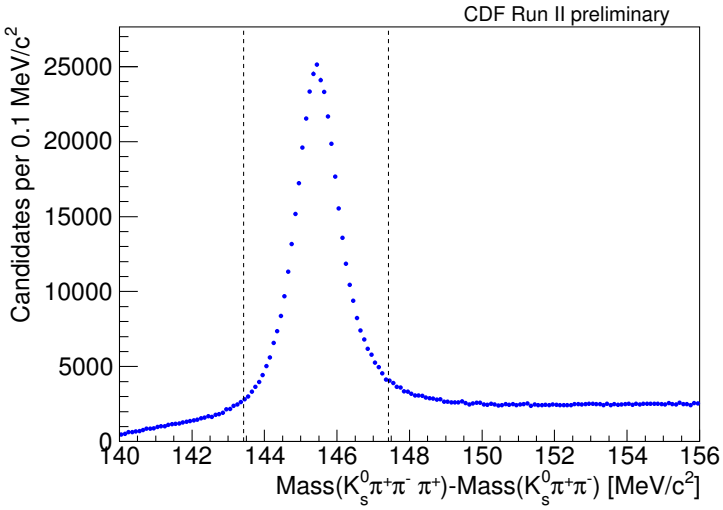

Figure 6.5.: Distribution of the mass difference $M(D^{*+}) - M(D^0)$ after precuts. The window $143.421 < \Delta M(D^{*+}) < 147.421\,\mathrm{MeV}/c^2$, indicated by the dashed vertical lines, is applied for the creation of the D^0 mass distribution in Figure 6.4.

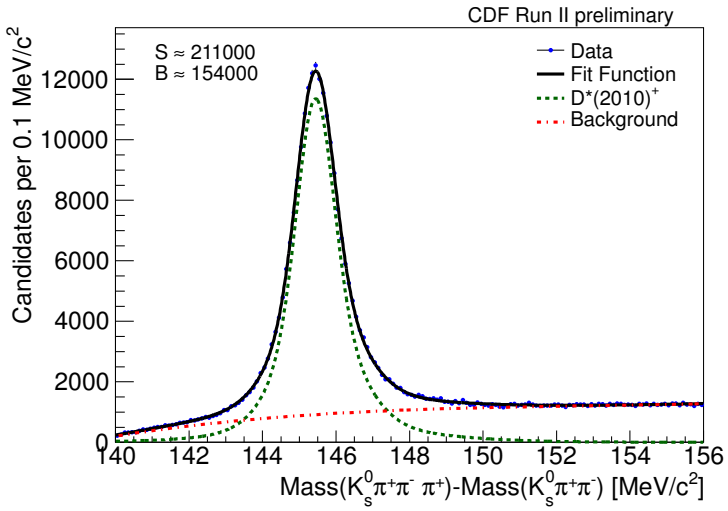

Figure 6.6.: $\Delta M(D^{*+})$ distribution of the even-numbered D^{*+} candidates after application of the precuts in table 6.2. All candidates used to fill this histogram are fed to the network as training pattern. The corresponding ${}_s\mathcal{P}lot$ weights are calculated by means of the fitted signal and background functions.

before decorrelation. There are no large correlations among the different quantities.

In Figure 6.8 separate distributions of the input variables, produced during the individual preprocessing, are shown. The black data points in the histograms represent the bin-by-bin signal fraction of the flattened spectra of the training events. Flat means that in every bin is approximately the same amount of signal plus background events. Spline fits (red) are used to avoid learning of statistical fluctuations.

Figure 6.9 shows the usual (not flat) distributions of the different variables of the even-numbered D^{*+} network separately for signal and background candidates. The spectra of the signal candidates are determined by means of sideband subtractions according to the signal region $143.5 < \Delta M < 147.5\,\mathrm{MeV}/c^2$ and the sidebands $140 < \Delta M < 142\,\mathrm{MeV}/c^2$, $150 < \Delta M < 152\,\mathrm{MeV}/c^2$. For the creation of the background distributions the sidebands are used.

In order to choose a value for a cut on the network output one needs to decide for an appropriate figure of merit. Here, the threshold on the output of the D^{*+} neural network is chosen to maximize $S/\sqrt{S+B}$, where S is the number of signal D^0 events and B is the number of background events in the range $1839.83 < M(K^0_S\pi^+\pi^-) < 1889.83\,\mathrm{MeV}/c^2$ after requiring $143.421 < \Delta M(D^{*+}) < 147.421\,\mathrm{MeV}/c^2$. The S and B yields are derived from a fit to the D^0 mass distribution which uses the weighted sum of two Gaussian functions for the signal and a second-order polynomial for the background and covers the range $1.8 <$

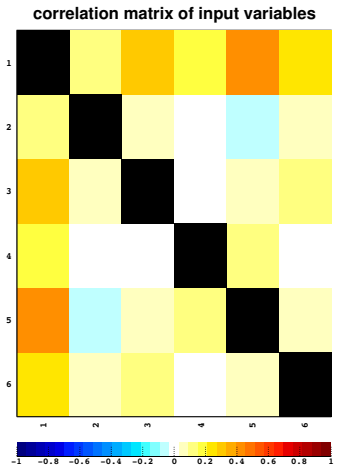

1 target
2 $L_{xy}/\sigma_{L_{xy}}(D^0)$
3 $\chi^2(D^{*+})$
4 $d_0/\sigma_{d_0}(\pi_{D^{*+}})$
5 $p_T(\pi_{D^{*+}})$
6 $m(K^0_S)$

Figure 6.7.: Correlation matrix of the D^{*+} network training with even-numbered events.

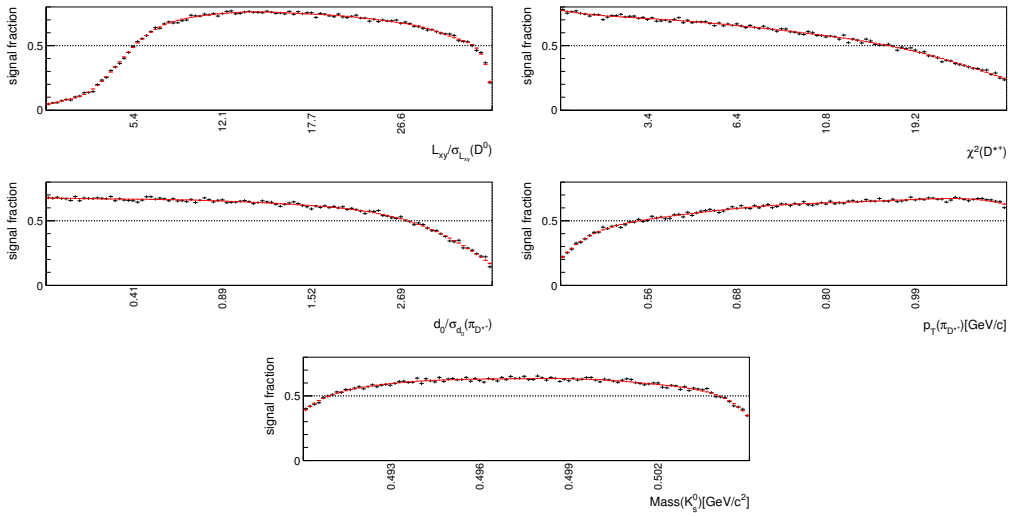

Figure 6.8.: Spline fits to the flat signal fraction distributions of the different input variables of the D^{*+} network training with even-numbered events.

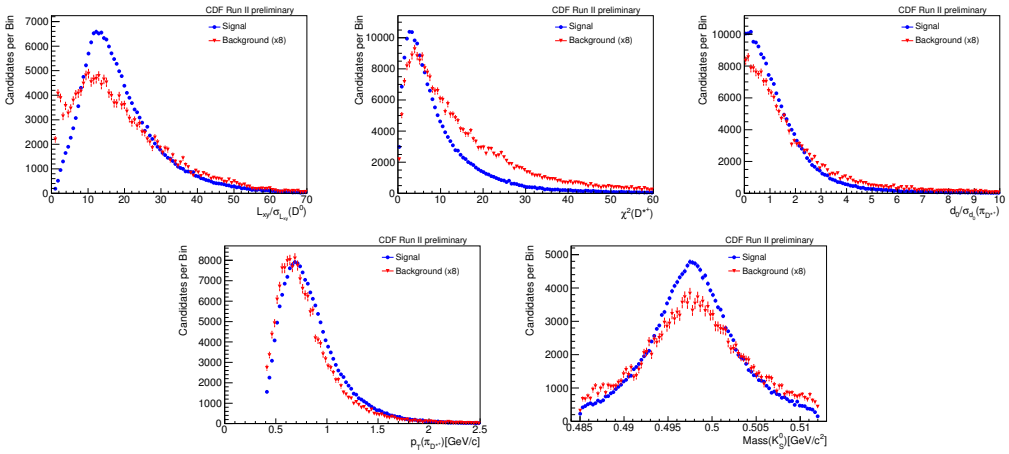

Figure 6.9.: Distributions of the different variables of the even-numbered D^{*+} network separately for signal and background candidates.

$M(K^0_S\pi^+\pi^-) < 2.0\,\mathrm{GeV}/c^2$. Figure 6.10 shows the values of $\mathrm{S}/\sqrt{\mathrm{S}+\mathrm{B}}$ in dependance on the cut on the network output variable for the combination of even- and odd-numbered events. The resulting neural network output requirement of $NN(D^{*+}) > -0.5$ corresponds to an *a posteriori* signal probability of the neural networks greater than 25%.

It happens that multiple D^{*+} candidates are reconstructed for a single D^0 candidate. Since this is unwanted for the studies of the $D^0 \to K^0_S \pi^+ \pi^-$ resonance structure, a best candidate selection is applied after imposing the network requirement. It is based upon the D^{*+} network by choosing the D^{*+} candidate with the highest network output out of all D^{*+} candidates reconstructed from the same D^0 candidate. In 89% of the cases there is only a single candidate.

The $M(D^0)$ and $\Delta M(D^{*+})$ distributions of the selected candidates are shown in Figures 6.11 and 6.12, respectively. Compared to the distributions after the precuts, shown in Figures 6.4 and 6.5, the network selection reduces the background in the signal windows from about 73000 to 38000 candidates, while retaining 352000 of 383000 signal candidates.

For the study of the resonant substructure of the decay $D^0 \to K^0_S \pi^+ \pi^-$, described in the following Sections, the two signal windows $1839.83 < M(D^0) < 1889.83\,\mathrm{MeV}/c^2$ and $143.421 < \Delta M(D^{*+}) < 147.421\,\mathrm{MeV}/c^2$, shown in Figures 6.11 and 6.12, are applied in conjunction.

The K^0_S mass distribution after the selection requirements can be found in Figure 6.13. The Podolanski-Armenteros plot [81] shown in Figure 6.14 demonstrates that there is no significant contamination from $\Lambda \to p\,\pi^-$ in the $K^0_S \to \pi^+\pi^-$ signal.

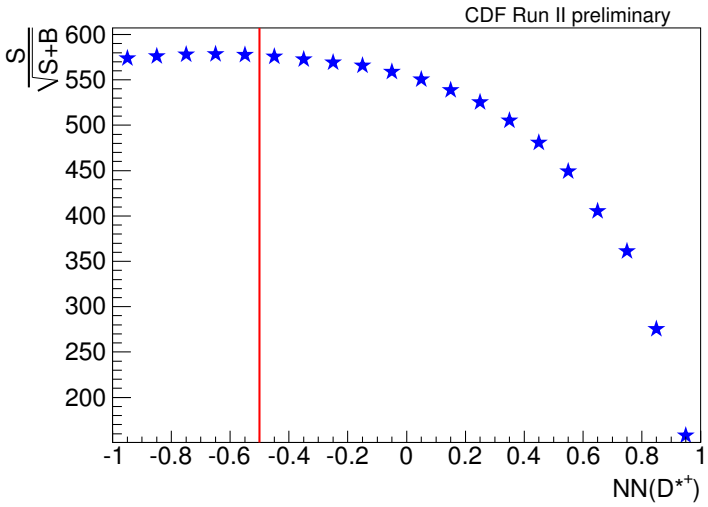

Figure 6.10.: $S/\sqrt{S+B}$ in dependance on the cut on the output variable of the D^{*+} network.

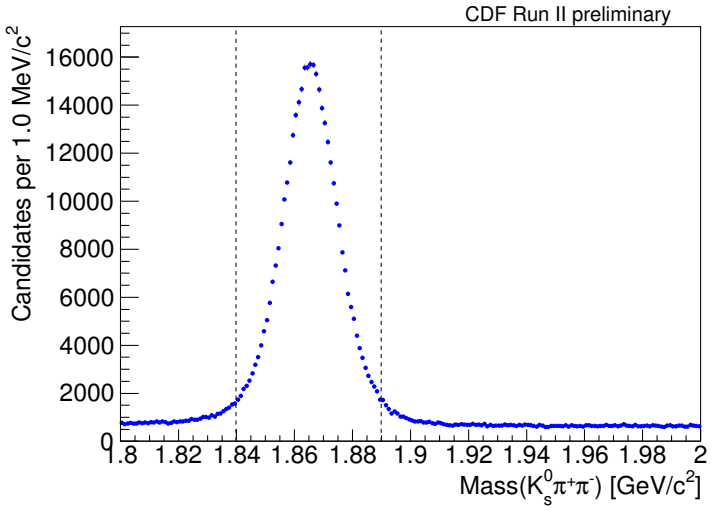

Figure 6.11.: Distribution of the D^0 mass after all selection cuts. The signal window $1839.83 < M(D^0) < 1889.83\,\mathrm{MeV}/c^2$, indicated by the dashed vertical lines, is applied for the creation of the $\Delta M(D^{*+})$ distribution in Figure 6.12.

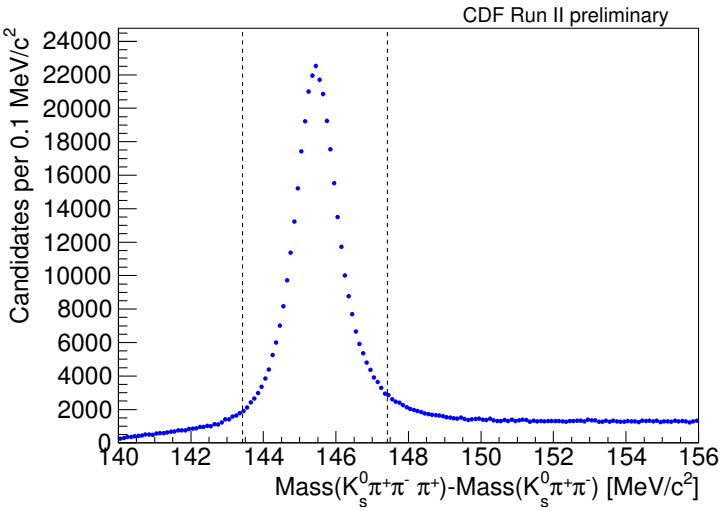

Figure 6.12.: Distribution of the mass difference $M(D^{*+}) - M(D^0)$ after all selection cuts. The signal window $143.421 < \Delta M(D^{*+}) < 147.421\,\mathrm{MeV}/c^2$, indicated by the dashed vertical lines, is applied for the creation of the D^0 mass distribution in Figure 6.11.

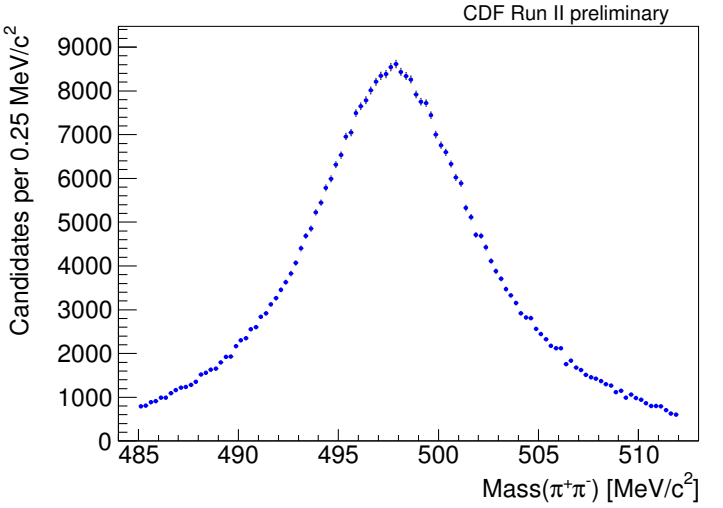

Figure 6.13.: K^0_S mass distribution after application of all selection requirements.

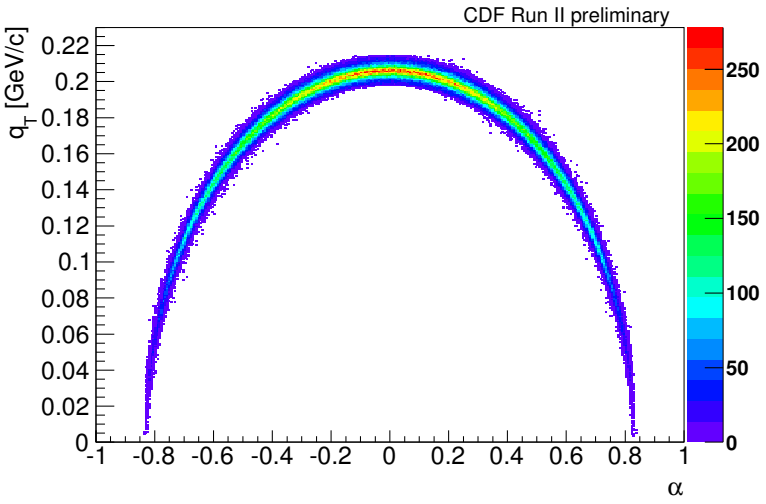

Figure 6.14.: Podolanski-Armenteros plot of the selected $K^0_S \to \pi^+\pi^-$ candidates. No significant contribution from $\Lambda \to p\,\pi^-$ contribution is evident.

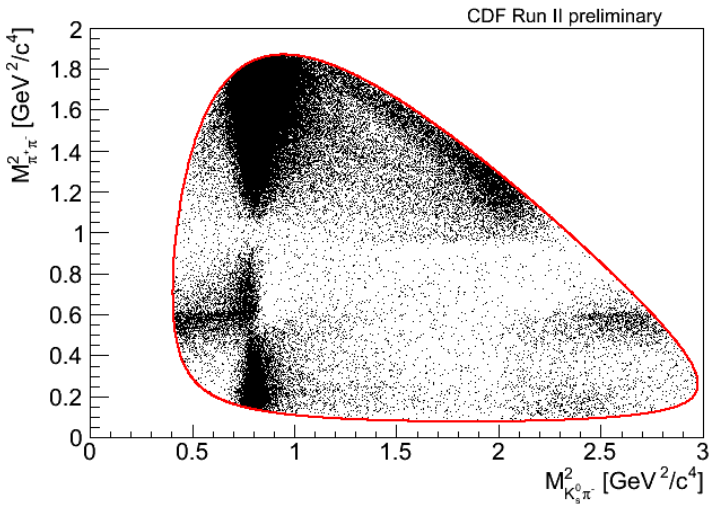

Figure 6.15.: Dalitz plot of the decay $D^0 \to K^0_S \pi^+ \pi^-$, where the squared invariant masses of the two-body combinations $K^0_S\pi^-$ and $\pi^+\pi^-$ are chosen as kinematic quantities. The red line indicates the kinematic boundaries.

6.4. $D^0 \to K^0_S \pi^+ \pi^-$ Dalitz Plot

The resonant substructure of a three-body decay, $D^0 \to K^0_S \pi^+ \pi^-$ in the analysis at hand, can be described with the Dalitz plot method [82]. It is based upon the kinematic relation

$$m^2_{D^0} + m^2_{K^0_S} + m^2_{\pi^+} + m^2_{\pi^-} = M^2_{K^0_S\pi^+} + M^2_{K^0_S\pi^-} + M^2_{\pi^+\pi^-} \tag{6.2}$$

between the squared invariant masses of the involved particles and the two-body combinations of the three decay particles. With the knowledge of the involved particle masses all the information about the resonant substructure is contained in two of the two-body combinations, as the third one can be calculated from them. This information can be visualized by a two-dimensional scatter plot of any two of the three two-body combinations, hence there exist three different such Dalitz plots with the same information.

In Figure 6.15 the Dalitz plot for the considered decay $D^0 \to K^0_S \pi^+ \pi^-$ is shown, where the included candidates are selected according to the requirements described in Section 6.3. The two chosen two-body combinations are $K^0_S\pi^-$ and $\pi^+\pi^-$, the mass-squared distributions of which are plotted on the x- and on the y-axis, respectively. Thereby, the $K^0_S\pi^-$ combination refers to the D^0 decays detected by a positive charge of the slow pion in $D^{*+} \to D^0 \pi^+$. This is the combination for the Cabibbo allowed intermediate resonances including the K^0_S, like $K^*(892)^- \to K^0_S \pi^-$. The $\bar{D}^0$ decays from $D^{*-} \to \bar{D}^0 \pi^-$ are also included in the

Dalitz plot shown in Figure 6.15. There, the $K^0_S\pi^+$ combination is the analog to the $K^0_S\pi^-$ combination in D^0 decays, and for simplification the notation $K^0_S\pi^-$ is used for the collective Cabibbo allowed combinations of both D^0 and $\bar{D}^0$ decays. This notation is maintained in the following, wherever D^0 and $\bar{D}^0$ decays are used together.

The red line corresponds to the kinematic boundaries of the decay, calculated as

$$\begin{aligned}
\left(M^2_{K^0_S\pi^-}\right)_{\min} &= (m_{K^0_S} + m_{\pi^+})^2\,, \\
\left(M^2_{K^0_S\pi^-}\right)_{\max} &= (m_{D^0} - m_{\pi^-})^2\,, \\
\left(M^2_{\pi^+\pi^-}\right)_{\min}\left(M^2_{K^0_S\pi^-}\right) &= (E^*_{\pi^+} + E^*_{\pi^-})^2 - \left(\sqrt{E^{*2}_{\pi^+} - m^2_{\pi^+}} + \sqrt{E^{*2}_{\pi^-} - m^2_{\pi^-}}\right)^2\,, \\
\left(M^2_{\pi^+\pi^-}\right)_{\max}\left(M^2_{K^0_S\pi^-}\right) &= (E^*_{\pi^+} + E^*_{\pi^-})^2 - \left(\sqrt{E^{*2}_{\pi^+} - m^2_{\pi^+}} - \sqrt{E^{*2}_{\pi^-} - m^2_{\pi^-}}\right)^2\,, \\
E^*_{\pi^+}\left(M^2_{K^0_S\pi^-}\right) &= \frac{M^2_{K^0_S\pi^-} - m^2_{K^0_S} + m^2_{\pi^+}}{2M_{K^0_S\pi^-}}\,, \\
E^*_{\pi^-}\left(M^2_{K^0_S\pi^-}\right) &= \frac{m^2_{D^0} - M^2_{K^0_S\pi^-} - m^2_{\pi^-}}{2M_{K^0_S\pi^-}}\,.
\end{aligned} \tag{6.3}$$

where $E^*_{\pi^+}$ and $E^*_{\pi^-}$ are the energies of the two pions in the $M_{K^0_S\pi^-}$ rest frame. Since these relations only hold for a fixed D^0 mass value without detector resolution, and there is no mass constraint in the reconstruction, it can happen that candidates are found outside this kinematic region. However, these candidates are thrown away to avoid problems with the Dalitz fit described in Section6.6, as already done for Figure 6.15.

Although in the following only the Dalitz plot of Figure 6.15 is used to perform a fit and search for CP violation, another Dalitz plot, where $M^2_{\pi^+\pi^-}$ on the y-axis is replaced by $M^2_{K^0_S\pi^+}$, the combination for the doubly Cabibbo suppressed intermediate resonances including the K^0_S, like $K^*(892)^+ \to K^0_S\,\pi^+$, is shown in Figure 6.16 for illustration.

In Figures 6.17–6.19 the mass-squared distributions of the two-body combinations $M^2_{K^0_S\pi^-}$, $M^2_{\pi^+\pi^-}$, and $M^2_{K^0_S\pi^+}$, corresponding to the projections on the different dimensions of the Dalitz plots, are shown. Projection means the integration over the perpendicular axis. Therefore, the projection on the x-axis is the integral over the y-axis and vice versa. According to Equation 6.2, the mass-squared distribution of the third two-body combination $M^2_{K^0_S\pi^+}$ can be identified as diagonal in the Dalitz plot of Figure 6.15. Thereby, it starts in the upper right corner of the Dalitz plot and goes up to the lower left corner. So the projection is the integral over the perpendicular diagonal.

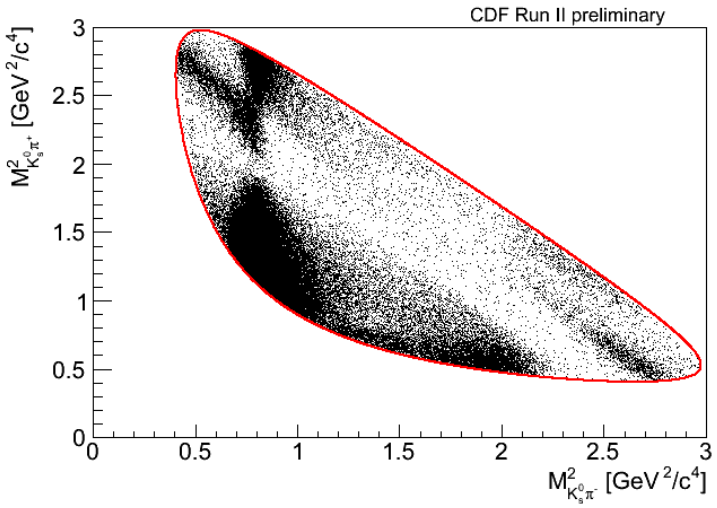

Figure 6.16.: Dalitz plot of the decay $D^0 \to K^0_S \pi^+ \pi^-$, where the squared invariant masses of the two-body combinations $K^0_S\pi^-$ and $K^0_S\pi^+$ are chosen as kinematic quantities. The red line indicates the kinematic boundaries.

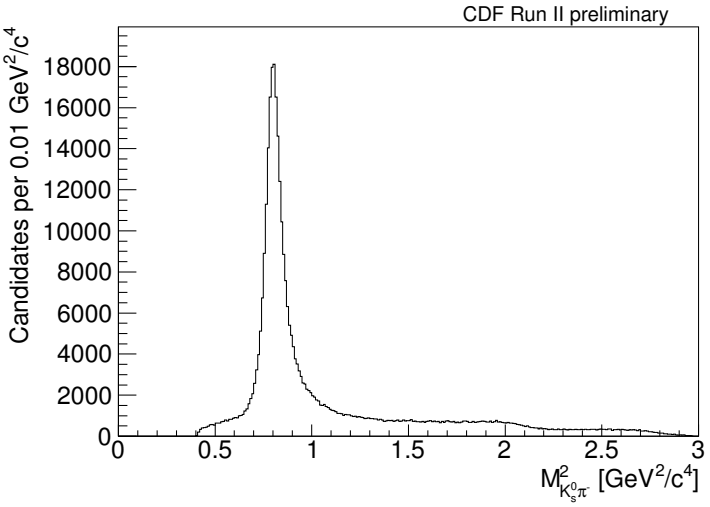

Figure 6.17.: Squared invariant mass distribution of the two-body combination $M^2_{K^0_S\pi^-}$. This corresponds to the projection on the x-axis of the Dalitz plot shown in Figure 6.15.

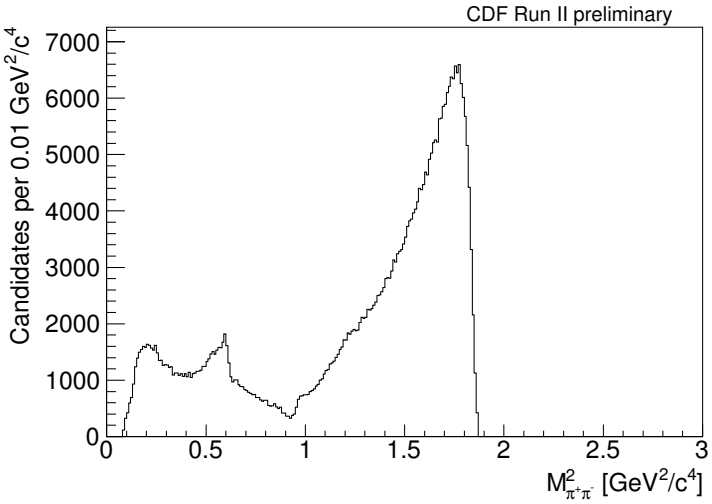

Figure 6.18.: Squared invariant mass distribution of the two-body combination $M^2_{\pi^+\pi^-}$. This corresponds to the projection on the y-axis of the Dalitz plot shown in Figure 6.15.

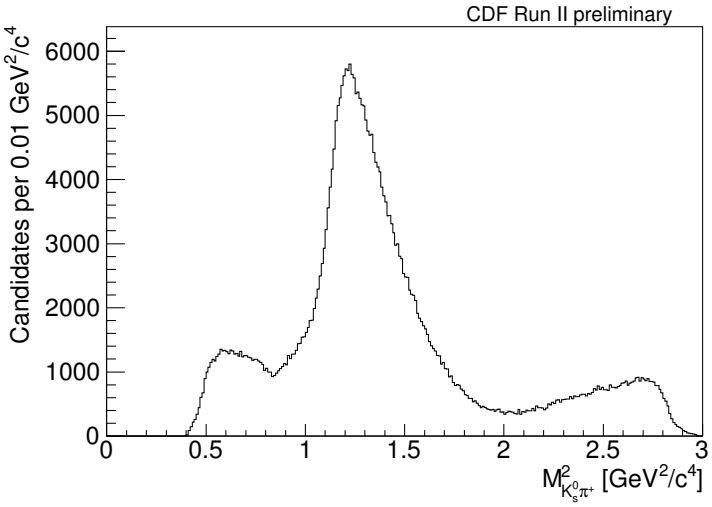

Figure 6.19.: Squared invariant mass distribution of the two-body combination $M^2_{K^0_S\pi^+}$. This corresponds to the projection on the diagonal of the Dalitz plot shown in Figure 6.15.

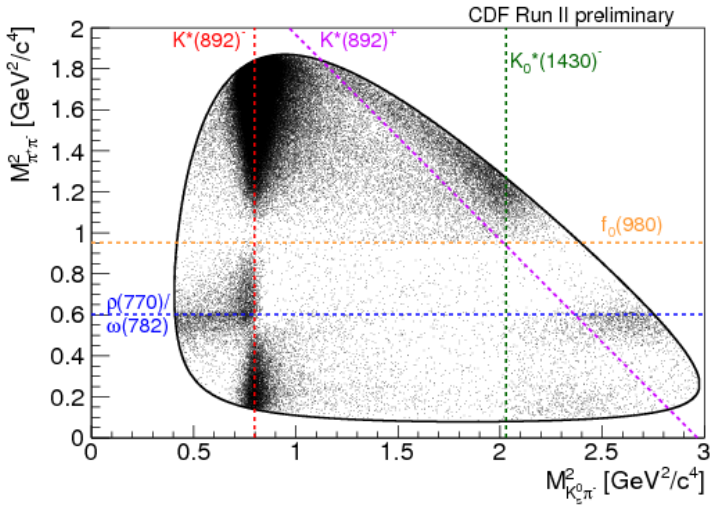

Figure 6.20.: Dalitz plot of the decay $D^0 \to K^0_S \pi^+ \pi^-$, where some selected intermediate resonances are indicated by colored dashed lines. The black line indicates the kinematic boundaries.

In order to give an imagination of the various contributions to the resonant substructure of the decay $D^0 \to K^0_S \pi^+ \pi^-$, the locations of some of the occurring intermediate resonances are indicated in Figures 6.20–6.23. The Dalitz plot features a complicated resonance structure with bands of intermediate resonances as well as regions populated or depopulated by constructive or destructive interferences.

The most prominent resonance is the $K^*(892)^-$ that can be seen as strongly populated band in the Dalitz plot and as high peak in the $M^2_{K^0_S\pi^-}$ distribution. The band structure with enhancements at low and high $M^2_{\pi^+\pi^-}$ values and a depopulation at intermediate ones is typical for a vector meson with spin-1 decaying to two scalar mesons via P-wave.

Perpendicular to $K^*(892)^-$ there is another visible band with the same structure originating from the resonance $\rho(770) \to \pi^+ \pi^-$. The closeness to the rarer $\omega(782) \to \pi^+ \pi^-$ leads to an interference that can be seen as steep decrease at the higher side of the corresponding peak in the $M^2_{\pi^+\pi^-}$ distribution of Figure 6.22.

The also indicated resonances $K^*_0(1430)^- \to K^0_S \pi^-$ and $f_0(980) \to \pi^+ \pi^-$ are two examples of occurring scalar mesons with spin-0 decaying via S-wave. Such intermediate resonances feature a continuous band structure.

As already mentioned, the distribution of $M^2_{K^0_S\pi^+}$, shown in Figure 6.19, can be found as diagonal in the Dalitz plot of Figure 6.20, like indicated by the line for its doubly Cabibbo suppressed intermediate resonance $K^*(892)^+$. There is no visible band or peak originating from this contribution. However, it can be identified by its interference with other resonances.

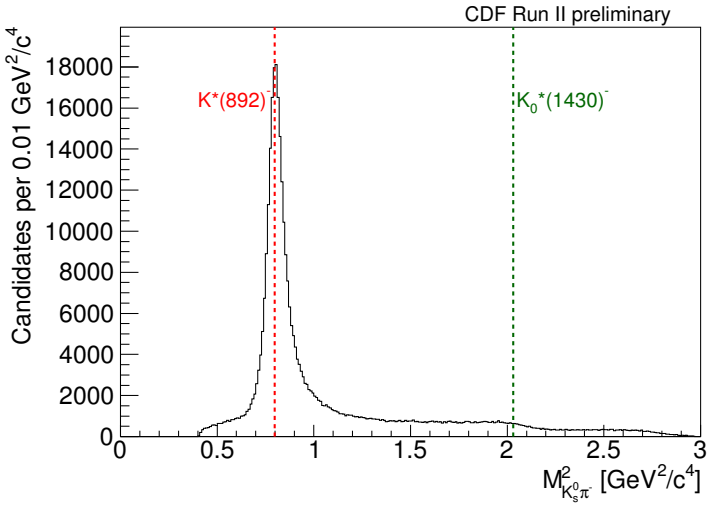

Figure 6.21.: Squared invariant mass distribution of the two-body combination $M^2_{K^0_S\pi^-}$, where the intermediate resonances $K^*(892)^-$ and $K^*_0(1430)^-$ are indicated by colored dashed lines.

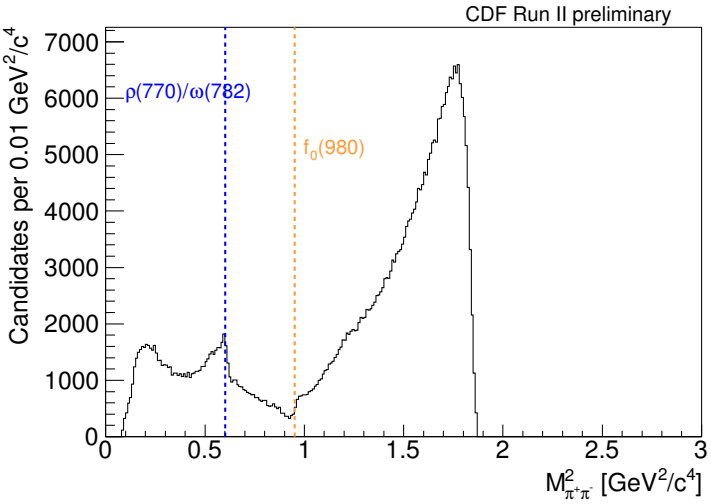

Figure 6.22.: Squared invariant mass distribution of the two-body combination $M^2_{\pi^+\pi^-}$, where the intermediate resonances $\rho(770)/\omega(782)$ and $f_0(980)$ are indicated by colored dashed lines.

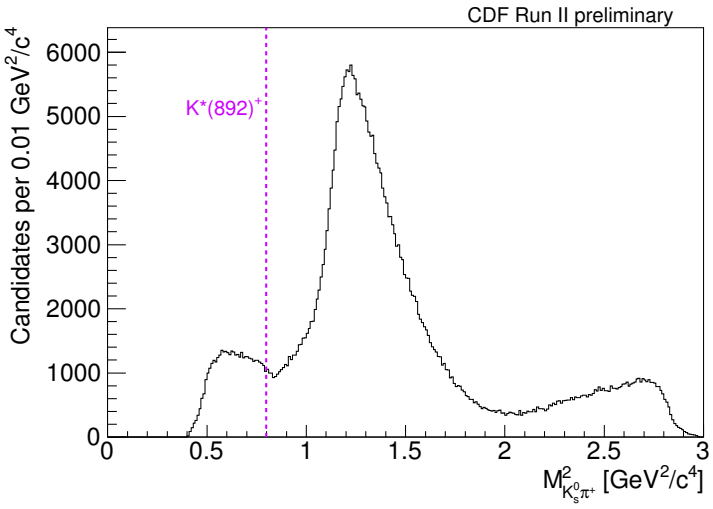

Figure 6.23.: Squared invariant mass distribution of the two-body combination $M^2_{K^0_S\pi^+}$, where the intermediate resonance $K^*(892)^+$ is indicated by the purple dashed line.

6.4.1. Background

The upper D^0 mass sideband $1.92 < M(K^0_S\pi^+\pi-) < 1.95\,\mathrm{GeV}/c^2$ is used to study the behavior of the background in the Dalitz plot. The corresponding distributions, with all other selection requirements resembling the ones for the signal region, are shown in Figures 6.24–6.26. Also shown are the comparisons with the $M^2_{K^0_S\pi^-}$ and $M^2_{\pi^+\pi^-}$ line shapes calculated from a completely flat phase space distribution over the Dalitz plot.

There is a small $K^*(892)^-$ contribution to the background from the D^0 mass sideband. Furthermore, it happens that the two pions in the $K^0_S\pi^+\pi-$ final state originate from a K^0_S, resulting in a narrow peak in the $M^2_{\pi^+\pi^-}$ distribution.

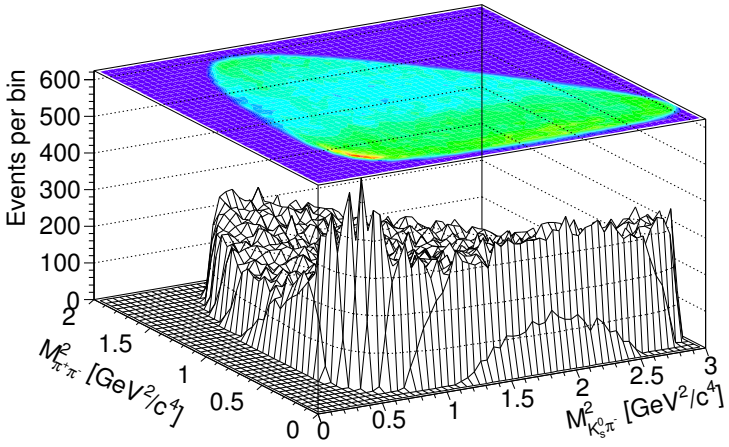

Figure 6.24.: Background in the Dalitz plot of the decay $D^0 \to K^0_S \pi^+ \pi^-$ estimated from the upper D^0 mass sideband $1.92 < M(K^0_S\pi^+\pi-) < 1.95\,\mathrm{GeV}/c^2$.

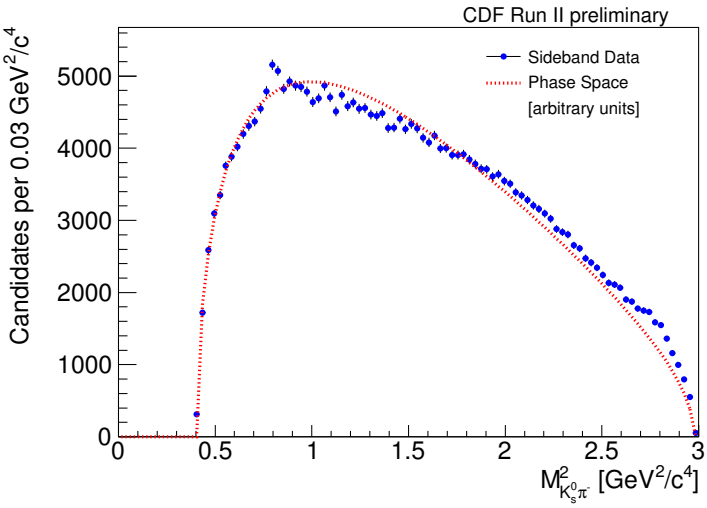

Figure 6.25.: Background in the squared invariant mass distribution of the two-body combination $M^2_{K^0_S\pi^-}$ estimated from the upper D^0 mass sideband $1.92 < M(K^0_S\pi^+\pi-) < 1.95\,\mathrm{GeV}/c^2$. The red dashed curve corresponds to the line shape resulting from a flat phase space distribution.

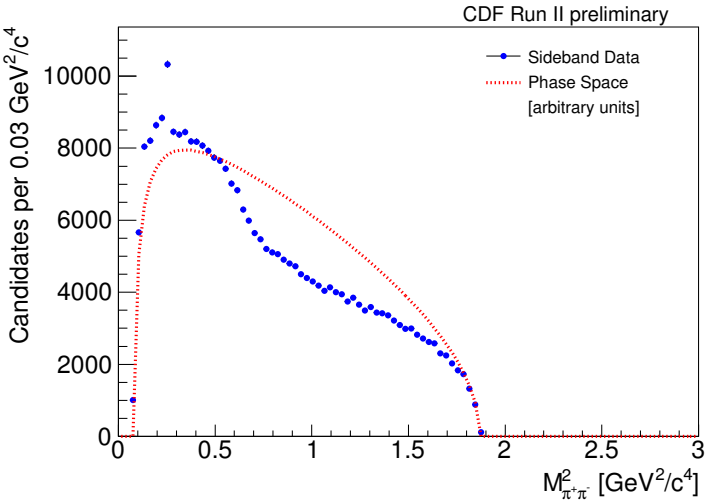

Figure 6.26.: Background in the squared invariant mass distribution of the two-body combination $M^2_{\pi^+\pi^-}$ estimated from the upper D^0 mass sideband $1.92 < M(K^0_S\pi^+\pi-) < 1.95\,\mathrm{GeV}/c^2$. The red dashed curve corresponds to the line shape resulting from a flat phase space distribution.

6.5. Simulated Events

Simulated events are used to estimate the relative reconstruction efficiency over the $D^0 \to K^0_S \pi^+ \pi^-$ Dalitz plot, knowledge on which is necessary to understand the resonant substructure in a quantitative way. For that purpose, a sample of $D(2010)^{*+}$ mesons is generated and then decayed as $D(2010)^{*+} \to D^0 \pi^+$, $D^0 \to K^0_S \pi^+ \pi^-$, $K^0_S \to \pi^+ \pi^-$ by means of the EVTGEN package [53]. Afterwards, the generated events are passed through a full detector simulation before they are reconstructed by the same software used for data. Finally, the selection described in Section 6.3 is also applied to the simulated events.

6.5.1. Relative Reconstruction Efficiency

In order to determine its relative reconstruction efficiency over the Dalitz plot, the decay $D^0 \to K^0_S \pi^+ \pi^-$ is generated without any intermediate resonances. This results in a flat distribution of the Dalitz plot in the borders of the phase space. However, the detector and trigger acceptance, that are simulated afterwards, influence this distribution in a complicated way. In particular the requirements of the two track trigger, which can be found in Table 5.3, lead to a strong variation of the efficiency over the Dalitz plot. The variables used for the final selection described in Section 6.3 are chosen in a way to minimize the impact on the relative efficiency over the Dalitz plot.

The resulting Dalitz plot of the simulated events is shown in Figure 6.27. Despite the completely nonresonant decay, it features a complex distribution. Since this distribution is expected to be uniform for vanishing acceptance effects, it is possible to determine the relative reconstruction efficiency directly by comparing the different regions of the Dalitz plot.

In Figures 6.28–6.30 the corresponding mass-squared distributions of the three two-body combinations $M^2_{K^0_S\pi^-}$, $M^2_{\pi^+\pi^-}$, and $M^2_{K^0_S\pi^+}$ are shown together with the relative bin-by-bin acceptances, defined as the fraction of selected and generated events. For vanishing acceptance variations this quantities would be constant over the allowed phase space.

6.5.2. Efficiency Fit

In order to parametrize the efficiency shape a binned maximum likelihood fit to the two-dimensional Dalitz plot distribution is performed, where a binning of $0.05\,\mathrm{GeV}^2/c^4$ in both dimensions is used.

Because of the complicated form of the distribution it is necessary to use a highly phenomenological function for this task, namely the sum of a ninth-order

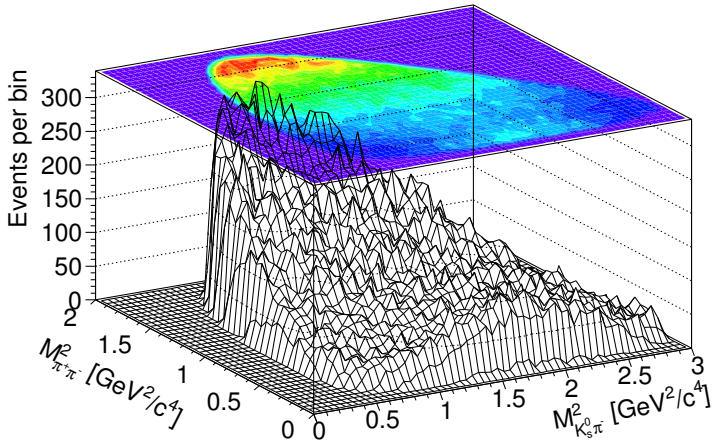

Figure 6.27.: Relative reconstruction efficiency over the $D^0 \to K^0_S \pi^+ \pi^-$ Dalitz plot. Shown are the simulated events after the final selection for a completely nonresonant generation of the decay.

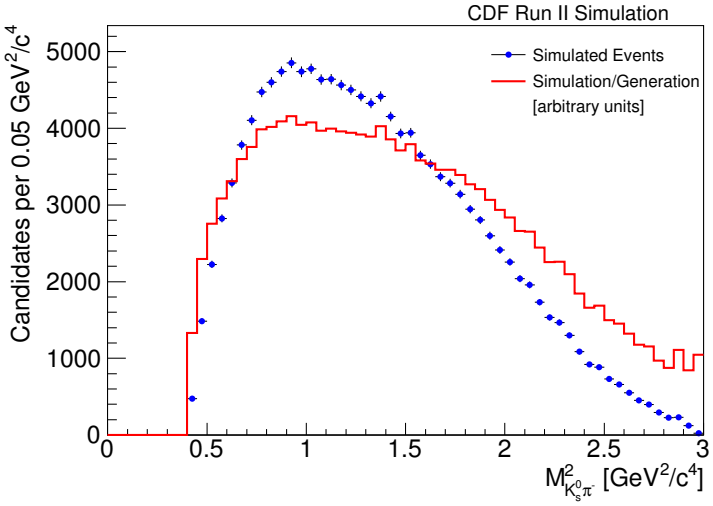

Figure 6.28.: $M^2_{K^0_S\pi^-}$ distribution of the simulated events. The red line shows the relative bin-by-bin acceptance.

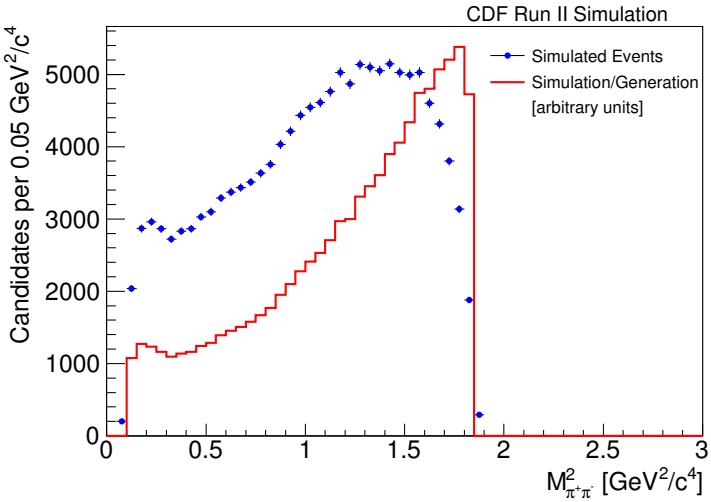

Figure 6.29.: $M^2_{\pi^+\pi^-}$ distribution of the simulated events. The red line shows the relative bin-by-bin acceptance.

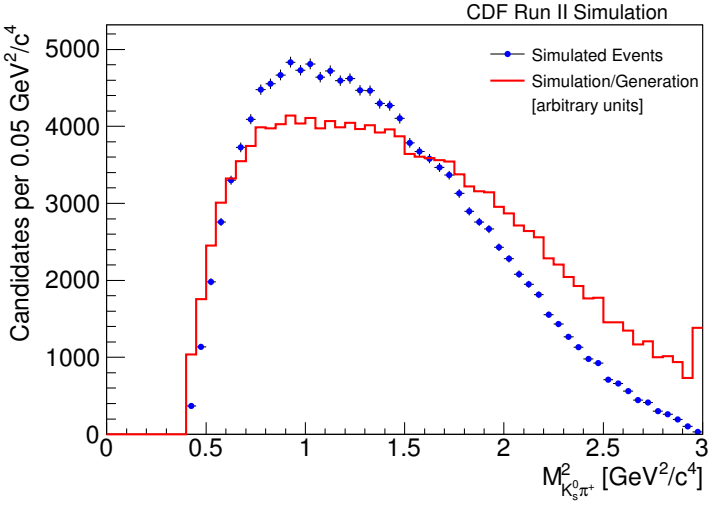

Figure 6.30.: $M^2_{K^0_S\pi^+}$ distribution of the simulated events. The red line shows the relative bin-by-bin acceptance.

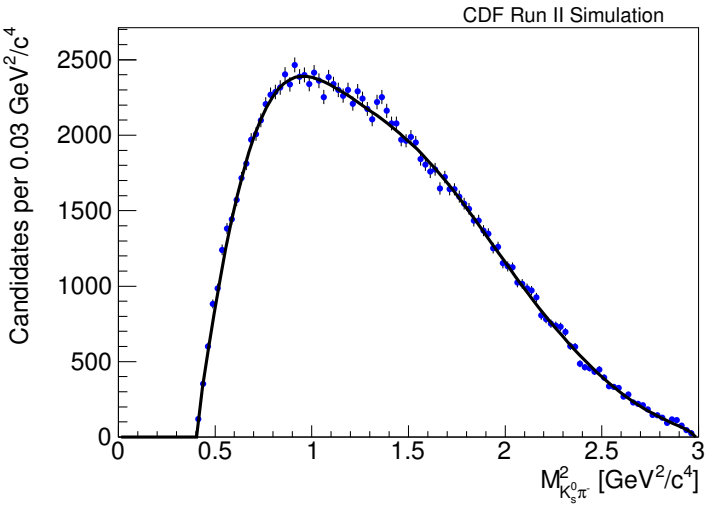

Figure 6.31.: Efficiency fit projection to $M^2_{K^0_S\pi^-}$.

polynomial and a Gaussian function,

$$\begin{aligned}\epsilon = {} & E_0 + E_x \cdot M^2_{K^0_S\pi^-} + E_y \cdot M^2_{\pi^+\pi^-} + E_{x^2} \cdot (M^2_{K^0_S\pi^-})^2 + E_{xy} \cdot M^2_{K^0_S\pi^-} M^2_{\pi^+\pi^-} \\ & + E_{y^2} \cdot (M^2_{\pi^+\pi^-})^2 + E_{x^3} \cdot (M^2_{K^0_S\pi^-})^3 + E_{x^2y} \cdot (M^2_{K^0_S\pi^-})^2 M^2_{\pi^+\pi^-} \\ & + E_{xy^2} \cdot M^2_{K^0_S\pi^-} (M^2_{\pi^+\pi^-})^2 + E_{y^3} \cdot (M^2_{\pi^+\pi^-})^3 + \ldots + G(M^2_{\pi^+\pi^-})\,.\end{aligned} \tag{6.4}$$

For simplification of the notation, the above formula of the polynomial is abbreviated after the third of nine orders. The Gaussian function $G(M^2_{\pi^+\pi^-})$ models the enhancement at low $M^2_{\pi^+\pi^-}$ values.

The fit projections together with the corresponding mass-squared distributions of the three two-body combinations are shown in Figures 6.31–6.33. The χ^2 value of the fit is 1783 with 1214 degrees of freedom. To make sure that the fit function properly describes all two-dimensional correlations, Figures 6.34 and fig:EffDiff show the distributions $M^2_{K^0_S\pi^-} + M^2_{\pi^+\pi^-}$ respective $M^2_{K^0_S\pi^-} - M^2_{\pi^+\pi^-}$, together with the corresponding fit projections.

6.5.3. Dalitz Plot Resolution

The simulated detector resolutions on the Dalitz plot variables $M^2_{K^0_S\pi^-}$, $M^2_{\pi^+\pi^-}$, and $M^2_{K^0_S\pi^-}$ can be found in Figures 6.36–6.36. They are determined as differences between the reconstructed and generated quantities and fitted by the sum of three Gaussian functions. The quoted values for σ are the weighted averages of the the three standard deviations in each case. Thus the resolutions are smaller than the employed quadratic bin widths of $0.025\,\mathrm{GeV}^2/c^4$.

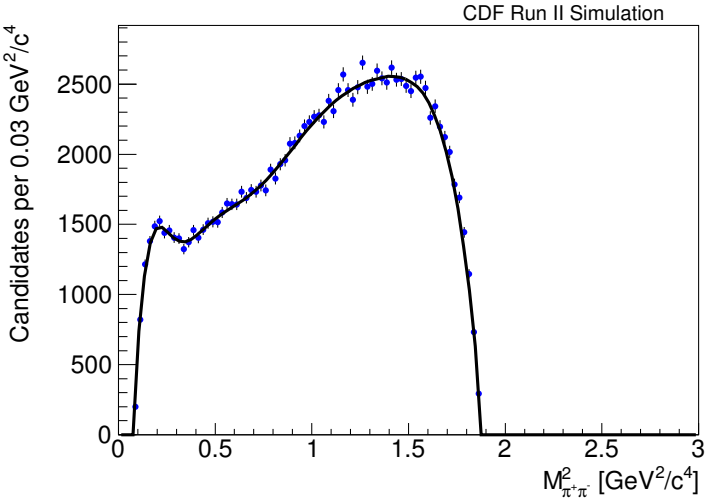

Figure 6.32.: Efficiency fit projection to $M^2_{\pi^+\pi^-}$.

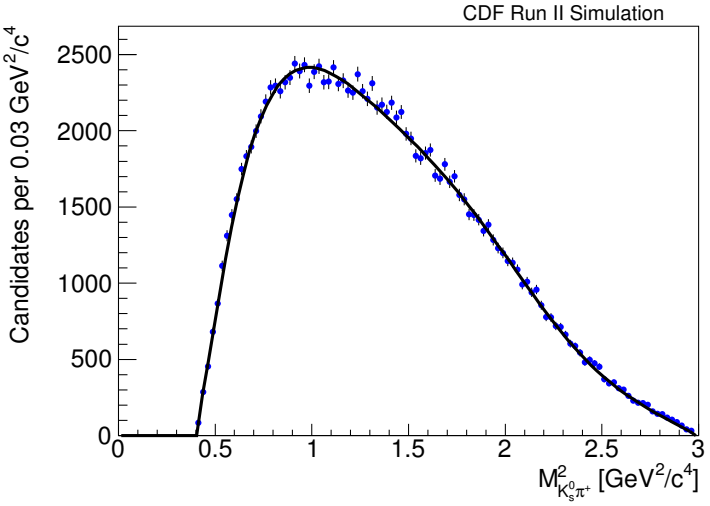

Figure 6.33.: Efficiency fit projection to $M^2_{K^0_S\pi^+}$.

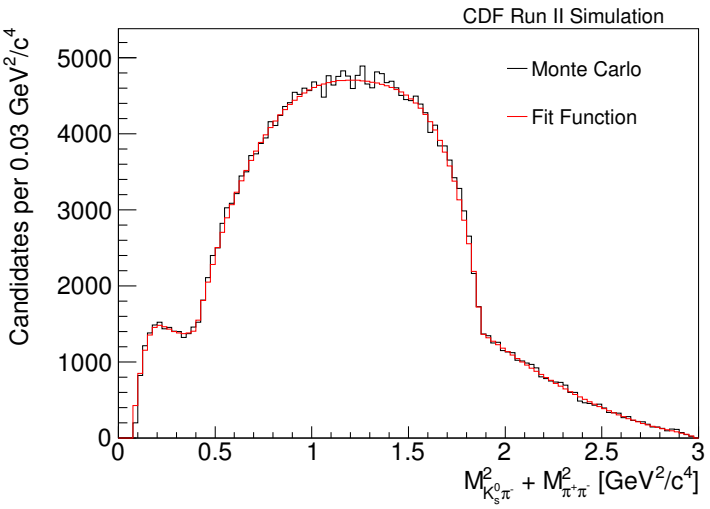

Figure 6.34.: Efficiency fit projection to $M^2_{K^0_S\pi^-} + M^2_{\pi^+\pi^-}$.

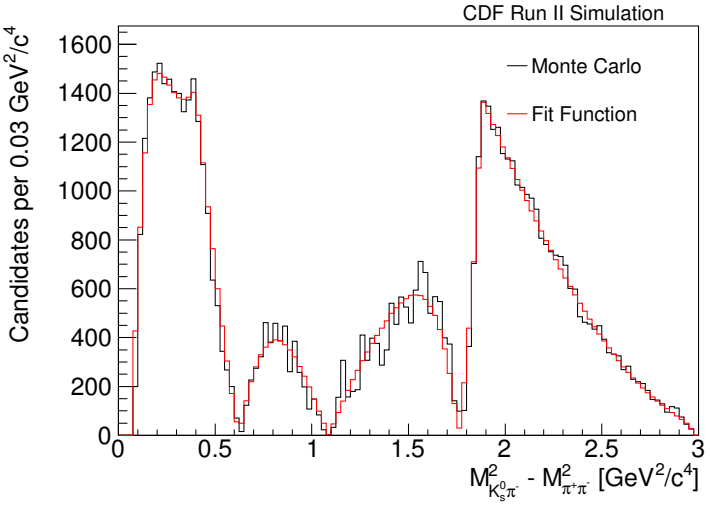

Figure 6.35.: Efficiency fit projection to $M^2_{K^0_S\pi^-} - M^2_{\pi^+\pi^-}$.

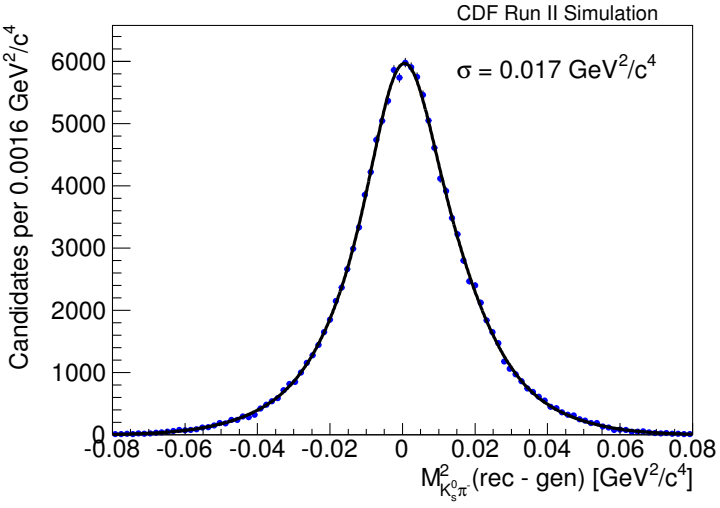

Figure 6.36.: Simulated detector resolution for $M^2_{K^0_S\pi^-}$.

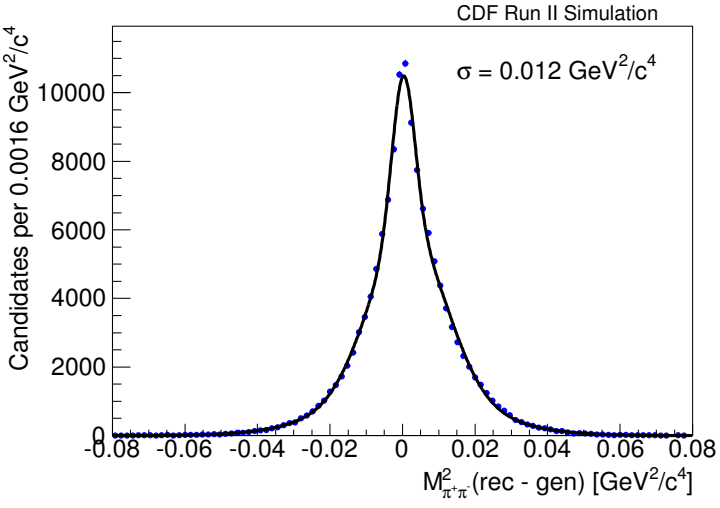

Figure 6.37.: Simulated detector resolution for $M^2_{\pi^+\pi^-}$.

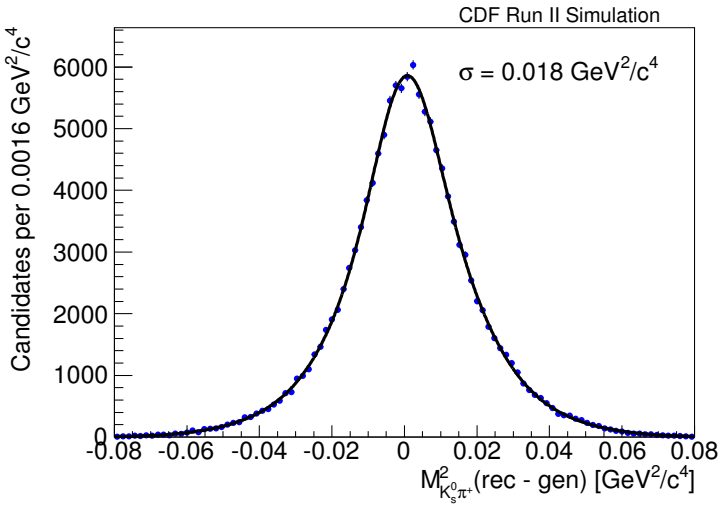

Figure 6.38.: Simulated detector resolution for $M^2_{K^0_S\pi^+}$.

6.5.4. D^{*+} Mass Resolution

The detector resolution on the signal structure in the $M(D^{*+}) - M(D^0)$ distribution, shown in Figure 6.39, is obtained by subtracting the generated mass difference ΔM_{gen} from the reconstructed one ΔM_{rec}. It is useful for the fit to the D^{*+} mass difference spectrum described in Section 6.6.1.

A combination of three Gaussian functions, as given by Equation 5.2, is fitted to the residual distribution. In Table 6.3 the fit results for the different parameters can be found, where μ is the mean and σ the standard deviation of the corresponding Gaussian function, and $\bar{\sigma}$ means the calculated average resolution defined in Equation 5.3.

6.5.5. Charge Asymmetry

A $\pi_{D^{*+}}$ charge asymmetry due to acceptance reasons is equivalent to a D^0-$\bar{D}^0$ asymmetry and thus faking a CP violating effect. This is especially relevant if this asymmetry is dependent on $p_T(\pi_{D^{*+}})$, as such a dependence could affect different regions of the Dalitz plot in a different way.

To give an extreme example for this, the sample of simulated events is divided into two parts by the median $\tilde{p_T}$ of the transverse momentum distribution of the pion from the D^{*+} decay shown in Figure 6.40, and the significance of the bin-by-bin deviations over the Dalitz plot (see Equation 6.22) between the numbers of events with $p_T(\pi_{D^{*+}}) < \tilde{p_T}$ and $p_T(\pi_{D^{*+}}) > \tilde{p_T}$, is shown in Figure 6.41. Since this leads to a significant effect, it is crucial to account for such an asymmetry.

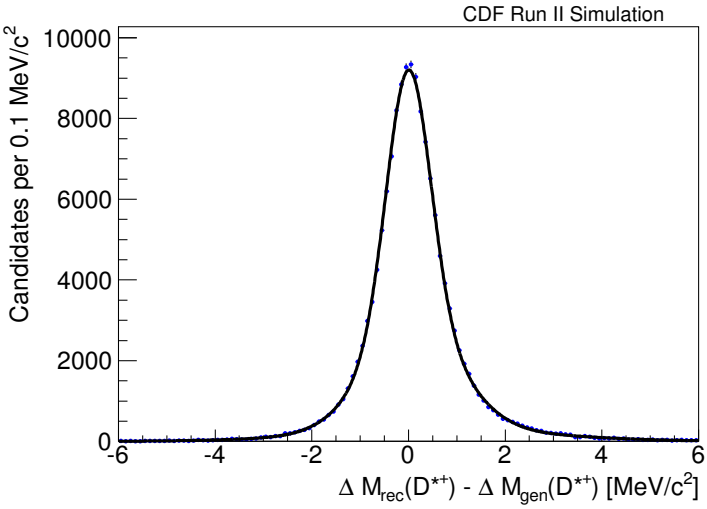

Figure 6.39.: Simulated detector resolution for D^{*+}.

Table 6.3.: Fit results for the parameters of the three Gaussian functions that are fitted to the simulated detector resolution of $M(D^{*+}) - M(D^0)$.

	$M(D^{*+}) - M(D^0)$
frac_1	0.548 ± 0.016
frac_2	0.891 ± 0.006
$\mu_1[\text{MeV}/c^2]$	0
$\sigma_1[\text{MeV}/c^2]$	0.453 ± 0.007
$\mu_2[\text{MeV}/c^2]$	0.087 ± 0.008
$\sigma_2[\text{MeV}/c^2]$	0.955 ± 0.021
$\mu_3[\text{MeV}/c^2]$	0.618 ± 0.031
$\sigma_3[\text{MeV}/c^2]$	2.284 ± 0.044
$\bar{\sigma}[\text{MeV}/c^2]$	0.855 ± 0.016

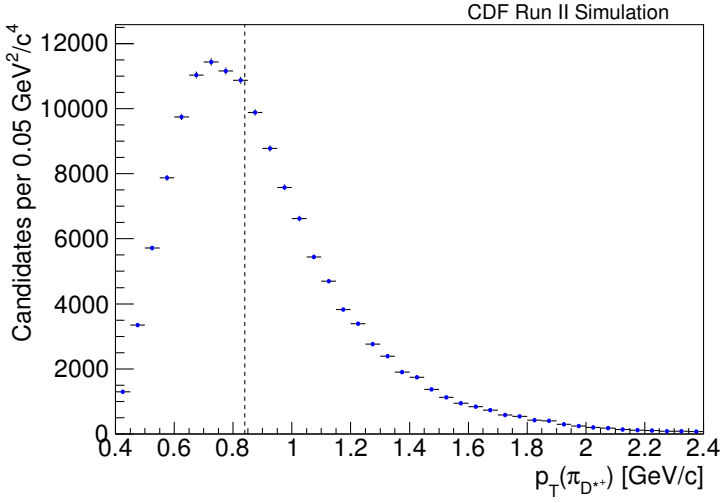

Figure 6.40.: Transverse momentum distribution of the pion from the D^{*+} decay in the sample of simulated events. The median of the distribution is indicated by the vertical dashed line.

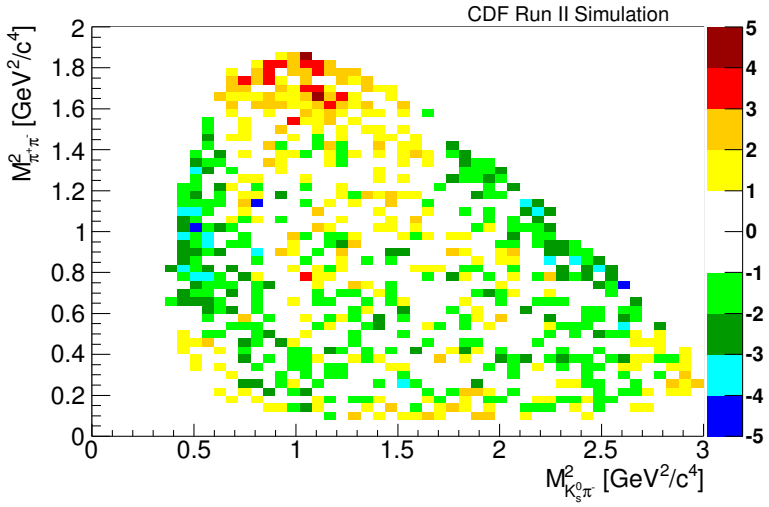

Figure 6.41.: Significance of the bin-by-bin deviations over the Dalitz plot between the numbers of events with $p_T(\pi_{D^{*+}})$ smaller and larger than the median in the sample of simulated events.

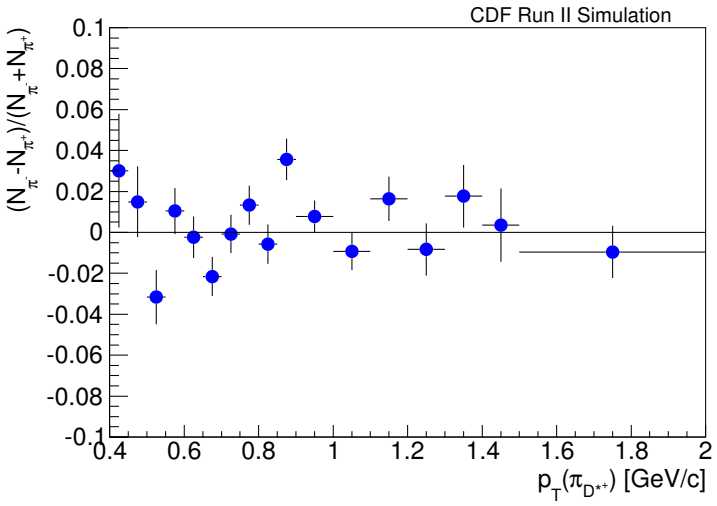

Figure 6.42.: $p_T(\pi_{D^{*+}})$-dependence of the $\pi_{D^{*+}}$ charge asymmetry in the sample of simulated events.

The $p_T(\pi_{D^{*+}})$ dependence of the $\pi_{D^{*+}}$ charge asymmetry

$$\mathcal{A} = \frac{N_{\pi^-} - N_{\pi^+}}{N_{\pi^-} + N_{\pi^+}} \tag{6.5}$$

obtained from the selected simulated events is shown in Figure 6.42. Since no significant asymmetry is apparent, the combination of the D^0 and $\bar{D}^0$ samples can be used for the determination of the efficiency for both individual D^0 and $\bar{D}^0$ Dalitz plots, too.

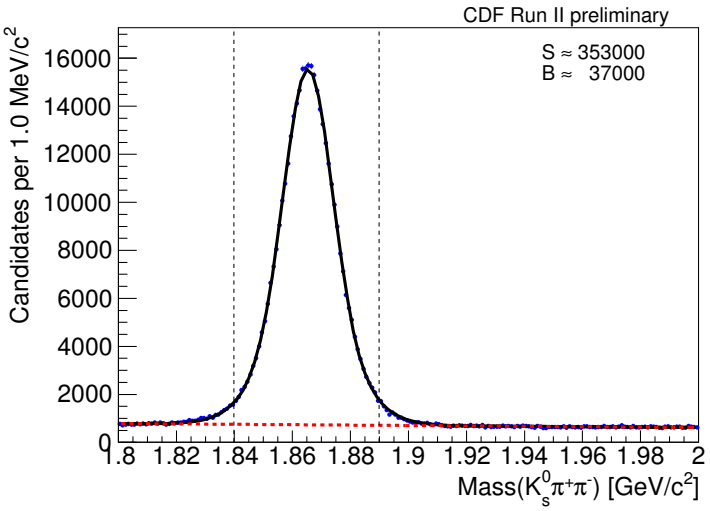

Figure 6.43.: The $M(K^0_S\pi^+\pi^-)$ distribution obtained from data (points with error bars) together with the D^0 fit (black solid line). The red dashed line corresponds to the background contribution.

6.6. Fitting Procedures

A Dalitz fit to the resonant substructure of the decay $D^0 \to K^0_S \pi^+ \pi^-$ is performed. Afterwards, the fit is repeated for separate D^0 and $\bar{D}^0$ samples, the flavor being determined through $D^*(2010)^+ \to D^0 \pi^+$, to search for hints of CP violation in the decay amplitudes of the intermediate resonances.

6.6.1. Mass Fits

Fits to the D^0 mass and D^{*+} mass difference distributions are performed to determine the signal and background yields that are used afterwards in the Dalitz fit. In Figures 6.43 and 6.44 these fits are shown together with the corresponding distributions after the final selection described in Section 6.3.

For the D^0 mass distribution, the signal is described by the sum of two Gaussian functions with the same mean value, and the background is modeled by a linear function.

The signal in the D^{*+} mass difference distribution is described by a nonrelativistic Breit-Wigner function given in Equation 5.15, convolved with the assigned resolution function. As described in Section 6.5.4, the resolution function consists of the weighted sum of three Gaussians. Technically, the convolution is realized as the normalized sum of three Voigt functions with the same Breit-Wigner part. The background is modeled by a third-order polynomial.

Table 6.4 shows the results of the fits to the D^0 mass and D^{*+} mass difference

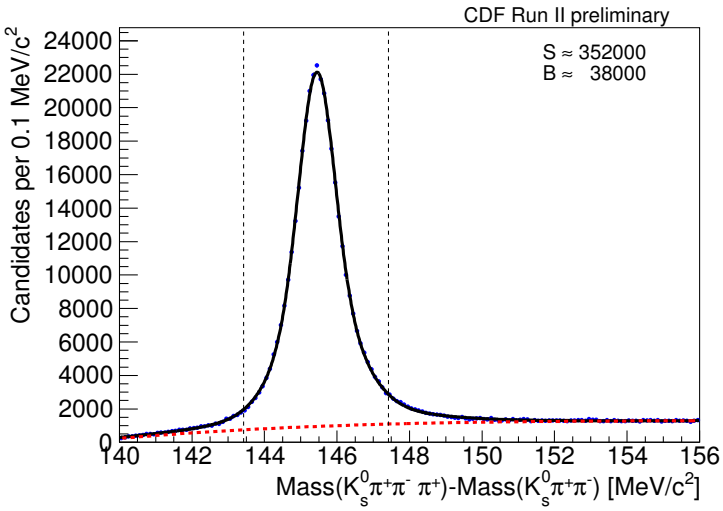

Figure 6.44.: The $M(K^0_S\pi^+\pi^-\,\pi^+) - M(K^0_S\pi^+\pi^-)$ distribution obtained from data (points with error bars) together with the D^{*+} fit (black solid line). The red dashed line corresponds to the background contribution.

distributions for the parameters describing the signal shapes. The measured D^0 mass of $1865.39 \pm 0.02\,\mathrm{MeV}/c^2$ as well as the D^{*+} mass difference of $145.439 \pm 0.001\,\mathrm{MeV}/c^2$ are in agreement with the world average values [1] when accounting for systematic uncertainties. Furthermore, compatible values are measured for both D^{*+} and D^{*-} respective D^0 and $\bar{D}^0$.

A signal purity of 91% results from the signal and background yields of the D^0 mass fit. However, a part of these signal candidates are combined with a random pion, and are therefore background in the D^{*+} fit. This means that it is not possible to determine the D^0 flavor, D^0 or $\bar{D}^0$, from the decay $D^*(2010)^+ \to D^0\,\pi^+$, and half of the background from true D^0 combined with a random pion are thus assigned the wrong flavor.

Unfortunately, it is not possible to determine the yield of the background from true D^0 combined with a random pion by comparing the signal yields in the D^0 and D^{*+} fits, because there is an additional peaking background below the D^{*+} signal originating from misreconstructed D^0. This peaking background can be seen as enhancement of D^{*+} signal events in the D^{*+} mass difference distribution from the D^0 mass sideband $1.80 < M(K^0_S\pi^+\pi^-) < 1.82\,\mathrm{GeV}/c^2$, shown in Figure 6.45.

But there is yet another way to determine the background from true D^0 combined with a random pion. Figure 6.46 shows the D^0 mass distribution from the D^{*+} mass difference sidebands $140 < \Delta M(D^{*+}) < 142\,\mathrm{MeV}/c^2$ and $150 < \Delta M(D^{*+}) < 152\,\mathrm{MeV}/c^2$ together with a fit performed in the same manner as for the signal region. One can derive the fraction of D^0 signal candidates with wrongly assigned

Table 6.4.: Results of the fits to the D^0 mass and D^{*+} mass difference distributions. The quoted D^0 width values correspond to the standard deviations of the narrower of the two employed Gaussian functions. The rows $D^{*\pm}$ and $D^0/\bar{D}^0$ represent the results of the combined fits.

	Mass [MeV/c^2]	Width [MeV/c^2]
$D^0/\bar{D}^0$	1865.39 ± 0.02	8.20 ± 0.08
D^0	1865.44 ± 0.03	8.27 ± 0.12
$\bar{D}^0$	1865.34 ± 0.03	8.13 ± 0.12
$D^{*\pm}$	145.439 ± 0.001	0.165 ± 0.003
D^{*+}	145.439 ± 0.002	0.170 ± 0.006
D^{*-}	145.439 ± 0.002	0.161 ± 0.005

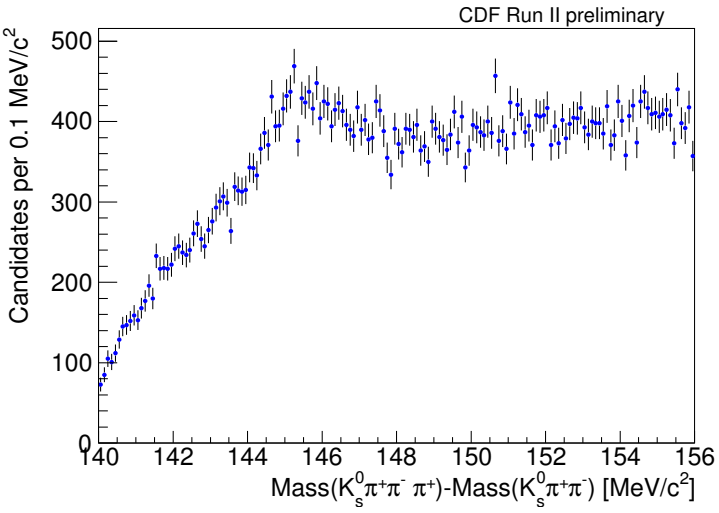

Figure 6.45.: D^{*+} mass difference distribution from the D^0 mass sideband $1.80 < M(K^0_S\pi^+\pi^-) < 1.82\,\mathrm{GeV}/c^2$.

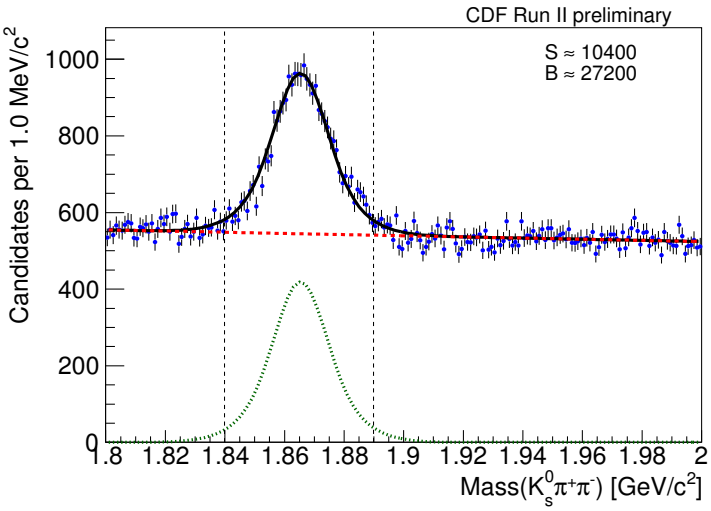

Figure 6.46.: D^0 mass distribution from the D^{*+} mass difference sidebands $140 < \Delta M(D^{*+}) < 142\,\mathrm{MeV}/c^2$ and $150 < \Delta M(D^{*+}) < 152\,\mathrm{MeV}/c^2$ together with the fit.

flavor, in the following referred to as mistag fraction, from the determined signal and background yield. For this, the signal to background ratio of the D^{*+} sideband fit is multiplied with the background yield in the D^{*+} signal region and divided by 2, in order to get the number of mistags in the selected D^0 candidates. The mistag fraction can then be obtained as the ratio of this number to the overall D^0 signal yield, resulting in a value of $1.48 \pm 0.01\%$. This value can serve as a cross check for the mistag fraction determined directly by the Dalitz fit described in the next Section.

6.6.2. Dalitz Fit

In the following, a description of the Dalitz fit is given. After a general overview of the theoretical model with the involved formulas, the employed likelihood function and the calculation of the fit fractions for the included resonances are described, before the results of the fit are presented.

Theoretical Model

The decay rate of the generic three-body decay $D \to A\,B\,C$ over the Dalitz plot depends on the overall complex matrix element $\mathcal{M}$ as

$$d\Gamma = \frac{|\mathcal{M}|^2}{256\pi^3 M_D^3} dM_{AB}^2 dM_{BC}^2 \,. \tag{6.6}$$

Table 6.5.: Spin-dependent Blatt-Weisskopf form factors. F_D represents the one for D^0 and F_r the ones for the different intermediate resonances. The meaning of p_r and p_{AB} is described in the text.

Spin	$F_{r/D}$
0	1
1	$\sqrt{\frac{1+R^2p_r^2}{1+R^2p_{AB}^2}}$
2	$\sqrt{\frac{9+3R^2p_r^2+R^4p_r^4}{9+3R^2p_{AB}^2+R^4p_{AB}^4}}$

Since D^0 three-body decays are dominated by resonant two-body contributions, the matrix element can have a very complicated structure. In the following, the Isobar model is used to describe it. Therein the different resonances are modeled by complex numbers $a_j \cdot e^{i\delta_j}$, composed of the amplitudes a_j and the phases δ_j, multiplied with the individual complex matrix elements $\mathcal{A}_j$. These complex numbers are added as

$$\mathcal{M} = a_0 \cdot e^{i\delta_0} + \sum_j a_j \cdot e^{i\delta_j} \cdot \mathcal{A}_j \,, \tag{6.7}$$

where $a_0 \cdot e^{i\delta_0}$ represents a possible nonresonant contribution. Since a_j and δ_j are relative amplitudes and phases, one resonance can be chosen as reference contribution. Following Reference [64], the amplitude and phase of the $\rho(770)$, being the largest color suppressed mode and thus out of phase with the unsuppressed modes, are fixed to the values $a_{\rho(770)} = 1$ and $\delta_{\rho(770)} = 0$ to minimize correlated errors.

The individual matrix elements $\mathcal{A}_r$ are composed of a Breit-Wigner part,

$$\frac{1}{M_r^2 - M_{AB}^2 - iM_r\Gamma_{AB}} \,, \tag{6.8}$$

multiplied with the Blatt-Weisskopf penetration factors F_D, F_r and an angular factor depending on the spin of the intermediate resonance.

The spin-dependent Blatt-Weisskopf penetration factors F_D, representing the one for D^0, and F_r, representing the ones for the different intermediate resonances, are listed in Table 6.5. Thereby, p_r corresponds to the identical momenta of the two decay particles of the considered intermediate resonance in the rest frame of the resonance, and p_{AB} is the same as p_r except for the substitution of the nominal mass of the resonance by the reconstructed mass of the two-body combination. For F_D, p_r and p_{AB} represent the identical momenta of the considered resonance and the remaining D^0 decay particle in the D^0 rest frame, where nominal respective reconstructed D^0 mass are used for the calculation. The radius R is set to $R = 5\,\mathrm{GeV}^{-1}$ for D^0 and $R = 1.5\,\mathrm{GeV}^{-1}$ for all intermediate resonances.

For spin-0 resonances the matrix element reads

$$\mathcal{A}_r(ABC|0) = F_D \cdot F_r \cdot \frac{1}{M_r^2 - M_{AB}^2 - iM_r\Gamma_{AB}}\,, \tag{6.9}$$

for vector resonances, that is spin-1,

$$\mathcal{A}_r(ABC|1) = F_D \cdot F_r \cdot \frac{M_{AC}^2 - M_{BC}^2 + \frac{(M_D^2 - M_C^2)(M_B^2 - M_A^2)}{M_r^2}}{M_r^2 - M_{AB}^2 - iM_r\Gamma_{AB}} \tag{6.10}$$

and for tensor resonances, that is spin-2,

$$\begin{aligned}\mathcal{A}_r(ABC|2) = \frac{F_D \cdot F_r}{M_r^2 - M_{AB}^2 - iM_r\Gamma_{AB}} \cdot \Bigg[\left(M_{BC}^2 - M_{AC}^2 + \frac{(M_D^2 - M_C^2)(M_A^2 - M_B^2)}{M_r^2}\right)^2 \\ -\frac{1}{3}\cdot\left(M_{AB}^2 - 2M_D^2 - 2M_C^2 + \frac{(M_D^2 - M_C^2)^2}{M_r^2}\right)\left(M_{AB}^2 - 2M_A^2 - 2M_B^2 + \frac{(M_A^2 - M_B^2)^2}{M_r^2}\right)\Bigg]\,.\end{aligned} \tag{6.11}$$

Thereby, the mass-dependent width Γ_{AB} can be calculated as

$$\Gamma_{AB} = \Gamma_r \cdot \left(\frac{p_{AB}}{p_r}\right)^{2J+1} \cdot \left(\frac{M_r}{M_{AB}}\right) \cdot F_r^2\,, \tag{6.12}$$

where J is the total angular momentum and p_r (p_{AB}) is the momentum of the daughters in the resonance rest frame calculated from the nominal (reconstructed) mass.

When these formula are applied to the different resonances assigned to the three axes of the Dalitz plot, a specific phase convention has to be chosen. This can be seen for example by switching the labels A and B in Equation 6.10, leading to a overall change of sign. In principal, there are eight possible phase conventions for a three-body decay. The one employed here is defined by

$$\begin{aligned}\mathcal{A}_r(ABC) &= \mathcal{A}_{K_S^0\pi^\mp}(K_S^0\pi\pi) \\ \mathcal{A}_r(ABC) &= \mathcal{A}_{\pi^+\pi^-}(\pi\pi K_S^0)\end{aligned} \tag{6.13}$$

for $K_S^0\pi^\mp$ respective $\pi^+\pi^-$ resonances.

For the intermediate resonances $\rho(770)$ and $\rho(1450)$ decaying to $\pi^+\pi^-$ the Breit-Wigner part is substituted by the Gounaris-Sakurai description [83]

$$\mathrm{GS}(M_{\pi\pi}^2) = \frac{M_\rho^2 + d\cdot M_\rho\cdot\Gamma_\rho}{M_\rho^2 - M_{\pi\pi}^2 - i\cdot M_\rho\cdot\Gamma_{\pi\pi} + \Gamma_\rho\cdot\frac{M_\rho^2}{p_\rho^3}\cdot\left[p_{\pi\pi}^2\cdot(h_{\pi\pi} - h_\rho) + p_\rho^2\cdot\left.\frac{dh_{\pi\pi}}{dM_{\pi\pi}^2}\right|_{M_\rho^2}\cdot(M_\rho^2 - M_{\pi\pi}^2)\right]}\,,$$

$$
\begin{aligned}
h_{\pi\pi} &= \frac{2}{\pi} \cdot \frac{p_{\pi\pi}}{M_{\pi\pi}} \cdot \ln\left(\frac{M_{\pi\pi} + 2 \cdot p_{\pi\pi}}{2 \cdot m_\pi}\right) , \\
d &= \frac{3}{\pi} \cdot \frac{m_\pi^2}{p_\rho^2} \cdot \ln\left(\frac{M_\rho + 2 \cdot p_\rho}{2 \cdot m_\pi}\right) + \frac{M_\rho}{2 \cdot \pi \cdot p_\rho} - \frac{m_\pi^2 \cdot M_\rho}{\pi \cdot p_\rho^3} .
\end{aligned}
\tag{6.14}
$$

An alternative to the Isobar model for the description of the $\pi\pi$ S-wave contribution, that is the spin-0 resonances decaying into $\pi^+\pi^-$, is the so-called K matrix model described in Reference [67]. However, the Isobar model is better suited for the search for CP violating effects in the amplitudes of the intermediate resonances because it treats all possible resonances separately.

For the description of the $K\pi$ S-wave contribution, that is the spin-0 resonances decaying into $K^0_S\pi^\mp$, there is also an alternative to the Isobar model, namely a phenomenological parametrization extracted from scattering data [84] described in Reference [67]. Again, the Isobar model is better suited for the search for CP violation because it treats all resonances separately.

Likelihood Function

A binned maximum likelihood fit to the two-dimensional Dalitz plot distribution with bin widths of $0.025\,\mathrm{GeV}^2/c^4$ in both dimensions is performed to determine the amplitudes a_j and phases δ_j of the intermediate resonances.

The negative logarithm of the likelihood function has the general form of Equation 4.5 and the expected number μ_i of entries in bin i are obtained using the function

$$
\begin{aligned}
\mu(M^2_{K^0_S\pi^-}, M^2_{\pi^+\pi^-}) = {} & T \cdot \epsilon(M^2_{K^0_S\pi^-}, M^2_{\pi^+\pi^-}) \cdot |\mathcal{M}(M^2_{K^0_S\pi^-}, M^2_{\pi^+\pi^-})|^2 \\
& + (1-T) \cdot \epsilon(M^2_{K^0_S\pi^-}, M^2_{\pi^+\pi^-}) \cdot |\mathcal{M}(M^2_{K^0_S\pi^+}, M^2_{\pi^+\pi^-})|^2 \\
& + B(M^2_{K^0_S\pi^-}, M^2_{\pi^+\pi^-}) ,
\end{aligned}
\tag{6.15}
$$

where $(1-T)$ is the mistag fraction, $\epsilon(M^2_{K^0_S\pi^-}, M^2_{\pi^+\pi^-})$ the relative efficiency over the Dalitz plot, and $B(M^2_{K^0_S\pi^-}, M^2_{\pi^+\pi^-})$ the background distribution. The function is evaluated at the bin center to calculate the expectation for μ_i.

Since the D^0 with a wrongly assigned flavor show a characteristic shape in the Dalitz plot, the mistag fraction is determined as a free parameter of the fit. It can be compared to the value obtained independently from the mass fits described in Section 6.6.1.

As described in Section 6.5.2, the relative efficiency is determined from a fit to the Dalitz plot distribution of a sample of simulated events, the $D^0 \to K^0_S\,\pi^+\,\pi^-$ decays of which are generated nonresonantly.

The distribution of the background is determined from the upper D^0 mass sideband $1.92 < M(K^0_S\pi^+\pi-) < 1.95\,\mathrm{GeV}/c^2$, as described in Section 6.4.1. It is not

parametrized but included as two-dimensional histogram in the fit. The background contribution to the total sample is obtained from the D^0 mass fit of Section 6.6.1 and amounts to about 9%.

The choice of considered resonances is identical to the one from Belle listed in Table 6.1. The scalar resonance called σ_1 there is named $f_0(600)$ in the following in order to match with the PDG notation [1]. All other included resonances are established and their properties listed in Reference [1], except for the scalar resonance σ_2 which is introduced to account for a structure near $1\,\mathrm{GeV}^2/c^4$ in the $M^2_{\pi^+\pi^-}$ distribution. Due to the lack of a fitting known meson an explanation for this structure, proposed in Reference [85], could be the decay $f_0(980) \to \eta\,\eta$ with rescattering of $\eta\eta$ to $\pi^+\pi^-$, resulting in a distortion of the $f_0(980) \to \pi^+\,\pi^-$ amplitude for $M^2_{\pi^+\pi^-}$ near the $\eta\eta$ production threshold.

The masses and decay widths of the included resonances are fixed to the values in Reference [86] for $f_0(980)$ and $f_0(1370)$, and to the world average values [1] for the others, except for $K^*(892)^\mp$, $f_0(600)$, and σ_2 which are free parameters in the fit. The reason for floating $K^*(892)^\mp$ resonance parameters is the prominent signal, allowing a precise determination of the mass and decay width. For $f_0(600)$ and σ_2 the reason is the poor knowledge on the parameters of these scalar resonances.

Fit Fractions

In order to estimate the contributions of the individual resonances to the total decay rate, the fit fractions

$$\mathrm{FF_r} = \frac{\int |a_r e^{i\delta_r} \mathcal{A}_r|^2 dM^2_{K^0_S\pi^-} dM^2_{\pi^+\pi^-}}{\int |\sum_j a_j e^{i\delta_j} \mathcal{A}_j|^2 dM^2_{K^0_S\pi^-} dM^2_{\pi^+\pi^-}} \tag{6.16}$$

are calculated from the fitted amplitudes and phases, being a measure for the relative branching fractions. However, the fit fractions do not add up to one in general because of interference effects between the different contributions. Their main benefit is that they are easier to compare with other measurements than the amplitudes depending on the phase convention.

The statistical uncertainties on the fit fractions are determined by 1000 random parameter sets generated according to the full covariance matrix of the fit. The procedure works as follows:

- A Cholesky decomposition is used to transform the covariance matrix of the fitted amplitudes and phases into a triangle matrix $\mathbf{T}$.
- For each fit parameter p_i a random number r_i is generated according to a Gaussian distribution with $\mu = 0$ and $\sigma = 1$.
- These random numbers are correlated to each other according to the calculated triangle matrix by $c_j = \sum_i \mathbf{T}_{ij} \cdot r_i$.

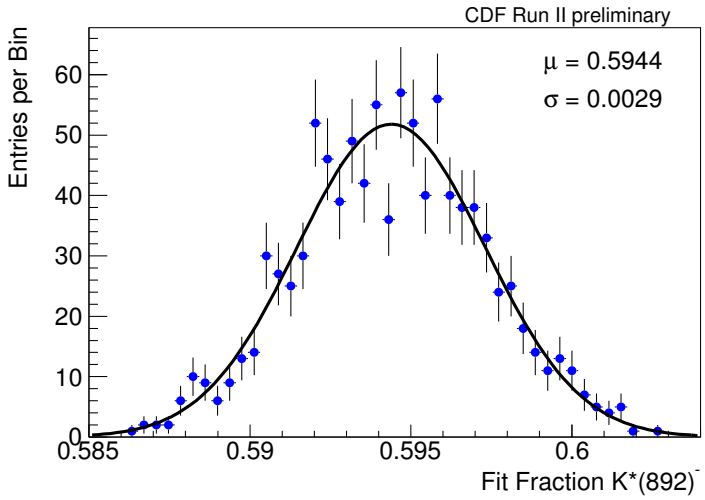

Figure 6.47.: Determination of the $K^*(892)^-$ fit fraction by means of 1000 random parameter sets generated according to the full covariance matrix of the fit. The parameters of the fitted Gaussian function correspond to the fit fraction and its statistical uncertainty.

- The correlated random numbers are added to the parameter values resulting from the fit: $x_i = p_i + c_i$.
- The random parameters x_i are used to calculate the fit fractions FF_i.
- The procedure is repeated 1000 times and for each resonance the FF_i are filled to a histogram.
- The histograms are fitted by a Gaussian function and the resulting standard deviations are used as statistical uncertainties on the fit fractions.

For illustration, the histogram used for the determination of the statistical uncertainty on the fit fraction of the dominant intermediate resonance $K^*(892)^-$ is shown in Figure 6.47.

Fit Results

The results of the Dalitz fit for the relative amplitudes and phases of the included intermediate resonances can be found in Table 6.6, together with the fit fractions calculated from them. Compared to previous experiments (see Table 6.1), the contributions from $K^*(1680)^{\mp}$ and the doubly Cabibbo suppressed $K^*(1410)^+$ are not found to be significant here and are therefore excluded in the fit.

Table 6.6.: Dalitz fit results for the relative amplitudes and phases of the included intermediate resonances together with the fit fractions calculated from them.

Resonance	a	δ [°]	FF [%]
$K^*(892)^-$	1.774 ± 0.010	130.0 ± 0.7	59.44 ± 0.29
$K_0^*(1430)^-$	1.677 ± 0.038	17.0 ± 1.4	4.01 ± 0.17
$K_2^*(1430)^-$	1.219 ± 0.027	305.9 ± 1.5	2.17 ± 0.09
$K^*(1410)^-$	0.877 ± 0.042	131.0 ± 2.6	0.72 ± 0.07
$\rho(770)$	1	0	21.08 ± 0.20
$\omega(782)$	0.038 ± 0.002	110.9 ± 1.7	0.52 ± 0.05
$f_0(980)$	0.453 ± 0.010	205.5 ± 2.1	5.20 ± 0.23
$f_2(1270)$	1.048 ± 0.033	340.1 ± 2.5	0.80 ± 0.05
$f_0(1370)$	0.727 ± 0.067	28.5 ± 6.6	0.34 ± 0.06
$\rho(1450)$	2.298 ± 0.151	346.9 ± 3.8	0.45 ± 0.06
$f_0(600)$	1.450 ± 0.051	193.8 ± 1.8	10.38 ± 0.41
σ_2	0.210 ± 0.022	165.7 ± 8.4	0.56 ± 0.04
$K^*(892)^+$	0.182 ± 0.008	318.5 ± 1.8	0.63 ± 0.05
$K_0^*(1430)^+$	0.621 ± 0.036	121.7 ± 3.5	0.55 ± 0.06
$K_2^*(1430)^+$	0.282 ± 0.030	232.0 ± 5.7	0.12 ± 0.02
Nonresonant	3.437 ± 0.123	112.7 ± 2.3	6.71 ± 0.47
Sum	$\cdots$	$\cdots$	113.7

Table 6.7.: Dalitz fit results for the masses and widths of the $K^*(892)^\mp$, $f_0(600)$, and σ_2 contributions. The world average values [1] as well as the measurements of the Belle experiment [65] are listed for comparison. The given uncertainties are statistical only, except for the world average values which are combined statistical and systematic uncertainties.

	CDF	PDG	Belle
$M(K^*(892)^\mp)[\mathrm{MeV}/c^2]$	894.42 ± 0.11	891.66 ± 0.26	893.7 ± 0.1
$\Gamma(K^*(892)^\mp)[\mathrm{MeV}/c^2]$	52.23 ± 0.21	50.8 ± 0.9	48.4 ± 0.2
$M(f_0(600))[\mathrm{MeV}/c^2]$	539.71 ± 4.92	400 – 1200	522 ± 6
$\Gamma(f_0(600))[\mathrm{MeV}/c^2]$	361.27 ± 9.49	600 – 1000	453 ± 10
$M(\sigma_2)[\mathrm{MeV}/c^2]$	1019.84 ± 4.64	$\cdots$	1033 ± 7
$\Gamma(\sigma_2)[\mathrm{MeV}/c^2]$	78.29 ± 5.62	$\cdots$	88 ± 7

Table 6.7 shows the results for the fitted masses and widths of the $K^*(892)^\mp$, $f_0(600)$, and σ_2 contributions. For comparison, the world average values [1] and the Belle measurements [65] are also listed, indicating a rough agreement.

The mistag fraction obtained from the Dalitz fit results is

$$1 - T = (1.65 \pm 0.11)\% \,,$$

which is consistent with the $1.48 \pm 0.01\%$ determined from the D^0 mass fits described in Section 6.6.1.

The fit quality, estimated according to Section 4.1.2 with the same Dalitz plot binning as used for the fit, is

$$\chi^2/\mathrm{NDF} = 1.70 \quad (\mathrm{NDF} = 5112) \,,$$

indicating some slight discrepancies between the data and the fit model which can be seen also in the projections to the three Dalitz plot axes $M^2_{K^0_S\pi^-}$,$M^2_{\pi^+\pi^-}$, and $M^2_{K^0_S\pi^+}$ shown in Figures 6.48–6.50.

However, besides the two $K^*(892)^-$ regions at low and high $M^2_{\pi^+\pi^-}$, which are further addressed in Section 6.7.6, these discrepancies mostly originate from the edges of phase space, as can be reasoned from the distribution of $(\mathrm{data} - \mathrm{fit})/\sqrt{\mathrm{fit}}$ over the Dalitz plot shown in Figure 6.51. They can be explained by the fact that the D^0 mass is not constrained to its nominal value for the creation of the Dalitz plot. Instead the reconstructed mass is used, which leads to resolution effects at the edges of phase space. Nevertheless, regarding the large data sample the main features of the Dalitz plot are well-described. Furthermore, the fit quality is at least comparable to the value $\chi^2/\mathrm{NDF} = 2.35$ reported by Belle [65].

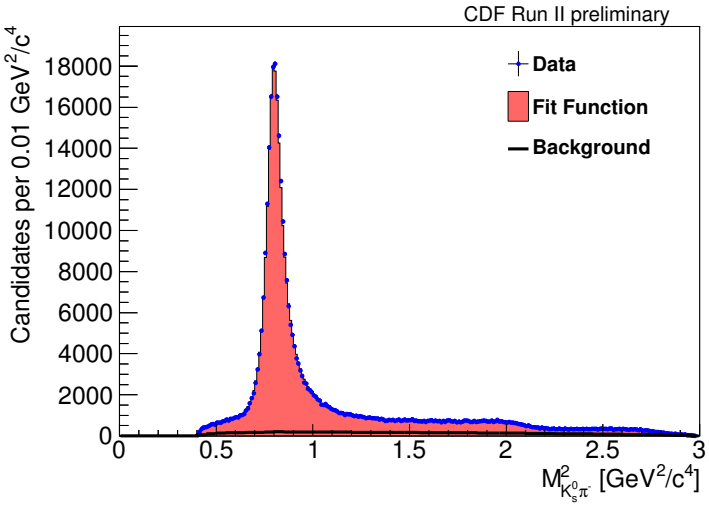

Figure 6.48.: Projection of the Dalitz fit to the axis $M^2_{K^0_S\pi^-}$ together with the corresponding distribution in data.

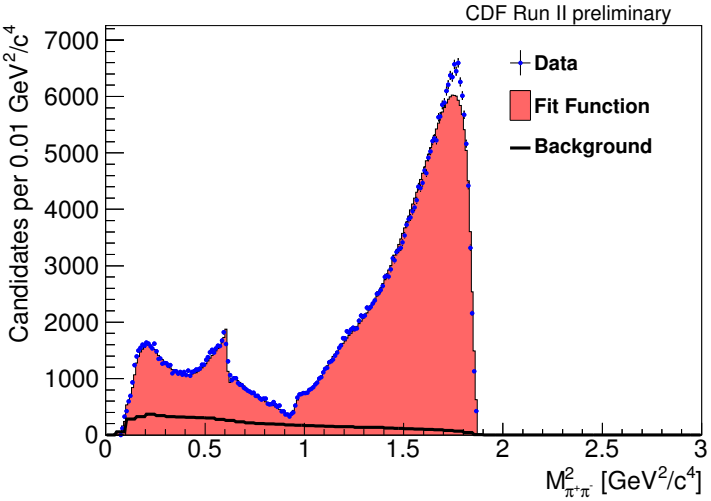

Figure 6.49.: Projection of the Dalitz fit to the axis $M^2_{\pi^+\pi^-}$ together with the corresponding distribution in data.

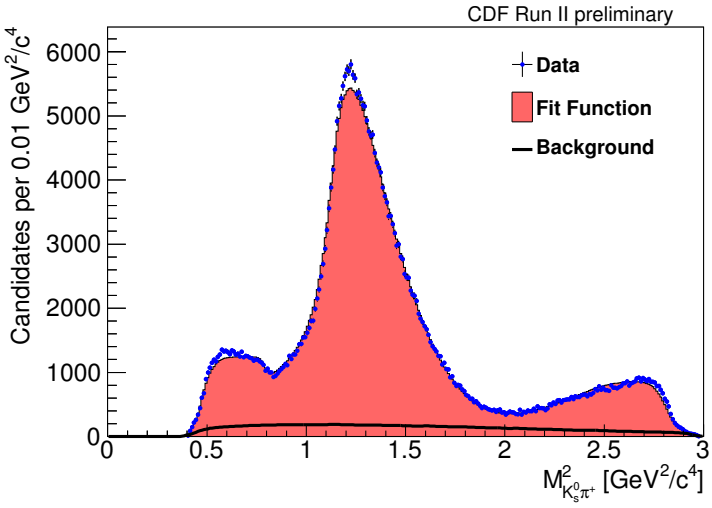

Figure 6.50.: Projection of the Dalitz fit to the axis $M^2_{K^0_S\pi^+}$ together with the corresponding distribution in data.

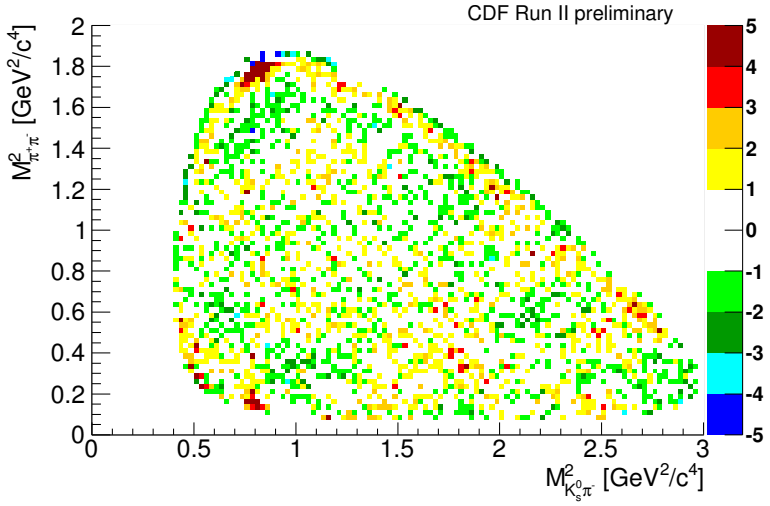

Figure 6.51.: Distribution of (data − fit)/$\sqrt{\text{fit}}$ over the Dalitz plot.

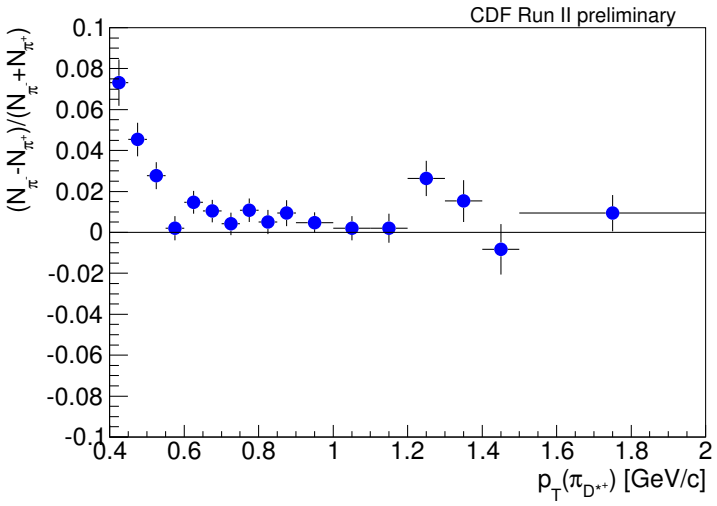

Figure 6.52.: $p_T(\pi_{D^{*+}})$-dependence of the $\pi_{D^{*+}}$ charge asymmetry.

6.6.3. Search for CP Violation

To search for CP violating effects in the Dalitz fit the production flavor of the D^0 decaying to $K^0_S\pi^+\pi^-$ has to be known. This is accomplished by the reconstruction of the decay $D^*(2010)^+ \to D^0\,\pi^+$, where the charge of the additional pion determines the production flavor of the D^0. However, the reconstruction efficiency of this additional pion causes an asymmetry in the D^0 and $\bar{D}^0$ samples. Whereas an absolute efficiency difference is no problem for the employed method, an asymmetry depending on the transverse momentum of the additional pion can lead to efficiency discrepancies between D^0 and $\bar{D}^0$ that vary over the Dalitz plot. Consequently, it has to be taken into account for the fits to avoid a fake CP violation.

After doing so, two different approaches to search for CP violation in the Dalitz fit are applied. For the first one, the D^0 and $\bar{D}^0$ samples are separated and two independent fits are performed, the results of which can be compared afterwards. The second approach is a simultaneous fit to both D^0 and $\bar{D}^0$ samples, where two additional parameters, representing CP violating amplitudes and phases, are introduced for each resonance.

Efficiency Discrepancies between D^0 and $\bar{D}^0$

Figure 6.52 shows the asymmetry of Equation 6.5 between the number of $\bar{D}^0$ and D^0 candidates, determined from the $\pi_{D^{*+}}$ charge, in dependence on the $\pi_{D^{*+}}$ transverse momentum. Besides the overall asymmetry one can see that the asymmetry is much stronger for low $p_T(\pi_{D^{*+}})$. This in turn means that the D^0 and $\bar{D}^0$ efficiencies can differ over the Dalitz plot, as illustrated in Figure 6.41 for simulated events.

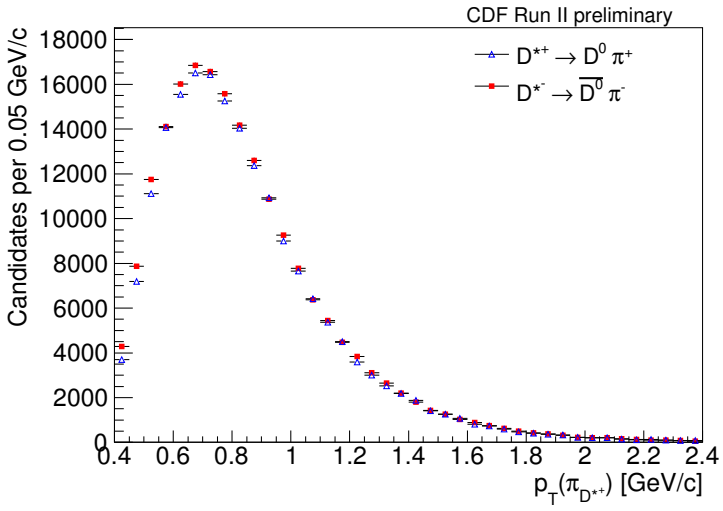

Figure 6.53.: Transverse momentum distributions of the pion from the D^{*+} decay separate for positive and negative pion charges.

Although the effect is immeasurable small in real data, as will be seen later (Figure 6.80), it is accommodated in the following because of a possible mimicking of CP violating effects. This is done by reweighting the $\bar{D}^0$ Dalitz plot according to the deviations between the $p_T(\pi_{D^{*+}})$ distributions for negative and positive pion charges shown in Figure 6.53.

Separated D^0 and $\bar{D}^0$ Dalitz Fits

The whole fitting procedure described in Section 6.6.2 is repeated for separate D^0 and $\bar{D}^0$ samples, meaning that two independent fits are performed. The differences in the estimated resonance parameters can then be interpreted as CP violating effects.

As described above, the $\bar{D}^0$ Dalitz plot distribution is reweighted before the fit, in order to account for possible efficiency discrepancies between D^0 and $\bar{D}^0$. In the two independent fits to the normalized D^0 and $\bar{D}^0$ Dalitz plots, the parameters for the nonresonant contribution, the $K^*(892)^{\mp}$, $f_0(600)$, and σ_2 masses and widths, as well as the mistag fraction are fixed to the values obtained from the combined fit (Section 6.6.2).

The results of the two fits for the amplitudes and phases are listed in Table 6.8. In Figures 6.54–6.56 the projections on the three Dalitz plot axes and in Figure 6.57 the discrepancies between fit and data are shown for both D^0 and $\bar{D}^0$. With $\chi^2/\text{NDF} = 1.35\,(\text{NDF} = 5034)$ for D^0 and $\chi^2/\text{NDF} = 1.34\,(\text{NDF} = 5029)$ for $\bar{D}^0$ the fit qualities of the two independent fits slightly improve compared to the combined fit.

Table 6.8.: Results for the relative amplitudes and phases of the two independent D^0 and $\bar{D}^0$ Dalitz fits.

Resonance	a_{D^0}	$a_{\bar{D}^0}$	δ_{D^0} [°]	$\delta_{\bar{D}^0}$ [°]
$K^*(892)^-$	1.764 ± 0.008	1.766 ± 0.008	129.6 ± 0.9	130.7 ± 0.9
$K_0^*(1430)^-$	1.654 ± 0.047	1.647 ± 0.045	15.5 ± 2.1	19.0 ± 2.1
$K_2^*(1430)^-$	1.249 ± 0.034	1.192 ± 0.033	304.5 ± 2.2	307.6 ± 2.3
$K^*(1410)^-$	0.804 ± 0.066	0.924 ± 0.061	128.9 ± 4.3	132.5 ± 3.7
$\omega(782)$	0.035 ± 0.003	0.040 ± 0.003	110.2 ± 2.5	112.5 ± 2.3
$f_0(980)$	0.453 ± 0.009	0.454 ± 0.009	204.7 ± 1.9	205.5 ± 1.9
$f_2(1270)$	1.034 ± 0.046	1.079 ± 0.046	340.2 ± 3.7	340.6 ± 3.4
$f_0(1370)$	0.748 ± 0.111	0.707 ± 0.101	26.5 ± 8.6	29.2 ± 8.6
$\rho(1450)$	2.342 ± 0.229	2.296 ± 0.217	340.3 ± 4.8	351.4 ± 5.2
$f_0(600)$	1.437 ± 0.035	1.449 ± 0.031	192.6 ± 1.5	195.0 ± 1.4
σ_2	0.211 ± 0.016	0.205 ± 0.016	165.7 ± 3.8	165.9 ± 3.9
$K^*(892)^+$	0.180 ± 0.007	0.182 ± 0.007	316.5 ± 2.3	320.9 ± 2.2
$K_0^*(1430)^+$	0.641 ± 0.051	0.614 ± 0.050	117.0 ± 5.0	125.5 ± 5.0
$K_2^*(1430)^+$	0.265 ± 0.049	0.306 ± 0.044	228.6 ± 8.7	231.7 ± 7.6

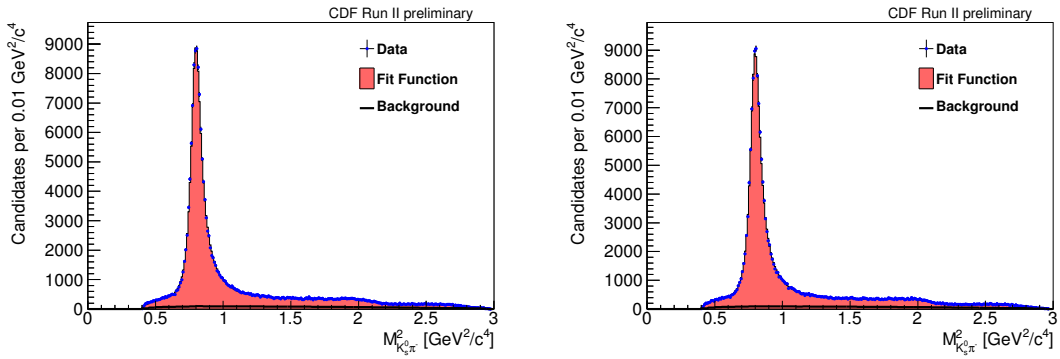

Figure 6.54.: Projections of the D^0 (left) and $\bar{D}^0$ (right) Dalitz fits to the axis $M^2_{K^0_S\pi^-}$ together with the corresponding distributions in data.

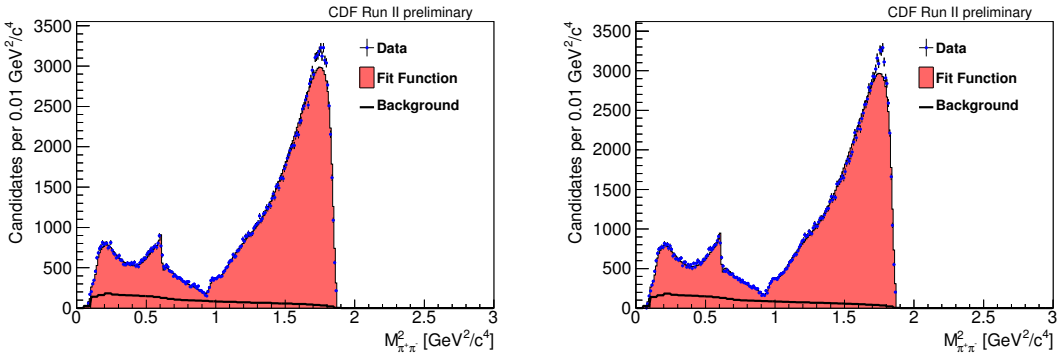

Figure 6.55.: Projections of the D^0 (left) and $\bar{D}^0$ (right) Dalitz fits to the axis $M^2_{\pi^+\pi^-}$ together with the corresponding distributions in data.

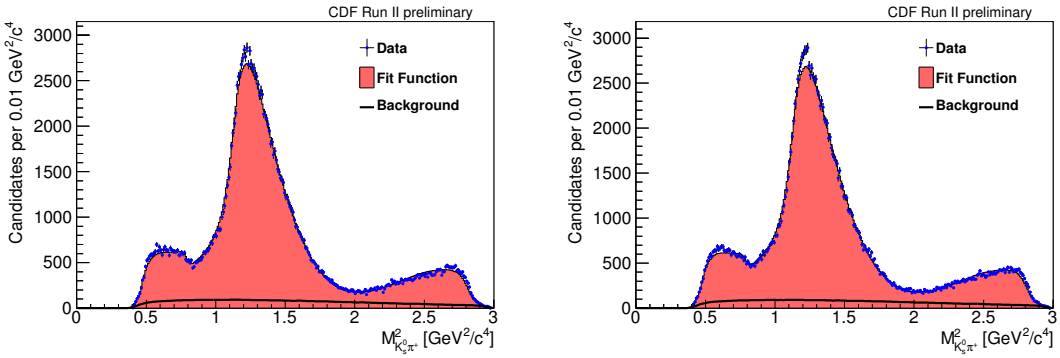

Figure 6.56.: Projections of the D^0 (left) and $\bar{D}^0$ (right) Dalitz fits to the axis $M^2_{K^0_S\pi^+}$ together with the corresponding distributions in data.

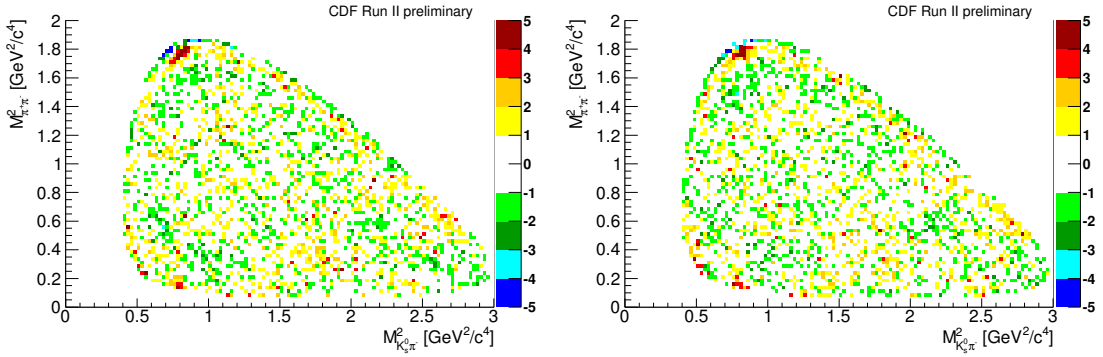

Figure 6.57.: Distribution of (data − fit)/$\sqrt{\text{fit}}$ over the D^0 (left) and $\bar{D}^0$ (right) Dalitz plots.

Table 6.9.: Fit fractions FF for the two independent D^0 and $\bar{D}^0$ Dalitz fits as well as the fit fraction asymmetries $\mathcal{A}_{\mathrm{FF}}$ calculated from them.

Resonance	FF_{D^0} [%]	$\mathrm{FF}_{\bar{D}^0}$ [%]	$\mathcal{A}_{\mathrm{FF}}$ [%]
$K^*(892)^-$	59.22 ± 0.46	59.28 ± 0.43	-0.05 ± 0.39
$K_0^*(1430)^-$	3.93 ± 0.23	3.89 ± 0.21	0.48 ± 2.89
$K_2^*(1430)^-$	2.30 ± 0.12	2.09 ± 0.11	4.80 ± 2.93
$K^*(1410)^-$	0.62 ± 0.10	0.81 ± 0.10	-13.66 ± 5.95
$\rho(770)$	21.27 ± 0.07	21.23 ± 0.07	0.09 ± 0.17
$\omega(782)$	0.46 ± 0.07	0.58 ± 0.08	-11.76 ± 5.77
$f_0(980)$	5.25 ± 0.19	5.27 ± 0.20	-0.20 ± 1.84
$f_2(1270)$	0.79 ± 0.07	0.86 ± 0.07	-4.10 ± 4.00
$f_0(1370)$	0.37 ± 0.10	0.33 ± 0.09	5.63 ± 15.47
$\rho(1450)$	0.47 ± 0.09	0.45 ± 0.08	1.96 ± 9.87
$f_0(600)$	10.31 ± 0.48	10.46 ± 0.44	-0.70 ± 2.31
σ_2	0.56 ± 0.08	0.53 ± 0.08	2.65 ± 7.67
$K^*(892)^+$	0.62 ± 0.05	0.64 ± 0.05	-1.00 ± 4.05
$K_0^*(1430)^+$	0.60 ± 0.09	0.55 ± 0.09	4.30 ± 8.33
$K_2^*(1430)^+$	0.11 ± 0.04	0.14 ± 0.04	-13.56 ± 13.59

To quantify possible CP violating effects the fit fraction asymmetries

$$\mathcal{A}_{\mathrm{FF}} = \frac{\mathrm{FF}_{D^0} - \mathrm{FF}_{\bar{D}^0}}{\mathrm{FF}_{D^0} + \mathrm{FF}_{\bar{D}^0}} \tag{6.17}$$

are calculated for each intermediate resonance, where the statistical uncertainties are determined by Gaussian error propagation from the statistical uncertainties of the individual fit fractions. The resulting values are listed in Table 6.9 together with the different fit fractions for D^0 and $\bar{D}^0$ as defined in Equation 6.16. None of the $\mathcal{A}_{\mathrm{FF}}$ values deviates significantly from zero.

A measure for the overall integrated CP asymmetry is given by

$$\mathcal{A}_{CP} = \frac{\int \frac{|\mathcal{M}|^2 - |\overline{\mathcal{M}}|^2}{|\mathcal{M}|^2 + |\overline{\mathcal{M}}|^2} dM^2_{K^0_S\pi^-} dM^2_{\pi^+\pi^-}}{\int dM^2_{K^0_S\pi^-} dM^2_{\pi^+\pi^-}}\,, \tag{6.18}$$

where $\mathcal{M}$ is the matrix element of Equation 6.7 for D^0 and $\overline{\mathcal{M}}$ the one for $\bar{D}^0$. The statistical uncertainty on $\mathcal{A}_{CP}$ is determined by means of the same procedure as used for the determination of the fit fraction uncertainties. Figure 6.58 shows the corresponding histogram with the 1000 statistical trials calculated according to the full covariance matrices of the D^0 and $\bar{D}^0$ Dalitz fits.

The resulting value is

$$\mathcal{A}_{CP} = (-4.45 \pm 5.62) \cdot 10^{-3}\,, \tag{6.19}$$

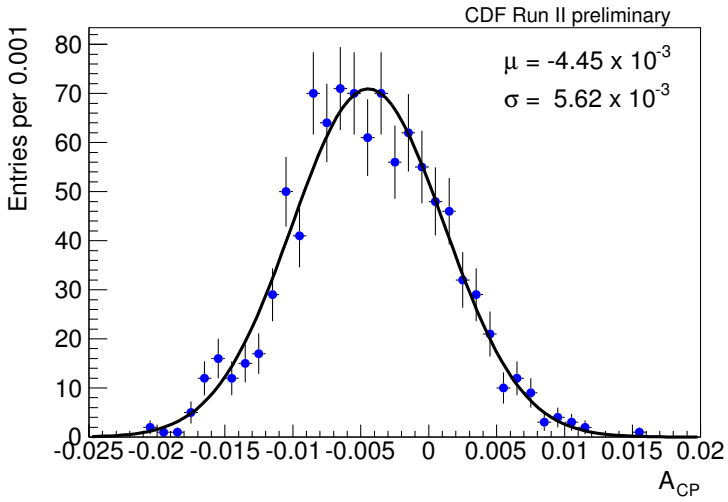

Figure 6.58.: Integrated CP asymmetry $\mathcal{A}_{CP}$ over the Dalitz plot, calculated from the matrix elements for D^0 and $\bar{D}^0$ according to Equation 6.18. The assigned statistical uncertainty is determined by means of 1000 random parameter sets generated according to the full covariance matrix of the fit. The parameters of the Gaussian function fitted to the resulting histogram correspond to $\mathcal{A}_{CP}$ and its statistical uncertainty.

completely compatible with no CP violation.

For illustration, the bin-by-bin difference between the D^0 and $\bar{D}^0$ distributions of the three Dalitz plot axes are shown in Figures 6.59–6.61 together with the corresponding projections of the Dalitz fits.

Simultaneous D^0-$\bar{D}^0$ Dalitz Fit

Following the description in Reference [78], a simultaneous fit to the D^0 and $\bar{D}^0$ samples is performed, where the matrix elements for D^0 respective $\bar{D}^0$ read

$$\begin{aligned} \mathcal{M} &= a_0 \cdot e^{i\delta_0} + \sum_j a_j \cdot e^{i(\delta_j+\phi_j)} \cdot (1 + \frac{b_j}{a_j}) \cdot \mathcal{A}_j \,, \\ \overline{\mathcal{M}} &= a_0 \cdot e^{i\delta_0} + \sum_j a_j \cdot e^{i(\delta_j-\phi_j)} \cdot (1 - \frac{b_j}{a_j}) \cdot \mathcal{A}_j \,. \end{aligned} \tag{6.20}$$

Compared to Equation 6.7 the additional parameters b_j and ϕ_j are introduced which represent the CP violating amplitudes and phases.

Again, the $\bar{D}^0$ Dalitz plot is reweighted according to the deviations between the $p_T(\pi_{D^{*+}})$ distributions for negative and positive pion charges, shown in Figure 6.53,

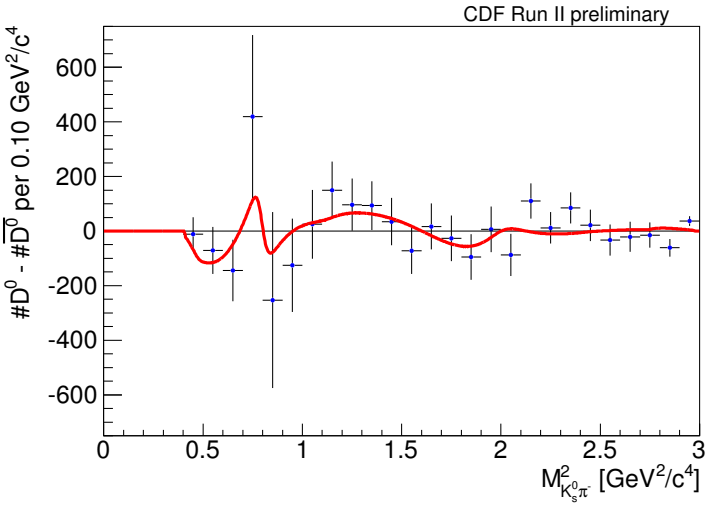

Figure 6.59.: Bin-by-bin difference between the D^0 and $\bar{D}^0$ $M^2_{K^0_S\pi^-}$ distributions together with the corresponding Dalitz fit projection indicated by the red line.

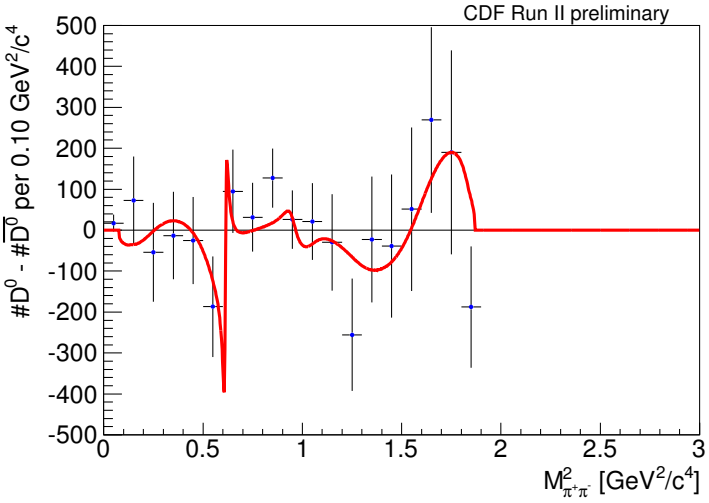

Figure 6.60.: Bin-by-bin difference between the D^0 and $\bar{D}^0$ $M^2_{\pi^+\pi^-}$ distributions together with the corresponding Dalitz fit projection indicated by the red line.

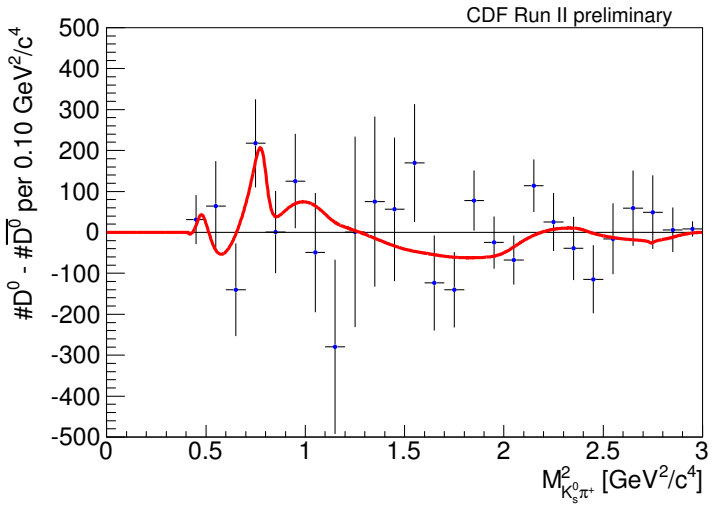

Figure 6.61.: Bin-by-bin difference between the D^0 and $\bar{D}^0$ $M^2_{K^0_S\pi^+}$ distributions together with the corresponding Dalitz fit projection indicated by the red line.

before the fit, in order to account for possible efficiency discrepancies between D^0 and $\bar{D}^0$. This leads to an overall normalization of the D^0 and $\bar{D}^0$ Dalitz plots.

The fit results for the CP conserving (a_j, δ_j) and CP violating (b_j, ϕ_j) amplitudes and phases are listed in Table 6.10. The CP conserving parameters are consistent with the ones from the combined fit without CP violation listed in Table 6.6 and none of the CP violating parameters is significantly different from zero.

For completeness, the fit values for the masses and widths of the resonances $K^*(892)^\mp$, $f_0(600)$, and σ_2 are listed in Table 6.11 and the obtained mistag fraction is

$$1 - T = (1.66 \pm 0.11)\% \,.$$

All values are consistent with the ones from the combined fit without CP violation in Section 6.6.2. Like for the two independent D^0 and $\bar{D}^0$ fits, the fit quality slightly improves compared to the combined fit without CP violation to the value $\chi^2/\mathrm{NDF} = 1.33\,(\mathrm{NDF} = 10174)$.

Table 6.10.: Results of the simultaneous D^0-$\bar{D}^0$ Dalitz fit for the CP conserving (a, δ) and CP violating (b, ϕ) amplitudes and phases.

Resonance	a	δ [°]	b	ϕ [°]
$K^*(892)^-$	1.777 ± 0.010	130.0 ± 0.7	-0.002 ± 0.004	0.2 ± 1.2
$K_0^*(1430)^-$	1.664 ± 0.038	17.6 ± 1.4	-0.010 ± 0.032	-1.3 ± 1.7
$K_2^*(1430)^-$	1.237 ± 0.028	305.8 ± 1.5	0.024 ± 0.024	-0.5 ± 1.6
$K^*(1410)^-$	0.875 ± 0.042	130.5 ± 2.6	-0.071 ± 0.040	-0.5 ± 2.6
$\rho(770)$	1	0	0.006 ± 0.007	0.9 ± 1.3
$\omega(782)$	0.037 ± 0.002	110.8 ± 1.7	-0.002 ± 0.002	0.2 ± 2.1
$f_0(980)$	0.461 ± 0.011	205.4 ± 2.1	-0.001 ± 0.006	0.3 ± 1.4
$f_2(1270)$	1.051 ± 0.032	340.0 ± 2.4	-0.021 ± 0.030	1.3 ± 2.7
$f_0(1370)$	0.718 ± 0.067	27.4 ± 6.8	0.003 ± 0.048	1.5 ± 5.2
$\rho(1450)$	2.273 ± 0.152	347.7 ± 3.9	0.092 ± 0.142	-6.5 ± 3.5
$f_0(600)$	1.477 ± 0.048	193.3 ± 1.7	-0.007 ± 0.021	-0.9 ± 1.0
σ_2	0.212 ± 0.021	161.7 ± 8.5	0.002 ± 0.010	0.4 ± 2.5
$K^*(892)^+$	0.183 ± 0.008	318.3 ± 1.8	-0.001 ± 0.005	-1.0 ± 1.8
$K_0^*(1430)^+$	0.623 ± 0.036	122.3 ± 3.5	0.025 ± 0.031	-4.2 ± 3.2
$K_2^*(1430)^+$	0.285 ± 0.031	231.5 ± 5.7	-0.015 ± 0.029	-1.7 ± 5.2
Nonresonant	3.488 ± 0.117	111.7 ± 2.2	...	...

Table 6.11.: Results for the masses and widths of the $K^*(892)^\mp$, $f_0(600)$, and σ_2 contributions in the simultaneous D^0-$\bar{D}^0$ Dalitz fit.

Resonance	Mass [MeV/c^2]	Γ [MeV/c^2]
$K^*(892)^\mp$	894.43 ± 0.11	52.23 ± 0.21
$f_0(600)$	539.05 ± 4.85	366.06 ± 8.95
σ_2	1018.16 ± 4.56	77.00 ± 5.21

Table 6.12.: Systematic uncertainties on the fit fraction asymmetry $\mathcal{A}_{\mathrm{FF}}$ for each included intermediate resonance. The contribution from the efficiency asymmetry (Eff.) is described in Section 6.7.1, the one from the background asymmetry (Bkg.) in Section 6.7.2, the one from the fit model (Model) in Section 6.7.3, the one from the efficiency model (Trigger) in Section 6.7.4, and the one from the Blatt-Weisskopf form factors (FF) in Section 6.7.5. The total systematic uncertainties are given by adding up the different contributions in quadrature. The corresponding statistical uncertainties are listed for comparison.

$\mathcal{A}_{\mathrm{FF}}$ [%]	Eff.	Bkg.	Model	Trigger	FF	Sum	Stat.
$K^*(892)^-$	0.09	0.13	0.27	0.09	0.23	0.40	0.39
$K_0^*(1430)^-$	0.88	0.45	3.23	1.08	1.27	3.77	2.89
$K_2^*(1430)^-$	0.78	0.33	3.94	0.11	0.58	4.07	2.93
$K^*(1410)^-$	0.37	0.98	6.21	0.61	0.91	6.39	5.95
$\rho(770)$	0.05	0.00	0.05	0.00	0.04	0.08	0.17
$\omega(782)$	0.64	0.31	1.14	1.01	1.97	2.59	5.77
$f_0(980)$	0.86	1.08	0.75	0.08	0.44	1.63	1.84
$f_2(1270)$	1.01	1.39	0.96	1.50	1.76	3.04	4.00
$f_0(1370)$	0.77	0.39	6.41	0.42	4.06	7.65	15.47
$\rho(1450)$	0.63	0.91	4.74	6.21	1.89	8.11	9.87
$f_0(600)$	0.17	0.19	2.89	0.24	2.14	3.61	2.31
σ_2	0.88	1.87	2.46	0.49	1.87	3.75	7.67
$K^*(892)^+$	0.30	0.59	1.27	0.13	1.47	2.06	4.05
$K_0^*(1430)^+$	0.20	0.10	5.42	7.49	4.52	10.29	8.33
$K_2^*(1430)^+$	0.31	0.78	13.56	0.48	25.77	29.14	13.59

6.7. Systematic Uncertainties

Generally, the systematic uncertainties on the measurements of the overall integrated CP asymmetry, the fit fraction asymmetries, and the CP violating amplitudes and phases can be categorized into experimental and modeling uncertainties. The considered experimental sources are efficiency asymmetries varying over the Dalitz plot, asymmetries of the background in the D^0 and $\bar{D}^0$ samples, and the applied efficiency distribution which is estimated by simulated events without guarantee of a perfectly realistic composition of trigger sub paths. Modeling uncertainties arise from the chosen values for the radius parameters in the Blatt-Weisskopf form factors and the limited knowledge on the complex dynamics of the three-body decay. In this context, the stability of the determined CP violating quantities under variations of the employed Dalitz model is tested.

The contributions from the different sources to the total systematic uncertainties can be found in Tables 6.12–6.15.

Table 6.13.: Systematic uncertainties on the CP violating amplitude b for each included intermediate resonance. Further explanations can be found in the caption of Table 6.12.

b	Eff.	Bkg.	Model	Trigger	FF	Sum	Stat.
$K^*(892)^-$	0.011	0.001	0.000	0.001	0.002	0.011	0.004
$K_0^*(1430)^-$	0.022	0.009	0.029	0.009	0.015	0.041	0.032
$K_2^*(1430)^-$	0.003	0.004	0.022	0.003	0.001	0.023	0.024
$K^*(1410)^-$	0.006	0.000	0.015	0.011	0.007	0.021	0.040
$\rho(770)$	0.007	0.003	0.003	0.001	0.001	0.008	0.007
$\omega(782)$	0.000	0.000	0.000	0.000	0.000	0.000	0.002
$f_0(980)$	0.002	0.003	0.001	0.000	0.001	0.004	0.006
$f_2(1270)$	0.003	0.008	0.008	0.003	0.005	0.013	0.030
$f_0(1370)$	0.002	0.005	0.008	0.008	0.017	0.021	0.048
$\rho(1450)$	0.016	0.023	0.107	0.071	0.032	0.135	0.142
$f_0(600)$	0.011	0.001	0.018	0.002	0.013	0.025	0.021
σ_2	0.002	0.002	0.002	0.001	0.001	0.004	0.010
$K^*(892)^+$	0.001	0.001	0.001	0.000	0.001	0.002	0.005
$K_0^*(1430)^+$	0.003	0.005	0.030	0.008	0.015	0.035	0.031
$K_2^*(1430)^+$	0.005	0.001	0.006	0.002	0.015	0.017	0.029

Table 6.14.: Systematic uncertainties on the CP violating phase ϕ for each included intermediate resonance. Further explanations can be found in the caption of Table 6.12.

ϕ [°]	Eff.	Bkg.	Model	Trigger	FF	Sum	Stat.
$K^*(892)^-$	0.0	0.1	1.0	0.2	0.8	1.3	1.2
$K_0^*(1430)^-$	0.0	0.0	2.1	0.2	0.7	2.2	1.7
$K_2^*(1430)^-$	0.1	0.2	1.0	0.3	0.4	1.1	1.6
$K^*(1410)^-$	0.1	0.0	0.8	1.3	1.6	2.2	2.6
$\rho(770)$	0.1	0.3	1.1	0.2	0.8	1.4	1.3
$\omega(782)$	0.3	0.6	0.9	0.1	0.8	1.4	2.1
$f_0(980)$	0.2	0.0	0.8	0.0	0.7	1.1	1.4
$f_2(1270)$	0.2	0.2	1.3	0.7	1.4	2.1	2.7
$f_0(1370)$	1.0	1.2	1.9	1.0	0.9	2.8	5.2
$\rho(1450)$	0.0	0.6	2.0	3.1	1.2	3.9	3.5
$f_0(600)$	0.1	0.2	1.3	0.2	0.3	1.4	1.0
σ_2	0.2	0.3	0.7	0.4	0.7	1.1	2.5
$K^*(892)^+$	0.1	0.5	1.1	0.1	0.1	1.2	1.8
$K_0^*(1430)^+$	0.0	0.3	3.5	1.0	1.3	3.9	3.2
$K_2^*(1430)^+$	0.6	0.5	2.3	0.5	1.7	3.0	5.2

Table 6.15.: Systematic uncertainties on the overall integrated CP asymmetry $\mathcal{A}_{CP}$. Further explanations can be found in the caption of Table 6.12.

	Eff.	Bkg.	Model	Trigger	FF	Sum	Stat.
$\mathcal{A}_{CP}[10^{-3}]$	3.61	0.89	3.70	0.45	0.99	5.36	5.62

6.7.1. Efficiency Asymmetry

Despite the reweighting procedure of the $\bar{D}^0$ Dalitz plot according to the deviations between the $p_T(\pi_{D^{*+}})$ distributions for negative and positive pion charges shown in Figure 6.53, there could still remain a small asymmetry between the D^0 and $\bar{D}^0$ efficiency distributions. To estimate the size of a systematic effect originating from such an asymmetry, the Dalitz fits of Section 6.6.3 are repeated without reweighting the $\bar{D}^0$ Dalitz plot. The resulting values of the fit fraction asymmetries $\mathcal{A}_{\mathrm{FF}}$ and the CP violating amplitudes b_j and phases ϕ_j are listed in Table 6.16. The overall integrated CP asymmetry results

$$\mathcal{A}_{CP} = (-0.84 \pm 5.59) \cdot 10^{-3} \,.$$

The systematic uncertainties, noted in Tables 6.12–6.15, are calculated as differences between these values and the ones from the default fits listed in Tables 6.9 and 6.10 as well as Equation 6.19.

6.7.2. Background Asymmetry

To investigate a possible systematic effect originating from different Dalitz plot distributions of the background in D^0 and $\bar{D}^0$, the Dalitz fits of Section 6.6.3 are repeated with two separate samples obtained according to the description in Section 6.4.1 and distinguished by the charge of the slow pion in the D^{*+} decay. The resulting values of the fit fraction asymmetries $\mathcal{A}_{\mathrm{FF}}$ and the CP violating amplitudes b_j and phases ϕ_j are listed in Table 6.17. The overall integrated CP asymmetry results

$$\mathcal{A}_{CP} = (-3.56 \pm 5.62) \cdot 10^{-3} \,.$$

The systematic uncertainties, noted in Tables 6.12–6.15, are calculated as differences between these values and the ones from the default fits listed in Tables 6.9 and 6.10 as well as Equation 6.19.

For illustration, the significance of the asymmetry between the normalized D^0 and $\bar{D}^0$ background Dalitz plots (see Equation 6.22) is shown in Figure 6.62. No significant deviation is evident.

Table 6.16.: Results of the Dalitz fits for the fit fraction asymmetries $\mathcal{A}_{\mathrm{FF}}$ and the CP violating amplitudes b_j and phases ϕ_j without reweighting the $\bar{D}^0$ Dalitz plot according to the deviations between the $p_T(\pi_{D^{*+}})$ distributions for negative and positive pion charges shown in Figure 6.53.

Resonance	$\mathcal{A}_{\mathrm{FF}}$ [%]	b	ϕ [°]
$K^*(892)^-$	-0.14 ± 0.39	-0.013 ± 0.005	0.2 ± 1.4
$K_0^*(1430)^-$	-0.40 ± 2.84	-0.032 ± 0.033	-1.4 ± 1.8
$K_2^*(1430)^-$	5.58 ± 2.98	0.021 ± 0.024	-0.4 ± 1.8
$K^*(1410)^-$	-13.29 ± 6.00	-0.077 ± 0.041	-0.5 ± 2.8
$\rho(770)$	0.04 ± 0.17	-0.001 ± 0.007	0.8 ± 1.5
$\omega(782)$	-12.40 ± 5.69	-0.002 ± 0.002	-0.1 ± 2.2
$f_0(980)$	0.66 ± 1.87	-0.003 ± 0.006	0.1 ± 1.5
$f_2(1270)$	-3.09 ± 4.09	-0.024 ± 0.030	1.5 ± 2.8
$f_0(1370)$	6.40 ± 15.70	0.001 ± 0.052	0.5 ± 5.6
$\rho(1450)$	1.33 ± 9.75	0.077 ± 0.150	-6.5 ± 3.6
$f_0(600)$	-0.54 ± 2.32	-0.017 ± 0.021	-1.0 ± 1.1
σ_2	1.76 ± 7.54	0.000 ± 0.010	0.6 ± 2.6
$K^*(892)^+$	-1.29 ± 4.02	-0.002 ± 0.005	-1.0 ± 2.0
$K_0^*(1430)^+$	4.49 ± 8.36	0.022 ± 0.032	-4.2 ± 3.4
$K_2^*(1430)^+$	-13.25 ± 13.69	-0.020 ± 0.029	-2.3 ± 5.2

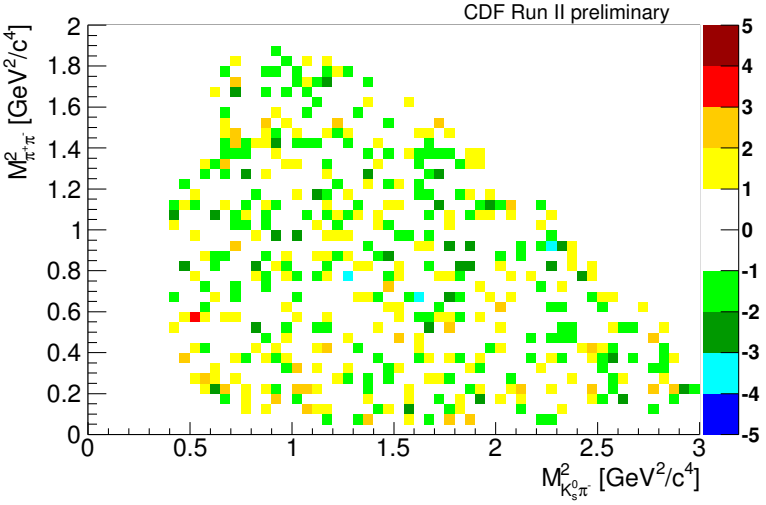

Figure 6.62.: Significance of the bin-by-bin deviations over the Dalitz plot between the numbers of D^0 and $\bar{D}^0$ background candidates obtained from the upper mass sideband $1.92 < M(K^0_S\pi^+\pi-) < 1.95\,\mathrm{GeV}/c^2$.

Table 6.17.: Dalitz fit results for the fit fraction asymmetries $\mathcal{A}_{\mathrm{FF}}$ and the CP violating amplitudes b_j and phases ϕ_j, where the background is determined separately for the D^0 and $\bar{D}^0$ samples.

Resonance	$\mathcal{A}_{\mathrm{FF}}$ [%]	b	ϕ [°]
$K^*(892)^-$	-0.19 ± 0.39	-0.003 ± 0.004	0.1 ± 1.1
$K^*_0(1430)^-$	0.93 ± 2.91	-0.001 ± 0.031	-1.3 ± 1.6
$K^*_2(1430)^-$	5.13 ± 2.94	0.029 ± 0.024	-0.7 ± 1.6
$K^*(1410)^-$	-14.65 ± 5.86	-0.071 ± 0.040	-0.5 ± 2.6
$\rho(770)$	-0.08 ± 0.17	0.003 ± 0.007	0.5 ± 1.2
$\omega(782)$	-12.06 ± 5.77	-0.002 ± 0.002	-0.4 ± 2.0
$f_0(980)$	0.87 ± 1.87	0.002 ± 0.006	0.3 ± 1.3
$f_2(1270)$	-5.49 ± 3.92	-0.029 ± 0.030	1.1 ± 2.6
$f_0(1370)$	5.24 ± 15.46	0.009 ± 0.047	0.3 ± 4.9
$\rho(1450)$	2.87 ± 10.06	0.070 ± 0.139	-6.0 ± 3.4
$f_0(600)$	-0.89 ± 2.31	-0.007 ± 0.021	-1.1 ± 1.0
σ_2	4.52 ± 7.87	0.005 ± 0.010	0.1 ± 2.5
$K^*(892)^+$	-1.59 ± 4.02	-0.001 ± 0.005	-1.5 ± 1.8
$K^*_0(1430)^+$	4.39 ± 8.36	0.020 ± 0.031	-4.4 ± 3.2
$K^*_2(1430)^+$	-12.78 ± 13.71	-0.016 ± 0.029	-2.2 ± 5.1

6.7.3. Fit Model

The systematic uncertainties on the measured CP violating quantities originating from the specific model used for the Dalitz fit are estimated by repeating the fits described in Section 6.6.3 when one of the resonances $K^*(1410)^-$, $f_0(1370)$, σ_2, $K^*_2(1430)^+$, or the nonresonant contribution is excluded from the model. For each case the resulting integrated CP asymmetry, fit fraction asymmetries, and CP violating amplitudes and phases are compared to the values from the default fits and the largest deviations are used as modeling systematic uncertainties listed in Tables 6.12–6.15.

6.7.4. Efficiency Model

Knowledge on the correct Dalitz plot distribution of the reconstruction efficiency is crucial for the fit to work, and simulated events are used for this purpose. Although it affects the D^0 and $\bar{D}^0$ Dalitz fits in the same way and a possible mismodeling is thus not expected to have a strong impact on the results for the CP violating quantities, a reasonable variation is helpful to build confidence in the chosen approach.

Therefore, the Dalitz fits are repeated when only events corresponding to the high-p_T part of the trigger simulation are employed for the efficiency estimation.

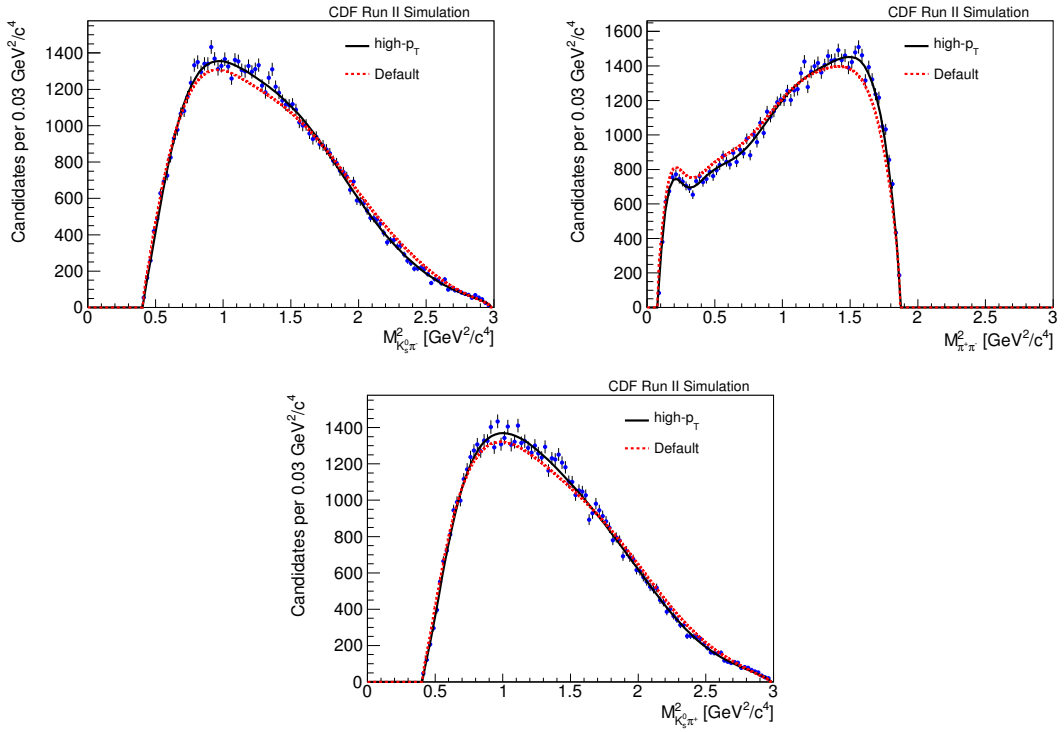

Figure 6.63.: Efficiency fit projections to the three Dalitz plot axes for the high-p_T sub path of the hadronic trigger. The red dashed lines correspond to the analogous projections using all simulated events (Figures 6.31–6.33) normalized to the high-p_T distributions.

Comparisons to the default efficiency distributions are shown in Figure 6.63.

The resulting values of the fit fraction asymmetries $\mathcal{A}_{\mathrm{FF}}$ and the CP violating amplitudes b_j and phases ϕ_j are listed in Table 6.18. The overall integrated CP asymmetry results

$$\mathcal{A}_{CP} = (-4.00 \pm 5.58) \cdot 10^{-3} \,.$$

The systematic uncertainties, noted in Tables 6.12–6.15, are calculated as differences between these values and the ones from the default fits listed in Tables 6.9 and 6.10 as well as Equation 6.19.

6.7.5. Blatt-Weisskopf Form Factors

In the default Dalitz fits, the chosen values for the radius parameter R in the Blatt-Weisskopf form factors are $R = 5\,\mathrm{GeV}^{-1}$ for the D^0 and $R = 1.5\,\mathrm{GeV}^{-1}$ for all intermediate resonances. To estimate the systematic uncertainties originating from deviations from these values, the Dalitz fits of Section 6.6.3 are repeated with both values for the radius parameter halved respective doubled. The systematic

Table 6.18.: Results of the Dalitz fits for the fit fraction asymmetries $\mathcal{A}_{\mathrm{FF}}$ and the CP violating amplitudes b_j and phases ϕ_j with the efficiency modeled by the high-p_T sub path of the hadronic trigger.

Resonance	$\mathcal{A}_{\mathrm{FF}}$ [%]	b	ϕ [°]
$K^*(892)^-$	0.04 ± 0.42	-0.001 ± 0.005	0.5 ± 1.5
$K^*_0(1430)^-$	1.56 ± 3.22	-0.001 ± 0.033	-1.5 ± 1.9
$K^*_2(1430)^-$	4.90 ± 2.99	0.027 ± 0.024	-0.3 ± 2.0
$K^*(1410)^-$	-13.06 ± 5.89	-0.060 ± 0.038	-1.9 ± 3.3
$\rho(770)$	0.08 ± 0.18	0.005 ± 0.007	1.1 ± 1.6
$\omega(782)$	-10.75 ± 5.60	-0.002 ± 0.002	0.3 ± 2.3
$f_0(980)$	-0.28 ± 1.85	-0.001 ± 0.005	0.3 ± 1.7
$f_2(1270)$	-2.60 ± 3.20	-0.018 ± 0.030	0.7 ± 2.4
$f_0(1370)$	5.21 ± 11.93	0.011 ± 0.033	2.5 ± 11.5
$\rho(1450)$	8.17 ± 10.39	0.163 ± 0.164	-3.5 ± 2.8
$f_0(600)$	-0.94 ± 2.16	-0.008 ± 0.021	-0.7 ± 1.2
σ_2	2.16 ± 7.74	0.001 ± 0.010	0.7 ± 2.6
$K^*(892)^+$	-1.13 ± 4.48	-0.001 ± 0.004	-1.0 ± 2.2
$K^*_0(1430)^+$	11.78 ± 14.72	0.033 ± 0.032	-5.2 ± 5.9
$K^*_2(1430)^+$	-14.04 ± 15.08	-0.013 ± 0.029	-1.2 ± 6.2

uncertainties, noted in Tables 6.12–6.15, are then calculated as largest differences between the resulting values for the CP violating quantities and the ones from the default fits listed in Tables 6.9 and 6.10 as well as Equation 6.19.

6.7.6. Fit Discrepancies

The fits are repeated when excluding the two Dalitz plot regions with the largest discrepancies between fit and data, indicated by the black dashed lines in Figure 6.64. Figures 6.65–6.67 show the distributions of the three Dalitz plot variables without these regions together with the corresponding fit projections.

The resulting values of the fit fraction asymmetries $\mathcal{A}_{\mathrm{FF}}$ and the CP violating amplitudes b_j and phases ϕ_j are listed in Table 6.19. The overall integrated CP asymmetry results

$$\mathcal{A}_{CP} = (-4.10 \pm 5.95) \cdot 10^{-3} \,.$$

Since the results agree with the values from the default fits within the statistical uncertainties, no additional systematic uncertainties are assigned.

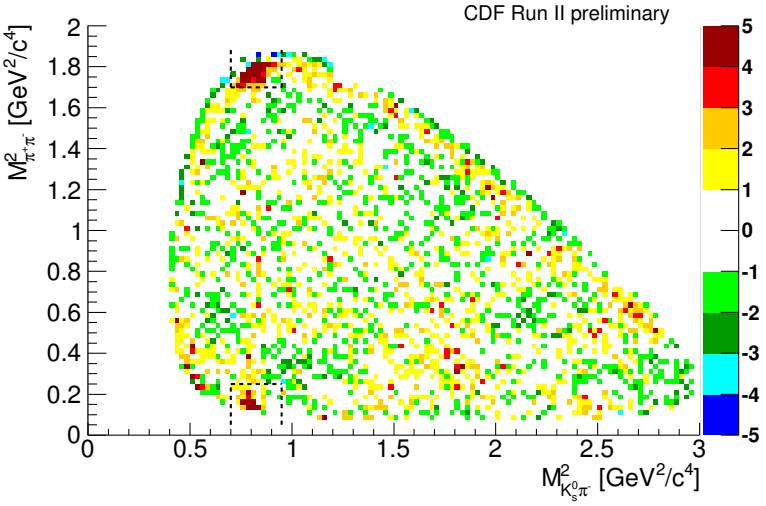

Figure 6.64.: Distribution of $(\text{data} - \text{fit})/\sqrt{\text{data}}$ over the Dalitz plot resulting from a fit where the two regions indicated by the black dashed lines are excluded.

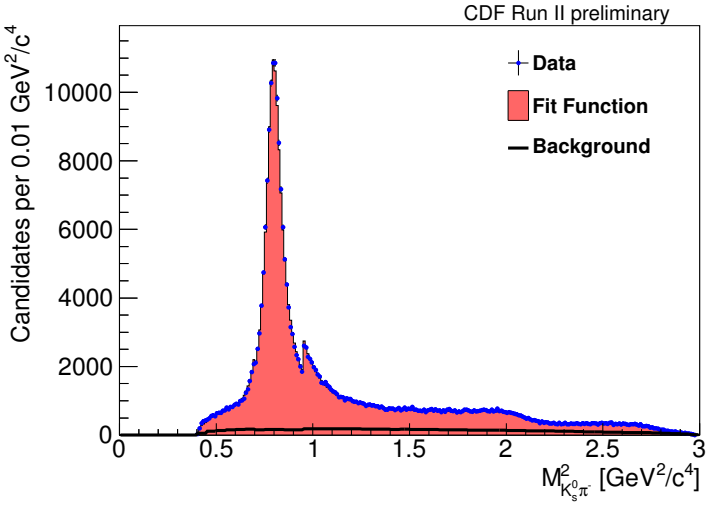

Figure 6.65.: $M^2_{K^0_S\pi^-}$ projection of the Dalitz fit when excluding the regions with the largest discrepancies between fit and data.

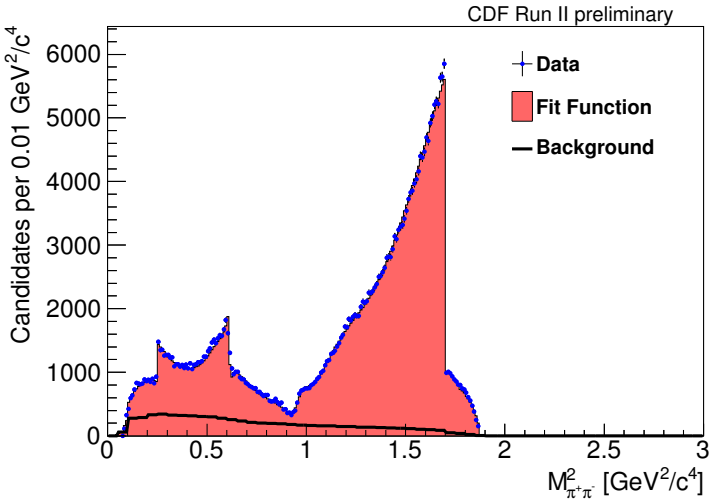

Figure 6.66.: $M^2_{\pi^+\pi^-}$ projection of the Dalitz fit when excluding the regions with the largest discrepancies between fit and data.

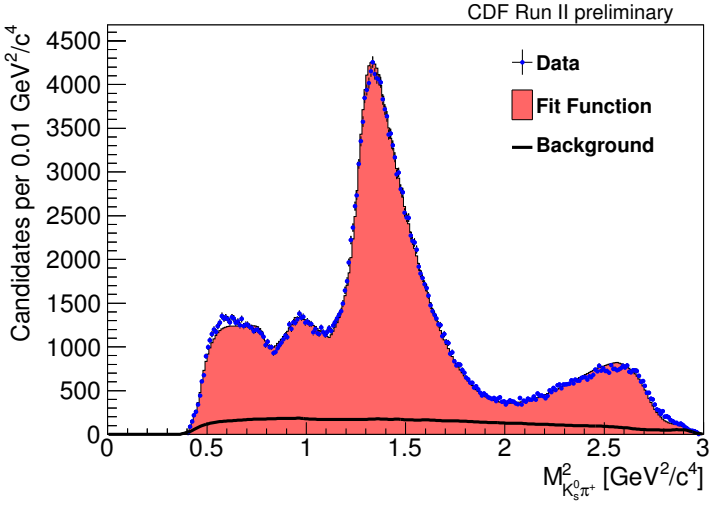

Figure 6.67.: $M^2_{K^0_S\pi^+}$ projection of the Dalitz fit when excluding the regions with the largest discrepancies between fit and data.

Table 6.19.: Results of the Dalitz fits for the fit fraction asymmetries $\mathcal{A}_{\mathrm{FF}}$ and the CP violating amplitudes b_j and phases ϕ_j when excluding the two Dalitz plot regions with the largest discrepancies between fit and data.

Resonance	$\mathcal{A}_{\mathrm{FF}}$ [%]	b	ϕ [°]
$K^*(892)^-$	-0.31 ± 0.43	-0.003 ± 0.005	-1.5 ± 1.2
$K_0^*(1430)^-$	1.52 ± 3.05	0.013 ± 0.033	-3.7 ± 1.7
$K_2^*(1430)^-$	5.22 ± 3.07	0.025 ± 0.025	-2.1 ± 1.7
$K^*(1410)^-$	-18.33 ± 6.08	-0.080 ± 0.041	-3.6 ± 2.8
$\rho(770)$	-0.03 ± 0.18	0.005 ± 0.007	-0.9 ± 1.3
$\omega(782)$	-12.60 ± 5.54	-0.002 ± 0.002	-1.8 ± 2.1
$f_0(980)$	-0.48 ± 1.78	-0.002 ± 0.005	-1.7 ± 1.4
$f_2(1270)$	-5.39 ± 3.73	-0.024 ± 0.031	0.1 ± 2.7
$f_0(1370)$	26.42 ± 25.67	0.110 ± 0.070	-3.3 ± 4.3
$\rho(1450)$	3.81 ± 9.63	0.099 ± 0.146	-4.8 ± 3.6
$f_0(600)$	-2.60 ± 2.28	-0.022 ± 0.022	-2.0 ± 1.0
σ_2	0.72 ± 6.84	-0.001 ± 0.011	-1.0 ± 2.3
$K^*(892)^+$	-1.00 ± 2.35	0.002 ± 0.005	-3.0 ± 1.9
$K_0^*(1430)^+$	13.39 ± 10.54	0.047 ± 0.034	-4.8 ± 3.2
$K_2^*(1430)^+$	-5.34 ± 15.88	-0.007 ± 0.029	-3.4 ± 5.6

6.8. Results

The results of the combined D^0-$\bar{D}^0$ Dalitz fit to the resonant substructure of the decay $D^0 \to K^0_S \pi^+ \pi^-$ are already listed in Table 6.6. In Table 6.20 the fit fractions are compared to values obtained from the Belle experiment [65]. Considering the complicated structure of this fit, the various fit fractions are in good agreement. For some of them, like the one for $K^*(892)^-$, the measurements at hand are more precise than the Belle measurements, while for others, like the one for $\omega(782)$, they are not. The reason for that is the different efficiency distribution. Whereas it is almost flat over the Dalitz plot for Belle, it varies strongly for this study because of the kinematic requirements of the two track trigger. The signal yields of the two measurements are comparable, about 350000 here and 290900 in Reference [65]. In Reference [66] BABAR reports 744000 signal events and Belle should have at least as much in their full data set. The smaller number from CDF is due to the mentioned efficiency limitation in parts of the phase space, the decay length requirement of the two track trigger, and the poor K^0_S reconstruction efficiency. However, this does not necessarily mean that the sensitivity to CP violating effects is worse than for the B factories, because the longer mean life time induced by the decay length requirement can lead to larger contributions from indirect CP violation and CP violation in the interference of mixing and decay.

CP violation is searched for in the Dalitz fits to the D^0 and $\bar{D}^0$ samples, and no hints of any effects are found. The results for the CP violating amplitudes and phases, defined in Equation 6.20 and obtained from the simultaneous fit to the D^0 and $\bar{D}^0$ Dalitz plots, can be found in Table 6.21. The fit fraction asymmetries for the intermediate resonances, defined in Equation 6.17, are listed in Table 6.22 together with the corresponding values from the CLEO experiment [78]. Since the CLEO data sample consists of only 5299 signal events, the results presented here are much more precise. This also holds for the overall integrated CP asymmetry defined in Equation 6.18, which yields

$$\mathcal{A}_{CP} = -0.0045 \pm 0.0056 \pm 0.0054\,.$$

The corresponding value from CLEO [78] reads

$$\mathcal{A}_{CP} = 0.009 \pm 0.021\,^{+0.010\ +0.013}_{-0.043\ -0.037}\,.$$

There are no comparable direct measurements of these CP violating quantities from the B factories.

To disentangle indirect from direct CP violating effects, like it was done in Reference [87] for the decays $D^0 \to K^+ K^-$ and $D^0 \to \pi^+ \pi^-$, the D^0 lifetime distribution, shown in Figure 6.68, is studied. In this distribution the background is subtracted by means of the D^0 mass sidebands $1.80 < M(K^0_S\pi^+\pi-) < 1.82\,\mathrm{GeV}/c^2$ and $1.91 < M(K^0_S\pi^+\pi-) < 1.94\,\mathrm{GeV}/c^2$, and nonprompt candidates with D^{*+}

Table 6.20.: Comparison of the determined fit fractions of the included intermediate resonances with the results from the Belle experiment [65]. The uncertainties are statistical only.

Resonance	FF (CDF) [%]	FF (Belle) [%]
$K^*(892)^-$	59.44 ± 0.29	62.9 ± 0.8
$K_0^*(1430)^-$	4.01 ± 0.17	7.93 ± 0.09
$K_2^*(1430)^-$	2.17 ± 0.09	1.40 ± 0.06
$K^*(1410)^-$	0.72 ± 0.07	0.49 ± 0.07
$K^*(1680)^-$	$\cdots$	0.06 ± 0.04
$\rho(770)$	21.08 ± 0.20	21.2 ± 0.5
$\omega(782)$	0.52 ± 0.05	0.526 ± 0.014
$f_0(980)$	5.20 ± 0.23	4.72 ± 0.05
$f_2(1270)$	0.80 ± 0.05	1.82 ± 0.05
$f_0(1370)$	0.34 ± 0.06	1.9 ± 0.3
$\rho(1450)$	0.45 ± 0.06	0.11 ± 0.04
$f_0(600)$	10.38 ± 0.41	11.0 ± 0.7
σ_2	0.56 ± 0.04	0.54 ± 0.10
$K^*(892)^+$	0.63 ± 0.05	0.526 ± 0.016
$K_0^*(1430)^+$	0.55 ± 0.06	0.22 ± 0.04
$K_2^*(1430)^+$	0.12 ± 0.02	0.093 ± 0.014
$K^*(1410)^+$	$\cdots$	0.21 ± 0.03
$K^*(1680)^+$	$\cdots$	0.30 ± 0.07
Nonresonant	6.71 ± 0.47	5.0 ± 1.0
Sum	113.7	120.9

Table 6.21.: Results of the simultaneous D^0-$\bar{D}^0$ Dalitz fit for the CP violating amplitudes b and phases ϕ. The first uncertainties are statistical and the second systematic.

Resonance	b	ϕ [°]
$K^*(892)^-$	$-0.002 \pm 0.004 \pm 0.011$	$0.2 \pm 1.2 \pm 1.3$
$K^*_0(1430)^-$	$-0.010 \pm 0.032 \pm 0.041$	$-1.3 \pm 1.7 \pm 2.2$
$K^*_2(1430)^-$	$0.024 \pm 0.024 \pm 0.023$	$-0.5 \pm 1.6 \pm 1.1$
$K^*(1410)^-$	$-0.071 \pm 0.040 \pm 0.021$	$-0.5 \pm 2.6 \pm 2.2$
$\rho(770)$	$0.006 \pm 0.007 \pm 0.008$	$0.9 \pm 1.3 \pm 1.4$
$\omega(782)$	$-0.002 \pm 0.002 \pm 0.000$	$0.2 \pm 2.1 \pm 1.4$
$f_0(980)$	$-0.001 \pm 0.006 \pm 0.004$	$0.3 \pm 1.4 \pm 1.1$
$f_2(1270)$	$-0.021 \pm 0.030 \pm 0.013$	$1.3 \pm 2.7 \pm 2.1$
$f_0(1370)$	$0.003 \pm 0.048 \pm 0.021$	$1.5 \pm 5.2 \pm 2.8$
$\rho(1450)$	$0.092 \pm 0.142 \pm 0.135$	$-6.5 \pm 3.5 \pm 3.9$
$f_0(600)$	$-0.007 \pm 0.021 \pm 0.025$	$-0.9 \pm 1.0 \pm 1.4$
σ_2	$0.002 \pm 0.010 \pm 0.004$	$0.4 \pm 2.5 \pm 1.1$
$K^*(892)^+$	$-0.001 \pm 0.005 \pm 0.002$	$-1.0 \pm 1.8 \pm 1.2$
$K^*_0(1430)^+$	$0.025 \pm 0.031 \pm 0.035$	$-4.2 \pm 3.2 \pm 3.9$
$K^*_2(1430)^+$	$-0.015 \pm 0.029 \pm 0.017$	$-1.7 \pm 5.2 \pm 3.0$

impact parameter significance less than 3.5, indicated by the vertical dashed line in Figure 6.69, are removed.

In the distribution of the D^{*+} impact parameter significance in Figure 6.69 the background is subtraced by means of the D^{*+} mass difference sidebands $140 < \Delta M(D^{*\pm}) < 142\,\mathrm{MeV}/c^2$ and $150 < \Delta M(D^{*\pm}) < 152\,\mathrm{MeV}/c^2$. The sum of two Gaussian functions is fitted to the data in order to determine the fractions of the prompt and nonprompt contributions below the indicated value of $d_0/\sigma_{d_0} = 3.5$.

This means that the lifetime distribution of Figure 6.68 still contains about 11% of nonprompt D^0 candidates. To account for that the correspondingly normalized nonprompt distribution, estimated by the candidates with D^{*+} impact parameter significance greater than 3.5, is subtracted. The quoted mean lifetime of $2.40 \cdot \tau(D^0)$ calculated from that corresponds to the mean lifetime of the prompt part (89%) of the signal. It is combined with the nonprompt part (11%) as

$$\frac{\langle t \rangle}{\tau} = 0.11 \cdot 1.33 + 0.89 \cdot 2.40 = 2.28\,,$$

where the value $1.33 \cdot \tau(D^0)$ for the nonprompt part corresponds to the mean B lifetime without detector resolution and is scaled from the value evaluated in Reference [87]. The indirect CP asymmetry a^{ind}_{CP} can then be determined from the

Table 6.22.: Comparison of the determined fit fraction asymmetries $\mathcal{A}_{\mathrm{FF}}$ for the included intermediate resonances with the results from the CLEO experiment [78]. For the CDF results the first uncertainties are statistical and the second combined systematic. For the CLEO results the first uncertainties are statistical, the second experimental systematic, and the third modeling systematic.

Resonance	$\mathcal{A}_{\mathrm{FF}}$ (CDF) [%]	$\mathcal{A}_{\mathrm{FF}}$ (CLEO) [%]
$K^*(892)^-$	$-0.05 \pm 0.39 \pm 0.40$	$2.5 \pm 1.9\,^{+1.5\ +2.9}_{-0.7\ -0.3}$
$K_0^*(1430)^-$	$0.48 \pm 2.89 \pm 3.77$	$-0.2 \pm 11.3\,^{+8.6\ +1.9}_{-4.9\ -1.0}$
$K_2^*(1430)^-$	$4.80 \pm 2.93 \pm 4.07$	$-7 \pm 25\,^{+8\ \ +10}_{-26\ -1}$
$K^*(1410)^-$	$-13.66 \pm 5.95 \pm 6.39$	$\cdots$
$\rho(770)$	$0.09 \pm 0.17 \pm 0.08$	$3.1 \pm 3.8\,^{+2.7\ +0.4}_{-1.8\ -1.2}$
$\omega(782)$	$-11.76 \pm 5.77 \pm 2.59$	$-26 \pm 24\,^{+22\ +2}_{-2\ \ -4}$
$f_0(980)$	$-0.20 \pm 1.84 \pm 1.63$	$-4.7 \pm 11.0\,^{+24.9\ +0.3}_{-7.4\ \ -4.8}$
$f_2(1270)$	$-4.10 \pm 4.00 \pm 3.04$	$34 \pm 51\,^{+25\ +21}_{-71\ -34}$
$f_0(1370)$	$5.63 \pm 15.47 \pm 7.65$	$18 \pm 10\,^{+2\ \ +13}_{-21\ -6}$
$\rho(1450)$	$1.96 \pm 9.87 \pm 8.11$	$\cdots$
$f_0(600)$	$-0.70 \pm 2.31 \pm 3.61$	$\cdots$
σ_2	$2.65 \pm 7.67 \pm 3.75$	$\cdots$
$K^*(892)^+$	$-1.00 \pm 4.05 \pm 2.06$	$-21 \pm 42\,^{+17\ +22}_{-28\ -4}$
$K_0^*(1430)^+$	$4.30 \pm 8.33 \pm 10.29$	$\cdots$
$K_2^*(1430)^+$	$-13.56 \pm 13.59 \pm 29.14$	$\cdots$
$K^*(1680)^-$	$\cdots$	$-36 \pm 19\,^{+9\ \ +5}_{-35\ -1}$

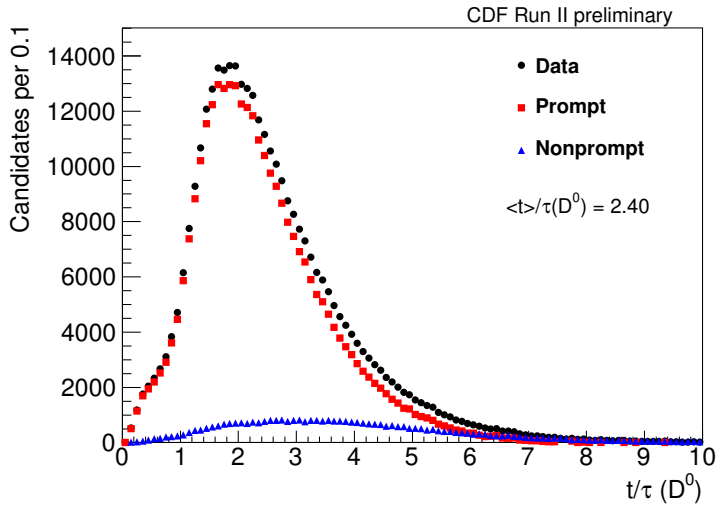

Figure 6.68.: D^0 lifetime distribution in units of the mean D^0 lifetime $\tau(D^0)$ (black dots). The background is subtracted by means of the D^0 mass sidebands $1.80 < M(K^0_S\pi^+\pi-) < 1.82\,\mathrm{GeV}/c^2$ and $1.91 < M(K^0_S\pi^+\pi-) < 1.94\,\mathrm{GeV}/c^2$. The nonprompt contribution (blue triangles) is estimated by the candidates with D^{*+} impact parameter significance less than 3.5, indicated by the vertical dashed line in Figure 6.69. The prompt contribution (red squares), resulting from the difference of the overall and the nonprompt one, is used to determine the average lifetime $\frac{\langle t \rangle}{\tau} = 2.40$ of the D^0 sample.

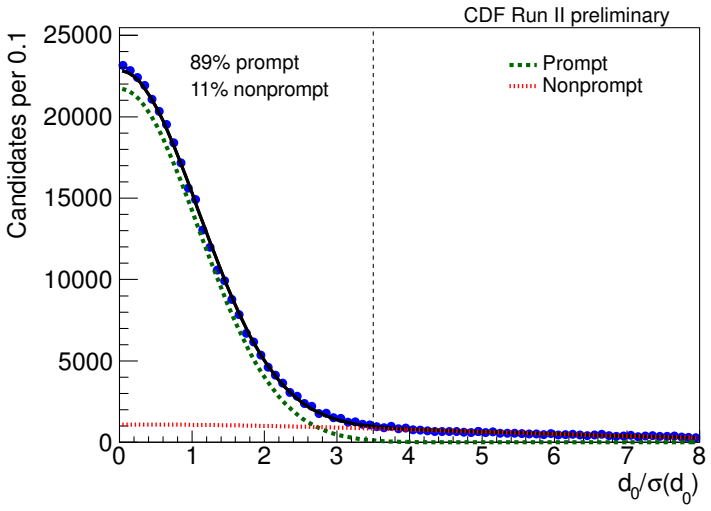

Figure 6.69.: D^{*+} impact parameter significance. The data distribution (blue dots) is fitted by two Gaussian functions representing the prompt (green dashed line) and nonprompt (red short-dashed line) contributions to the D^0 sample. The corresponding fractions are calculated for the region below 3.5, indicated by the dashed vertical line.

measured $\mathcal{A}_{CP}$ by means of the approximation

$$\mathcal{A}_{CP} = a_{CP}^{\mathrm{dir}} + \frac{\langle t \rangle}{\tau} \cdot a_{CP}^{\mathrm{ind}} \tag{6.21}$$

for slow D^0 mixing, when a_{CP}^{dir} is set to zero. By using the combined statistical and systematic uncertainty 0.03 on the mean lifetime, estimated in Reference [87], the indirect CP asymmetry yields

$$a_{CP}^{\mathrm{ind}} = -0.0020 \pm 0.0025 \pm 0.0024\,.$$

This result is very robust against reasonable variations of the mean lifetime and its uncertainty.

Inversely, when setting a_{CP}^{ind} to zero, the direct CP asymmetry a_{CP}^{dir} corresponds to the measured value of $\mathcal{A}_{CP}$,

$$a_{CP}^{\mathrm{dir}} = -0.0045 \pm 0.0056 \pm 0.0054\,.$$

6.9. Model-independent search for CP Asymmetries in the Dalitz Plot

Following the so-called Miranda procedure described in Reference [88], a model-independent search for CP violation in the Dalitz plot distribution of the decay $D^0 \to K^0_S \pi^+ \pi^-$ is performed by comparing the binned, normalized Dalitz plots for D^0 and $\bar{D}^0$. Model-independent means that no assumptions about the resonant substructure of the decay are used. In this context, the approach can serve as a complementary verification of the results from the Dalitz fits described in Section 6.6.3.

In detail, the method works as follows:

- An appropriate binning of the separate D^0 and $\bar{D}^0$ Dalitz plots is chosen, where the production flavor is determined from $D^*(2010)^+ \to D^0 \pi^+$. Here, two different uniform Dalitz plot binnings with quadratic bin sizes of 0.025 respective $0.1\,\mathrm{GeV}^2/c^4$ are used.

- The significance of the asymmetry between the numbers of D^0 and $\bar{D}^0$ candidates,
$$\frac{N_{D^0} - N_{\bar{D}^0}}{\sqrt{N_{D^0} + N_{\bar{D}^0}}}\,, \tag{6.22}$$
is calculated for each bin and drawn in the two-dimensional pattern of the Dalitz plot. CP asymmetries should show up as clustering of discrepancies with the same sign.

- A profitable feature for a statistical test is that the sum of squares of the significance asymmetries in each bin corresponds to a χ^2 value. With the number of degrees of freedom NDF being the number of Dalitz plot bins minus 1 (for the normalization), the p-value prob, that is the probability to obtain this or a larger χ^2 value for two consistent distributions, can be calculated as the integral of the corresponding χ^2 distribution from χ^2 to infinity.

- A histogram of the asymmetry significance distribution is plotted. For vanishing CP violation one expects a Gaussian distribution with $\mu = 0$ and $\sigma = 1$.

In the following, pseudoexperiments are used to demonstrate the functionality of the method before it is applied to the data sample selected according to Section 6.3.

6.9.1. Pseudoexperiments

The aim of the studies with pseudoexperiments is to verify the statistical procedure. That means if the events are generated without CP violation, no asymmetry should

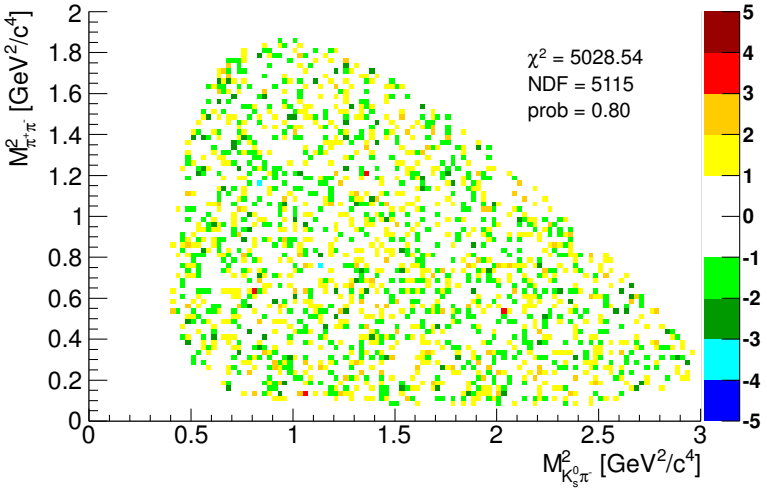

Figure 6.70.: Dalitz plot distribution (quadratic bin sizes of $0.025\,\mathrm{GeV}^2/c^4$) of the asymmetry significance between the numbers of D^0 and $\bar{D}^0$ candidates in samples of pseudoexperiments generated without CP violation.

be detected. On the other hand, it should be possible to find a generated CP violation if it is large enough. The random events of the pseudoexperiments are generated according to the PDF of the Dalitz fit model described in Section 6.6.2 with parameters obtained from the fit to data.

In Figures 6.70–6.73 the outcome of the Miranda method for D^0 and $\bar{D}^0$ samples generated according to identical parameter sets, that is without CP violation, is presented. Figures 6.70 and 6.72 show the Dalitz plot distributions of the asymmetry significance between the numbers of D^0 and $\bar{D}^0$ candidates according to Equation 6.22 for quadratic bin sizes of $0.025\,\mathrm{GeV}^2/c^4$ and $0.1\,\mathrm{GeV}^2/c^4$, respectively. Figures 6.71 and 6.73 show the corresponding histograms of the asymmetry significance, each together with a Gaussian function fitted to the data. The resulting Gaussian parameters are consistent with $\mu = 0$, $\sigma = 1$ and the p-values calculated from the asymmetry significance distributions are much higher than zero. So, as desired, no asymmetry is detected.

To demonstrate the effect of CP violation and the ability of the applied method to detect it, D^0 and $\bar{D}^0$ samples are generated with a difference in the $f_0(980)$ phase $\Delta\delta_{f_0(980)}$. For illustration, the Dalitz plot distribution (quadratic bin sizes of $0.025\,\mathrm{GeV}^2/c^4$) and the corresponding histogram of the asymmetry significance for an extreme example with $\Delta\delta_{f_0(980)} = 45°$ are shown in Figures 6.74 and 6.75, respectively. The discrepancies in the D^0 and $\bar{D}^0$ Dalitz plots are evident. Furthermore, the resulting Gaussian parameters are not consistent with $\mu = 0$, $\sigma = 1$ and the p-value calculated from the asymmetry significance distribution is almost

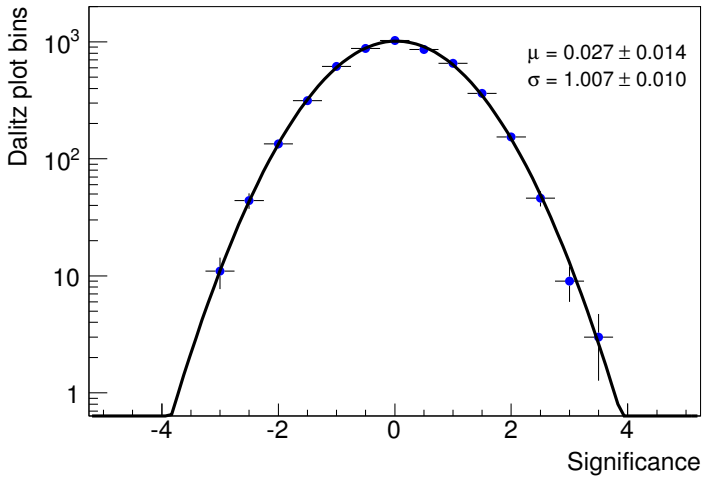

Figure 6.71.: Histogram of the asymmetry significance among the Dalitz plot (quadratic bin sizes of $0.025\,\mathrm{GeV}^2/c^4$) between the numbers of D^0 and $\bar{D}^0$ candidates in samples of pseudoexperiments generated without CP violation.

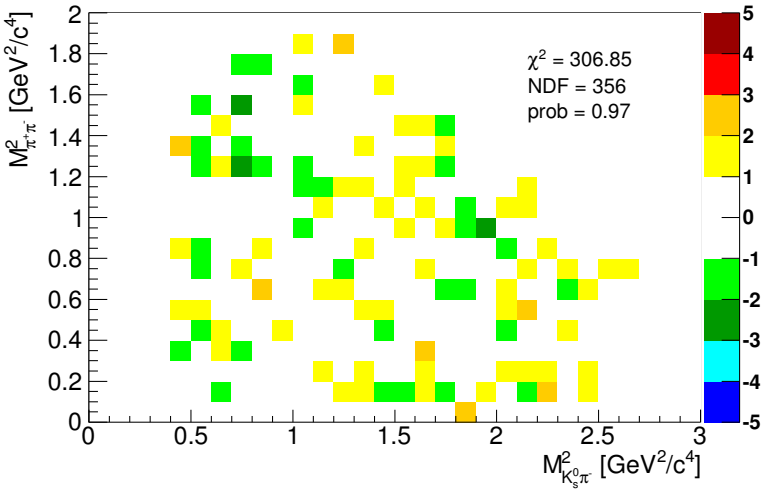

Figure 6.72.: Dalitz plot distribution (quadratic bin sizes of $0.1\,\mathrm{GeV}^2/c^4$) of the asymmetry significance between the numbers of D^0 and $\bar{D}^0$ candidates in samples of pseudoexperiments generated without CP violation.

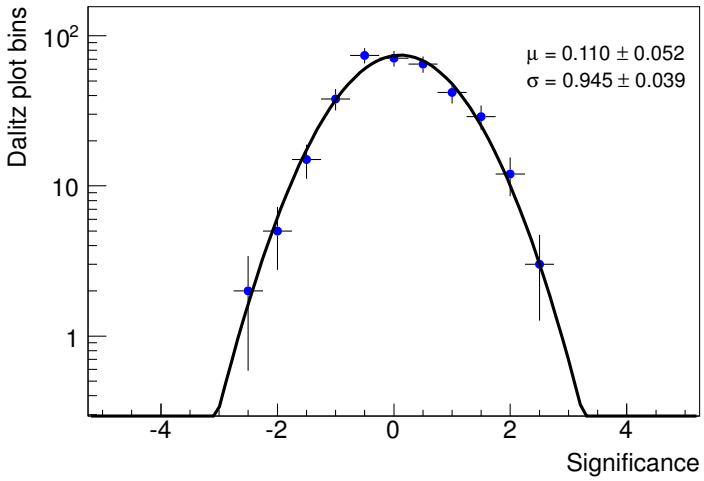

Figure 6.73.: Histogram of the asymmetry significance among the Dalitz plot (quadratic bin sizes of $0.1\,\mathrm{GeV}^2/c^4$) between the numbers of D^0 and $\bar{D}^0$ candidates in samples of pseudoexperiments generated without CP violation.

zero.

The corresponding asymmetry significance plots for a smaller effect of $\Delta\delta_{f_0(980)} = 15°$ can be found in Figures 6.76–6.77, where only the Dalitz plot region between the two dashed lines in Figure 6.76, enclosing the major part of the $f_0(980)$ signal, is used for the creation of the histogram in Figure 6.77 and the calculation of the χ^2, NDF, and p-value listed in this region. Compared to the usage of the whole Dalitz plot, this restriction to the part with the strongest discrepancies leads to clearer signs of CP asymmetries. Figures 6.78 and 6.79 show the same as Figures 6.76 and 6.77 for the broader binning of $0.1\,\mathrm{GeV}^2/c^4$, leading to an even lower p-value.

6.9.2. Real Data

After the successful verification of the method by means of pseudoexperiments, it is applied to real data in order to search for hints of CP violation. The normalization of the D^0 and $\bar{D}^0$ distributions leads to a complete cancellation of all asymmetries that are flat over the Dalitz plot. However, an efficiency asymmetry varying over the Dalitz plot could be misinterpreted as CP violation. As described in Section 6.6.3, this problem is also relevant for the CP violation search in the Dalitz fits, and the reweighting procedure used there is applied here as well. This implicitly normalizes the $\bar{D}^0$ according to the D^0 Dalitz plot.

The resulting Dalitz plot distributions of the asymmetry significance between the numbers of D^0 and $\bar{D}^0$ candidates for quadratic bin sizes of $0.025\,\mathrm{GeV}^2/c^4$ and

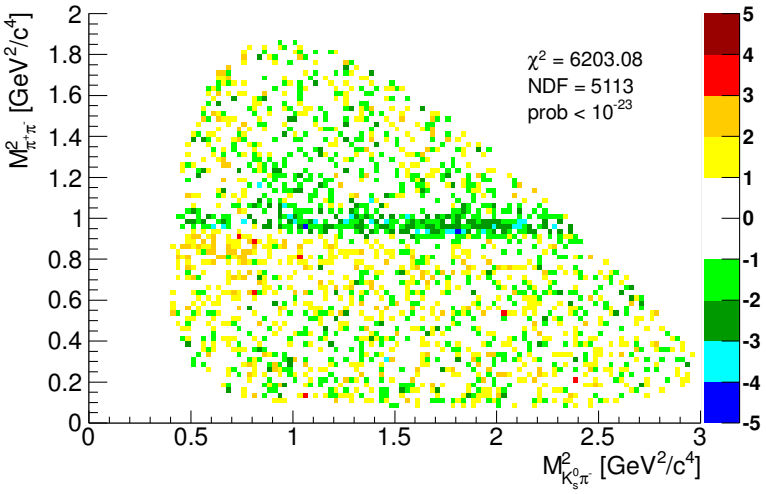

Figure 6.74.: Dalitz plot distribution (quadratic bin sizes of $0.025\,\mathrm{GeV}^2/c^4$) of the asymmetry significance between the numbers of D^0 and $\bar{D}^0$ candidates in samples of pseudoexperiments generated with $\Delta\delta_{f_0(980)} = 45°$.

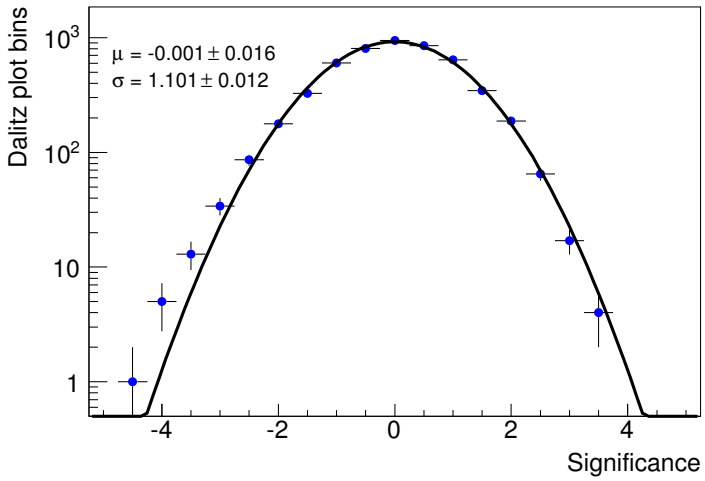

Figure 6.75.: Histogram of the asymmetry significance among the Dalitz plot (quadratic bin sizes of $0.025\,\mathrm{GeV}^2/c^4$) between the numbers of D^0 and $\bar{D}^0$ candidates in samples of pseudoexperiments generated with $\Delta\delta_{f_0(980)} = 45°$.

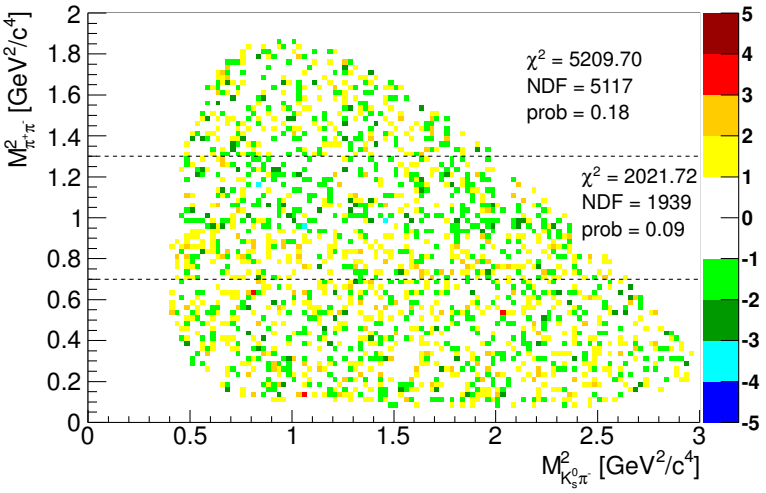

Figure 6.76.: Dalitz plot distribution (quadratic bin sizes of $0.025\,\mathrm{GeV}^2/c^4$) of the asymmetry significance between the numbers of D^0 and $\bar{D}^0$ candidates in samples of pseudoexperiments generated with $\Delta\delta_{f_0(980)} = 15°$. The horizontal dashed lines indicate the Dalitz plot region used for the calculation of the χ^2, NDF, and p-value listed therein.

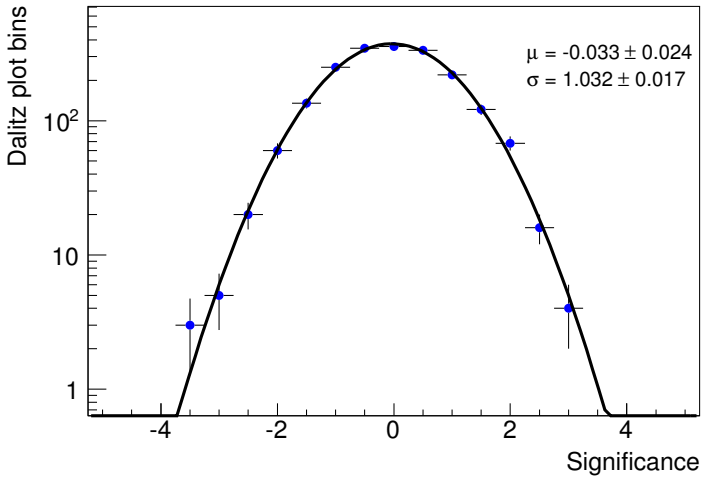

Figure 6.77.: Histogram of the asymmetry significance among the Dalitz plot (quadratic bin sizes of $0.025\,\mathrm{GeV}^2/c^4$) between the numbers of D^0 and $\bar{D}^0$ candidates in samples of pseudoexperiments generated with $\Delta\delta_{f_0(980)} = 15°$. Only the Dalitz plot region between the two dashed lines in Figure 6.76 is used for the creation of this histogram.

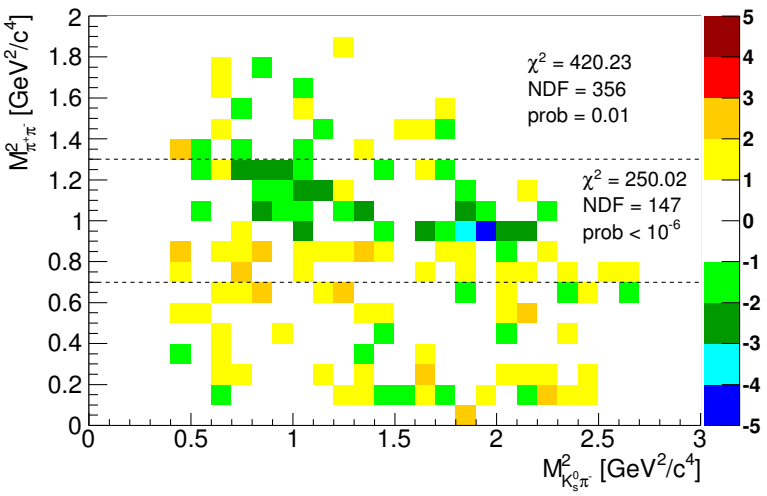

Figure 6.78.: Dalitz plot distribution (quadratic bin sizes of $0.1\,\mathrm{GeV}^2/c^4$) of the asymmetry significance between the numbers of D^0 and $\bar{D}^0$ candidates in samples of pseudoexperiments generated with $\Delta\delta_{f_0(980)} = 15°$. The horizontal dashed lines indicate the Dalitz plot region used for the calculation of the χ^2, NDF, and p-value listed therein.

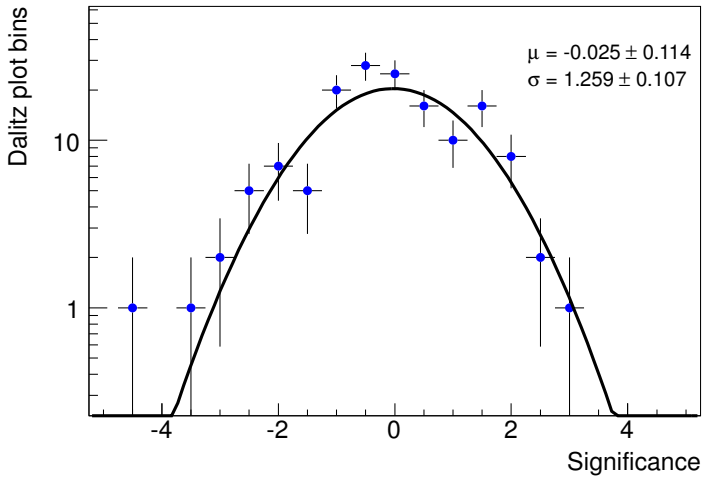

Figure 6.79.: Histogram of the asymmetry significance among the Dalitz plot (quadratic bin sizes of $0.1\,\mathrm{GeV}^2/c^4$) between the numbers of D^0 and $\bar{D}^0$ candidates in samples of pseudoexperiments generated with $\Delta\delta_{f_0(980)} = 15°$. Only the Dalitz plot region between the two dashed lines in Figure 6.78 is used for the creation of this histogram.

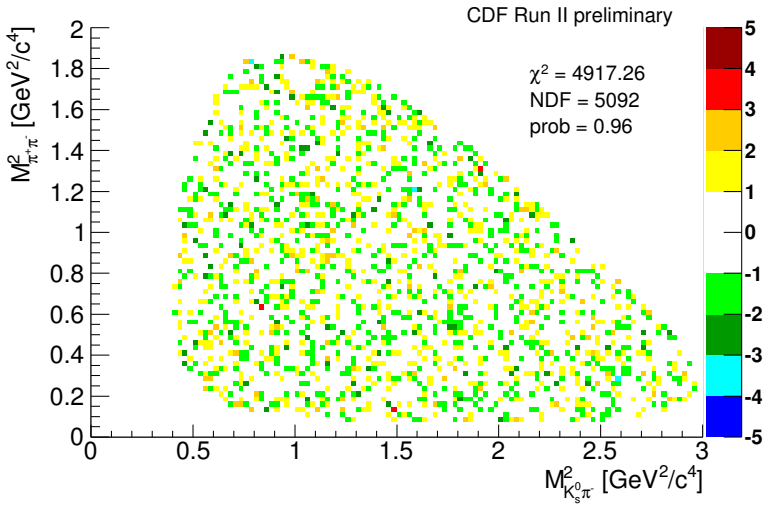

Figure 6.80.: Dalitz plot distribution (quadratic bin sizes of $0.025\,\mathrm{GeV}^2/c^4$) of the asymmetry significance between the numbers of D^0 and $\bar{D}^0$ candidates in real data.

$0.1\,\mathrm{GeV}^2/c^4$ as well as the corresponding histograms of the asymmetry significance are shown in Figures 6.80–6.83. The Gaussian parameters obtained from the fits are consistent with $\mu = 0$, $\sigma = 1$ and the p-values calculated from the asymmetry significance distributions are much higher than zero. So the result of this model-independent approach is that no hints for CP asymmetries between the D^0 and $\bar{D}^0$ Dalitz plots are found.

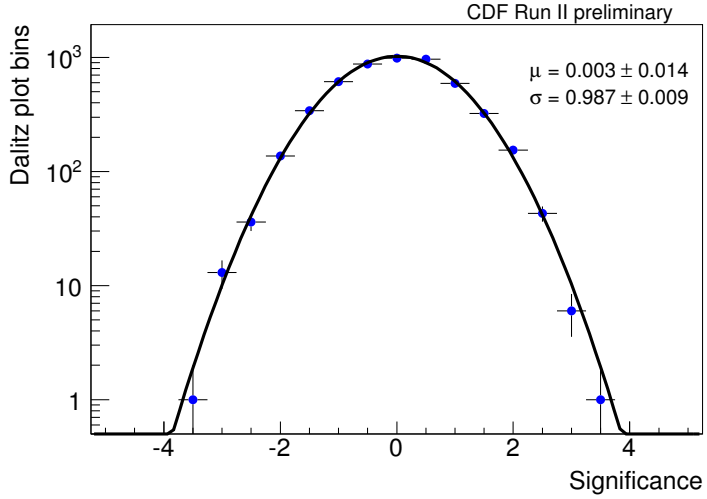

Figure 6.81.: Histogram of the asymmetry significance among the Dalitz plot (quadratic bin sizes of $0.025\,\mathrm{GeV}^2/c^4$) between the numbers of D^0 and $\bar{D}^0$ candidates in real data.

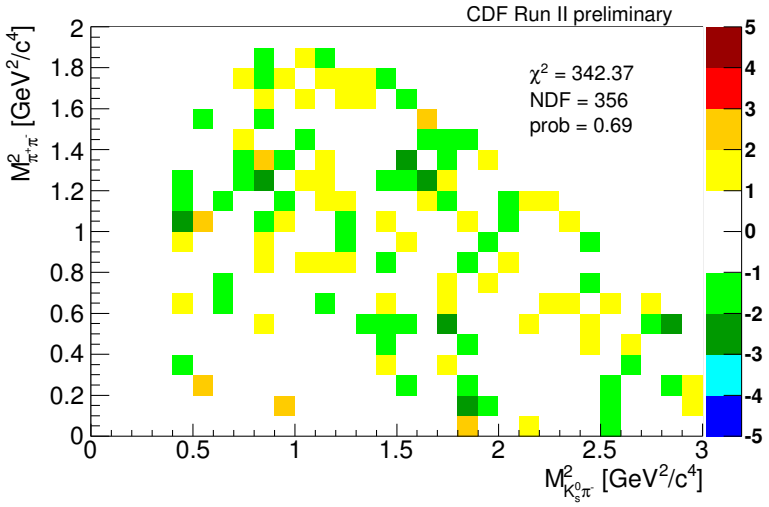

Figure 6.82.: Dalitz plot distribution (quadratic bin sizes of $0.1\,\mathrm{GeV}^2/c^4$) of the asymmetry significance between the numbers of D^0 and $\bar{D}^0$ candidates in real data.

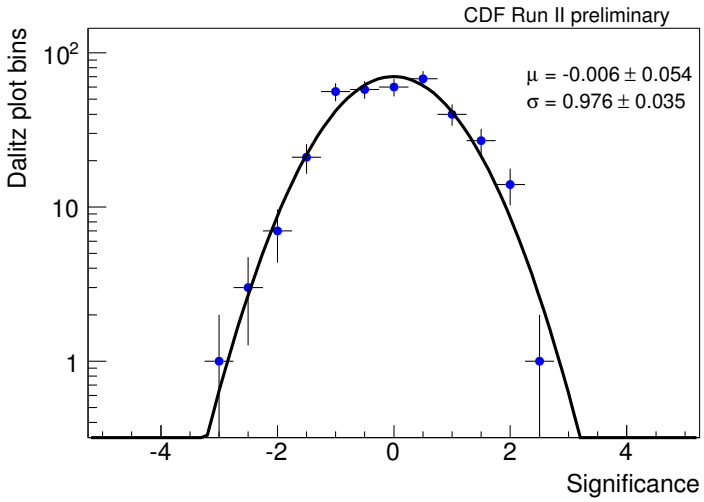

Figure 6.83.: Histogram of the asymmetry significance among the Dalitz plot (quadratic bin sizes of $0.1\,\mathrm{GeV}^2/c^4$) between the numbers of D^0 and $\bar{D}^0$ candidates in real data.

7. Conclusion

In this thesis two different analyses are presented, namely the measurements of the properties of $\Lambda_c(2595)^+$, $\Lambda_c(2625)^+$, $\Sigma_c(2455)^{++,0}$, and $\Sigma_c(2520)^{++,0}$ baryons as well as the search for CP violation in the Dalitz plot of the decay $D^0 \to K^0_S\,\pi^+\,\pi^-$. Both studies are performed using data corresponding to $5.2\,\mathrm{fb}^{-1}$ respective $6.0\,\mathrm{fb}^{-1}$ of integrated luminosity from $p\bar{p}$ collisions at a center-of-mass energy of 1.96 TeV, collected with the CDF II detector at the Fermilab Tevatron.

To measure the mass differences to the Λ_c^+ groundstate as well as the decay widths of the six charmed baryon resonances $\Sigma_c(2455)^0$, $\Sigma_c(2520)^0$, $\Sigma_c(2455)^{++}$, $\Sigma_c(2520)^{++}$, $\Lambda_c(2595)^+$, and $\Lambda_c(2625)^+$, the decay channels $\Lambda_c^+\,\pi^-$, $\Lambda_c^+\,\pi^+$ and $\Lambda_c^+\,\pi^+\,\pi^-$ are reconstructed, where Λ_c^+ decays to $p\,K^-\,\pi^+$.

The multivariate selection of the desired states is performed by means of the NeuroBayes program package, where the neural networks are trained using real data only by applying sideband subtractions with the ${}_s\mathcal{P}lot$ technique. This method has the advantage that no simulated events are needed for the training process. It is used for the first time in this analysis.

It turns out that the decay $\Lambda_c(2595)^+ \to \Lambda_c^+\,\pi^+\,\pi^-$ proceeds almost exclusively via the intermediate resonances $\Sigma_c(2455)^0\,\pi^+$ and $\Sigma_c(2455)^{++}\,\pi^-$. Since the sum of the $\Sigma_c(2455)^{++,0}$ and $\pi^\mp$ masses is very close to the $\Lambda_c(2595)^+$ mass, the $\Lambda_c(2595)^+$ signal structure is strongly distorted from the usual Breit-Wigner shape by kinematical threshold effects. By taking this modification into account the mass difference of the $\Lambda_c(2595)^+$ is measured approximately $3\,\mathrm{MeV}/c^2$ lower than in previous determinations. The large data sample at hand facilitates the distinction between the modified and the usual Breit-Wigner line shape, which was not possible for previous experiments. The strong pion coupling constant h_2 in the decay $\Lambda_c(2595)^+ \to \Sigma_c(2455)^{0,++}\,\pi^\pm$ is measured instead of the usual decay width. This quantity is of theoretical interest for the prediction of other excited charmed and bottom baryons.

The data used for this work correspond to the world largest samples of the studied excited charmed baryons. Therefore, these measurements provide a significant improvement in the knowledge on their resonance parameters and represent the first analysis of charmed baryons at a hadron collider.

To search for time-integrated CP violation in the decay $D^0 \to K^0_S\,\pi^+\,\pi^-$, the production flavor, that is D^0 or $\bar{D}^0$, is tagged by the charge of the slow pion in the preceding decay $D^*(2010)^+ \to D^0\,\pi^+$. Like for the charmed baryon resonances, the $D^*(2010)^+$ signal selection is also performed by means of NeuroBayes in combina-

tion with the ${}_s\mathcal{P}lot$ technique using real data only for the training.

The Dalitz plot technique is employed to study the rich resonant substructure of the considered three-body D^0 decay. In performing the first full Dalitz fit at a hadron collider the relative amplitudes, phases, and fit fractions of the various intermediate resonances are determined, the results being compatible and comparable in precision to the measurements from previous experiments.

CP asymmetries are searched for in distinct fits to the D^0 and $\bar{D}^0$ Dalitz plots as well as a simultaneous fit. For each included intermediate resonance a CP violating fit fraction, amplitude, and phase are determined. None of these values is significantly different from zero. This also holds for the overall integrated CP asymmetry which is obtained as

$$\mathcal{A}_{CP} = -0.0045 \pm 0.0056 \pm 0.0054\,.$$

Besides, a complementary model-independent search for localized CP anisotropies in the binned D^0 and $\bar{D}^0$ Dalitz plots is performed, that yields a zero result, too. So in conclusion, no hints for any CP violating effects in $D^0 \to K^0_S\,\pi^+\,\pi^-$ are found and the most precise values for the overall integrated CP asymmetry as well as the CP violating fit fractions, amplitudes, and phases are reported.

The analysis at hand could also serve as starting point for further CDF measurements basing on the Dalitz structure of $D^0 \to K^0_S\,\pi^+\,\pi^-$, namely a study of D^0-$\bar{D}^0$ mixing and a determination of the CKM angle γ by means of $B^\mp \to D\,K^\mp$.

A. Charmed Baryon Networks for odd-numbered Events

A.1. Λ_c^+ Selection

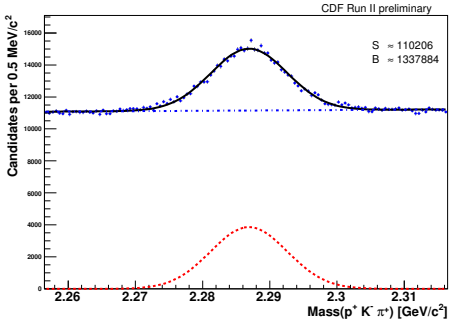

Figure A.1.: Invariant mass distribution of the odd-numbered Λ_c^+ candidates after application of the precuts in Table 5.4. All candidates used to fill this histogram are fed to the network as training pattern. The corresponding ${}_s\mathcal{P}lot$ weights are calculated by means of the fitted signal and background functions.

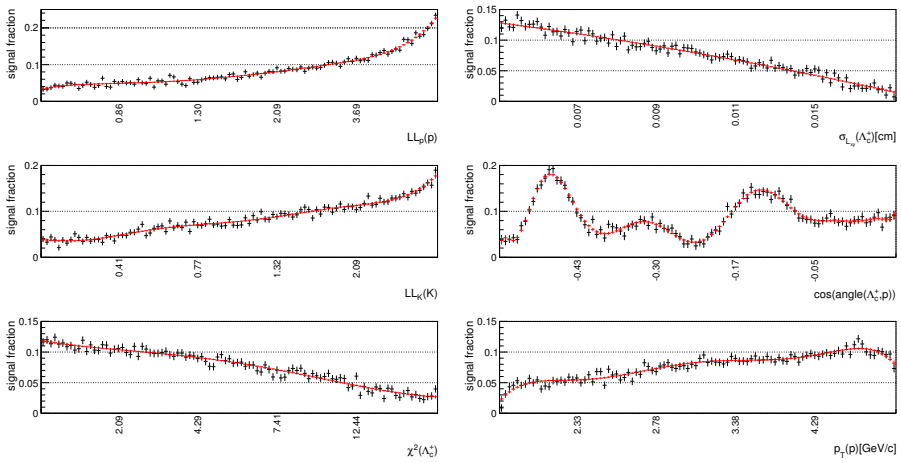

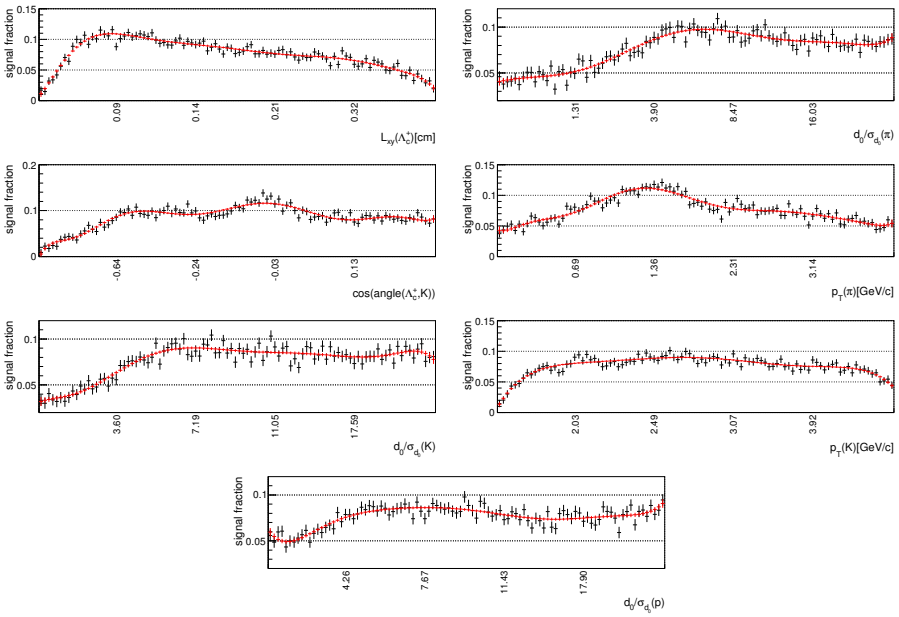

Figure A.2.: Spline fits to the flat signal fraction distributions of the different input variables of the Λ_c^+ network training with odd-numbered events.

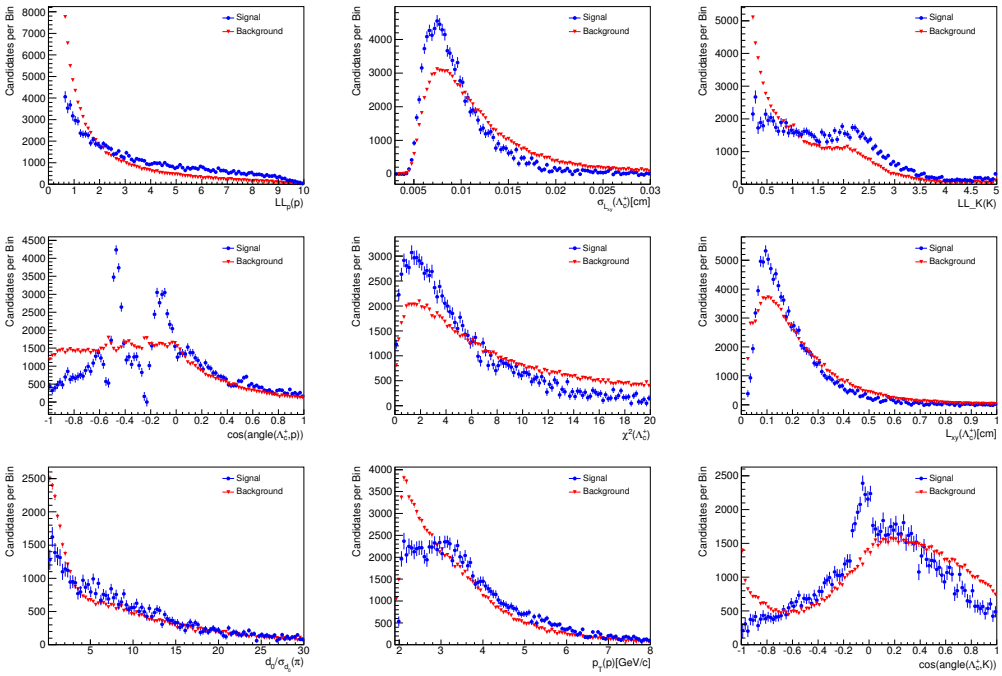

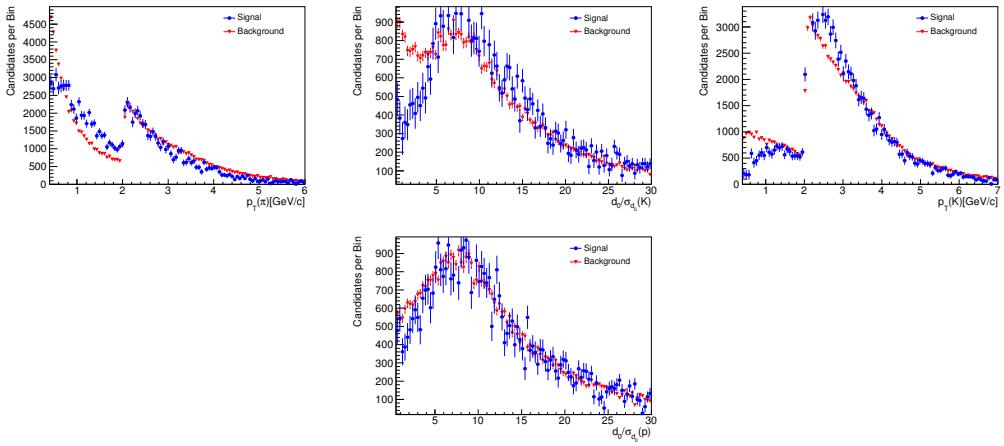

Figure A.3.: Distributions of the different variables of the odd-numbered Λ_c^+ network separately for signal and background candidates.

A.2. $\Sigma_c(2455)$ and $\Sigma_c(2520)$ Selection

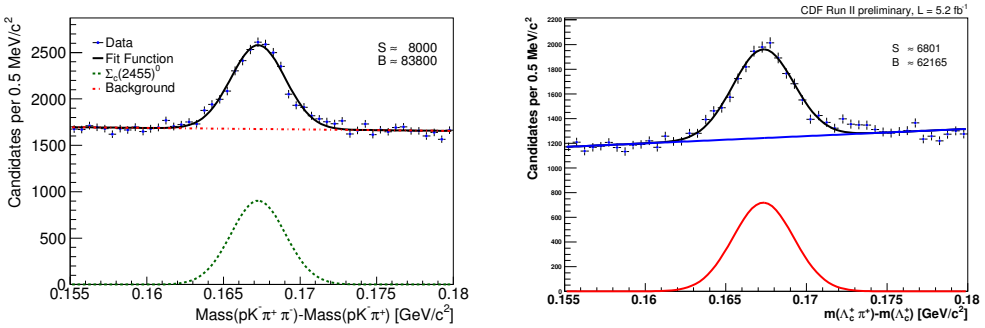

Figure A.4.: Spectra of the mass differences $m(\Lambda_c^+\,\pi^-) - m(\Lambda_c^+)$ (left) and $m(\Lambda_c^+\,\pi^+) - m(\Lambda_c^+)$ (right) of the odd-numbered $\Sigma_c(2455)^0$ respective $\Sigma_c(2455)^{++}$ candidates after application of the precuts. All candidates used to fill this histogram are fed to the network as training pattern. The corresponding ${}_s\mathcal{P}lot$ weights are calculated by means of the fitted signal and background functions.

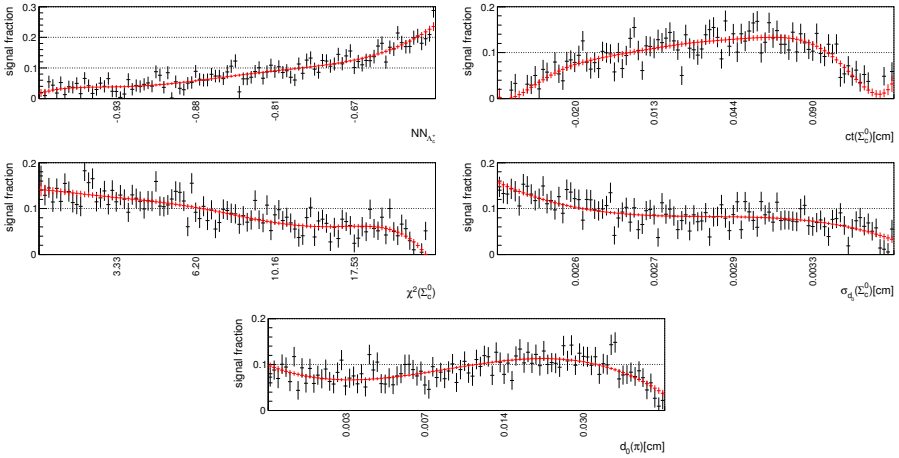

Figure A.5.: Spline fits to the flat signal fraction distributions of the different input variables of the Σ_c^0 network training with odd-numbered events ordered by their importance for the network.

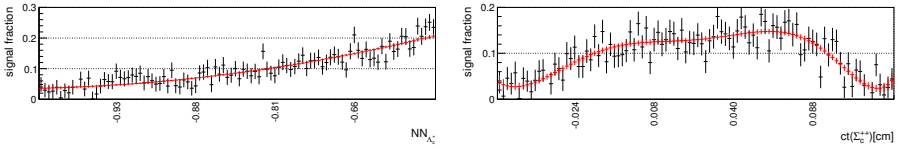

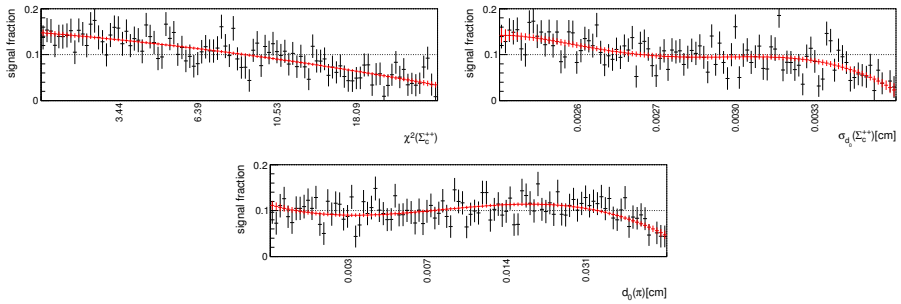

Figure A.6.: Spline fits to the flat signal fraction distributions of the different input variables of the Σ_c^{++} network training with odd-numbered events ordered by their importance for the network.

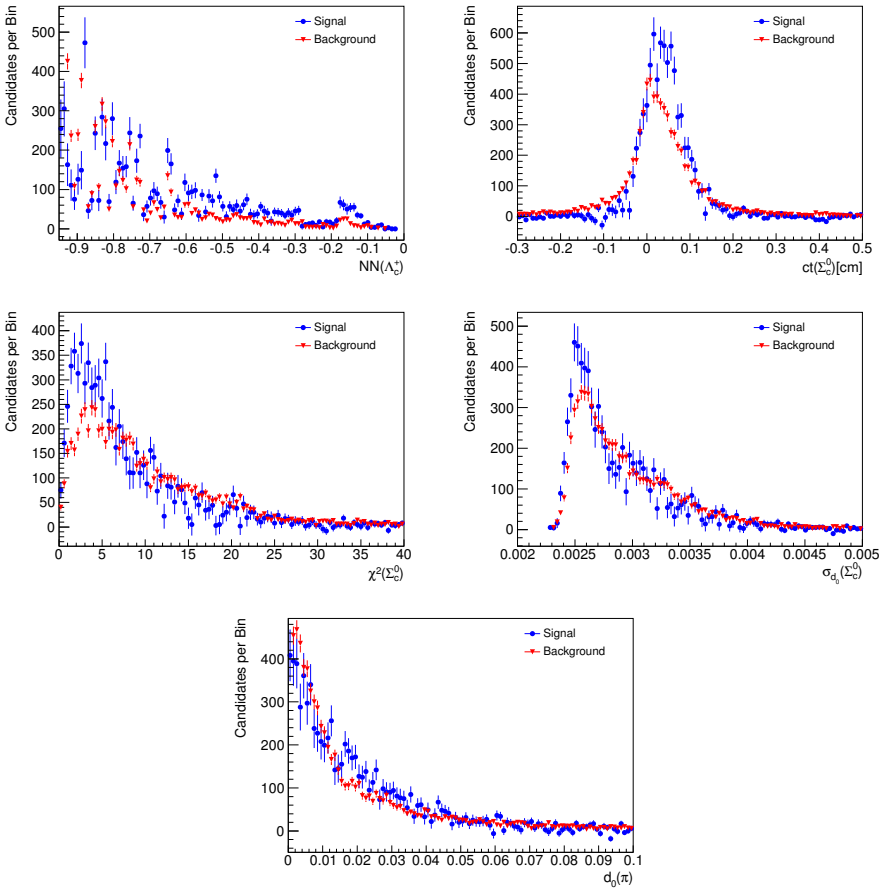

Figure A.7.: Distributions of the different variables of the even-numbered Σ_c^0 network separately for signal and background candidates.

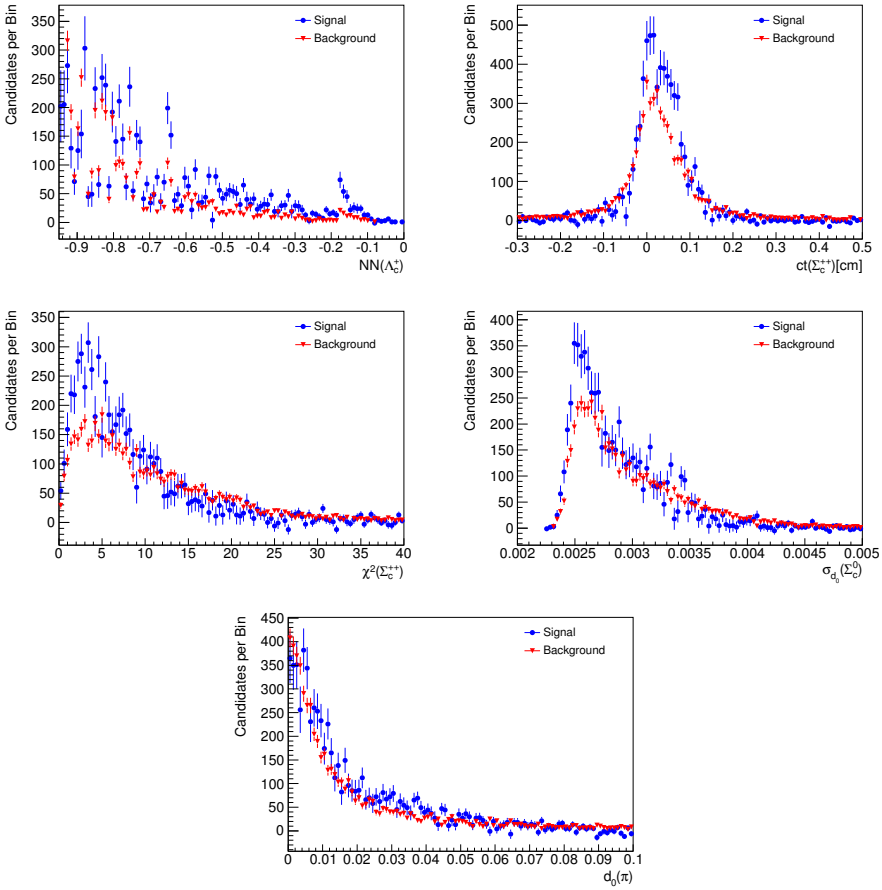

Figure A.8.: Distributions of the different variables of the even-numbered Σ_c^{++} network separately for signal and background candidates.

A.3. $\Lambda_c(2595)^+$ and $\Lambda_c(2625)^+$ Selection

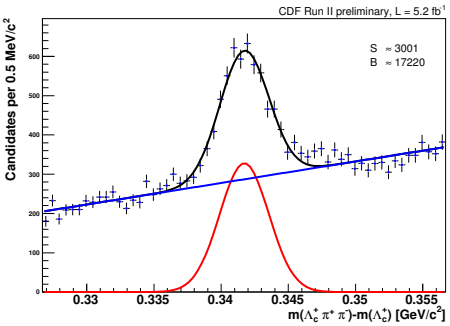

Figure A.9.: Spectrum of the mass difference $m(\Lambda_c^+ \pi^+ \pi^-) - m(\Lambda_c^+)$ of the odd-numbered $\Lambda_c(2625)^+$ candidates after application of the precuts. All candidates used to fill this histogram are fed to the network as training pattern. The corresponding ${}_s\mathcal{P}lot$ weights are calculated by means of the fitted signal and background functions.

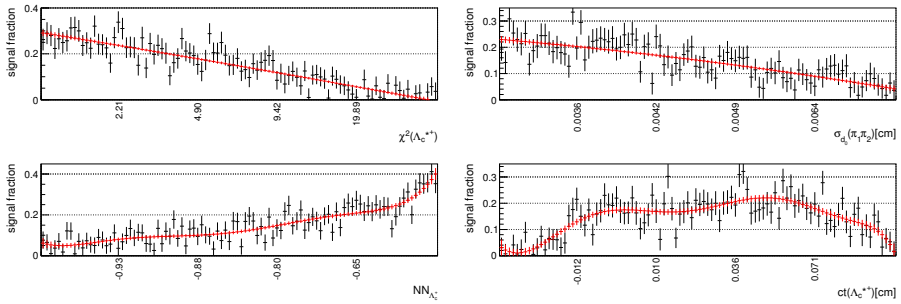

Figure A.10.: Spline fits to the flat signal fraction distributions of the different input variables of the Λ_c^* network training with odd-numbered events ordered by their importance for the network.

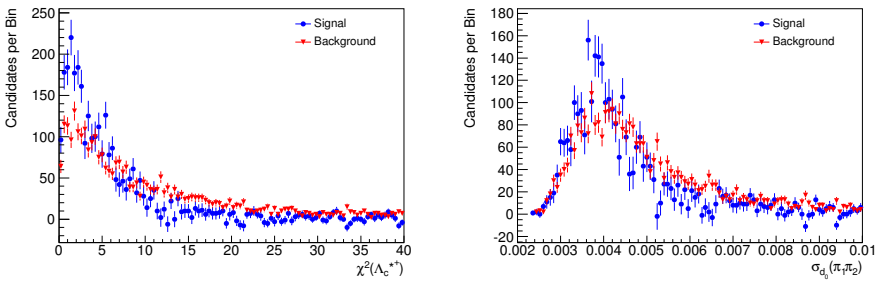

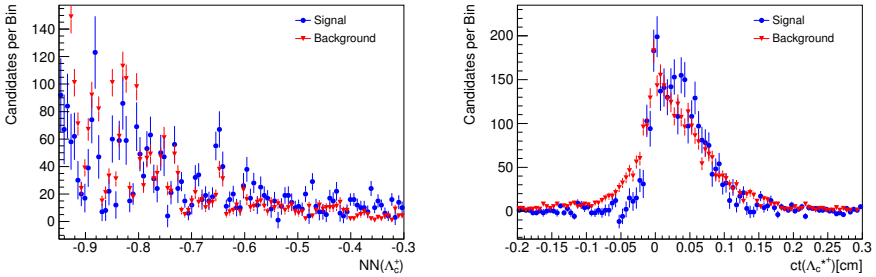

Figure A.11.: Distributions of the different variables of the odd-numbered Λ_c^* network separately for signal and background candidates.

A.4. Validation of Neural Networks

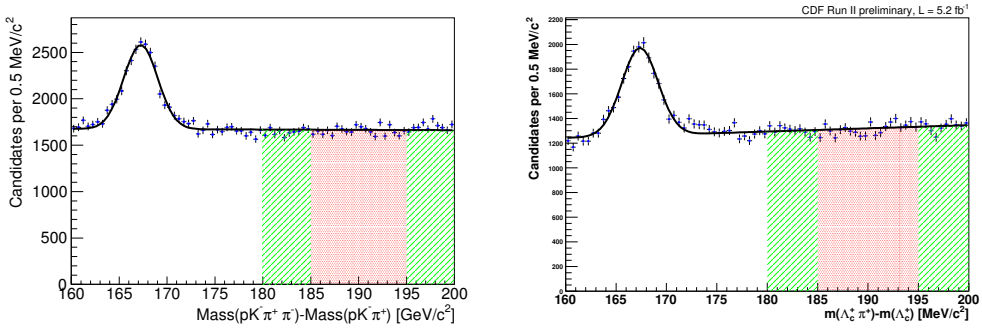

Figure A.12.: Upper $\Sigma_c(2455)^0$ (left) respective $\Sigma_c(2455)^{++}$ (right) sideband used for the odd-numbered background versus background training. The candidates populating the middle red respective outer green mass difference regions are used for the two classification patterns.

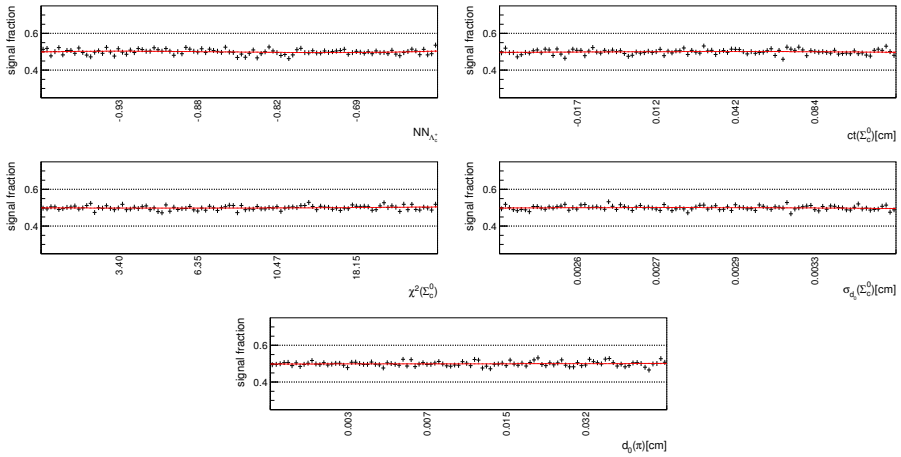

Figure A.13.: Spline fits to the flat signal fraction distributions of the different input variables of the Σ_c^0 background versus background network training with odd-numbered events.

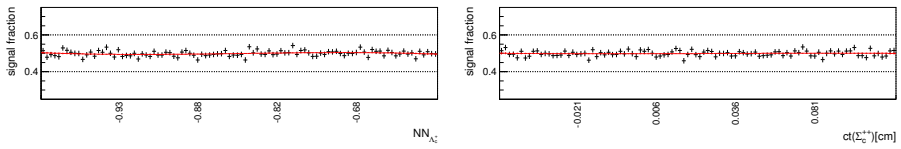

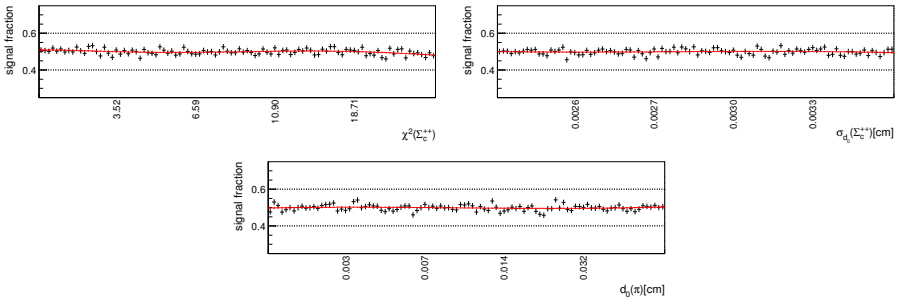

Figure A.14.: Spline fits to the flat signal fraction distributions of the different input variables of the Σ_c^{++} background versus background network training with odd-numbered events.

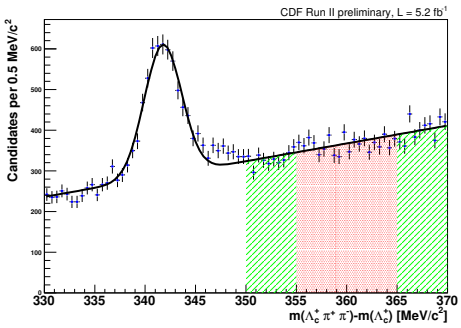

Figure A.15.: Upper $\Lambda_c(2625)^+$ sideband used for the odd-numbered background versus background training. The candidates populating the middle red respective outer green mass difference regions are used for the two classification patterns.

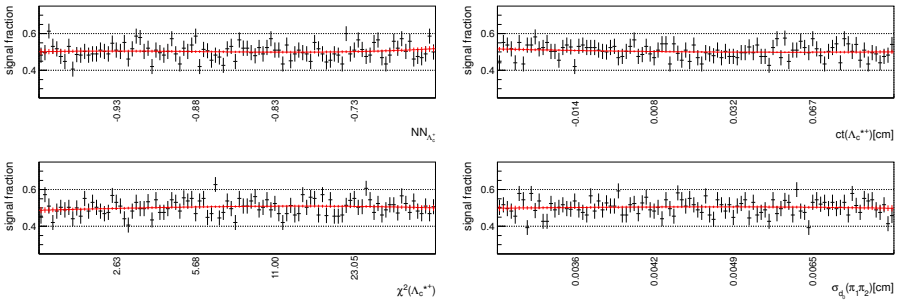

Figure A.16.: Spline fits to the flat signal fraction distributions of the different input variables of the Λ_c^{*+} background versus background network training with odd-numbered events.

B. $D^*(2010)^+$ Network for odd-numbered Events

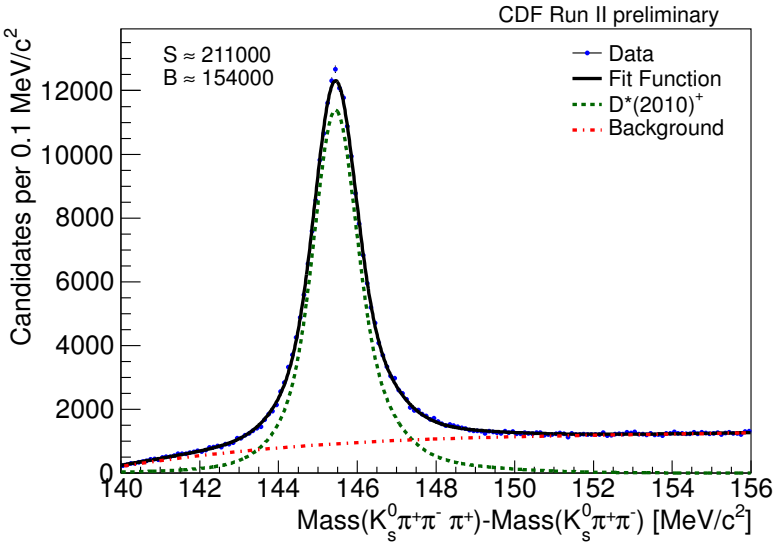

Figure B.1.: Spectrum of the invariant mass of the odd-numbered D^{*+} candidates after application of the precuts in table 6.2. All candidates used to fill this histogram are fed to the network as training pattern. The corresponding ${}_s\mathcal{P}lot$ weights are calculated by means of the fitted signal and background functions.

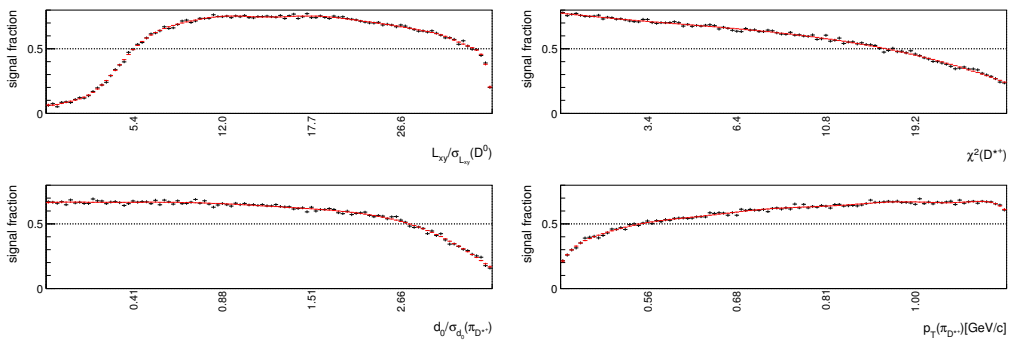

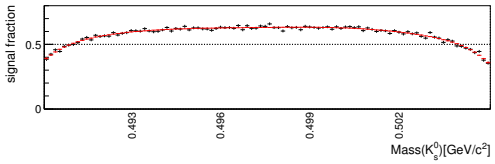

Figure B.2.: Spline fits to the flat signal fraction distributions of the different input variables of the D^{*+} network training with odd-numbered events.

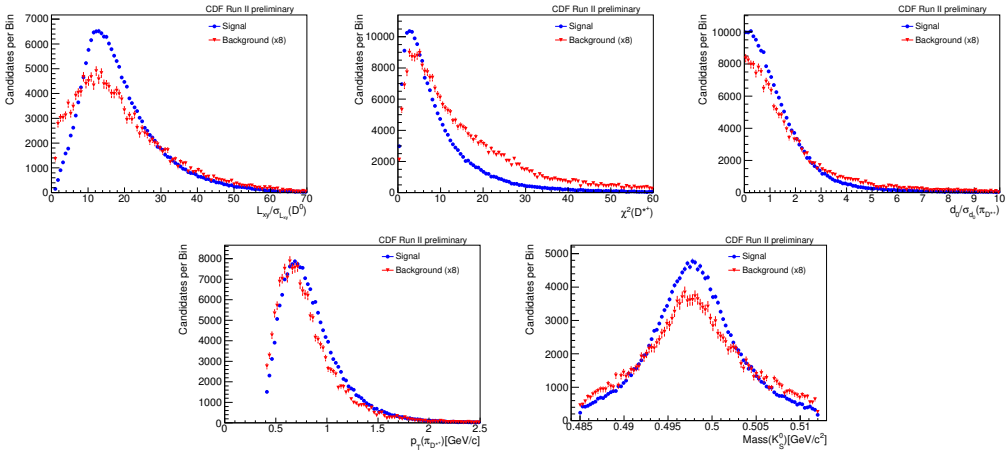

Figure B.3.: Distributions of the different variables of the odd-numbered D^{*+} network separately for signal and background candidates.

List of Figures

List of Tables

Bibliography

[1] K. Nakamura et al. Review of Particle Physics. *J. Phys. G*, 37:075021, 2010.

[2] D. J. Gross and F. Wilczek. Ultraviolet behavior of non-abelian gauge theories. *Phys. Rev. Lett.*, 30(26):1343–1346, 1973.

[3] H. D. Politzer. Reliable perturbative results for strong interactions? *Phys. Rev. Lett.*, 30(26):1346–1349, 1973.

[4] `http://www.fnal.gov/`.

[5] N. Cabibbo. Unitary Symmetry and Leptonic Decays. *Phys. Rev. Lett.*, 10:531–533, 1963.

[6] M. Kobayashi and T. Maskawa. CP Violation in the Renormalizable Theory of Weak Interaction. *Prog. Theor. Phys.*, 49:652–657, 1973.

[7] J. H. Christenson, J. W. Cronin, V. L. Fitch, and R. Turlay. Evidence for the 2π Decay of the K_2^0 Meson. *Phys. Rev. Lett.*, 13:138–140, 1964.

[8] `http://www-bd.fnal.gov/`.

[9] The CDF II Detector Technical Design Report. FERMILAB-Pub-96/390-E.

[10] D. Acosta et al. Measurement of the J/psi meson and b-hadron production cross sections in p anti-p collisions at s(NN)**(1/2) = 1960-GeV. *Phys. Rev. D*, 71:032001, 2005.

[11] `http://www-cdf.fnal.gov/`.

[12] A. Sill. CDF Run II Silicon Tracking Projects. *Nucl. Instrum. Methods A*, 447:1–8, 2000.

[13] A. Affolder et al. Intermediate Silicon Layers Detector for the CDF Experiment. *Nucl. Instrum. Methods A*, 453:84–88, 2000.

[14] C. S. Hill. Operational experience and performance of the CDF II silicon detector. *Nucl. Instrum. Methods A*, 530:1–6, 2004.

[15] A. A. Affolder et al. CDF central outer tracker. *Nucl. Instrum. Methods A*, 526:249–299, 2004.

[16] D. Acosta et al. A time-of-flight detector in CDF-II. *Nucl. Instrum. Methods A*, 518:605–608, 2004.

[17] S. Kuhlmann et al. The CDF Calorimetry Upgrade for Run IIb. *Nucl. Instrum. Methods A*, 518:39–41, 2004.

[18] A. Artikov et al. Design and construction of new central and forward muon counters for CDF II. *Nucl. Instrum. Methods A*, 538:358–371, 2005.

[19] A. Annovi. CDF: B physics performance and trigger - Operational experience. *Nucl. Phys. Proc. Suppl.*, 170:283–287, 2007.

[20] E. J. Thomson et al. Online track processor for the CDF upgrade. *IEEE Trans. Nucl. Sci.*, 49:1063–1070, 2002.

[21] B. Ashmanskas et al. The CDF Silicon Vertex Trigger. *Nucl. Instrum. Methods A*, 518:532–536, 2004.

[22] L. Ristori and G. Punzi. Triggering on Heavy Flavors at Hadron Colliders. *Ann. Rev. Nucl. Part. Sci*, 60:595–614, 2010.

[23] G. Gomez-Ceballos et al. Event builder and Level 3 at the CDF experiment. *Nucl. Instrum. Methods A*, 518:522–524, 2004.

[24] M. Feindt and U. Kerzel. The NeuroBayes neural network package. *Nucl. Instrum. Methods A*, 559:190–194, 2006.

[25] Michael Feindt. A neural bayesian estimator for conditional probability densities. arXiv:physics/0402093, 2004.

[26] M. Pivk and F. R. Le Diberder. sPlot: a statistical tool to unfold data distributions. *Nucl. Instrum. Methods A*, 555:356–369, 2005.

[27] M. Pivk. sPLOT: A quick introduction. arXiv:physics/0602023, 2006.

[28] T. Aaltonen et al. Measurements of the properties of $\Lambda_c(2595)$, $\Lambda_c(2625)$, $\Sigma_c(2455)$, and $\Sigma_c(2520)$ baryons. *Phys. Rev. D*, 84:012003, 2011.

[29] T. Mannel, W. Roberts, and Z. Ryzak. Baryons in the heavy quark effective theory. *Nucl. Phys.*, B355(1):38–53, 1991.

[30] D. B. Lichtenberg, W. Namgung, E. Predazzi, and J. G. Wills. Baryon masses in a relativistic quark-diquark model. *Phys. Rev. Lett.*, 48(24):1653–1656, 1982.

[31] T. Onogi. Progress in lattice QCD. arXiv:hep-ph/0906.2344, 2009.

[32] N. Mathur, R. Lewis, and R. M. Woloshyn. Charmed and bottom baryons from lattice NRQCD. *Phys. Rev. D*, 66:014502, 2002.

[33] W. Roberts and M. Pervin. Heavy baryons in a quark model. *Int. J. Mod. Phys. A*, 23:2817–2860, 2008.

[34] D. Ebert, R. N. Faustov, and V. O. Galkin. Masses of excited heavy baryons in the relativistic quark model. *Phys. Lett. B*, 659:612–620, 2008.

[35] D. Ebert, R. N. Faustov, and V. O. Galkin. Masses of heavy baryons in the relativistic quark model. *Phys. Rev. D*, 72:034026, 2005.

[36] J. Zhang and M. Huang. Heavy baryon spectroscopy in QCD. *Phys. Rev. D*, 78:094015, 2008.

[37] A. Bernotas and V. Simonis. Heavy hadron spectroscopy and the bag model. *Lith. J. Phys.*, 49:19, 2009.

[38] M. A. Ivanov, J. G. Körner, V. E. Lyubovitskij, and A. G. Rusetsky. One pion charm baryon transitions in a relativistic three quark model. *Phys. Lett. B*, 442:435–442, 1998.

[39] M. A. Ivanov, J. G. Körner, V. E. Lyubovitskij, and A. G. Rusetsky. Strong and radiative decays of heavy flavored baryons. *Phys. Rev. D*, 60:094002, 1999.

[40] S. Tawfiq, P. J. O'Donnell, and J. G. Körner. Charmed baryon strong coupling constants in a light front quark model. *Phys. Rev. D*, 58:054010, 1998.

[41] M. Huang, Y. Dai, and C. Huang. Decays of excited charmed Lambda type and Sigma type baryons in heavy hadron chiral perturbation theory. *Phys. Rev. D*, 52:3986–3992, 1995.

[42] D. Pirjol and T. Yan. Predictions for s wave and p wave heavy baryons from sum rules and constituent quark model. 1. Strong interactions. *Phys. Rev. D*, 56:5483–5510, 1997.

[43] J. L. Rosner. Charmed baryons with J = 3/2. *Phys. Rev. D*, 52:6461–6465, 1995.

[44] M. Artuso et al. Measurement of the masses and widths of the Sigma++(c) and Sigma0(c) charmed baryons. *Phys. Rev. D*, 65:071101, 2002.

[45] J. M. Link et al. Measurement of natural widths of Sigma0(c) and Sigma++(c) baryons. *Phys. Lett. B*, 525:205–210, 2002.

[46] G. Brandenburg et al. Observation of two excited charmed baryons decaying into Lambda(c)+ pi+-. *Phys. Rev. Lett.*, 78:2304–2308, 1997.

[47] S. B. Athar et al. A New measurement of the masses and widths of the Sigma*++(c) and Sigma*0(c) charmed baryons. *Phys. Rev. D*, 71:051101, 2005.

[48] H. Albrecht et al. Evidence for Lambda(c)+ (2593) production. *Phys. Lett. B*, 402:207–212, 1997.

[49] P. L. Frabetti et al. An observation of an excited state of the Λ_c^+ baryon. *Phys. Rev. Lett.*, 72:961–964, 1994.

[50] P. L. Frabetti et al. Study of higher mass charm baryons decaying to Lambda(c)+. *Phys. Lett. B*, 365:461–469, 1996.

[51] K. W. Edwards et al. Observation of excited baryon states decaying to Lambda(c)+ pi+ pi-. *Phys. Rev. Lett.*, 74:3331–3335, 1995.

[52] A. E. Blechman, A. F. Falk, D. Pirjol, and J. M. Yelton. Threshold effects in excited charmed baryon decays. *Phys. Rev. D*, 67:074033, 2003.

[53] D. J. Lange. The EvtGen particle decay simulation package. *Nucl. Instrum. Methods A*, 462:152–155, 2001.

[54] P. L. Cho. Strong and electromagnetic decays of two new Lambda(c)* baryons. *Phys. Rev. D*, 50:3295–3302, 1994.

[55] E. Follana, C.T.H. Davies, G.P. Lepage, and J. Shigemitsu. High Precision determination of the pi, K, D and D(s) decay constants from lattice QCD. *Phys. Rev. Lett.*, 100:062002, 2008.

[56] D. Acosta et al. Measurement of b hadron masses in exclusive J/ψ decays with the CDF detector. *Phys. Rev. Lett.*, 96:202001, 2006.

[57] T. Aaltonen et al. Precision Measurement of the X(3872) Mass in J/psi pi+ pi- Decays. *Phys. Rev. Lett.*, 103:152001, 2009.

[58] A. Abulencia et al. Measurement of mass and width of the excited charmed meson states D0(1) and D*0(2) at CDF. *Phys. Rev. D*, 73:051104, 2006.

[59] D. Aston et al. A Study of K- pi+ Scattering in the Reaction K- p $\rightarrow$ K- pi+ n at 11-GeV/c. *Nucl. Phys.*, B296:493, 1988.

[60] S. Godfrey and N. Isgur. Mesons in a Relativized Quark Model with Chromodynamics. *Phys. Rev. D*, 32:189–231, 1985.

[61] G. Chiladze and A. F. Falk. Phenomenology of new baryons with charm and strangeness. *Phys. Rev. D*, 56:R6738–6741, 1997.

[62] E. M. Aitala et al. Mass Splitting and Production of Σ_c^0 and Σ_c^{++} Measured in 500 GeV π^--N Interactions. *Phys. Lett. B*, 379:292–298, 1996.

[63] D. J. Herndon, P. Söding, and R. J. Cashmore. Generalized isobar model formalism. *Phys. Rev. D*, 11:3165–3182, 1975.

[64] H. Muramatsu et al. Dalitz Analysis of $D^0 \to K_S^0\,\pi^+\,\pi^-$. *Phys. Rev. Lett.*, 89:251802, 2002.

[65] A. Poluektov et al. Evidence for direct CP violation in the decay $B^\pm \to D^{(*)}\,K^\pm$, $D^0 \to K_S^0\,\pi^+\,\pi^-$ and measurement of the CKM phase Φ_3. *Phys. Rev. D*, 81:112002, 2010.

[66] P. del Amo Sanchez et al. Measurement of D^0-$\bar{D}^0$ Mixing Parameters Using $D^0 \to K_S^0\,\pi^+\,\pi^-$ and $D^0 \to K_S^0\,K^+\,K^-$ Decays. *Phys. Rev. Lett.*, 105:081803, 2010.

[67] B. Aubert et al. Improved measurement of the CKM angle γ in $B^\mp \to D^{(*)}K^{(*)\mp}$ decays with a Dalitz plot analysis of D decays to $K_S^0\pi^+\pi^-$ and $K_S^0K^+K^-$. *Phys. Rev. D*, 78:034023, 2008.

[68] V. V. Anisovich and A. V. Sarantsev. K-matrix analysis of the $(IJ^{PC} = 00^{++})$-wave in the mass region below 1900 MeV. *Eur. Phys. J.*, A16:229–258, 2003.

[69] J. Adler et al. Resonant Substructure in $K\pi\pi$ Decays of Charmed D Mesons. *Phys. Lett.*, B196:107, 1987.

[70] J. C. Anjos et al. A Dalitz plot analysis of $D \to K\,\pi\,\pi$. *Phys. Rev. D*, 48:56–62, 1993.

[71] H. Albrecht et al. A Partial wave analysis of the decay $D^0 \to K_S^0\,\pi^+\,\pi^-$. *Phys. Lett.*, B308:435–443, 1993.

[72] P. L. Frabetti et al. Analysis of three $D \to K\,\pi\,\pi$ Dalitz plots. *Phys. Lett.*, B331:217–226, 1994.

[73] D. M. Asner et al. Search for D^0-$\bar{D}^0$ mixing in the Dalitz plot analysis of $D^0 \to K_S^0\,\pi^+\,\pi^-$. *Phys. Rev. D*, 72:012001, 2005.

[74] L. M. Zhang et al. Measurement of D^0-$\bar{D}^0$ Mixing Parameters in $D^0 \to K_S\,\pi^+\,\pi^-$ Decays. *Phys. Rev. Lett.*, 99:131803, 2007.

[75] D. Asner et al. Averages of b-hadron, c-hadron, and tau-lepton Properties. arXiv:hep-ex/1010.1589v2, 2011.

[76] I. I. Bigi and H. Yamamoto. Interference between Cabibbo allowed and doubly forbidden transitions in $D \to K_{S,L} + \pi' s$ decays. *Phys. Lett.*, B349:363–366, 1995.

[77] Z.-Z. Xing. Effect of K^0-$\bar{K}^0$ mixing on CP asymmetries in weak decays of D and B mesons. *Phys. Lett.*, B353:313–318, 1995.

[78] D. M. Asner et al. Search for CP violation in $D^0 \to K^0_S \pi^+ \pi^-$. *Phys. Rev. D*, 70:091101, 2004.

[79] A. Giri, Y. Grossman, A. Soffer, and J. Zupan. Determining γ using $B^\pm \to D K^\pm$ with multibody D decays. *Phys. Rev. D*, 68:054018, 2003.

[80] P. del Amo Sanchez et al. Evidence for Direct CP Violation in the Measurement of the Cabbibo-Kobayashi-Maskawa Angle γ with $B^\mp \to D^{(*)} K^{(*)\mp}$. *Phys. Rev. Lett.*, 105:121801, 2010.

[81] J. Podolanski and R. Armenteros. *Phil. Mag.*, 45:13, 1954.

[82] R. H. Dalitz. On the analysis of τ-meson data and the nature of the τ-meson. *Phil. Mag.*, 44:1068, 1953.

[83] G. J. Gounaris and J. J. Sakurai. Finite width corrections to the vector meson dominance prediction for $\rho \to e^+ e^-$. *Phys. Rev. Lett.*, 21:244–247, 1968.

[84] D. Aston et al. A Study of $K^-\pi^+$ Scattering in the Reaction $K^- p \to K^-\pi^+ n$ at 11 GeV/c. *Nucl. Phys.*, B296:493, 1988.

[85] A. Poluektov et al. Measurement of Φ_3 with Dalitz plot analysis of $B^\pm \to D^{(*)} K^\pm$, $D^0 \to K^0_S \pi^+ \pi^-$ decay. *Phys. Rev. D*, 70:072003, 2004.

[86] E. M. Aitala et al. Study of the $D_s^+ \to \pi^-\pi^+\pi^+$ Decay and Measurement of f_0 Masses and Widths. *Phys. Rev. Lett.*, 86:765–769, 2001.

[87] Improved measurement of time-integrated CP violation in $D^0 \to h^+h^-$ decays. Public CDF Note 10296, 2010.

[88] I. Bediaga et al. On a CP anisotropy measurement in the Dalitz plot. *Phys. Rev. D*, 80:096006, 2009.

Danksagung

Mein besonderer Dank gebührt Herrn Prof. Dr. Michael Feindt für die Aufnahme in seine Arbeitsgruppe und die Ermöglichung dieser Doktorarbeit. Außerdem danke ich Herrn Prof. Dr. Günter Quast für die Übernahme des Korreferats.

Desweiteren möchte ich mich bei Dr. Thomas Kuhr und Dr. Michal Kreps für die sehr gute Betreuung und unzähligen Hilfestellungen herzlich bedanken. Dr. Thomas Kuhr danke ich auch für das Korrekturlesen dieser Arbeit.

Allen Mitgliedern des Instituts für Experimentelle Kernphysik danke ich für die sehr angenehme Arbeitsatmosphäre. Vielen Dank auch an das Administratoren-Team und unsere Institutssekretärin Frau Bärbel Bräunling.

Finanziert wurde diese Dissertation durch ein Stipendium des Graduiertenkollegs Hochenergiephysik und Teilchenastrophysik der Deutschen Forschungsgemeinschaft.